SISSA
Scuola
Internazionale
Superiore di
Studi Avanzati

Physics Area - PhD course in
Astrophysics and Cosmology

Relativistic accretion disk models for Active Galactic Nuclei:

mass and spin of Supermassive black holes

Candidate:
Samuele CAMPITIELLO

Advisors:
Annalisa Celotti
Gabriele Ghisellini

Academic Year 2020 - 21

DOCTORAL THESIS

Relativistic accretion disk models for Active Galactic Nuclei:

mass and spin of Supermassive black holes

Candidate:
Samuele CAMPITIELLO

Advisors:
Annalisa Celotti
Gabriele Ghisellini

A thesis submitted in fulfillment of the requirements for the degree of Doctor of Philosophy

Astrophysics and Cosmology Group
SISSA

To My mother and father, an example of pure and true simplicity
To My brother, an example of precision and commitment

Abstract

SISSA

Doctor of Phylosophy

Relativistic accretion disk models for Active Galactic Nuclei: mass and spin of Supermassive black holes

by Samuele CAMPITIELLO

Active Galactic Nuclei are among the brightest and most energetic objects in the Universe and determining their **mass** M and **spin** a is crucial for understanding their physical nature, the link with the host galaxy and their possible evolution in time. The commonly accepted scenario describes them with a supermassive black hole of $10^6 - 10^{10} M_\odot$ at their center along with an accretion disk of hot rotating matter. The surrounding environment (e.g., dusty torus, Broad and Narrow Line Region) is thought to be shaped by both the strong gravitational field of the black hole and the disk radiation.

Uncertainties on their mass and spin are still too large and new methods have to be used to set more stringent constraints. In this thesis, I used different accretion disk models to predict the main black hole features (i.e., mass and spin), comparing them with different independent measurements, and to study the surrounding environment (i.e., the dusty torus), shaped by the relativistic disk radiation pattern.

The topics and results discussed in this thesis have been published in refereed journals.

- **Chapter 3 - 4.1**: *How to constrain mass and spin of supermassive black holes through their disk emission*, **Campitiello, S.**, Ghisellini, G., Sbarrato, T. and Calderone, G., 2018, A&A, 612, A59.

- **Chapter 4.2**: *Black hole mass and spin estimates of the most distant quasars*, **Campitiello, S.**, Celotti, A., Ghisellini, G. and Sbarrato, T, 2019, A&A, 625, A23.

- **Chapter 4.3**: *Estimating black hole masses: Accretion disk fitting versus reverberation mapping and single epoch*, **Campitiello, S.**, Celotti, A., Ghisellini, G. and Sbarrato, T, 2020, A&A, 640, A39.

- **Chapter 5**: *The disk - torus system in Active Galactic Nuclei: possible evidence of highly spinning black holes*, **Campitiello, S.**, Celotti, A., Ghisellini, G. and Sbarrato, T., 2021, submitted to A&A.

Contents

List of Figures

List of Tables

List of Abbreviations

AD	**A**ccretion **D**isk
ADAF	**A**dvection **D**ominated **A**ccretion **Flow**
AGN	**A**ctive **G**alactic **N**ucleus
BBB	**B**ig **B**lue **B**ump
BH	**B**lack **H**ole
BLR	**B**road **L**ine **R**egion
FIRST	**F**aint **I**mages of the **R**adio **S**ky at **T**wenty-centimeter
FUSE	**F**ar **U**ltraviolet **S**pectroscopic **E**xplorer
FWHM	**F**ull **W**idth **H**alf **M**aximum
GRAD	**G**eneral **R**elativistic **A**ccretion **D**sik
HST	**H**ubble **S**pace **T**elescope
IGM	**I**nter**G**alactic **M**edium
ISCO	**I**nnermost **S**table **C**ircular **O**rbit
ISM	**I**nter**S**tellar **M**edium
IUE	**I**nternational **U**traviolet **E**xplorer
KERRBB	**KERR B**lack **B**ody
NLR	**N**arrow **L**ine **R**egion
QSO	**Q**uasi **S**tellar **O**bject (Quasar)
RM	**R**everberation **M**apping
SDSS	**S**loan **D**igital **S**ky **S**urvey
SE	**S**ingle **E**poch
SED	**S**pectral **E**nergy **D**istribution
SMBH	**S**uper **M**assive **B**lack **H**ole
SS	**S**hakura & **S**unyaev
VP	**V**irial **P**roduct
WISE	**W**ide-field **I**nfrared **S**urvey **E**xplorer

Chapter 1

Introduction

"The unknown always passes for the marvelous"
— Tacitus, *De vita et moribus Iulii Agricolae*

Contents

1.1 Active Galactic Nuclei

Supermassive black holes (SMBHs) are located at the center of massive galaxies and determining their **mass** M and **spin** a is crucial for understanding their physical nature, the link with the host galaxy and their possible evolution in time (e.g., Magorrian et al., 1998; Ferrarese and Merrit, 2000; Häring and Rix, 2004; Gültekin, Richstone, and Gebhardt, 2009; Beifiori et al., 2012; Reines and Volonteri, 2015).

Generally, the term SMBH refers to black holes (BHs) with a mass in the range $10^6 < M_{\rm BH}/M_\odot < 10^{10}$ whose gravitational energy can be released through the accretion of matter onto them. *Accretion* can occurs in 1) a chaotic way (see e.g., Pan and Yang, 2020 and references therein) or 2) in a more structured manner with the formation of an **Accretion Disk** (AD; Salpeter, 1964; Zeldovich and Novikov, 1964; Ruszkowski and Begelman, 2003; Koushiappas, Bullock, and Dekel, 2004; Volonteri and Rees, 2005; Dotti et al., 2013).

In the first case, accretion can be described assuming a spherical symmetry (e.g., Hoyle and Lyttleton, 1939; Bondi, 1952; Shima et al., 1985);[1] in the second case, accretion occurs only on the equatorial plane (with respect to the BH rotation axis): matter is heated to high temperatures ($T \sim 10^4 - 10^5$ K), part of it accretes the SMBH while a small fraction (depending on the modality of the accretion and the BH spin; Thorne, 1974) is converted into radiation.

In a disk-like configuration, the infalling mechanism of matter is caused by the loss of angular momentum due to friction between different layers of the disk (see next Chapter): the stability of the rotating matter is guaranteed up to the last stable annulus of the disk called *Innermost Stable Circular Orbit* (ISCO), whose distance from the SMBH depends on its spin: the ISCO is 3 times the Schwarzschild radius (defined as $2GM_{\rm BH}/c^2$) for a non-rotating BH while, if relativistic effects are taken into account, for a maximally rotating BH ($a = 0.9982$) with an AD co-rotating with it, the ISCO is equal to one R_g ($1.24R_g$ if the radiation capture of the BH is considered), where $R_g = GM/c^2$ is the gravitational radius. In the counter-rotating case the ISCO is $9R_g$ (Thorne, 1974; see Fig. 1.4). The fraction of matter released as radiation is referred as *radiative efficiency* η (see Sect. 1.2).[2] Objects which release energy in this way are classified as **Active Galactic Nuclei** (AGNs).

The emitted radiation coming from the accreting matter can be identified with the so-called "*Big Blue Bump*" (BBB): generally, this feature is located in the Optical-UV frequency range (i.e., $10^{14.5} < \nu/\mathrm{Hz} < 10^{16}$) of the Spectral Energy Distribution (SED) and several models have been developed to describe it in terms of the main BH-disk parameters (e.g., mass, spin, accretion rate; see Sect. 2.1). The radiation emitted by the AD can shape the surrounding environment and the relative emission (see Chap. 5). The general picture of an AGN includes different structures located at different distances from the central engine:

- Close to the inner region of the disk ($\sim 10R_{\rm g}$), a hot plasma (i.e., *X-ray Corona*) is thought to intercept part of the disk radiation that is up-scattered in the X band. The mechanism responsible for its emission is the thermal Comptonization of the electrons (e.g. Fabian et al., 2015;

[1] In the so-called Advection-dominated Accretion Flows, or ADAF, the energy is advected into the BH rather than radiated. This quasi-spherical accretion regime is applied to low luminosity sources (e.g., Ichimaru, 1977; Rees et al., 1982; Chen et al., 1995; Narayan and Yi, 1995).

[2] The efficiency depends on the BH spin: for a non-rotating BH, it is $\eta \sim 0.057$ while, for a maximally rotating BH (with a disk co-rotating with it), the efficiency is $\eta \sim 0.32$ (Thorne, 1974. See Fig. 1.4.

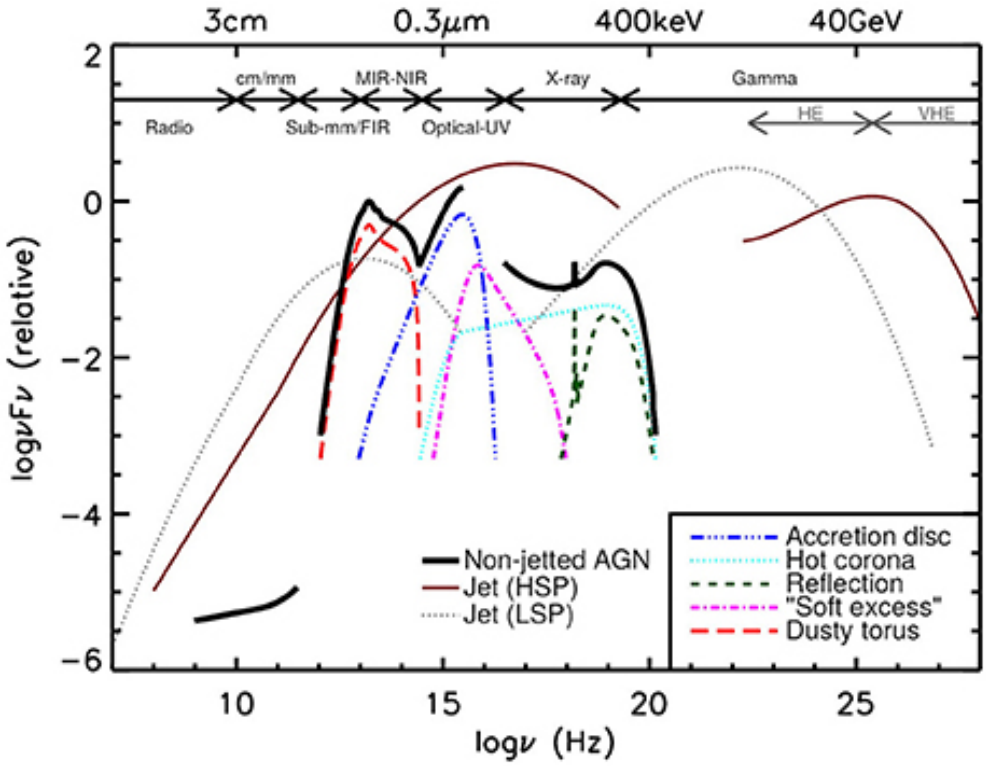

FIGURE 1.1: Average AGN Spectral Energy Distribution. HSP and LSP stand for High Synchrotron Peaked and Low Synchrotron Peaked, respectively. Figure from Padovani et al., 2017.

Lubinski et al., 2016). In the spectral shape of the X-ray Corona, sometimes it is possible to see the Iron 6.4 KeV fluorescent line whose profile is modified by the strong gravitational field of the SMBH: the study of its profile can be used to infer the BH spin (e.g., Fabian et al., 1989). The Corona is thought to be compact (e.g., Miniutti and Fabian, 2004; Done et al., 2012; Reis and Miller, 2013; Sazonov et al., 2012; Lusso and Risaliti, 2017) although several of its properties are still debated (e.g., Caballero-Garcia et al., 2019);

- The *Broad Line Region* (BLR), located close to the SMBH ($10 - 100$ light days from Reverberation Mapping studies; e.g., Kaspi et al., 2000; Peterson et al., 2004) and thought to be made of fast rotating gas clouds in a disk-like structure rather than a spherical one (as also confirmed by the GRAVITY collaboration; Sturm et al., 2018; Amorim et al., 2020), intercepts part of the disk radiation ($\sim$ 10%; e.g., Baldwin and Netzer, 1978; Smith et al., 1981; Osterbrock and Mathews, 1986; Peterson, 2006) that ionizes the surrounding gas: this latter recombines and re-emits the radiation at particular frequencies, in the form of broad emission lines.

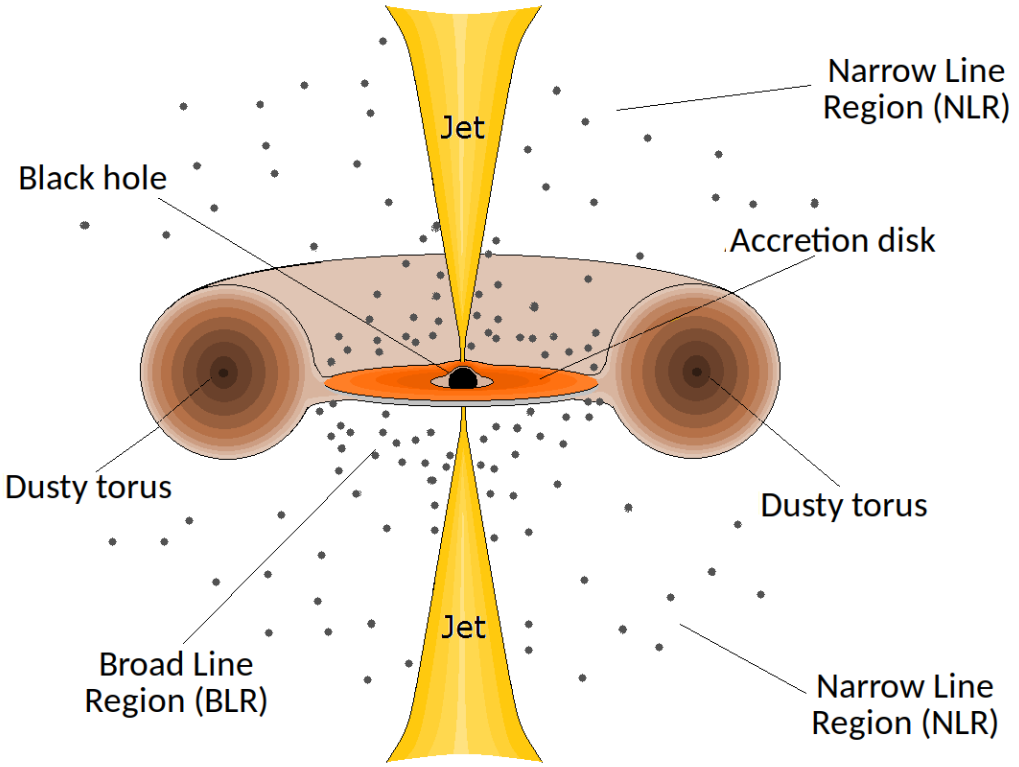

FIGURE 1.2: Schematic (not in scale) view of an AGN.

The geometry of the BLR plays a very important role in estimating the BH mass (e.g. Reverberation Mapping technique; see Sect. 4.3);

- Dust located at $1 - 10$ pc from the disk (with a temperature smaller than the sublimation value, $\sim$ 2000 K), forming a toroidal structure (i.e., *dusty torus*), intercepts part of the disk and Corona radiation and re-emits it in the IR band (e.g., Rees et al., 1969; Neugebauer et al., 1979; Barvainis, 1987). The average covering factor of the dusty torus, i.e. the fraction of solid angle covered by it as seen by the disk and a distant observer, is thought to be $\sim$ 0.7 (corresponding to an average aperture angle of $\sim 45°$) which can be inferred with different methods (see Chap. 5) and responsible for the dichotomy between Type I and Type II AGNs (e.g., Antonucci, 1993; Ghisellini, Haardt, and Matt, 1994; Urry and Padovani, 1995). As the disk, many models have been developed to describe its emission in terms of its main properties (e.g., covering factor, dust size, optical depth; see Chap. 5).

- The *Narrow line Region* NLR is the equivalent of the BLR located at a larger distance from the SMBH ($\sim$ 100 pc), composed of small gas

Class/Acronym	Meaning/Main properties	Class/Acronym	Meaning/Main properties	Class/Acronym	Meaning/Main properties
Quasar	Quasi-stellar radio source (originally)	BLAGN	Broad-line AGN, FWHM $\gtrsim$ 1,000 km s^{-1}	LPQ	Low polarization quasar
Sey1	Seyfert 1, FWHM $\gtrsim$ 1,000 km s^{-1}	BLRG	Broad-line radio galaxy	NLAGN	Narrow-line AGN, FWHM $\lesssim$ 1,000 km s^{-1}
Sey2	Seyfert 2, FWHM $\lesssim$ 1,000 km s^{-1}	CDQ	Core-dominated quasar	NLRG	Narrow-line radio galaxy
QSO	Quasi-stellar object	CSS	Compact steep spectrum radio source	NLS1	Narrow-line Seyfert 1
QSO2	Quasi-stellar object 2, high power Sey2	CT	Compton-thick	OVV	Optically violently variable (quasar)
RQ AGN	Radio-quiet AGN	FR 0	Fanaroff-Riley class 0 radio source	Population A	
RL AGN	Radio-loud AGN	FSRQ	Flat-spectrum radio quasar	Population B	
Jetted AGN	With strong relativistic jets	GPS	Gigahertz-peaked radio source	Radiative-mode	
Non-jetted AGN	Without strong relativistic jets	HBL/HSP	High-energy cutoff BL Lac/blazar	RBL	Radio-selected BL Lac
Type 1	Sey1 and quasars	HEG	High-excitation galaxy	Sey1.5	Seyfert 1.5
Type 2	Sey2 and QSO2	HPQ	High polarization quasar	Sey1.8	Seyfert 1.8
FR I	Fanaroff-Riley class I radio source	Jet-mode		Sey1.9	Seyfert 1.9
FR II	Fanaroff-Riley class II radio source	IBL/ISP	Intermediate-energy cutoff BL Lac/blazar	SSRQ	Steep-spectrum radio quasar
BL Lac	BL Lacertae object	LINER	Low-ionization nuclear emission-line regi	USS	Ultra-steep spectrum source
Blazars	BL Lacs and FSRQs	LLAGN	Low-luminosity AGN	XBL	X-ray-selected BL Lac
		LBL/LSP	Low-energy cutoff BL Lac/blazar	XBONG	X-ray bright optically normal galaxy
BAL	Broad absorption line (quasar)	LDQ	Lobe-dominated quasar		
BLO	Broad-line object, FWHM $\gtrsim$ 1,000 km s^{-1}	LEG	Low-excitation galaxy		

FIGURE 1.3: List of AGN classes. Table from Padovani et al., 2017.

clouds that, as the BLR, absorb part of the disk radiation and re-emit it in form of lines less broadened because of the smaller motion velocities.

The overall SED for an AGN is shown in Fig. 1.1. In that schematic representation, it is shown also the AGN contribution in the Radio and Gamma bands: $\sim$ 10% of AGNs show two prominent features associated with the presence of *relativistic jets* (Fig. 1.2) launched in two opposite directions along the rotation axis of the SMBH (e.g., Begelman, Blandford, and Rees, 1984; Kellermann et al., 1989; Urry and Padovani, 1995), which can 'cover' the IR-to-UV emission:[3] these jets are responsible for the acceleration of the electrons in the Synchrotron process.

Objects with a very bright radio emission are classified as *radio–loud* AGN, based on the classification criterium given by the ratio between the rest–frame radio ($\nu = 5$ GHz) and Optical (blue band B) fluxes called *radio-loudness* ($\mathcal{R} = F_{5\mathrm{GHz}}/F_{\mathrm{B}}$; e.g., Jiang et al., 2007). More in details, a radio-loud AGN is defined when $\mathcal{R} > 10$, otherwise it is classified as a *radio–quiet* (Kellermann et al., 1989). A further classification is based on the direction of relativistic jets: if they point towards our line of sight (implying a small disk inclination angle, $\theta < 5°$; e.g., Ghisellini et al., 2014), these jetted AGNs are called *Blazar*, otherwise they are simply called *Radio-galaxies*. For a list of AGN classes, see Tab. 1.3 (from the work of Padovani, 1997).

1.2 Mass and Spin of SMBHs

The *mass* of SMBHs can be estimated through many methods: *indirect methods* are related to particular relations between the BH mass and some features of the host galaxy environment (e.g., the correlation between the BH mass and

[3] In the mm-FIR bands, it is also present the contribution from the *dust heated by stars*, not represented in Fig. 1.1 for clarity.

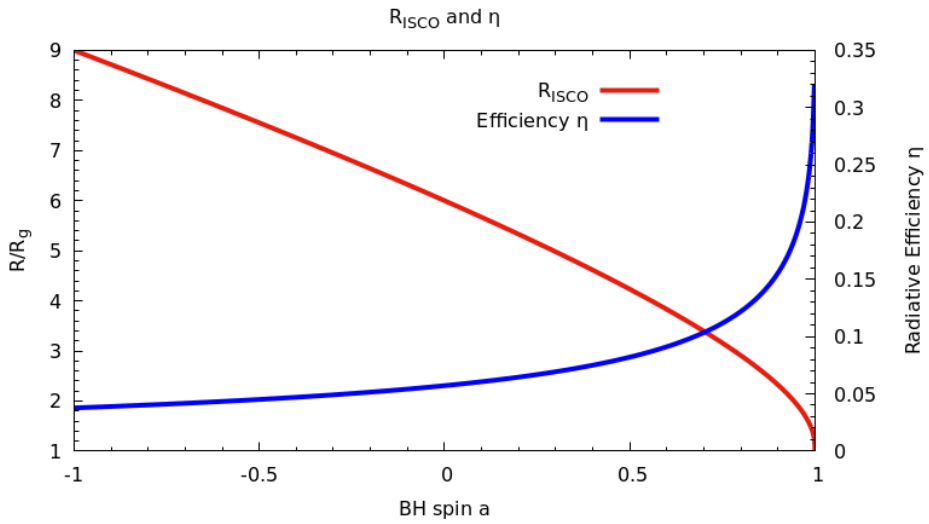

FIGURE 1.4: Innermost Stable Circular Orbit (ISCO, red line) and radiative efficiency η (blue line) as a function of the BH spin, computed by using the equations shown in Thorne, 1974.

the stellar velocity dispersion in the host bulge or elliptical galaxy; Ferrarese and Merrit, 2000); *direct methods* use the vicinity of test objects around BHs (e.g., stars or rotating matter forming an AD) to estimate their mass (e.g., *virial mass*). Here I list the most used methods for estimating the SMBH mass:

- The *Reverberation mapping* (RM) technique is based on direct measurements related to the BLR response to the continuum changes (e.g., Blandford and McKee, 1982; Peterson, 1993; Netzer and Peterson, 1997; Wandel, Peterson, and Malkam, 1999; Kaspi et al., 2000; Peterson et al., 2004; Bentz et al., 2009; Fausnaugh et al., 2017; Bentz and Manne-Nicholas, 2018; Shen et al., 2019; see also the 2D velocity-delay maps, e.g., Grier et al., 2013). The mass can be expressed as

$$M_{\rm BH} = f_{\rm BLR} \underbrace{\frac{c\ \tau_{LT}\ \sigma^2_{\rm line}}{G}}_{=VP},$$

  where the *Virial Product* (VP) is a function of $\tau_{\rm LT}$, the light-travel time (i.e., the time related to the emission-line response delayed with respect to changes in the continuum) and $\sigma_{\rm line}$, the line velocity dispersion (or the line Full Width Half Maximum - FWHM; e.g., Ho, 1999; Wandel, Peterson, and Malkam, 1999). The factor $f_{\rm BLR}$ is the so-called *geometrical factor* which is linked to the unknown kinematics and geometry of the BLR: many authors have calibrated it by comparing BH masses

obtained with different approaches (see Bentz and Katz, 2015 and references therein).[4] Some authors use $f_{\rm BLR} = 3\ (3/4)$, if the VP is computed using $\sigma_{\rm line}$ (FWHM), considering a spherical distribution of BLR clouds in randomly orientated orbits (Netzer, 1990; Wandel, Peterson, and Malkam, 1999; Kaspi et al., 2000).[5] RM estimates have a systematic uncertainty of $\sim 0.4 - 0.5$ dex (e.g., Vestergaard and Osmer, 2009);

- The *Single Epoch* (SE) virial mass is a method based on RM results which showed a link between the BH mass, the continuum/line luminosity and the $\sigma_{\rm line}$/FWHM of some lines (e.g., McLure and Jarvis, 2002; Vestergaard, 2004; McLure and Dunlop, 2004; Vestergaard and Peterson, 2006; Wang et al., 2009; Vestergaard and Osmer, 2009; Greene et al., 2010; Shen et al., 2011; Trakhtenbrot and Netzer, 2012). The mass can be expressed as

$$M_{\rm BH} = a + b\ {\rm Log}\ L_* + c\ {\rm Log\ FWHM}.$$

  Usually, many authors set $c = 2$ and calibrated the other two parameters on RM results. L_* can be either the continuum luminosity at a particular wavelength or the luminosity of a particular emission line (e.g., Hβ, MgII, CIV). As for RM estimates, SMBH masses inferred with this method have a systematic uncertainty of $0.4 - 0.5$ dex (e.g., Peterson et al., 2004; Vestergaard and Peterson, 2006; Shen et al., 2008; Park et al., 2012);

- *Water megamaser* detections in Keplerian circumnuclear disks (e.g., Miyoshi et al., 1995; Greene et al., 2010; Kuo et al., 2011 and the review by Tarchi, 2012) are close to an ideal dynamical tracer of the central SMBH as they delineate disks with well-measured Keplerian rotation curves within fractions of a pc from the center. They are detectable when the disk is aligned within a few degrees of the line of sight, and characterized by triple-peaked spectral profiles. Although SMBH mass measurements based on this method are not prone to the same systematic uncertainties as the dynamical methods, this approach has been applied to very few sources (e.g., Gao et al., 2017; Masini et al., 2019).

- The *AD fitting procedure* is based on the application of disk models to the Optical-UV BBB (e.g., Malkan, 1983; Sun and Malkan, 1989; Wandel

[4] See Li et al., 2018 for a list of $f_{\rm BLR}$ values found in literature.

[5] The line velocity dispersion is often identified either as the line FWHM or as the σ of the Gaussian profile used to fit the emission line.

and Petrosian, 1988; Laor, 1990; Rokaki, Boisson, and Collin-Souffrin, 1992; Tripp, Bechtold, and Green, 1994; Ghisellini et al., 2010; Calderone et al., 2013; Sbarrato et al., 2013; Trakhtenbrot, Volonteri, and Natarajan, 2017; Campitiello et al., 2018; Campitiello et al., 2019). Many models have been developed, also including relativistic effects (e.g., Novikov and Thorne, 1973; Page and Thorne, 1974; Riffert and Herold, 1995; Li et al., 2005) to infer the main properties of the AD and the central SMBH, showing a general agreement with the Optical-UV SED and SE BH mass estimates (e.g., Davis and Laor, 2011; Laor and Davis, 2011; Calderone et al., 2013; Castignani et al., 2013; Capellupo et al., 2015; Capellupo et al., 2016; Majia-Restrepo et al., 2016; Campitiello et al., 2018; Campitiello et al., 2019; Marculewicz and Nikolajuk, 2020).

- *Microlensing in gravitationally lensed Quasars* (QSOs) provides a direct measurement of the internal structure of the lensed QSOs (e.g., Irwin et al., 1989; Lewis et al., 1998; Richards et al., 2004; Dai et al., 2010; Mosquera and Kochanek, 2011; Sluse et al., 2011; Guerras, 2013). In principle, it is possible to reconstruct the two-dimensional structure of a particular emitting region (corresponding to a specific wavelength) up to scales of a few Astronomical Units (e.g., Moustaka et al., 2019).

- *Polarization in broad emission lines* (e.g., Savic et al., 2018); this method assumes that the broad line photons are emitted from a disk-like region undergoing Keplerian motion, after which they are scattered by the surrounding dusty torus and resulting in polarization in the broad emission lines. For details, see Afanasiev and Popovic, 2015.

- *Dynamical BH mass estimates* (e.g., Davies, 2006; Onken et al., 2007; Hicks and Malkan, 2008) which rely on direct measurements of the motion of gas or stars close to the SMBH.

- *Redshift of the Fe III lines* in QSOs accountable to the gravitational field of the central SMBH (e.g., Mediavilla et al., 2018; Mediavilla et al., 2019).

Each of the methods listed above carries some uncertainties linked to the features of the system, to the parameters of the model involved for the estimates (e.g. Laor, 1990; McLure and Jarvis, 2002; Vestergaard and Peterson, 2006; Marconi et al., 2008; Peterson, 2010; Calderone et al., 2013) and clearly to the quality of data.

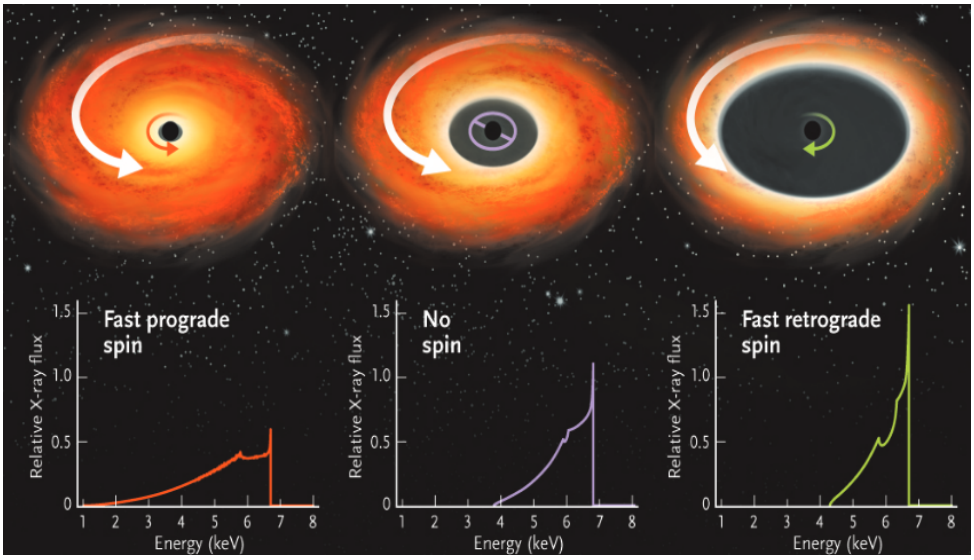

FIGURE 1.5: Iron 6.4 keV fluorescent line shape for different BH spin values.

Also for the BH *spin*, several methods have been proposed to constrain it for AGNs, although measurements still have large uncertainties given the sensitive analysis required along with good quality data (see e.g., Kammoun, Nardini, and Risaliti, 2018).

- The *Thermal Continuum Fitting method* (e.g. Zhang, Cui, and Chen, 1997; McClintock et al., 2006; McClintock, Narayan, and Steiner, 2013) treats the inner AD around a BH as a modified black-body from which it is possible to compute the ISCO and therefore the BH spin (see Fig. 1.4).

- The *Reflection method* (e.g., Fabian et al., 1989) uses the Fe fluorescent line shape, strongly modified by relativistic effects, to estimate the BH spin (see Fig. 1.5). In the classical non-relativistic Newtonian case, a line shows two peaks with equal fluxes related to the fact that matter moves both towards and away from an observer (i.e. light is blueshifted and redshifted equally) in a disk-line configuration around the SMBH. If the material is very close to the hole, the Doppler enhancement modifies the peak fluxes and the gravitational redshift shifts the peaks towards smaller frequencies (depending on the distance from the BH). Moreover, light-bending, due to the strong gravitational field and depending on the viewing angle of the system and the BH spin, changes the amount of received flux. The final broadened line profiles, for different spin values, are shown in Fig. 1.5.

- *High-frequency quasi-periodic oscillation* in the X-ray spectra, observed in X-ray Binaries (e.g., Belloni, Sanna, and Mendez, 2012), micro-quasars

Source	En. range (keV)	$C_{PIN/XIS}$	Γ	A_{Fe} (solar)	ξ (erg cm s^{-1})	q	i (°)	a^*	χ^2_ν (χ^2/d.o.f.)
Mrk 509	0.6–44.0	1.17	2.04 ± 0.01	0.5 ± 0.1	170^{+30}_{-80}	>7.4	<18	$0.86^{+0.02}_{-0.01}$	1314/1333
3C 382	0.6–53.0	1.14	1.81 ± 0.01	>5.1	500^{+60}_{-240}	>6.1	(40)	$0.75^{+0.07}_{-0.04}$	1366/1317
Mrk 335	0.6–36.0	1.17	2.16 ± 0.01	1.4 ± 0.2	220 ± 10	>4.9	50^{+8}_{-7}	$0.83^{+0.10}_{-0.13}$	1233/1152
Fairall 9	0.6–39.0	1.16	1.99 ± 0.01	1.1 ± 0.2	140^{+60}_{-30}	>3.5	45^{+13}_{-9}	>0.64	1276/1253
1H 0419−577	0.6–48.0	1.19	$1.98^{+0.01}_{-0.02}$	0.9 ± 0.1	104^{+4}_{-26}	$5.4^{+0.2}_{-1.0}$	51^{+4}_{-6}	>0.88	1384/1294
Ark 564	0.6–22.0	1.20	2.52 ± 0.01	$1.0^{+0.2}_{-0.1}$	540^{+40}_{-20}	>6.2	64^{+1}_{-11}	$0.96^{+0.01}_{-0.06}$	1081/1011
Ark 120	0.6–53.0	1.22	2.13 ± 0.01	2.7 ± 0.6	9^{+2}_{-4}	$7.0^{+2.7}_{-2.2}$	54^{+6}_{-5}	$0.81^{+0.10}_{-0.18}$	1316/1177
3C 390.3	0.6–49.0	1.16	1.66 ± 0.01	$3.1^{+1.2}_{-0.5}$	840^{+490}_{-220}	(3)	(35)	U	1302/1259
PKS 0558−504	0.6–24.0	1.13	$2.30^{+0.02}_{-0.01}$	$0.9^{+0.3}_{-0.1}$	270^{+70}_{-30}	4.0 ± 0.7	(45)	>0.80	990/1022
NGC 7469	0.6–52.0	1.19	$1.84^{+0.03}_{-0.02}$	$2.9^{+1.7}_{-1.0}$	200^{+20}_{-50}	>4.6	<54	>0.96	1262/1139
Mrk 110	0.6–45.0	1.19	$1.96^{+0.02}_{-0.01}$	0.7 ± 0.2	310^{+220}_{-80}	>7.4	31^{+4}_{-6}	>0.99	1184/1115
Swift J0501.9−3239	0.6–36.0	1.22	$2.06^{+0.04}_{-0.03}$	$1.8^{+0.9}_{-0.5}$	200^{+10}_{-40}	>5.1	<48	>0.96	1025/1056
Mrk 841	0.6–53.0	1.19	$1.85^{+0.03}_{-0.01}$	1.0 ± 0.2	210^{+20}_{-70}	$4.1^{+2.8}_{-1.9}$	45^{+7}_{-5}	>0.56	1089/1053
Ton S180	0.6–23.0	1.16	2.36 ± 0.01	$0.9^{+0.2}_{-0.1}$	280^{+50}_{-20}	>8.1	60^{+3}_{-1}	$0.91^{+0.02}_{-0.09}$	876/838
PDS 456	0.6–17.0	1.15	$2.30^{+0.03}_{-0.01}$	>8.4	59^{+17}_{-4}	$5.9^{+1.8}_{-1.5}$	70^{+3}_{-5}	>0.97	829/826
1H 0323+342	0.6–42.0	1.25	$1.91^{+0.03}_{-0.01}$	0.8 ± 0.2	250^{+40}_{-20}	(3)	(45)	>0.48	864/922
UGC 6728	0.6–26.0	1.27	$2.00^{+0.04}_{-0.03}$	$0.7^{+0.6}_{-0.3}$	190^{+80}_{-170}	$6.8^{+2.8}_{-1.4}$	<55	>0.95	877/885
Mrk 359	0.6–21.0	1.15	$1.89^{+0.04}_{-0.03}$	$1.5^{+0.9}_{-0.6}$	21^{+32}_{-16}	>4.1	47 ± 6	$0.66^{+0.30}_{-0.46}$	820/833
MCG−2-14-9	0.6–37.0	1.19	1.89 ± 0.02	(1)	<10	(3)	(45)	U	802/804
ESO 548-G081	0.6–36.0	1.23	1.70 ± 0.03	$3.5^{+4.1}_{-1.5}$	570^{+560}_{-380}	(3)	(45)	U	853/845
Mrk 1018	0.6–41.0	1.21	$1.94^{+0.04}_{-0.03}$	$2.0^{+1.4}_{-0.7}$	5^{+10}_{-4}	>3.9	45^{+14}_{-10}	$0.57^{+0.31}_{-0.82}$	681/721
RBS 1124	0.6–23.0	1.22	$1.86^{+0.04}_{-0.02}$	$2.9^{+1.5}_{-0.9}$	51^{+7}_{-9}	>8.4	66^{+5}_{-15}	>0.98	661/668
IRAS 13224−3809	0.6–7.6	–	(2.7)	(20)	22 ± 3	$6.1^{+0.7}_{-0.6}$	(64)	>0.995	447/412
1H 0707−495	0.6–6.7	–	(2.7)	(10)	53^{+1}_{-2}	$7.6^{+0.4}_{-0.3}$	(58)	>0.994	278/236
IRAS 05262+4432	0.6–7.8	–	$2.18^{+0.13}_{-0.06}$	(1)	<51	(3)	(45)	U	234/231

FIGURE 1.6: Spin estimates constrained with the reflection method. The table is from the work of Walton et al., 2013.

(e.g., Abramowicz and Kluzniak, 2001) but also in AGNs (e.g., Alton et al., 2016) provide a way to measure the BH spin by using the time lags measured at different frequencies.

- Also *AD models* have been used to infer the BH spin (e.g., Capellupo et al., 2015; Capellupo et al., 2016 although results are highly degenerate (e.g., Majia-Restrepo et al., 2018, their Fig. E6).

- The *Imaging of the Event Horizon Shadow* (e.g., Broderick et al., 2011, Event Horizon Telescope Collaboration, 2019 and references therein), is the most recent technique which can produce images of the innermost AD surrounding a BH from which it is possible to constrain the BH spin.

Despite the theory being robust, the BH spin estimate is still an open issue. This is also due to the fact that the presence of many parameters in the relativistic models (see Fig. 1.6) can make the results degenerate (e.g., Kammoun, Nardini, and Risaliti, 2018). Therefore the comparison between different methods can help to set more robust constraints.

In this thesis, I discuss how to use accretion disk models to estimate both the SMBH masses and possibly their spin in AGNs. In the next Chapter, I will describe the accretion physics employing models including also relativistic effects, important in the strong gravity regime.

Chapter 2

Black hole Accretion

"The most beautiful experience we can have is the mysterious. It is the fundamental emotion that stands at the cradle of true art and true science"

— Albert Einstein, *Mein Weltbild*

Contents

The extraction of gravitational energy from matter orbiting and accreting onto a gravitating body is known to be the principal source of power in several types of close binary systems and it is also believed to provide the power supply in AGNs and QSOs. The importance of accretion, as a powerful mechanism producing high-energy radiation, has been followed by the observations of the full electromagnetic spectrum from the radio to γ-rays.

In this thesis, I will consider the particular case in which accretion occurs on the equatorial plane with respect to the central object, where matter forms a rotating AD, in the so-called *thin disk regime*.

2.1 Accretion disk physics

In order to describe the BBB observed in many AGN SED, Shakura and Sunyaev, 1973 (SS, thereafter) proposed a model in which radiation is produced by an AD around a central massive object.

The basic idea is that the gravitational pull of the central object makes the disk material lose angular momentum (because of rotation), making it move towards smaller and closer orbits until the fall onto the central object. The AD is considered optically thick and geometrically thin in rapid rotation. The parameters used for such description (e.g., disk thickness, density, surface density, temperature, viscosity) are all functions of three quantities: the central object mass M, the accretion rate $\dot{M}$ and the distance R from the center of the disk. Moreover, in this description, the incomplete knowledge of the value of the disk viscosity (i.e. the efficiency with which the angular momentum of the matter is lost and transferred to the material at greater distances) is described by the presence of a parameter α (the so-called *alpha parametrization* or *alpha disk*) connected to the magnetic field and turbulence in the disk (Shakura and Sunyaev, 1973).

The SS model does not take into account any relativistic effects due to the strong gravitational field. Other and more accurate models have been developed to describe the AD spectral shape as best as possible, including all the possible gravitational effects (see Sect. 2.7).

2.2 Shakura & Sunyaev model: main equations

The basic assumptions on the AD require that its structure is very close to the equatorial plane with a negligible thickness (hence *thin disk*). For its description, it is useful to consider cylindrical coordinates (R, ϕ, z), where R is the distance from the central object and ϕ is the angle, and define the disk surface density as $\Sigma(R, t)$, depending also on time. Although the classical calculations describe also the disk height z (as a function of the other parameters of the accretion; see Shakura and Sunyaev, 1973; Franck, King, and Raine, 2002), this latter can be neglected assuming $z \sim 0$, which does not affect the final results.

The friction between adjacent layers of the disk, caused by the existence of turbulence due to small scale magnetic fields in the disk itself (Shakura and Sunyaev, 1973), leads to the loss of angular momentum. The radial *drift velocity*, $v_R(R, t)$, is assumed negative and not zero, to describe the accretion of matter.

For a rotating annulus of the disk between the radius R and $R + \Delta R$, the angular velocity and the rotation velocity can be written as

$$\Omega(R) = \sqrt{\frac{GM}{R^3}} \qquad\qquad v_\phi(R) = R\Omega(R). \tag{2.1}$$

The annulus mass is $M_* = 2\pi R\ \Delta R\ \Sigma(R,t)$ and the total angular momentum is $J_* = RM_* v_\phi = 2\pi R\ \Delta R \Sigma(R,t) R^2 \Omega(R)$ (using Eq. 2.1). The temporal variation of an annulus mass is given by the flow of material between two adjacent annuli:

$$\begin{aligned} \frac{\partial M_*}{\partial t} &= 2\pi \frac{\partial[\ R\Delta R \Sigma(R,t)\ ]}{\partial t} \\ &= 2\pi[\ R\ v(R,t)\ \Sigma(R,t) - (R+\Delta R)\ v(R+\Delta R,t)\ \Sigma(R+\Delta R,t)\ ] \\ &\approx -2\pi \Delta R \frac{\partial[\ v_R(R,t)\Sigma(R,t)R\ ]}{\partial R}, \end{aligned} \tag{2.2}$$

where the sign $-$ is given by the fact that the drift velocity is assumed negative. At the first order of R (and imposing $\Delta R \to 0$), one can obtain the *mass conservation law*:

$$R\frac{\partial \Sigma(R,t)}{\partial t} + \frac{\partial[\ v_R(R,t)\Sigma(R,t)R\ ]}{\partial R} = 0. \tag{2.3}$$

Similarly, it is possible to derive the *angular momentum conservation law*: given the friction between different layers of the disk which have different angular momenta and angular velocities, a viscous torque $G(R,t)$ is responsible for the transfer of angular momentum from an annulus to another (Franck, King, and Raine, 2002). Assuming a non-zero viscosity ν throughout the disk, the viscous torque can be expressed as

$$G(R,t) = 2\pi R\ \nu\ \Sigma(R,t)\ R^2 \frac{\partial \Omega(R)}{\partial R}. \tag{2.4}$$

In the case of a rigid rotation of different adjacent annuli (i.e. $\partial\Omega(R)/\partial R = 0$), the torque is zero, i.e., there is no friction between different disk layers and therefore no angular momentum transfer. Given that $\partial\Omega(R)/\partial R < 0$, it means that $G(R,t) < 0$ i.e., the inner annuli lose angular momentum to the outer ones and the gas of the disk slowly spirals in. The temporal variation of the angular momentum must include the transport due to the effects of the

torque (Franck, King, and Raine, 2002) and, as Eq. 2.2, one can write

$$\begin{aligned}\frac{\partial J_*}{\partial t} &= 2\pi\frac{\partial[\, R\Delta R\Sigma(R,t)R^2\Omega(R)\,]}{\partial t} \\ &\approx -2\pi\Delta R\frac{\partial[\, R\Sigma(R,t)Rv(R,t)R^2\Omega(R)\,]}{\partial R} + \frac{\partial G(R,t)}{\partial R}\Delta R.\end{aligned} \tag{2.5}$$

As before, at the first order of R with $\Delta R \to 0$, one can obtain

$$R\frac{\partial[\,\Sigma(R,t)R^2\Omega_K(R)\,]}{\partial t} + \frac{\partial[\, R\Sigma(R,t)v_R(R,t)R^2\Omega_K(R)\,]}{\partial R} = \frac{1}{2\pi}\frac{\partial G(R,t)}{\partial R} \tag{2.6}$$

and, by using Eq. 2.2, the latter equation becomes:

$$R\Sigma(R,t)v_R(R,t)\frac{\partial[\, R^2\Omega_K(R)\,]}{\partial R} = \frac{1}{2\pi}\frac{\partial G(R,t)}{\partial R}, \tag{2.7}$$

where it was used the assumption $\partial\Omega(R)/\partial t = 0$, true for a time-independent gravitational potential.

2.3 Static thin disk: flux and temperature

The *static* case is described by setting up $\partial/\partial t = 0$ in the latter equations. From Eq. 2.2, it is easy to find that $v_R(R)\Sigma(R)R = constant$: that is the amount of matter that falls per unit of time towards the center from any position in the disk. It is useful to define the **accretion rate** $\dot{M}$, i.e. the mass falling towards to disk center per unit of time, as

$$\dot{M} = \frac{dM}{dt} = \frac{\Sigma(R)dA}{dt} = \frac{\Sigma(R)2\pi RdR}{dt} = -2\pi R\Sigma(R)v_R(R),$$

where dA is the infinitesimal annulus area and the sign $-$ is given by the drift velocity definition. In the static case, *the accretion rate is constant throughout the disk*. By integrating Eq. 2.6 with respect to R, it is possible to write

$$R\Sigma(R)v_R(R)R^2\Omega(R) = \frac{G(R)}{2\pi} + \frac{C}{2\pi},$$

where C is a constant. The definition given by Eq. 2.4 leads to

$$-\nu\Sigma(R)\frac{\partial\Omega(R)}{\partial R} = \Sigma(R)v_R(R)\Omega(R) + \frac{C}{2\pi R^3}. \tag{2.8}$$

In the case where the disk truncates at a particular radius R_0 (e.g., that could be the surface of the central objects) and that at that radius $\partial\Omega(R_0)/\partial R =$

0, Eq. 2.8 and the definition of $\dot{M}$ (which is constant at any radius) lead to

$$C = -\dot{M}\sqrt{GMR_0}.$$

Therefore, putting this latter result in Eq. 2.8 leads to

$$\nu\Sigma(R) = \frac{\dot{M}}{3\pi}\left(1 - \sqrt{\frac{R_0}{R}}\right). \tag{2.9}$$

The viscous torque $G(R,t)$ (that has the dimension of an energy) of an annulus of the disk (with width dR) causes a *viscous dissipation* of radiation with a rate that can be written as $dE/dt = G(R)(\partial\Omega(R)/\partial R)dR$ (Franck, King, and Raine, 2002). Such energy is radiated away from the two faces of the disk per unit area according to this expression:

$$F(R) = \frac{dE}{dAdt} = \frac{1}{2\times 2\pi R dR}\frac{dE}{dt} = \frac{G(R)}{4\pi R}\frac{\partial\Omega(R)}{\partial R}.$$

This expression is the **flux** radiated from the different annuli of the disk at different distances R from its center. Using the definition of G (Eq. 2.4), the expression given by Eq. 2.9 and setting $R_0 = R_{\rm ISCO}$, uqual to $6R_{\rm g}$ for a Schwarzschild BH, it is possible to find

$$F(R) = \frac{3GM\dot{M}}{8\pi R^3}\left(1 - \sqrt{\frac{R_{\rm ISCO}}{R}}\right). \tag{2.10}$$

This expression, independent from the unknown disk viscosity ν, describes how the disk emits radiation and it depends only on the BH mass M, the accretion rate $\dot{M}$ and the distance R from the SMBH.

2.4 Emitted and observed spectra

Since the disk is assumed to be optically thick, it is reasonable to consider that every annulus emits like a black-body. The *specific intensity* (energy per unit time, unit area, unit frequency and unit solid angle) will be simply the *Planck distribution*. Therefore, flux and temperature are linked by the *Stefan-Boltzmann law*:

$$T(R) = \left[\frac{F(R)}{\sigma_{\rm SB}}\right]^{1/4}, \tag{2.11}$$

where $\sigma_{\rm SB}$ is the Stefan-Boltzmann constant. It is worth noticing that at the ISCO, the associated black-body temperature is zero meaning that, from the innermost orbit, there is no escaping radiation and the flux will be zero (see

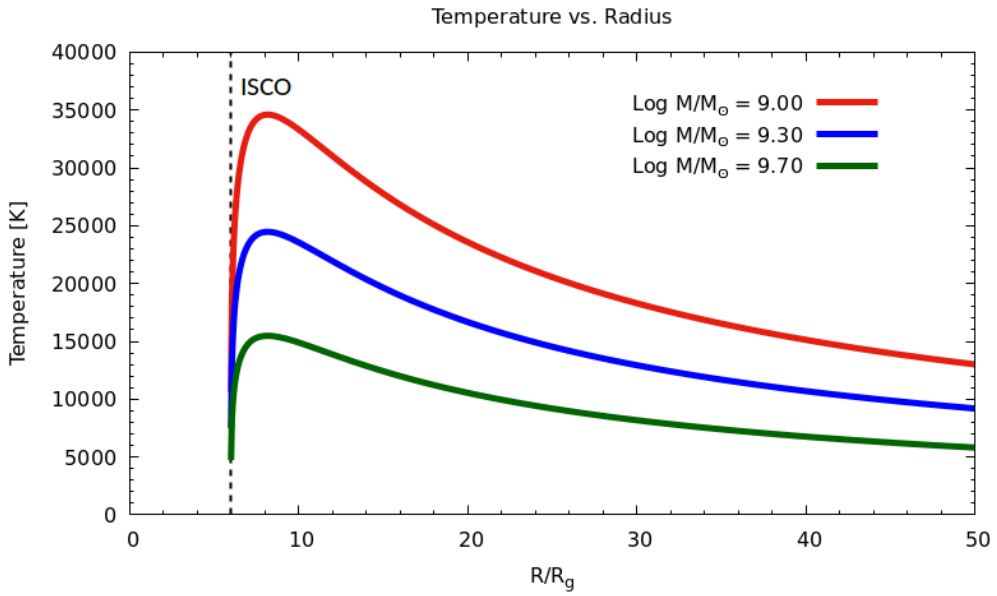

FIGURE 2.1: Temperature profile (given by Eq. 2.11) of an AD with different SMBH masses (the accretion rate is fixed to $\dot{M}/M_\odot \mathrm{yr}^{-1} = 1$).

Fig. 2.1). In the real case, some photons can escape from matter inside the ISCO because their geodesics do not end up onto the BH: the SS model does not take into account any relativistic effects therefore, inside the last stable orbit, all photons are trapped and cannot escape.

The specific intensity, as a function of the radius R and frequency ν, is

$$I_\nu(R) = \frac{2h\nu^3}{c^2} \frac{1}{\exp\left[\frac{h\nu}{k_B T(R)}\right] - 1}.$$

The specific disk flux and intensity at the surface of the disk are linked by the expression $F_\nu(R) = \pi I_\nu(R)$.[1] The specific luminosity L_ν of the AD comes from the integration of the specific flux:

$$L_\nu = 2 \times \int_{R_{\mathrm{ISCO}}}^{R_{\mathrm{out}}} 2\pi R dR F_\nu(R) = 2 \times \int_{R_{\mathrm{ISCO}}}^{R_{\mathrm{out}}} 2\pi R dR \pi I_\nu(R), \tag{2.12}$$

where the factor 2 accounts for the two faces of the disk. The integration is

[1] Consider a sphere of radius R and an observer at the distance r with θ_c the angle between the two radii: if the observer is at $r \gg R$, the angle will be $\theta_c \sim 0°$ while, on the surface of the sphere (where $r = R$), the angle will be $\theta_c = \pi/2$. The relation between the flux and the intensity is

$$F_\nu(R) = \int_0^{\theta_c} I_\nu(R) \cos\theta d\Omega = \pi I_\nu(R) \sin^2\theta_c,$$

where azimutal simmetry is considered (i.e., $d\Omega = 2\pi \sin\theta d\theta$). On the surface of the object, $F_\nu = \pi I_\nu$ (see Ghisellini, 2012).

performed from the ISCO to the outer radius of the disk, $R_{\rm out}$. Eqs. 2.10-2.11 in Eq. 2.12 lead to:

$$L_\nu = \frac{8\pi^2 h\,\nu^3}{c^2}\int_{R_{\rm ISCO}}^{R_{\rm out}} \frac{R\,dR}{\exp\left[\frac{h\nu}{k_B T(R)}\right]-1}. \tag{2.13}$$

This expression represents the emitted specific luminosity of the AD around a BH. The integral over the whole range of frequencies must give the total amount of energy radiated by the disk, i.e.

$$L_d = \int_0^\infty L_\nu d\nu = \eta \dot{M} c^2, \tag{2.14}$$

which is the **total disk luminosity**. In general, the *emitted* and *observed* luminosities of the disk could be different since that a distant observer sees the disk from a certain viewing angle $\theta_{\rm v}$ and a certain (luminosity) distance $d_{\rm L}$. The sum of all the contribution in the whole solid angle and in the whole range of frequencies must give the total disk luminosity, i.e.

$$L_{\rm d} = \int_\nu \int_\Omega F_\nu^{\rm obs}(\theta) d_{\rm L}^2 d\nu d\Omega. \tag{2.15}$$

Assuming azimuthal symmetry (i.e., $d\Omega = 2\pi \sin\theta d\theta$) and accounting for the two faces of the disk (assumed to have the same radiation angular pattern) lead to

$$L_{\rm d} = \int_0^{\pi/2} L_{\rm d}^{\rm obs}(\theta) \sin\theta d\theta, \tag{2.16}$$

where it has been used the definitions $4\pi d_{\rm L}^2 F_\nu^{\rm obs}(\theta) = L_\nu^{\rm obs}(\theta)$ and $\int L_\nu^{\rm obs} d\nu = L_{\rm d}^{\rm obs}$, where $L_{\rm d}^{\rm obs}$ is the **observed disk luminosity**, often called as *isotropic equivalent luminosity*. In general, the observed disk luminosity is linked to $L_{\rm d}$ by a function depending on the viewing angle: for an anisotropic disk, it is expected to be $L_{\rm d}^{\rm obs} = k \cos\theta_{\rm v} L_{\rm d}$, where k is a constant or any function not depending on $\theta_{\rm v}$. Using this latter information, from Eq. 2.16, it is possible to find that in the classical non-relativistic SS case, $k = 2$ and

$$L_{\rm d}^{\rm obs}(\theta_{\rm v}) = 2\cos\theta_{\rm v} L_{\rm d}. \tag{2.17}$$

This result corresponds to the Newtonian case (see e.g., Cunningham, 1975; see also Calderone et al., 2013). Following this correction, the observed spectrum must take into account the $2\cos\theta_{\rm v}$ factor, i.e., this latter must be included in Eq. 2.13 in order to evaluate the SMBH properties correctly, leading

to the final expression

$$L_\nu = \frac{16\pi^2 h\,\nu^3 \cos\theta}{c^2} \int_{R_{\rm ISCO}}^{R_{\rm out}} \frac{R\,dR}{\exp\left[\frac{h\nu}{k_B T(R)}\right] - 1}. \tag{2.18}$$

The observed disk luminosity can be derived from the integration of Eq. 2.18 over the frequency range in which an AD emits its radiation, identified with the BBB in the Optical-UV bands: this quantity must not be confused with the *bolometric luminosity* $L_{\rm bol}$, normally used in spectroscopic studies (e.g., Shen et al., 2011) to estimate the accretion power output from the monochromatic luminosity at a specific wavelength, using a bolometric correction (e.g., Richards et al., 2006). In general, $L_{\rm bol}$ normally includes the IR and the X-ray emissions, produced by the dusty torus (re-processed disk radiation) and the X-ray Corona (up-scattered disk radiation) and $L_{\rm d}^{\rm obs}$: Calderone et al., 2013 derived that on average $L_{\rm bol} \sim 2L_{\rm d}^{\rm obs}$.

2.5 Asymptotic behaviors

In the $\nu - \nu L_\nu$ plane, the SS AD spectrum can be divided into three parts which are related to different regions of the disk according to their distance from the central SMBH. Figure 2.2 shows the SED of an AGN AD with its asymptotic behaviors:

- The outer region of the disk, far from the central BH, is characterized by low temperatures therefore it contributes to the low-frequency part of the spectrum. The Planck distribution is well approximated by the *Reyleigh-Jeans distribution* and the asymptotic behavior of Eq. 2.18 is

$$\nu L_\nu \propto \nu^3. \tag{2.19}$$

- In the intermediate region of the disk, at frequencies lower than the spectrum peak, the evaluation of the integral in Eq. 2.18 (with $R_{\rm out} \gg R_{\rm ISCO}$) leads to

$$\nu L_\nu \propto \nu^{4/3}. \tag{2.20}$$

- The inner region of the disk, where the temperatures are larger, is responsible for the high-frequency part of the spectrum. The emission

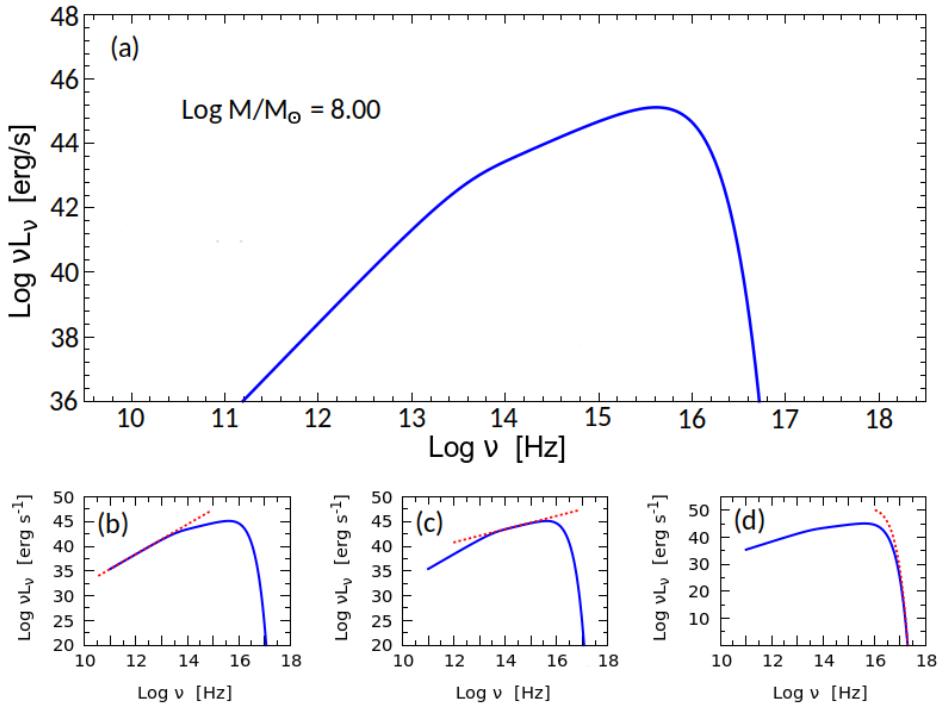

FIGURE 2.2: Complete SS spectrum (a) with the asymptotic behaviors in different frequency ranges: (b) $\propto \nu^3$, (c) $\propto \nu^{4/3}$, (d) $\propto \nu^4 e^{-\nu}$. The viewing angle is $\theta_v = 0°$ and the accretion rate $\dot{M}/M_\odot \mathrm{yr}^{-1} = 0.25$.

follows the *Wien distribution* and the asymptotic behavior is:

$$\nu L_\nu \propto \nu^4 \exp\left(-\frac{h\nu}{k_B T_{\max}}\right). \tag{2.21}$$

where $T_{\max}$ is the maximum temperature of the disk (see next Section). The low frequency ($\propto \nu^3$) region radiation is highly unobserved given that the disk SED is 'covered' by other kinds of emissions (i.e., dust, Synchrotron); also the intermediate region ($\propto \nu^{4/3}$) is partially observed since it can be contaminated by the NIR dust emission or the NIR-Optical galaxy emission (see Fig. 1.1). The only visible region is the one around the peak which, on the other hand, could be absorbed and/or contaminated by other emissions as well (see Chap. 4).

2.6 Peak frequency and luminosity

From Eq. 2.11 and Eq. 2.18, it is possible to find analytical expression for the spectrum peak frequency ν_p and luminosity $\nu_p L_{\nu_p}$ (in the $\nu - \nu L_\nu$ plane). The spectrum peak is related to the maximum temperature of the disk which can

be found by deriving Eq. 2.11 with respect to R. The derivative leads to:

$$\frac{dT(R)}{dR} = 0 \qquad \rightarrow \qquad R_{\rm max} = \frac{49}{36} R_{\rm ISCO} = \frac{49}{6}\frac{GM}{c^2}, \tag{2.22}$$

where $R_{\rm max}$ is the distance from the SMBH and the temperature is maximal:

$$T_{\rm max} = T(R_{\rm max}) = \Big[\frac{3^2\, 6^2\, \dot{M}c^6}{4\, 7^7\, \pi\sigma_{\rm SB} G^2 M^2}\Big]^{1/4}. \tag{2.23}$$

The derivative of Eq. 2.18 with respect to the frequency ν leads to the expression $h\nu_{\rm p} = 2.82 k_{\rm B} T_{\rm max}$: using Eq. 2.23 leads to

$$\frac{\nu_{\rm p}}{[\rm Hz]} = \mathcal{A}\Big(\frac{\dot{M}}{M_\odot {\rm yr}^{-1}}\Big)^{1/4}\Big(\frac{M}{10^9 M_\odot}\Big)^{-1/2}, \tag{2.24}$$

where Log $\mathcal{A} = 15.25$. From this expression, it is easy to see that the BBB for an AGN is peaked in the UV band. Using this latter expression in Eq. 2.18 leads to

$$\nu_{\rm p} L_{\nu_{\rm p}} = \frac{6^6\, 2.82^4\, \pi k_{\rm B}^4\, \dot{M}\cos\theta_{\rm v}}{7^7\, \sigma_{\rm SB} h^3} \underbrace{\int_1^{y_{\rm out}} \frac{y dy}{\exp[1.38 y^3 (1 - y^{-0.5})^{-1}] - 1}}_{=\Theta},$$

where it has been performed the substitution $y = R/R_{\rm ISCO}$. The integral is equal to $\Theta \approx 0.29$ for $y_{\rm out} = R_{\rm out}/R_{\rm ISCO} \gg 1$. The whole expression can be re-arranged as the following

$$\frac{\nu_{\rm p} L_{\nu_{\rm p}}}{\rm erg/s} = \mathcal{B}\frac{\dot{M}}{M_\odot {\rm yr}^{-1}}\cos\theta_{\rm v}, \tag{2.25}$$

where Log $\mathcal{B} = 45.66$ (the same expression was derived by Calderone et al., 2013). In the latest expressions for the peak frequency and luminosity, the SS radiative efficiency is already included in the constants: η is linked to the ISCO of the AD and, as shown by Calderone et al., 2013, for the SS model it is $\eta_{\rm SS} = R_g/2R_{\rm ISCO} = 1/12 \sim 0.083$, slightly larger than the real one, computed by including the relativistic effects ($\eta \sim 0.057$; Thorne, 1974). In this classical treatment, for a fixed viewing angle, the total disk luminosity can be directly inferred from 2.17 which can be approximated by:

$$L_{\rm d}^{\rm obs} \sim 2\nu_p L_{\nu_{\rm p}} \qquad \rightarrow \qquad L_{\rm d} = \eta_{\rm SS}\dot{M}c^2 = \frac{\nu_{\rm p} L_{\nu_{\rm p}}}{\cos\theta_{\rm v}}, \tag{2.26}$$

and from this latter, it is possible to compute the Eddington ratio, defined

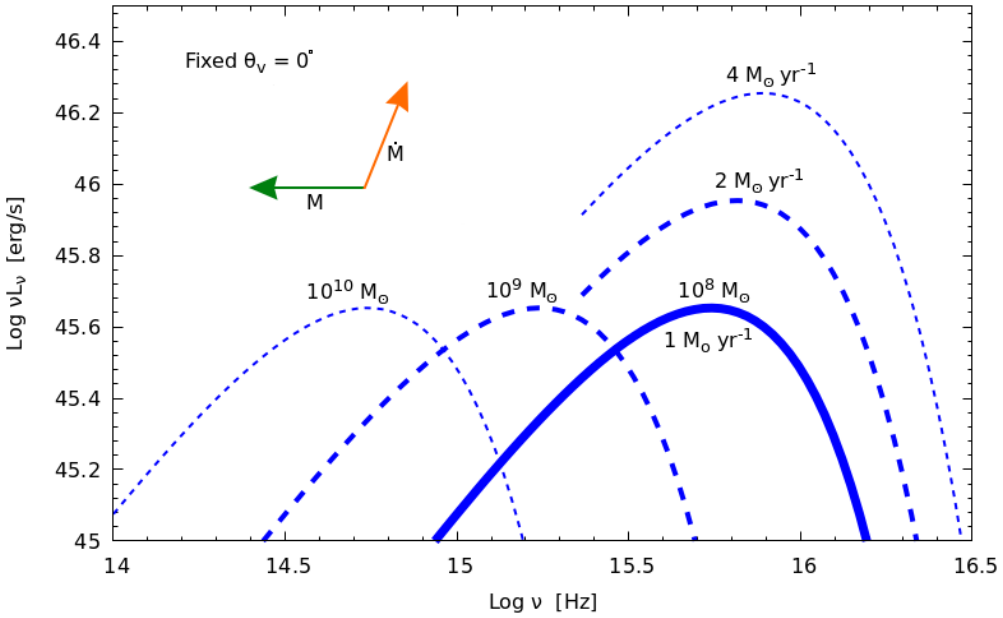

FIGURE 2.3: SS spectrum dependence on the BH mass M and the accretion rate $\dot{M}$ (the angle is fixed to $\theta_v = 0°$.

as the ratio between L_d and the Eddington luminosity (defined as $L_{Edd} = 1.26 \times 10^{38}[M/M_\odot]$):

$$\lambda_{Edd} = \frac{L_d}{L_{Edd}} \approx \mathcal{D}\, \eta_{SS} \frac{\nu_p^2 \sqrt{\nu_p L_{\nu_p}}}{\cos\theta_v} \tag{2.27}$$

where Log $\mathcal{D} = -53.674$ and $\eta_{SS} = 1/12$. From Eqs. 2.24 - 2.25 - 2.26 - 2.27, it is straightforward to deduce that, for the SS model, once the spectrum peak is fixed (e.g., constrained by observed data), only one value for M, $\dot{M}$, L_d and λ_{Edd} can be found.

Eqs. 2.24-2.25 show how the AD spectrum moves on the $\nu - \nu L_\nu$ plane, depending only on three parameters: the SMBH mass M, the accretion rate $\dot{M}$ and the viewing angle of the system θ_v with respect to our line of sight and measured from the normal of the disk plane (see Fig. 2.3).

- Changing the BH mass leads only to a modification of the peak frequency: the higher the mass, the smaller the frequency. This is because for larger values of M, R_{max} becomes larger and T_{max} smaller, i.e., the spectrum black-bodies become colder and ν_p shifts to smaller frequencies.

- Instead, changing the accretion rate leads to modifications both for the peak frequency and luminosity: this is linked to the fact that for larger

values of $\dot{M}$, the disk luminosity (i.e., $L_{\rm d} = \eta \dot{M} c^2$) is larger leading to larger values of $\nu_{\rm p} L_{\nu_{\rm p}}$; moreover, also $T_{\rm max}$ will be larger, i.e., the spectrum black-bodies become hotter and $\nu_{\rm p}$ shifts to larger frequencies.

- Finally, changing the viewing angle modifies only the peak luminosity by shifting it vertically to lower values for larger viewing angles: $\nu_{\rm p} L_{\nu_{\rm p}}$ (and so $L_{\rm d}^{\rm obs}$) is maximal for $\theta_{\rm v} = 0^\circ$ (face-on configuration) and null for $\theta_{\rm v} = 90^\circ$ (edge-on configuration). In the realistic case, relativistic effects modify the radiation pattern with respect to the classical SS treatment drastically: even at large angles, there is always a significant fraction of photons that travel towards our line of sight direction because their geodesics are modified by the curved space in the inner region around the SMBH (see next Section).

2.7 Relativistic disk models

Having reliable estimates of the parameters of the SMBH and its accretion is extremely important and, for this reason, more sophisticated and realistic models must be considered. Many models have been developed to account for relativistic effects which, as pointed out before, are due to the strong gravitational field of the SMBH: they play an important role in what concerns the observed spectrum (as seen by a distant observer), especially in the extreme cases (i.e., when the BH is rapidly spinning). One crucial point is that the modifications cannot be treated analytically (as in the SS case) and a numerical approach must be considered.

The main effects (both from the Special and General Relativity) are listed below:

- *Doppler boosting* (or *relativistic beaming*): the process by which relativistic effects modify the apparent luminosity of emitting matter that is moving at speeds close to the speed of light. This effect is more important in the inner region of the disk where matter is moving faster because of its small distance from the BH. The Doppler factor can be written as

$$D = \frac{1}{\Gamma(1 - \beta \cos\theta)},$$

where Γ is the Lorentz factor, β is the ratio between the matter velocity and the speed of light, and θ is the angle between the matter's motion

direction and the observer. This process can be divided into three effects: relativistic aberration (change in a photon's apparent direction caused by the relative transverse motion of a distant observer), time dilation (a consequence of Special Relativity) and blue/red-shifting (see Ghisellini, 2012).

- *Gravitational redshift*: the process by which the electromagnetic radiation, coming from a source that is in a gravitational field, is reduced in frequency, or red-shifted, when observed far from the gravitational field. For a Schwarzschild BH, the expression can be written as

$$z + 1 = \frac{1}{\sqrt{1 - \frac{2GM}{Rc^2}}},$$

from which, it is easy to notice that the effect gets stronger when going closer to the event horizon.

- *Frame-dragging* (also known as *Lense-Thirring effect*): the process related to a spinning BH that drags the space-time itself with its rotation. Such effect can be derived from the geodesics related to an infalling particle around a BH. Even if its initial rotational velocity is null (basically, a radial free fall), during the fall, a particle will gain angular momentum that makes it rotate in the same direction of the BH rotation, with an equatorial velocity that can be expressed as

$$\Omega = \frac{d\phi}{dt} = \frac{2Ma}{R^3 + aR^2\left(1 + \frac{2GM}{Rc^2}\right)},$$

where a is the BH spin. Even at large distances from the BH, the particle is affected by the rotation of the compact object and begins to rotate.

- *Light bending*: for a better description of the AD spectrum, this phenomenon is one of the most important. It is due to the strong gravitational pull of the central BH that bends the trajectories of the photons. Such effect is enhanced by the BH spin and the frame-dragging effect and must be treated numerically.

- *Self-irradiation*: due to the light deflection, is the phenomenon when photons emitted by the disk can irradiate the disk itself, because of the strong gravitational pull that bends their trajectories (for this reason, it is also called *returning radiation*), making the disk brighter.

As pointed out above, all these effects are stronger in the extreme environments corresponding to the cases in which the SMBH is rapidly spinning: those affect the emitted and observed disk spectrum which departs from the classical non-relativistic SS treatment.

Some others often included few other effects to describe the observed disk spectrum, as the *limb-darkening* effect, which is an optical phenomenon that makes the central part of the disk brighter than its edge (assuming an electron-scattering atmosphere above the disk; e.g., Chandrasekhar, 1950; Cunningham, 1976). Moreover, although the issue is still under debate, some theoretical works suggested that a *nonzero torque* can arise at the inner boundary of the disk from a magnetic field (connecting the disk to a central BH or to the infalling material; e.g., Krolik, 1999; Gammie, 1999; Agol and Krolik, 2000; Li, 2004; Wang et al., 2003; Uzdensky, 2004), which can modify the disk luminosity (see Li et al., 2005 for an implementation).

2.8 Novikov & Thorne model

In their work published in 1973 (Novikov and Thorne, 1973), the two authors describe the BH accretion physics taking into account the effects of Special and General Relativity in their treatment.

Starting from the first works on this matter (e.g., Bardeen, 1970; Bardeen, Press, and Teukolsky, 1972), they extended the equations of structure from the classical Newtonian theory to General Relativity, by assuming that the space-time geometry outside the BH is that of Kerr (i.e., rotating BH) with a disk lying on the equatorial plane of the Kerr metric. Solving the equations, the authors ended up in analytical expressions for a relativistic AD. Notice that, more complicated effects (such as light-bending and self-irradiation) are not included since they require a different and more sophisticated treatment (e.g., Li et al., 2005).

As done by Shakura and Sunyaev, 1973, the authors divided the disk into three regions, depending on the distance from the BH. The inner region, where radiation pressure dominates over gas pressure, is responsible for most of the disk radiation (and thus $L_{\rm d}^{\rm obs}$). Following the works of Novikov

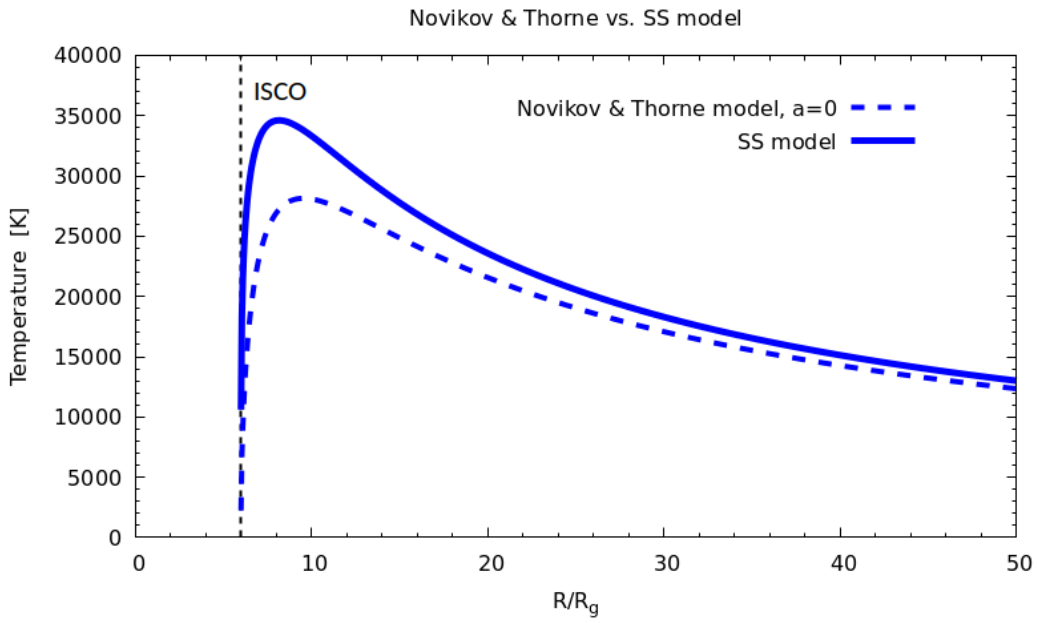

FIGURE 2.4: Comparison between the relativistic Novikov & Thorne disk model (with $a = 0$) and the classical SS model (the BH mass is Log $M/M_{\odot} = 9.00$ and the accretion rate $\dot{M}/M_{\odot}\mathrm{yr}^{-1} = 1$.

and Thorne, 1973 and Page and Thorne, 1974, the disk flux is expressed as

$$\begin{aligned} F(x) &= \frac{3\dot{M}c^6}{8\pi G^2 M^2}\left(x^7 - 3x^5 + 2ax^4\right)^{-1}\Big[x - x_0 - \frac{3}{2}a\ln\Big(\frac{x}{x_0}\Big) - \\ &- \frac{3(x_1-a)^2}{x_1(x_1-x_2)(x_1-x_3)}\ln\Big(\frac{x-x_1}{x_0-x_1}\Big) - \\ &- \frac{3(x_2-a)^2}{x_2(x_2-x_1)(x_2-x_3)}\ln\Big(\frac{x-x_2}{x_0-x_2}\Big) - \\ &- \frac{3(x_3-a)^2}{x_3(x_3-x_1)(x_3-x_2)}\ln\Big(\frac{x-x_3}{x_0-x_3}\Big)\Big], \end{aligned} \tag{2.28}$$

where the following adimensional quantities have been defined in this way:

$$x_1 = 2\cos\Big(\frac{1}{3}\cos^{-1}a - \frac{\pi}{3}\Big) \qquad x_2 = 2\cos\Big(\frac{1}{3}\cos^{-1}a + \frac{\pi}{3}\Big)$$

$$x_3 = -2\cos\Big(\frac{1}{3}\cos^{-1}a\Big) \qquad x = \sqrt{\frac{Rc^2}{GM}} \qquad x_0 = \sqrt{\frac{R_{\mathrm{ISCO}}c^2}{GM}}.$$

As for the SS model, the overall relativistic spectrum is obtained as a superposition of black-bodies with a temperature depending on the radius R, linked to the flux (Eq. 2.28). The relativistic disk flux for $a = 0$ is different

with respect to the SS case (Eq. 2.10) and the relativistic expression is

$$F(R) = \frac{3G\dot{M}M}{8\pi R^3}\left(1-\frac{3GM}{c^2R}\right)^{-1}\left[1-\sqrt{\frac{6GM}{c^2R}}-\sqrt{\frac{3GM}{4c^2R}}\ln\left(\frac{1-\sqrt{\frac{3GM}{c^2R}}}{1+\sqrt{\frac{3GM}{c^2R}}}\frac{2+\sqrt{2}}{2-\sqrt{2}}\right)\right], \tag{2.29}$$

whose temperature can be found by using Eq. 2.11. Fig. 2.4 shows the comparison between the two models: the relativistic model is colder with respect to the SS one in the inner region of the disk due to a smaller radiative efficiency (0.057 versus 0.083). The two models overlap for large values of R.[2] As for the SS model, the spectrum peak of the relativistic version scales with the BH mass and accretion rate in the same way, as shown in Sect. 2.6. However, the presence of relativistic effects, and the different radiative efficiency, linked to the additional parameter represented by the BH spin, modify Eqs. 2.24-2.25 with extra terms.

In the next chapter, I will focus on the description of the relativistic AD model KERRBB for which analytical expressions (describing its emission) have been found (see Campitiello et al., 2018), and comparing it with other relativistic models.

[2]The Novikov & Thorne AD emission for $a = 0$ is described by the General Relativistic Accretion Disk (GRAD) model, implemented in the XSPEC routine (Arnaud, 1996). For more details about the model, see Hanawa, 1989 and Ebisawa, Mitsuda, and Hanawa, 1991.

Chapter 3

Relativistic accretion disk model KERRBB

"The Intellect engages us in the pursuit of Truth. The Passions impel us to Action"
— Marcus Tullius Cicero, *De Officiis ad Marcum Filium: Libri Tres*

Contents

As discussed in the previous Chapter, having reliable estimates of the parameters of the SMBH and its accretion is extremely important therefore more sophisticated and realistic models must be considered, i.e., models that include relativistic effects in the strong gravity regime.

The most complete and public AD model is **KERRBB** (KERR Black Body), describing the emission of a thin, steady-state, general relativistic AD around a rotating BH. The model was developed and compared with other models by Li et al., 2005 which implemented it in the interactive routine XSPEC. This model is the finest one for fitting AD spectra because it takes into account all the relativistic effects discussed in Sect. 2.7.

In the next Sections, I will describe the main basic equations implemented in the code and its analytical approximation (published in Campitiello et al., 2018).

3.1 Main KERRBB equations

As the SS (Sect. 2.3) and the Novikov & Thorne model (Sect. 2.8), KERRBB treats the AD as a superposition of black-bodies with a different temperature, linked to the flux according to Eq. 2.28. The flux density emitted by the disk $F_{\rm out}$ is given by a sum of three terms:

$$F_{\rm out} = F_0 + F_{\rm in} + F_{\rm S},$$

where F_0 is the standard Novikov & Thorne flux, $F_{\rm in}$ is the ingoing component i.e., the radiation focused back onto the disk by the BH gravity (or *returning radiation*), and F_S that represents the work done by the returning radiation on the disk (Li et al., 2005). A distant observer will see the observed specific flux $F_{\nu,\rm obs}$ expressed as follows:

$$F_{\nu,\rm obs} = \int_\Omega I_{\nu,\rm obs} d\Omega_{\rm obs}, \tag{3.1}$$

where $I_{\nu,\rm obs}$ is the specific intensity of the radiation observed by a distant observer and $d\Omega_{\rm obs}$ is the observed solid angle. Using the invariance of the quantity I_ν / E^3 (where E is the energy of the photons), it is possible to write:

$$\frac{I_{\nu,\rm obs}}{E^3_{\rm obs}} = \frac{I_{\nu,\rm em}}{E^3_{\rm em}} \qquad \rightarrow \qquad I_{\nu,\rm obs} = \frac{E^3_{\rm obs}}{E^3_{\rm em}} I_{\nu,\rm em} = g^3 I_{\nu,\rm em},$$

where $I_{\nu,\rm em}$ is the emitted intensity, $E_{\rm em}$ is the energy of the photon at the emission point of the disk, $E_{\rm obs}$ is the energy of the photon as measured by a distant observer and g is the photon redshift. Hence, Eq. 3.1 becomes

$$F_{\nu,\rm obs} = \int_\Omega g^3 I_{\nu,\rm em} d\Omega_{\rm obs}.$$

One peculiarity of the KERRBB model (also adopted by others, e.g., GRAD) is that it treats the black-body emission of each annulus of the disk as a *diluted* or *color-corrected* black-body by introducing the color-correction or *hardening*

factor $f_{\rm col}$. The corrected specific intensity and the temperature are

$$I_\nu(R) = \frac{2h\nu^3}{f_{\rm col}^4 c^4} \frac{1}{\exp\left(\frac{h\nu}{k_{\rm B}T_{\rm col}}\right)-1} \qquad T_{\rm col} = f_{\rm col} T(R)$$

where $T(R)$ is given by Eq. 2.11 (computed from the relative Novikov & Thorne flux). The hardening factor has been introduced to account for the fact that, in the disk atmosphere, electron scattering could dominate over absorption and the spectrum could be affected by Comptonization (this is the case of a X-ray Corona located above and below an AD, mimicking the effect of assuming $T_{\rm col} > T_{\rm eff}$) and shifting the spectrum to larger frequencies (due to scattering). Its value is generally assumed < 2 both for X-ray binaries and AGNs, although the issue is still not clear (e.g., Shimura and Takahara, 1995; Davis and El-Abd, 2019; see also Czerny et al., 2011). Moreover, in AGNs, a constant hardening factor is an oversimplification of the Comptonization process since a hot Corona is present only in the inner regions of the AD (e.g., Fabian et al., 2015; Miniutti and Fabian, 2004), while its effect is unimportant at larger radii. Therefore, in the real case, the effect must be treated as radius-dependent or as a separate process (see Sect. 3.4.2).

Using the previous equations, the final expression for the observed specific flux can be written as:

$$F_{\nu,obs} = \frac{2g^3 E_{\rm em}^3}{f_{col}^4} \int_\Omega \frac{\Upsilon(\theta)}{\exp[E_{\rm em}/k_{\rm B}T_{\rm col}(R)] - 1} d\Omega_{\rm obs}$$

where $\Upsilon(\theta_{\rm v})$ is a function describing the limb-darkening effect (equal to 1 if the emission is assumed isotropic; see Li et al., 2005).

The observed flux is computed with the technique of "ray-tracing" (e.g., Rauch and Blandford, 1994; Fanton et al., 1997; Schnittman and Bertschinger, 2003): the disk as seen by a distant observer, is divided into small elements and for each one of them, the orbit of a photon is traced backward from the observer by following the geodesics in a Kerr space-time, until the orbit crosses the plane of the disk, where the emitted radiation is calculated. Finally, the observed flux density is given by the sum of all the contributions of each element (for all the details, see Li et al., 2005).

3.1.1 KERRBB parameters

As already mentioned before, KERRBB is designed for Galactic binaries and implemented in the interactive X-ray spectral fitting program XSPEC.[1] Here the list of the parameters:

- *Ratio* ζ between the disk power produced by a torque at the disk inner boundary and the disk power arising from accretion, allowed to vary between 0 and 1. As mentioned before, the torque can arise from a magnetic field connecting the disk to the BH of the infalling matter: when $\zeta = 0$, the solution corresponds to that of a standard Keplerian disk with zero torque at the inner boundary.

- *Specific angular momentum* a of the BH in units of the BH mass M (in geometrized units $G = c = 1$). The model allows the value to vary in the range $-1 \leq a \leq 0.9999$. However, following Thorne, 1974, the radiation emitted by the disk and swallowed by the hole produces a counteracting torque that prevents spin-up beyond a limiting state ($a \sim 0.998$).

- *Inclination angle* $\theta_{\rm v}$ of the disk i.e., the angle between the axis of the disk and the line of sight. For $\theta_{\rm v} = 0^\circ$ the disk is seen in a face-on configuration. The angles are allowed to vary up to 85°.

- *Mass* of the BH in units of the solar masses. Since the model is designed for stellar BHs, the allowed range is $1M_\odot \leq M \leq 100M_\odot$.

- *Effective mass accretion rate* of the disk in units of 10^{18} g/s, allowed to vary in the range 0 and 1000. When the torque at the inner disk boundary is zero, the effective accretion rate is just the mass accretion rate of the disk. When ζ is nonzero, the effective mass accretion rate is $M_{\rm eff} = (1+\zeta)\dot{M}$ and the total disk luminosity is then $L_{\rm d,eff} = \eta(a)\dot{M}_{\rm eff}c^2$.

- *Spectral hardening factor* $f_{\rm col} = T_{\rm col}/T_{\rm eff}$, between 1 and 10. If $f_{\rm col} = 1$, the emission is given by a standard black-boby superposition.

- *Distance* between the observer and the BH in units of kpc and two flags to switch on/off the effect of self-irradiation and limb-darkening.[2]

[1] The model is based on pre-calculated tables used to fit the data.
[2] The model has also a normalization parameter used in the XSPEC fitting routine.

3.2 KERRBB analytical approximation

As shown in Chap. 2, for the SS model, the peak frequency ν_p, peak luminosity $\nu_p L_{\nu_p}$ and the observed disk luminosity L_d^{obs} have simple analytical expressions, given by Eqs. 2.24 - 2.25 - 2.17. In this Section, I will describe the approach followed to obtain simple analytic tools to describe the KERRBB spectral emission, published in Campitiello et al., 2018 (see also Campitiello et al., 2019).

In this context, the study of the impact of different spin values and inclination angles on observable features of the AD surrounding SMBHs is an improvement with respect to early works (e.g., Cunningham, 1975; Zhang, Cui, and Chen, 1997), mostly in the field of X-ray binary BHs, since those works explored relativistic correction factors for a limited range of a and θ_v. My approximation provides analytic expressions for these factors across the full parameter range, under the assumption that KERRBB provides a reasonable description of the spectrum emitted by a disk around both stellar and SMBHs. In this context, the analytical expressions were found by assuming no torque at the disk inner boundary, a hardening factor fixed to 1, including the self-irradiation of the disk and neglecting the limb-darkening effect.

The choice of assuming a constant $f_{col} = 1$ is based on the work of Czerny et al., 2011: in their Section 2.2.2, they discuss the value of the hardening factor to adopt in their fitting procedure and compute it as a function of the radius of the disk (assuming a viscosity $\alpha = 0.1$) for two BHs, as stellar (10 $M_\odot$) and a supermassive ($2.7 \times 10^9 M_\odot$); in their Figure 2, they plot it in the two cases and it is easy to see that for the SMBH, the value is almost constant ($f_{col} < 1.1$) and, using their approximation, for different values of $\dot{M}$, f_{col} is still lower than ~ 1.1. With such a choice, the results related to the BH mass and accretion rate are not drastically affected (see Sect. 3.2.3).

For the SS model, L_d^{obs} depends only on the viewing angle of the system. However, in the General relativistic case, that is no longer valid (Cunningham, 1975): in fact, relativistic effects modify not only the size of the ISCO but also the pattern of the emitted photons. Fig. 3.1 compares the photon paths in the cases of SS and KERRBB with $a = 0$: in this latter case, light-bending plays a crucial role because it bends the photon trajectories towards different directions with respect to the normal of the disk; this effect, along with a lower efficiency η, makes the $a = 0$ KERRBB model dimmer than the SS one when observed face-on. If the BH is maximally spinning, the ISCO moves closer to the hole and relativistic effects become stronger; the

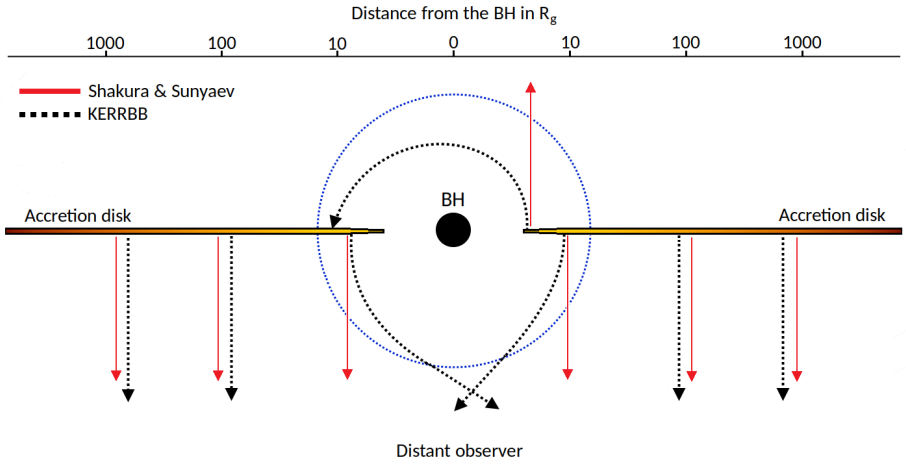

FIGURE 3.1: Schematic view of the photon emission pattern of an AD around a BH. A distant observer is at the bottom of the figure and sees the disk face-on. For the classical SS model (red rays), photon trajectories go straight to a distant observer (i.e., no light-bending or any other relativistic effect). For the KERRBB model (dashed black rays), photon trajectories are bent and their paths are changed towards different directions with respect to the SS case (the region where light-bending is stronger is schematically represented with a dashed blue circle). The top axis is the logarithmic distance from the BH in units of R_g.

efficiency grows and the disk is bright even for edge-on observers (see Fig. 3.4). Thus, the emission pattern depends strongly on the BH spin. It is worth noticing that the photons emitted in the outer region of the disk are not affected by relativistic effects since they are far from the SMBH strong gravity influence and the radiation pattern is similar for both models.

For KERRBB, an expression similar to Eq. 2.17 can be written for the observed disk luminosity, linked to the total disk luminosity L_d, i.e.,

$$L^{obs}_{d,Kerr}(\theta_v, a) = f(\theta_v, a) L_d(a) = f(\theta_v, a)\eta(a)\dot{M}c^2. \tag{3.2}$$

where the function $f(\theta_v, a)$ contains all the modifications due to the BH spin a and the viewing angle of the system θ_v. In order to find the value of f, $L^{obs}_{d,Kerr}$ has been calculated for different values of the spin and angle, with fixed M and $\dot{M}$. Then, an analytic expression was found to interpolate the numerical results with a good accuracy: the first term of the analytic expression is chosen to be $\cos\theta$, for an easy comparison with Eq. 2.17. A good match is found using the following functional form:

$$f(\theta_v, a) = A\cos\theta[1 - (\sin\theta_v)^C]^B[1 - E(\sin\theta_v)^F]^D \tag{3.3}$$

In this form, $f(\theta, a)$ differs from the numerical result by a factor $< 1\%$ (see

Appendix A). All the parameters A, B, C, D, E, F are functions of the spin a: for fixed values of θ_v, analytical expressions were found by varying the BH spin, in the form

$$\mathcal{F}(a) = \alpha + \beta x_1 + \gamma x_1^2 + \delta x_1^3 + \epsilon x_1^4 + \iota x_1^5 + \kappa x_1^6 \tag{3.4}$$

with $x_1 = \mathrm{Log}(1-a)$. The values of α, β, γ, ϵ, ι, κ are listed in Tab. A.1 (see Appendix A).

As examples, in the case with $a = -1$ ($\eta = 0.037$), $a = 0$ ($\eta = 0.057$) and $a = 0.9982$ ($\eta = 0.324$), the functions describing the observed disk luminosity for different angles θ_v are

$$\frac{L^{\mathrm{obs}}_{\mathrm{d,Kerr}}(\theta_v)}{\dot{M}c^2} \approx \begin{cases} 0.065\cos\theta\dfrac{[1-\sin^5\theta_v]^{1/10}}{[1-\sin^2\theta_v]^{1/5}} & \text{for } a = -1 \\ 0.094\cos\theta\dfrac{[1-\sin^7\theta_v]^{1/10}}{[1-\sin^2\theta_v]^{1/5}} & \text{for } a = 0 \\ 0.287\cos\theta\dfrac{[1-\sin^{12}\theta_v]^{1/5}}{[1-\sin^{1.9}\theta_v]^{3/5}} & \text{for } a = 0.9982 \end{cases}$$

where, it is easy to notice the similarity between the cases with $a = -1$ and $a = 0$: this is related to the fact that for low spin values, the angular pattern is almost the same given that relativistic effects are less strong with respect to the case with large spin values.

3.2.1 Relativistic radiation angular pattern

The relativistic angular dependence of the observed disk luminosity as seen by a distant observer is described by the function $f(\theta_v, a)$ (in the SS case, this function corresponds to the factor $2\cos\theta_v$; Eq. 2.17). As in the classical treatment, $L^{\mathrm{obs}}_{\mathrm{d}}$ must satisfy Eq. 2.16 that, in the KERRBB case, becomes

$$L_{\mathrm{d}}(a) = \int_0^{\pi/2} L^{\mathrm{obs}}_{\mathrm{d,Kerr}}(\theta, a)\sin\theta d\theta, \tag{3.5}$$

which implies

$$\int_0^{\pi/2} f(\theta, a)\sin\theta d\theta = 1 \tag{3.6}$$

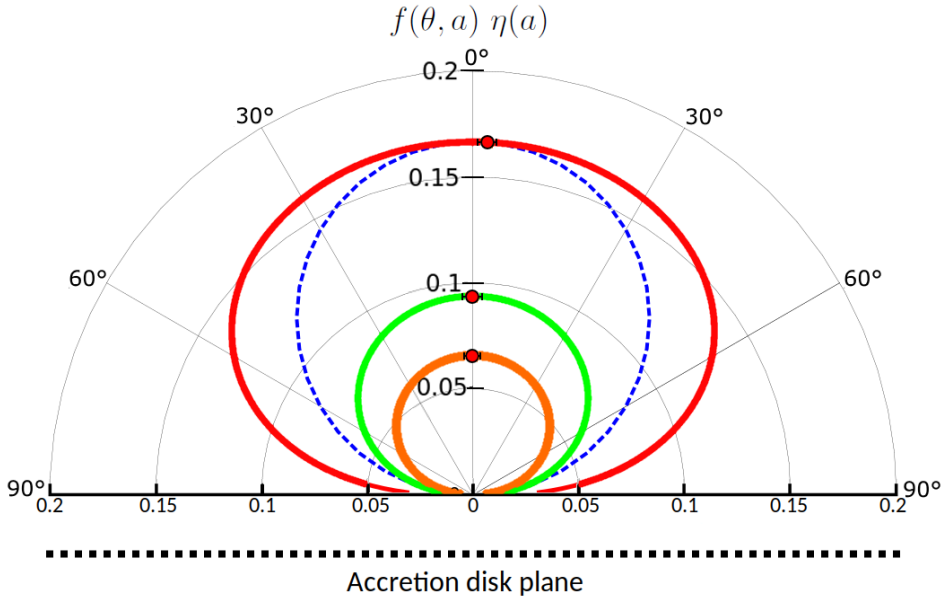

FIGURE 3.2: Radiation angular pattern of KERRBB for different spin values. The radial axis is given by the product $f(\theta_v, a)\eta(a)$ (i.e., the observed disk luminosity $L_d^{obs}(\theta_v, a)$ normalized on $\dot{M}c^2$). The classical non-relativistic SS pattern (dashed blue line) is compared with the $a = -1$ (orange line), $a = 0$ (green line) and $a = 0.797$ (red line) KERRBB patterns (for the SS model, the radial axis is $2\cos\theta_v\eta_{SS} \approx 0.17\cos\theta_v$). The angle at which the observed disk luminosity is maximized is represented with a red dot.

This normalization is always valid for any spin values with a precision $< 3\%$ (Eq. 3.6 is valid also in the SS case with the substitution $f(\theta_v, a) \to 2\cos\theta_v$).

Figures 3.2-3.3 show the relativistic radiation angular pattern of KERRBB for different spin values, compared with the non-relativistic SS model (dashed blue line). The KERRBB model with $a = 0.797$ (red line) represents the better approximation of the classical SS model with the same parameters (M, $\dot{M}$) for $\theta_v = 0°$: this similarity is due to the fact that the efficiency of a non-spinning BH ($\eta = 0.057$) is lower than the Newtonian one ($\eta_{SS} \sim 0.083$) therefore, to match the SS luminosity, a larger efficiency is needed, and hence a larger spin, also enhanced by light-bending. Notice that, for $\theta_v > 0°$, the similarity between SS and KERRBB (with the same parameters), is reached for smaller spin values.

In both Figures, it is easy to notice that, for $a < 0.8$, the KERRBB angular pattern is very similar to the classical $\cos\theta_v$ behavior. For larger spins, the pattern is strongly modified by the relativistic effects and the observed disk luminosity L_d^{obs} is larger at larger angles, close to the equatorial plane: the

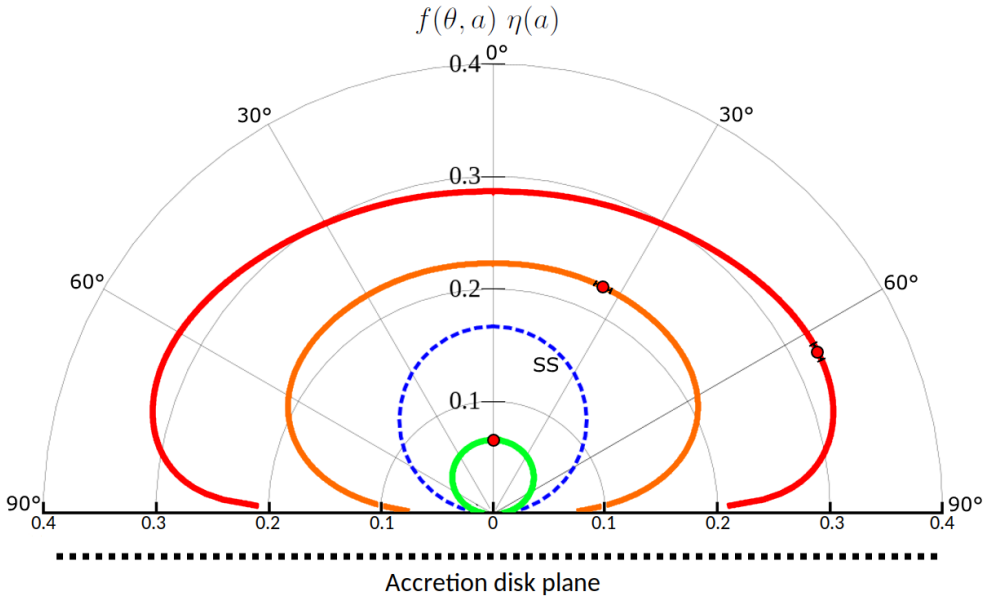

FIGURE 3.3: Same as Fig. 3.2. The SS model (dashed blue line) is compared with the $a = -1$ (green line), $a = 0.95$ (orange line) and $a = 0.9982$ (red line) KERRBB patterns. The angle at which the observed disk luminosity is maximized is represented with a red dot.

maximum value depends on the BH spin which "shifts" it to larger angles. This angle θ_{max} can be found by setting the derivative of Eq. 3.3 with respect to θ equal to zero: for $a < 0.8$, the angle is close to the polar axis of the disk while, as examples, for $a = 0.9$, $\theta_{max} \sim 9°$, for $a = 0.95$, $\theta_{max} \sim 25°$ and for $a = 0.9982$, $\theta_{max} \sim 65°$ (see Tab. 3.1 for some reference values). Notice that the derivative of Eq. 3.3 is equal to zero also for $\theta_v = 90^{\theta}$: this solution must not be considered since $f(\theta_v, a)$ is defined in the KERRBB angle range $[0° : 85°]$.

Spin value [a]	θ_{max}	Spin value [a]	θ_{max}
0.9982	65°	0.6	0.4°
0.98	46°	0.5	0.2°
0.95	25°	0.4	0.1°
0.94	19°	0.3	0.03°
0.92	13°	0.2	0.01°
0.9	9°	0.1	$\sim 0°$
0.8	2°	0	$\sim 0°$
0.7	1°	-1	$\sim 0°$

TABLE 3.1: Values of the viewing angle θ_{max} at which the observed disk luminosity is maximized, for different a values (the precision is $< 5\%$). These results show the deviation of the relativistic angular pattern from the classical $\cos\theta$ law.

The strong modification of the spectrum emission due to relativistic effects makes the pattern more *isotropic* for $a > 0.9$ (as shown in Fig. 3.3). Such an effect is visualized on the $\nu - \nu L_\nu$ plane in Fig. 3.4: in the case with $a = 0$ (blue lines), relativistic effects are weak and spectra follows a behavior similar to the classical $\cos\theta$ law. Instead, in the case with $a = 0.9982$ (red lines), the spectrum peaks (and so $L^{\rm obs}_{\rm d,Kerr}$) are almost constant, even for large viewing angles. This is due to the combination of different relativistic effects (Doppler beaming, gravitational redshift and light-bending) enhanced by the large BH spin: the trajectories of the most energetic photons, coming from the innermost region of the disk and horizon) are bent in all directions and the intensity of radiation is almost the same at all viewing angles. It is worth noticing that, for a fixed viewing angle, the low-frequency part of the spectra is almost the same in both $a = 0$ and $a = 0.9982$ cases: in fact, this emission is related to the outer region of the disk where relativistic effects are negligible (a complete overlapping occurs at lower frequencies not visible in the plot).

Radiation angular pattern vs. frequency

It is important to notice that the radiation pattern function depends on ν since the emission at different frequencies is produced by different regions of the AD: the outer disk annuli are responsible for the spectrum produced at smaller frequencies (i.e. NIR - Optical bands) where relativistic effects are negligible, therefore the function $f(\theta, a)$ can be approximated by the classical $\cos\theta$ pattern. Instead, the inner annuli close to the BH are responsible for the large frequency emission around the spectrum peak where relativistic effects are stronger: for those frequencies, the radiation pattern function is similar to the one of $L^{\rm obs}_{\rm d}$ since this latter is proportional to $\nu_{\rm p} L_{\nu_{\rm p}}$ and is mostly produced by those annuli. In Fig. 3.4, it is easy to notice that in the case with $a = 0$, the emissions at all frequencies follow the $\cos\theta$ law (i.e., relativistic effects are negligible). Instead, in the case with $a = 0.9982$, the emission at larger frequencies is more isotropic and follows the function $f(\theta, a)$ (this isotropic behavior can be seen also in Fig. 3.3), while the low frequency part shifts towards lower luminosities as in the $a = 0$ case.

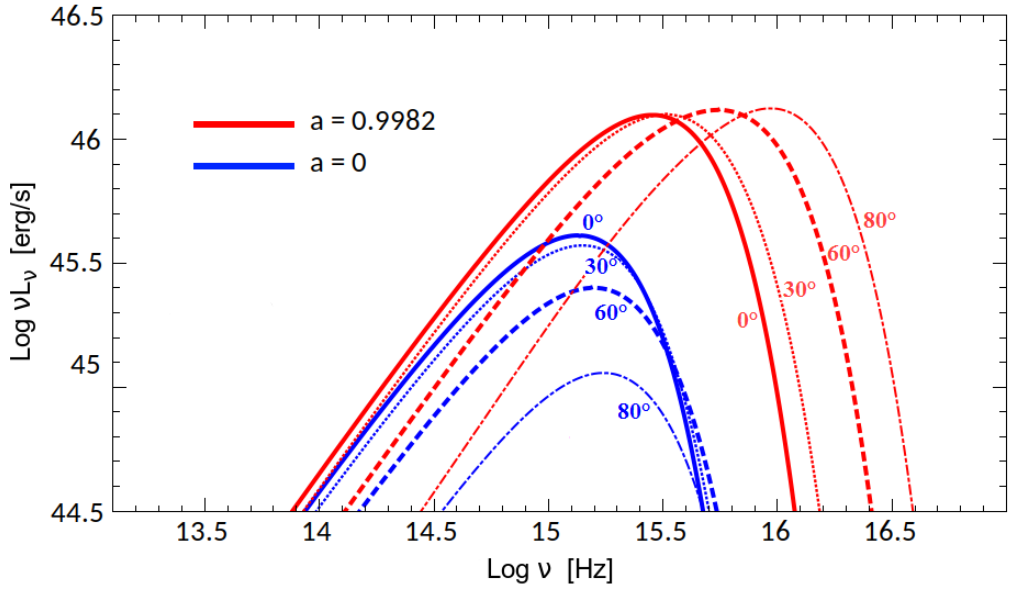

FIGURE 3.4: KERRBB spectra for different viewing angles and spins. All models have the same BH mass (Log $M/M_\odot = 9$) and accretion rate ($\dot{M}/M_\odot \mathrm{yr}^{-1} = 1.6$).

3.2.2 Scaling with black hole mass and accretion rate

For the non-relativistic SS model, the position of the peak frequency ν_p and the peak luminosity $\nu_\mathrm{p} L_{\nu_\mathrm{p}}$ scale with the BH mass and the accretion rate according to Eqs. 2.24-2.25. Analogous scalings for the KERRBB model have been found by Campitiello et al., 2018: as in the SS case, given that the emitted spectrum is a superposition of black-bodies whose flux is given by Eq. 2.28, the peak frequency and luminosity have the same dependencies on M and $\dot{M}$. However, the presence of the spin and relativistic effects modifies the basic equations with some additional terms.

Following Campitiello et al., 2018, it is possible to write the general KERRBB scaling relations as

$$\frac{\nu_\mathrm{p}}{\mathrm{Hz}} = \mathcal{A}\left[\frac{\dot{M}}{M_\odot \mathrm{yr}^{-1}}\right]^{1/4}\left[\frac{M}{10^9 M_\odot}\right]^{-1/2} g_1(a, \theta_\mathrm{v}), \tag{3.7}$$

$$\frac{\nu_\mathrm{p} L_{\nu_\mathrm{p}}}{\mathrm{erg/s}} = \mathcal{B}\frac{\dot{M}}{M_\odot \mathrm{yr}^{-1}} \cos\theta_\mathrm{v}\, g_2(a, \theta_\mathrm{v}), \tag{3.8}$$

where the functions g_1 and g_2 describe the dependencies of the spectrum on the BH spin a and the viewing angle θ_v. Those functions can be expressed as polynomials (see Appendix A): Campitiello et al., 2018 derived the following

functional

$$g_{\rm i}(a,\theta_{\rm v}=0^{\circ}) = \alpha_{\rm g} + \beta_{\rm g} y_1 + \gamma_{\rm g} y_2 + \delta_{\rm g} y_3 + \epsilon_{\rm g} y_4 + \zeta_{\rm g} y_5 + \iota_{\rm g} y_6 + \kappa_{\rm g} y_7 \quad (3.9)$$

where $i = 1,2$ is the index related to the specific g function, and $y_{\rm n} = {\rm Log}(n-a)$. Each of the parameters in Eq. 3.9 depends on the BH spin (see Appendix A). Such an approximation has a precision of $< 1\%$.[3] It is worth noticing that, as for the SS model (Eq. 2.26), the KERRBB observed disk luminosity is linked to the spectrum peak luminosity and a good approximation is $L^{\rm obs}_{\rm d,Kerr} \sim 2\nu_{\rm p} L_{\nu_{\rm p}}$.

3.2.3 KERRBB spectrum degeneracy

From Eqs. 3.7 - 3.8, it is easy to notice that, once the viewing angle is fixed, there is a degeneracy between the other three main parameters: in other words, the same peak frequency and luminosity (i.e., the same set of data) can be described with different combination of M, $\dot{M}$ and a. Moreover, this degeneracy is also marked by the fact that the different KERRBB models (given by different sets of parameters) show a similar spectral shape: this latter is similar to the SS one (with the same asymptotic behaviors given by Eqs. 2.19 - 2.20 - 2.21) since the overall emission is assumed to be a superposition of black-bodies in both models.

Figure 3.5 shows how changing M, $\dot{M}$ and a in a proper way leads to the same spectrum: from model A, increasing M shifts the peak to lower frequencies (model B); if the BH spin a is increased (model C) and the accretion rate $\dot{M}$ decreased, it is possible to obtain the spectrum D which is equal to the initial spectrum. Strictly speaking, different KERRBB models show small differences in the high-frequency UV exponential part of the spectra,[4] which can be highly absorbed due to the Galactic or Intergalactic Medium (IGM, see

[3] Since the KERRBB spectra move on the $\nu - \nu L_\nu$ plane according to Eqs. 3.7 - 3.8, it is possible to scale the KERRBB spectra (obtained from XSPEC) from stellar to SMBH masses, with fixed a and $\theta_{\rm v}$, assuming that the emission is a superposition of black-bodies in both systems. The shifting equations are summarized below:

$$\frac{\nu_{\rm fin}}{\nu_{\rm in}} = \left[\frac{\dot{M}_{\rm fin}}{\dot{M}_{\rm in}}\right]^{1/4} \left[\frac{M_{\rm in}}{M_{\rm fin}}\right]^{1/2} \qquad \frac{\nu L_{\nu,{\rm fin}}}{\nu L_{\nu,{\rm fin}}} = \frac{\dot{M}_{\rm fin}}{\dot{M}_{\rm in}} \quad (3.10)$$

where the subscript *in* (*fin*) refers to the initial (final) parameters of the spectrum.

[4] Spectra related to large spin values have a brighter exponential tail because the high-frequency photons, produced in the inner region of the disk, have an energy which is enhanced by the strong relativistic effects linked to the BH spin.

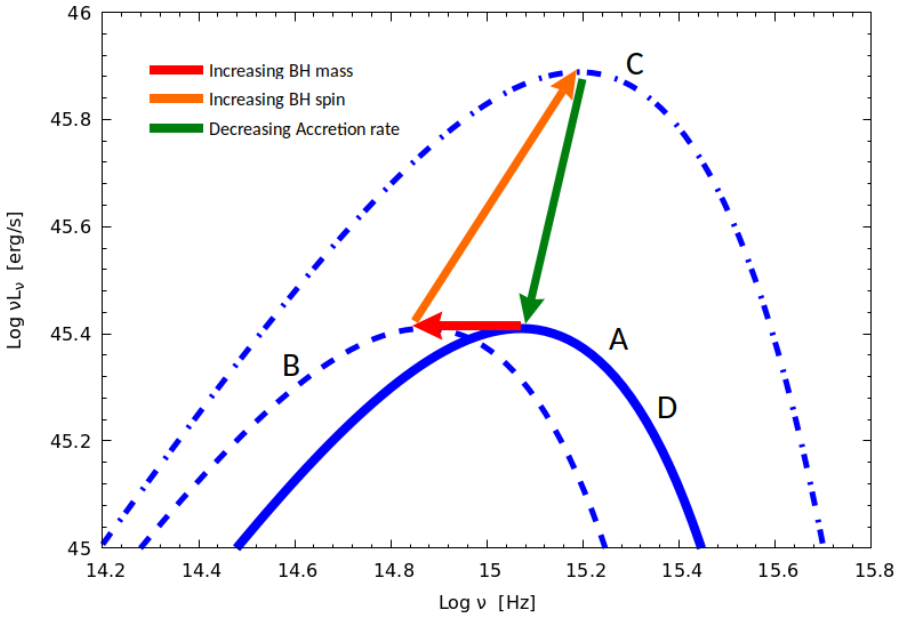

FIGURE 3.5: Dependence of KERRBB on M, $\dot{M}$ and a. Changing the three parameters conveniently leads to the same spectrum with the peak in the same position. Model A has Log $M/M_\odot = 9.00$, $\dot{M}/M_\odot \mathrm{yr}^{-1} = 1$ and $a = 0$. Model B has Log $M/M_\odot = 9.40$, $\dot{M}/M_\odot \mathrm{yr}^{-1} = 1$ and $a = 0$. Model C has Log $M/M_\odot = 9.40$, $\dot{M}/M_\odot \mathrm{yr}^{-1} = 1$ and $a = 0.9982$, and model D has Log $M/M_\odot = 9.40$, $\dot{M}/M_\odot \mathrm{yr}^{-1} = 0.33$ and $a = 0.9982$. In this example, the viewing angle is $\theta_\mathrm{v} = 0°$.

e.g., Madau, 1995; Haardt and Madau, 2012; Castignani et al., 2013; Campitiello et al., 2020; see also Chap. 4).

If the observables, ν_p and $\nu_\mathrm{p} L_{\nu_\mathrm{p}}$, are known, it is possible to find all the solutions (in term of M, $\dot{M}$ and a, for a fixed θ_v) by re-arranging Eqs. 3.7 - 3.8:

$$\frac{M}{10^9 M_\odot} = \left[g_1(\theta_\mathrm{v}, a) \frac{\mathcal{A}}{\nu_\mathrm{p}} \right]^2 \sqrt{\frac{\nu_\mathrm{p} L_{\nu_\mathrm{p}}}{\mathcal{B} \cos\theta_\mathrm{v} \, g_2(\theta_\mathrm{v}, a)}} \tag{3.11}$$

$$\frac{\dot{M}}{M_\odot \mathrm{yr}^{-1}} = \frac{\nu_\mathrm{p} L_{\nu_\mathrm{p}}}{\mathcal{B} \cos\theta_\mathrm{v} \, g_2(\theta_\mathrm{v}, a)} \tag{3.12}$$

Figure 3.6 shows the connection between the BH mass M, the accretion rate $\dot{M}$ and BH spin a, for a KERRBB spectrum with a fixed peak frequency and luminosity, in the case with $\theta_\mathrm{v} = 0°$. In principle, the $M - \dot{M}$ plane can be useful to set constraints on the parameters:

- *Constraining a and $\dot{M}$*: if an independent estimate of the BH mass is available (e.g., virial mass), it is possible to constrain the BH spin and the accretion rate. Fig. 3.6 shows how $\dot{M}$ and a can be constrained with this approach: the made-up independent BH mass (Log $M/M_\odot =$

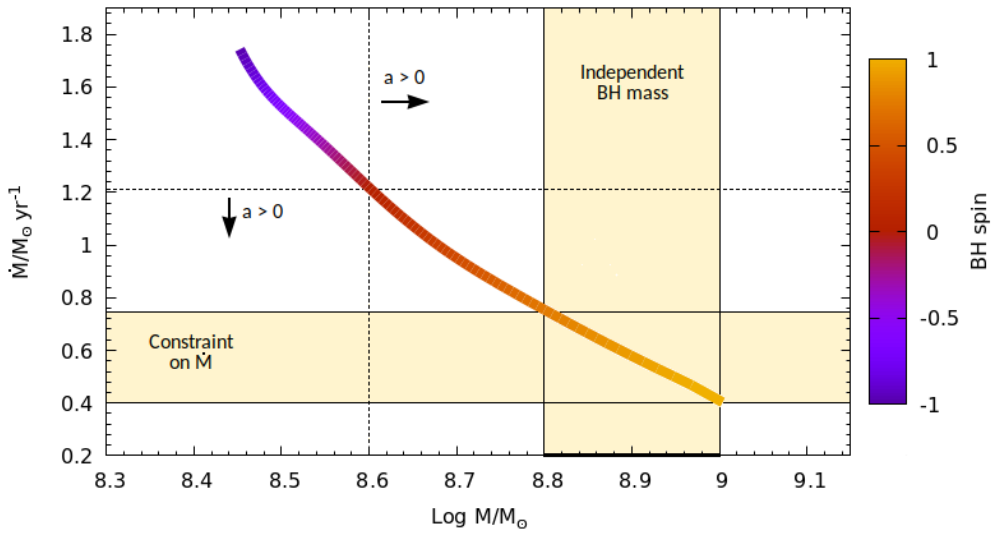

FIGURE 3.6: KERRBB solutions for a fixed peak frequency (Log $\nu_{\rm p}/{\rm Hz} = 15.30$) and luminosity (Log $\nu_{\rm p} L_{\nu_{\rm p}}/{\rm erg/s} = 45.50$, in the case with $\theta_{\rm v} = 0°$ (see Table 3.2). In principle, an independent BH mass estimate (vertical yellow region, Log $M/M_{\odot} = 8.9 \pm 0.1$) can be used to put constraints on $\dot{M}$ and a. In the same way, a spin estimate ($a > 0$, horizontal dashed black line) can set constraints on $\dot{M}$ and M.

8.9 ± 0.1, vertical stripe) intercepts the curve of solutions and identifies a range of possible accretion rates ($\dot{M}/M_{\odot}{\rm yr}^{-1} = 0.58 \pm 0.18$) and spin values ($a = 0.86 \pm 0.14$). The narrower the range of the independent BH mass is, the more precise the $\dot{M}$ and a estimates are.

- *Constraining M and $\dot{M}$*: parallel to the previous subsection, an independent estimate on the BH spin could set constraints on M and $\dot{M}$ as shown in Fig. 3.6, by identifying a section of the solution curve for $a > 0$. Differently from the BH mass estimates, estimating the BH spin is not trivial and uncertainties are still large (see Chap. 1.2). However, for some classes of AGNs (i.e., blazars), there is a general consensus that relativistic jets are generated by tapping the rotational energy of SMBHs with large spins (e.g., Tchekhovskoy, Narayan, and McKinney, 2011; Gardner and Done, 2018): this information can be used to put constraints on the BH mass (see Chap. 4).

Knowing how the BH mass and the accretion rate are linked together with the BH spin (Eqs. 3.7 - 3.8), for a given set of data (i.e., an observed spectrum), it is straightforward to deduce that also the relative total disk luminosity $L_{\rm d}$

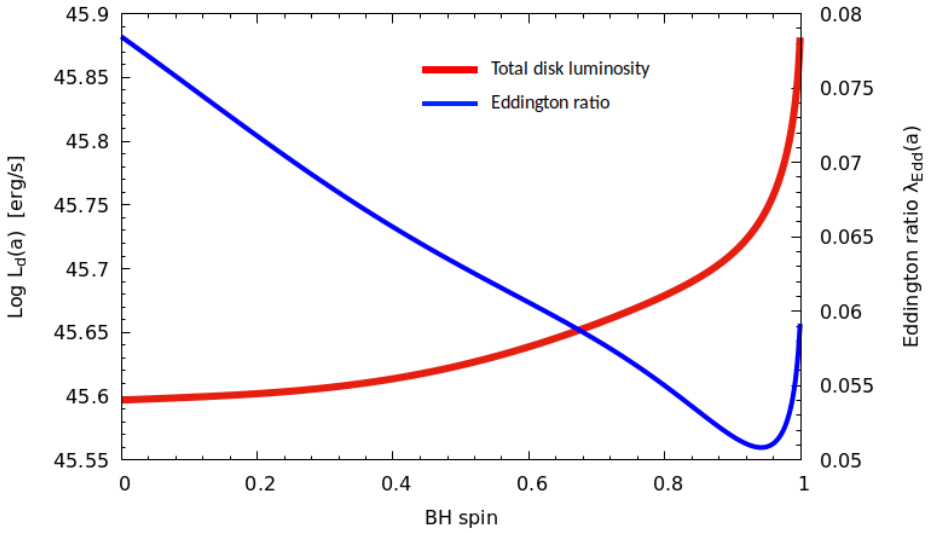

FIGURE 3.7: KERRBB total disk luminosity (red line) and Eddington ratio (blue line) as functions of the BH spin, for a fixed peak frequency (Log $\nu_{\rm p}/{\rm Hz} = 15.30$) and luminosity (Log $\nu_{\rm p} L_{\nu_{\rm p}}/{\rm erg/s} = 45.50$). In this example, the angle is $\theta_{\rm v} = 0°$. For the SS model, Log $L_{\rm d,SS}/{\rm erg/s} = 45.50$ and $\lambda_{\rm Edd,SS} = 0.04$.

and the Eddington ratio $\lambda_{\rm Edd}$ are spin-dependent:

$$L_{\rm d}(a) = \eta(a)\dot{M}(a)c^2 \approx 12.49\ \frac{\eta(a)}{g_2(\theta_{\rm v}, a)}\frac{\nu_{\rm p} L_{\nu_{\rm p}}}{\cos\theta_{\rm v}} \tag{3.13}$$

$$\lambda_{\rm Edd}(a) = \frac{L_{\rm d}(a)}{L_{\rm Edd}(a)} \approx \mathcal{D}\frac{\eta(a)}{g_1^2(\theta_{\rm v}, a)\ \sqrt{g_2(\theta_{\rm v}, a)\ \cos\theta_{\rm v}}}\nu_{\rm p}^2\ \sqrt{\nu_{\rm p} L_{\nu_{\rm p}}} \tag{3.14}$$

As Eqs. 2.26 - 2.27 found for the SS model, these latter expressions preserve the common proportionality with the peak frequency and luminosity. However, given the presence of relativistic effects, Eqs. 3.13 - 3.14 have additional terms depending on the BH spin therefore, for a given set of data (i.e., a fixed peak position), more solutions are allowed contrary to the SS case.

Figure 3.7 shows the total disk luminosity $L_{\rm d}$ and the Eddington ratio $\lambda_{\rm Edd}$ as functions of the BH spin a, for a fixed peak frequency and luminosity: despite the decreasing trend of $\dot{M}$ with the BH spin (Fig. 3.6), the dependence on the radiative efficiency η makes the disk luminosity increase as the BH spin increases. Instead, the Eddington ratio decreases with a, following the same behavior of the BH mass (Fig. 3.6) until $a \sim 0.95$ and then it grows with a: for $a < 0.95$, the value of $\lambda_{\rm Edd}$ decreases because the Eddington luminosity $L_{\rm Edd}$ increases by a factor of ~ 2 with respect to the disk luminosity $L_{\rm d}$, which is almost constant (there is a small increment of a factor of ~ 1.2); instead, for spin values close to the maximum, the disk luminosity increases

Spin a	η	Log M	$\dot{M}$	$\lambda_{\rm Edd}$
-1	0.038	8.45	1.74	0.106
-0.8	0.040	8.48	1.59	0.095
-0.6	0.043	8.51	1.51	0.091
-0.4	0.047	8.53	1.42	0.089
-0.2	0.051	8.56	1.33	0.085
0	0.057	8.60	1.21	0.078
0.2	0.064	8.65	1.09	0.071
0.4	0.075	8.70	0.96	0.065
0.6	0.091	8.76	0.84	0.060
0.8	0.122	8.84	0.69	0.055
0.9	0.156	8.90	0.58	0.052
0.9982	0.321	9.00	0.40	0.058

TABLE 3.2: Some of the KERRBB solutions shown in Fig. 3.6 for a spectrum with a fixed peak frequency and luminosity. Masses are in units of $M_\odot$ and accretion rates in units of $M_\odot \mathrm{yr}^{-1}$.

more significantly than the Eddington luminosity due to a larger radiative efficiency. For larger viewing angles ($\theta_{\rm v} > 50°$) the value of $\lambda_{\rm Edd}$ is always decreasing for all spin values (see Sect. 4.2 and Appendix A).

In this context, the choice of fixing the hardening factor to 1 does not affect the results related to M, $\dot{M}$ and $\lambda_{\rm Edd}$ drastically: as already discussed in Sect. 3.2, from the work of Czerny et al., 2011, $f_{\rm col}$ is always less than ~ 1.1 for SMBHs and different $\dot{M}$. The presence of such an extra parameter modifies only $\nu_{\rm p}$ which is shifted towards larger frequencies as $\propto f_{\rm col}$: Eq. 3.11 and Eq. 3.14 are modified with the extra term $\propto f_{\rm col}^2$ and $\propto 1/f_{\rm col}^2$, respectively. Therefore, assuming $f_{\rm col} < 1.1$, the results related to both M and $\lambda_{\rm Edd}$ are modified only by a factor < 1.2.

3.3 Accretion disk models: uncertainties

Despite the numerous models developed to describe the AD emission around a SMBH, the origin of the BBB in AGNs is still under debate. As discussed extensively in Koratkar and Blaes, 1999 and references therein (see also Netzer, 2015), simple thermal models do not provide a good description of the AD emission. As these authors point out, some of the most significant inconsistencies of the standard SS thin disk (and the relativistic versions) are:

- The broadband continuum slopes β (with $L_\nu \propto \nu^\beta$) in the Optical - UV bands found in the literature (e.g., Neugebauer et al., 1979; Berk et al., 2001a; Bonning et al., 2007; Davis et al., 2007) are incompatible with the theoretical slope $\beta = 1/3$, expected from the AD model (Eq.

2.20). However, the characteristic 1/3 slope can be seen at frequencies much lower than the peak, namely in the NIR - Optical bands (Fig. 2.2), where other components contribute, like the host-galaxy emission and the dusty torus (see, e.g., Kishimoto et al., 2008; Calderone et al., 2013; see also Chap. 4). Moreover, the observed spectrum slope (in a particular frequency range) may depend on other factors linked to the properties of the accretion and the SMBH (see e.g., Hubeny et al., 2000; Davis and Laor, 2011).

- On average, AGNs with different peak luminosities show similar peak frequencies (e.g., Sanders et al., 1989; Walter and Fink, 1993; Davis et al., 2007; Laor and Davis, 2011). However, this average estimate must not be considered an evidence against the AD models such as SS and KERRBB: in fact, for SMBH masses in the range $10^8 < M/M_\odot < 10^{10}$ and Eddington ratios in the range $0.01 < \lambda_{\rm Edd} < 1$, the peak frequency for a classical SS model is expected to span a range of 1 order of magnitude (i.e., $14.85 < \mathrm{Log}\ \nu_{\rm p}/\mathrm{Hz} < 15.85$) while for the KERRBB model the range is even larger, considering also the presence of the BH spin (see e.g., Calderone et al., 2013; Campitiello et al., 2020).

- Microlensing observations in AGNs suggest that the ADs are larger than what the standard alpha-disk model predicts: Rauch and Blandford, 1994, using the equations for a Schwarzschild BH, found that a thermal AD is too large to fit within the microlensing size constraint by a factor of ~ 3. However, Jaroszynski, Wambsganss, and Paczynski, 1992 found instead that ADs were consistent with the microlensing constraint, using Kerr BHs.

- A truncated disk (from a radius $> 10R_{\rm g}$) has been proposed to reconcile the observations of narrow iron lines and the Optical-UV disk luminosity and, in a few works (e.g., Reb et al., 2018; Younes, Ptak, Ho, et al., 2019) the authors found that such a solution is more appropriate than a full AD up to the ISCO. If this is the case for all AGNs, relativistic effects are negligible since they are important in the innermost region of the disk (see Sect. 3.2) and relativistic models can be approximated with a truncated SS model. However, these conclusions have been drawn for low-luminosity AGNs ($L_{\rm bol} < 10^{43}$ erg/s) which can also be described in the ADAF regime. For very bright sources, no indication of a truncated disk has been observed.

- The alpha-disks are characterized by a non-zero thickness which depend $\dot{M}$, M and the value of α. In the classical calculations, the disk thickness is considered $z \ll r$ and hence negligible. However, Laor and Netzer, 1989 (see also McClintock et al., 2006) stated that, in order for the AD to be thin, the constraint $z_r/r < 0.1$ (where z_r is the disk half-thickness), described in the full relativistic regime (Novikov and Thorne, 1973, Eq. 5.9.10), leads to

$$\frac{z_r}{r} \propto \lambda_{\rm Edd} \frac{\mathcal{C}(a,r)}{\eta(a)} \tag{3.15}$$

  where $\mathcal{C}(a,r)$ it the relativistic corrections depending on the radius and the BH spin (see Novikov and Thorne, 1973). For each spin value, at a particular radius, the ratio $\mathcal{C}(a,r)/\eta(a)$ reaches a maximum: using this latter leads to the limiting cases, i.e. $\lambda_{\rm Edd} < 0.3$ for $a = 0.9982$ and $\lambda_{\rm Edd} < 0.25$ for $a < 0$. Based on these results, the black-body thin AD models (such as SS and KERRBB) are trustworthy for $\lambda_{\rm Edd} < 0.3$: for larger values others models must used that account for the disk vertical structure (e.g., *Polish doughnuts, thick disks and magnetized tori*, Paczynski and Wiita, 1980; Jaroszynski, Abramowicz, and Paczynski, 1980; Abramowicz, Calvani, and Nobili, 1983; Wielgus et al., 2016; *Slim disks*, Abramowicz et al., 1988; Sadowski et al., 2011; Straub et al., 2011; see next Section). On the same line, in order for the disk to be thin, the Eddington ratio must be larger than $\lambda \sim 0.01$, since for smaller accretion rates the ADAF regime sets in, changing the main properties of the accretion disk (e.g., Ichimaru, 1977; Rees et al., 1982; Chen et al., 1995; Narayan and Yi, 1995).

- The spectrum from a simple AD does not reproduce the observed power-law extending in the UV-X bands, the so-called "Soft X-ray excess". This component, observed in many objects, have been described by several models (e.g., relativistically blurred photoionized disc reflection model, Ross and Fabian, 2005; Crummy et al., 2006; Comptonization by an X-ray Corona, Done et al., 2012; Kubota and Done, 2018 and references therein; see next Section), although the origin is not well established (e.g. Caballero-Garcia et al., 2019).

  As already discussed before, many others used a constant hardening factor $f_{\rm col} > 1$ to mimic the effect of an X-ray Corona above the disk, even though it is an oversimplified assumption: if the Corona is present

above and in the inner region of the AD, only those annuli will be "hidden", leaving the outer region emission unaffected. This will result in a dimmer observed disk luminosity with respect to the intrinsic one (see Kubota and Done, 2018 and next Section).

To address all those mentioned problems that cannot be solved in the thin disk regime implemented in several models, many authors explored different possibilities of accretion around a SMBH. In the next Section, I will discuss some of them which will be used in the next Chapters.

3.4 Other accretion disk models

In this Section, I will review about two relativistic accretion disk models for which the vertical structure of the disk and the effect of the presence of an X-ray Corona above the disk are taken into account. In the last part, I will mention disk-wind models for completeness even though they are not used in the final Chapters.

3.4.1 Slim disk

The usual α-viscosity prescription assumes that all the heat generated in the disk is immediately radiated away. This assumption leads to disks that are thermally and viscously unstable when the accretion rate is high (see, e.g., Shakura and Sunyaev, 1976): the disk inflates due to the inner radiation pressure and enters the *slim regime* where the flow is dominated by advection of heat (over radiative energy transport) in the inner parts of the disk (Abramowicz et al., 1988). These models are more appropriate for bright AGNs (where the accretion rate is larger) than the standard thin disk models.

As already mentioned before, the threshold between the thin and the slim regimes can be obtained by assuming that the half-thickness of the disk is $z_r < 0.1\ r$ (Eq. 3.15; see Laor and Netzer, 1989; McClintock et al., 2006): this constraint leads to the limiting cases for each BH spin value in terms of Eddington ratios, in general $\lambda_{\rm Edd} < 0.3$ (see Sect. 4.2).

The first calculations about the emergent slim disk spectrum were done by Szuszkiewicz, Malkan, and Abramowicz, 1996, assuming that each annulus emits as a modified black-body: at low accretion rates, the slim disk spectra are identical to the thin disk ones, instead, for larger $\dot{M}$ values, the SED of a slim disk becomes redder in the extreme UV than that of a thin disk

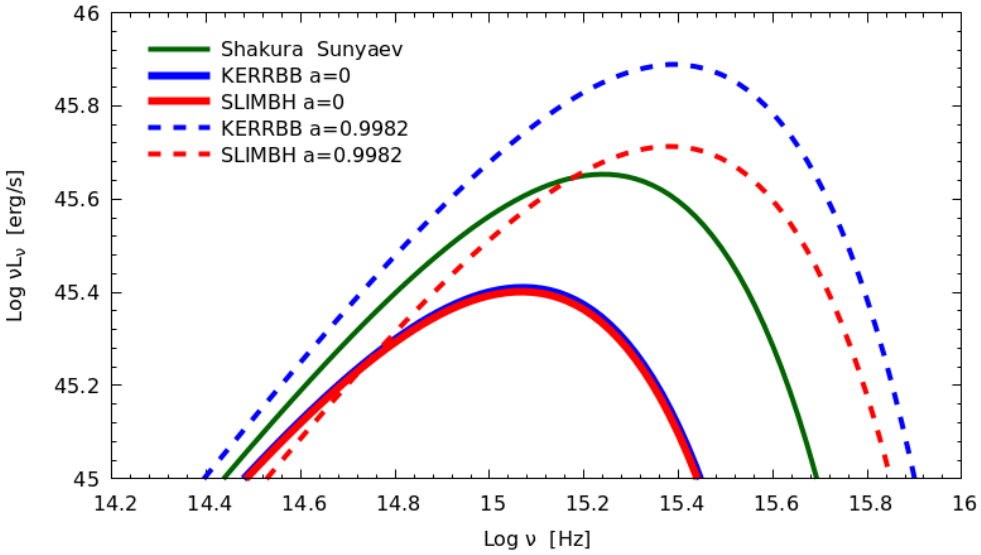

FIGURE 3.8: Comparison between the SS model (green line), KERRBB (blue lines) and SLIMBH (red lines) for the same BH mass (Log $M/M_\odot = 9$), accretion rate ($\dot{M}/M_\odot \mathrm{yr}^{-1} = 1$) and viewing angle ($\theta_\mathrm{v} = 0°$). The SLIMBH viscosity is set to $\alpha = 0.1$. The Eddington luminosities are $\lambda_{\mathrm{Edd,SS}} = 0.04$ for the SS model, $\lambda_{\mathrm{Edd}} = 0.03$ and $\lambda_{\mathrm{Edd}} = 0.15$ for both relativistic models for $a = 0$ and $a = 0.9982$, respectively.

model with the same M and $\dot{M}$. Moreover, for the same set of parameters, slim disks are dimmer than the thin ones due to a lower radiative efficiency η: part of the energy dissipated in the disk is trapped in the accreting flow and not radiated away (e.g., Katz, 1977; Begelman, 1978) and this *photon-trapping effect* is more prominent for large spin values (see Sadowski, 2009).

Relativistic slim disk model SLIMBH

The relativistic model SLIMBH (Abramowicz et al., 1988; Sadowski, 2009; Sadowski et al., 2009; Sadowski et al., 2011; Straub, Done, and Middleton, 2013) describes the emission produced by a slim disk around a Kerr BH. It is based on the relativistic description of Novikov and Thorne, 1973 and it accounts also for the vertical radiative energy transport which is not negligible for high accretion rates. As KERRBB, the observed spectrum is computed using the ray-tracing technique and it is implemented in the interactive X-ray spectral fitting program XSPEC for stellar BHs.[5]

[5] Li, Yuan, and Cao, 2010 used the ray-tracing technique to calculate the emitted spectra for a slim disk around Kerr BHs, studying the effect of photon-trapping and self-shadowing (due to the non-negligible disk thickness): their work is an improvement of the KERRBB model in the slim regime, although there is no public code available.

SLIMBH adopts some of the KERRBB parameters (a, θ_v, M, f_{col}, distance from the observer, flag to switch on/off the limb-darkening effect), neglects others (i.e., the inner torque of the disk) and introduces new ones as the Eddington ratio λ_{Edd} (instead of the accretion rate $\dot{M}$), the alpha-viscosity α and a flag to calculate the disk surface profile from the actual photosphere or the equatorial plane (ignoring the disk height profile).[6]

Figure 3.8 shows the comparison between SLIMBH, KERRBB and SS models for the same set of parameters (Log $M/M_\odot = 9$, $\dot{M}/M_\odot \mathrm{yr}^{-1} = 1$, $\theta_v = 0°$), with the hardening factor $f_{col} = 1$: both KERRBB and SLIMBH with $a = 0$ are dimmer with respect the SS model due to the lower radiative effiency (0.057 vs. 0.083); moreover, the two relativistic models overlap since the Eddington ratio is small and the photon-trapping effect is negligible. Instead, in the case with $a = 0.9982$, both relativistic models are brighter then the SS one but SLIMBH is dimmer than KERRBB because its radiative efficiency is lower.

SLIMBH analytical approximation

The procedure to find analytic expression for SLIMBH is similar to the one adopted for KERRBB in Sect. 3.2. For this work, it is assumed a viscosity $\alpha = 0.1$ although the range found in literature is $0.01 < \alpha < 0.5$ (see King, Pringle, and Livio, 2007),[7] hardening factor $f_{col} = 1$ (constant throughout the disk) and no limb-darkening effect (the flux is calculated from the disk photosphere). Since the Eddington ratio is a free parameter of the model (instead of $\dot{M}$), Eqs. 3.7 - 3.8 are re-written using the definition for λ_{Edd} and including all the effects due to spin and viewing angle in the new analytical functions $g_{1,s}$ and $g_{2,s}$:

$$\frac{\nu_p}{\mathrm{Hz}} = \mathcal{A}\left[\frac{\lambda_{Edd}}{0.45}\right]^{1/4}\left[\frac{M}{10^9 M_\odot}\right]^{-1/4} g_{1,s}(\theta_v, a, \lambda_{Edd}) \tag{3.16}$$

$$\frac{\nu_p L_{\nu_p}}{\mathrm{erg/s}} = \mathcal{B}\left[\frac{\lambda_{Edd}}{0.45}\right]\left[\frac{M}{10^9 M_\odot}\right] \cos\theta_v \; g_{2,s}(\theta_v, a, \lambda_{Edd}) \tag{3.17}$$

The new functions, $g_{1,s}$ and $g_{2,s}$, depend also on the Eddington ratio, contrary to the KERRBB case. Their value has been computed in the following

[6] SLIMBH introduces the possibility to calculate the spectra using the TLUSTY code (Hubeny and Lanz, 1995; Hubeny et al., 2011 and references therein): the code was designed to study stellar atmospheres but also to calculate the vertical structure of accretion disks (assumed in hydrostatic equilibrium).

[7] SLIMBH allows to vary the alpha parameter in the range $0.005 < \alpha < 0.1$: changing this parameter does not affect the resulting spectra drastically.

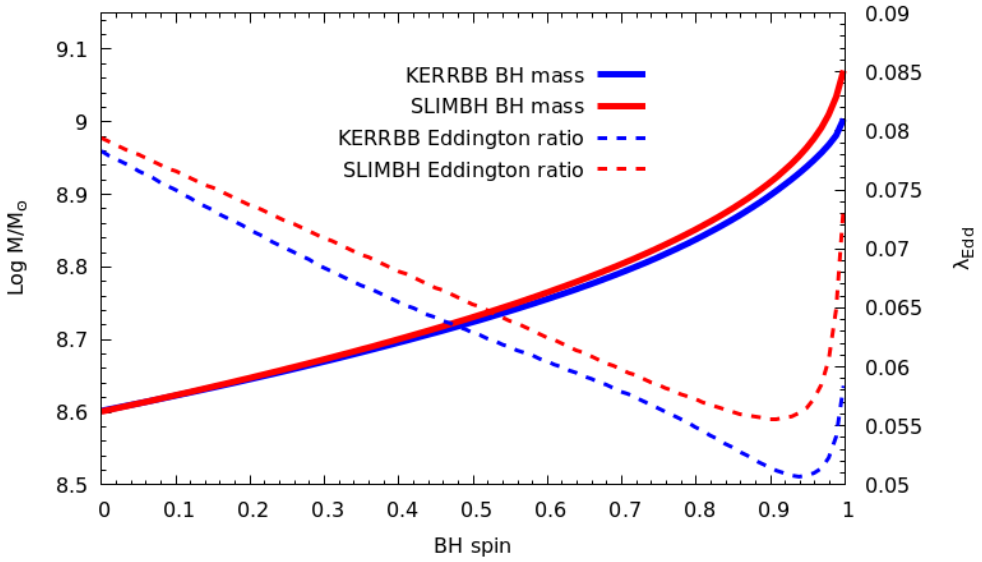

FIGURE 3.9: Comparison between the KERRBB (blue lines) and SLIMBH (red lines) solutions (M and $\lambda_{\rm Edd}$) as functions of the spin, for a fixed spectrum peak position (Log $\nu_{\rm p}$/Hz = 15.3 and Log $\nu_{\rm p} L_{\nu_{\rm p}}$/erg/s = 45.5) and viewing angle ($\theta_{\rm v} = 0°$).

way: for fixed values of $\theta_{\rm v}$, M and $\lambda_{\rm Edd}$, SLIMBH results were used to compute the spectrum peak frequency and luminosity for different spin values. For that particular value of $\lambda_{\rm Edd}$, an analytical function was found for both $g_{1,\rm s}$ and $g_{2,\rm s}$, depending on the BH spin. To compute the exact solutions, the following product has been considered

$$[\nu_{\rm p} L_{\nu_{\rm p}}]^{1/4} \nu_{\rm p} = \mathcal{E} [g_{2,\rm s}(\theta_{\rm v}, a, \lambda_{\rm Edd}) \cos\theta_{\rm v}]^{1/4} \, g_{1,\rm s}(\theta_{\rm v}, a, \lambda_{\rm Edd}) \sqrt{\lambda_{\rm Edd}}$$

where Log $\mathcal{E}$ = 26.84: the left-hand side of the expression was estimated from an observed spectrum while the right-hand side is derived by knowing $g_{1,\rm s}$ and $g_{2,\rm s}$. The comparison leads to the only value of the BH spin corresponding to the fixed $\lambda_{\rm Edd}$ (the BH mass M then can be inferred from Eqs. 3.16 - 3.17). The procedure has been conducted for different Eddington ratios values leading to the following analytic functions for $g_{1,\rm s}$ and $g_{2,\rm s}$:

$$g_{\rm i,s}(a, \theta_{\rm v}, \lambda_{\rm Edd}) = \alpha_{\rm i,s} + \beta_{\rm i,s} y_1(a) + \gamma_{\rm i,s} y_1^2(a) + \delta_{\rm i,s} y_1^3(a) + \epsilon_{\rm i,s} y_1^4(a) \qquad (3.18)$$

where the subscript $i = 1, 2$ and $y_1(a) = \mathrm{Log}(1 - a)$. The coefficients $\alpha_{\rm i,s}$,...,$\epsilon_{\rm i,s}$ are functions of the Eddington ratio $\lambda_{\rm Edd}$ and can be approximated with the following polynomial

$$\chi_{\rm i,s}(\theta_{\rm v}, \lambda_{\rm Edd}) = \bar{a} + \bar{b}\lambda_{\rm Edd} + \bar{c}\lambda_{\rm Edd}^2 + \bar{d}\lambda_{\rm Edd}^3 + \bar{e}\lambda_{\rm Edd}^4 + \bar{f}\lambda_{\rm Edd}^5 \qquad (3.19)$$

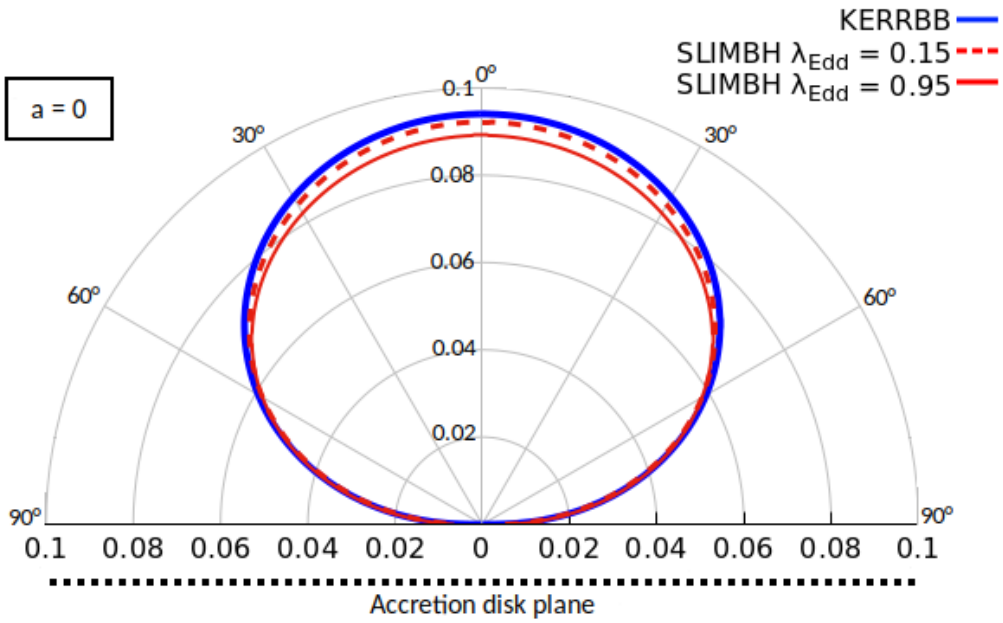

FIGURE 3.10: Comparison between the KERRBB (blue lines) and SLIMBH (red lines) radiation angular pattern for $a = 0$ and different Eddington ratios ($\lambda_{\rm Edd} = 0.15 - 0.95$). The radial axis is given by the product between the angular function $f(\theta_{\rm v})$ and the efficiency η (i.e. the observed disk luminosity normalized on $\dot{M}c^2$, as in Figs. 3.2 - 3.3).

The values of each coefficient are reported in Tab. A.4 (see Appendix A). As for KERRBB: 1) only the spectrum peak frequency $\nu_{\rm p}$ and luminosity $\nu_{\rm p} L_{\nu_{\rm p}}$ are required in order to extrapolate information about the BH, and 2) the space of solutions is degenerate for M, $\lambda_{\rm Edd}$ and a (for a fixed spectrum peak position and viewing angle $\theta_{\rm v}$) as shown in Fig. 3.9 (the solution curves are similar for both models; see Appendix A for the solutions for different viewing angles).

As for SS and KERRBB, the observed disk luminosity can be inferred from the spectrum and, even for this model, a good approximation is $L^{\rm obs}_{\rm d,Slim} \sim 2\nu_{\rm p} L_{\nu_{\rm p}}$ (see Eq. 2.26). The SLIMBH radiation angular pattern depends not only on the BH spin but also on the Eddington ratio since the geometry of the disk (i.e., its vertical structure) changes for large luminosities. In this case, since $\lambda_{\rm Edd}$ is a free parameter instead of $\dot{M}$, it is useful to write

$$L^{\rm obs}_{\rm d,Slim} = f_{\rm s}(\theta_{\rm v}, a, \lambda_{\rm Edd})\ \lambda_{\rm Edd}\ L_{\rm Edd} \tag{3.20}$$

An approximation of $f_{\rm s}$ is given by the following expression

$$f_{\rm s}(\theta_{\rm v}, a, \lambda_{\rm Edd}) = \mathcal{M}_{\rm s} + \mathcal{N}_{\rm s}\mathcal{Z}(\theta_{\rm v}) + \mathcal{O}_{\rm s}\mathcal{Z}(\theta_{\rm v})^2 + \mathcal{P}_{\rm s}\mathcal{Z}(\theta_{\rm v})^3 + \mathcal{Q}_{\rm s}\mathcal{Z}(\theta_{\rm v})^4 \tag{3.21}$$

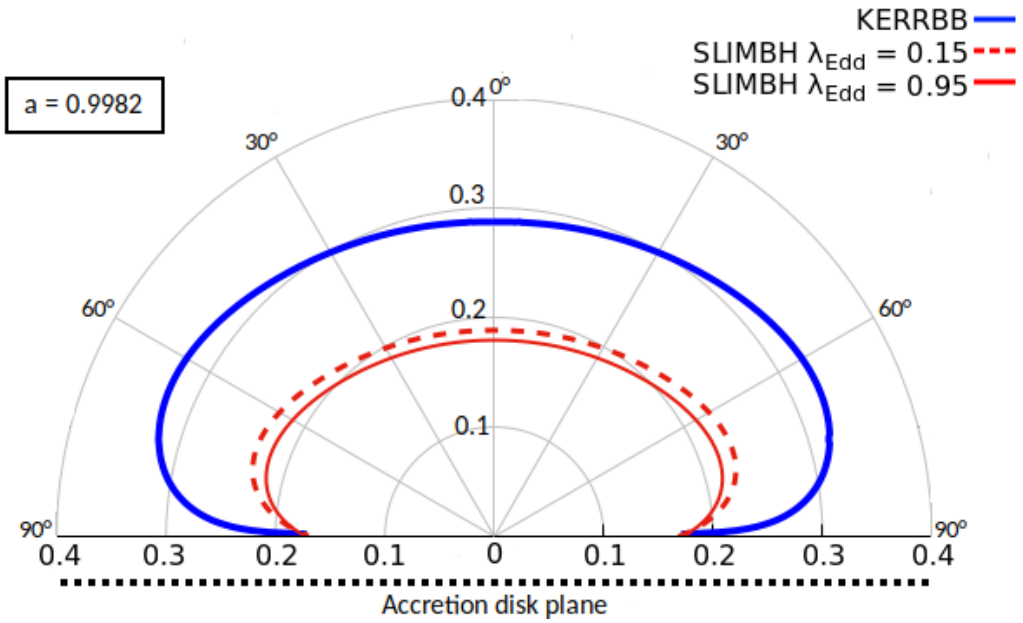

FIGURE 3.11: Same as Fig. 3.10 for $a = 0.9982$.

where $\mathcal{Z}(\theta_v) = \cos\theta_v$. The coefficient $\mathcal{M}_s$,...,$\mathcal{Q}_s$ are functions of the BH spin and the Eddington ratio. If this latter is fixed, they can be written in the following form

$$\mathcal{R}(a) = \alpha_{slim} + \beta_{slim} y_1(a) + \gamma_{slim} y_1^2(a) + \delta_{slim} y_1^3(a) + \epsilon_{slim} y_1^4(a) + \zeta_{slim} y_1^5(a) \tag{3.22}$$

where $y_1(a) = \mathrm{Log}(1-a)$. See Appendix A for the value of each coefficient for different Eddington ratios. Figures 3.10-3.11 show the comparison between the radiation angular pattern of KERRBB and the one of SLIMBH, computed for two different Eddington ratios ($\lambda = 0.15 - 0.95$) and two different spin values ($a = 0 - 0.9982$): in the non-rotating case, the pattern of the two models is almost the same while in the maximally spinning case, the SLIMBH pattern is dimmer than the KERRBB one because of the lower radiative efficiency. It is worth noticing that the SLIMBH pattern for large Eddington ratios is dimmer than the one computed for smaller values of λ_{Edd}: in the limit $\lambda_{Edd} \ll 0.1$ (for small BH spin values), the two models coincide (i.e., disk thickness $z_r \ll r$ and negligible photon-trapping effect).

3.4.2 Effect of the X-ray Corona above the disk

Koratkar and Blaes, 1999 discussed several issues related to the black body-like AD models for AGNs for estimating the SMBH masses: one of them

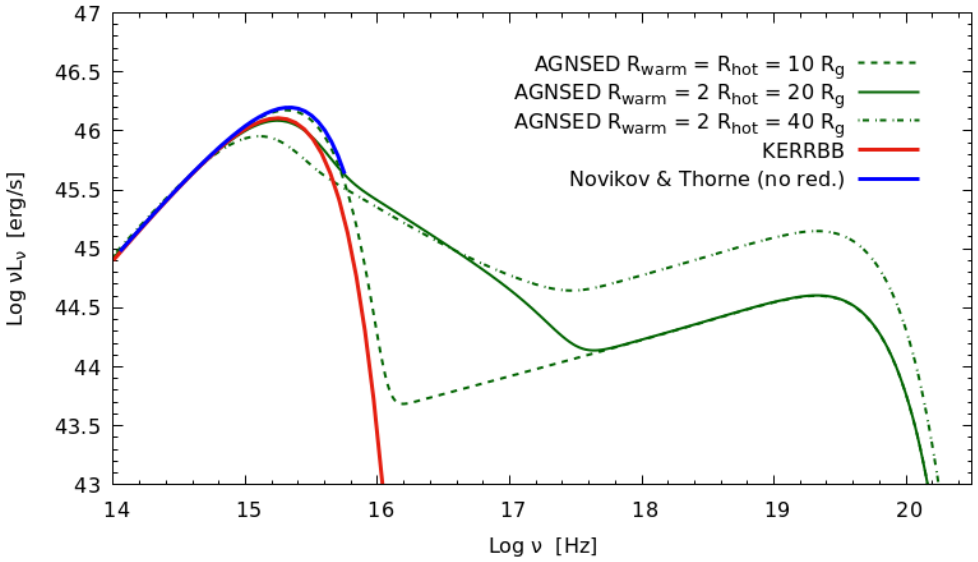

FIGURE 3.12: Comparison between the KERRBB (red line) and AGNSED (green lines) with the same set of parameters (Log $M/M_{\odot} = 9$, $\dot{M}/M_{\odot}\mathrm{yr}^{-1} = 5$, $a = 0$, $\theta_{v} = 0°$) and different Corona sizes. The blue line is the Novikov & Thorne model with the same parameters where the gravitational redshift effect is not included.

is related to the presence of a hot Corona above the disk. This structure is thought to be compact (e.g., Miniutti and Fabian, 2004; Done et al., 2012; Reis and Miller, 2013; Sazonov et al., 2012; Lusso and Risaliti, 2017) and made of two components: the primary hot one is a plasma of 10-100 keV electrons responsible for hard X-ray emission (with an unknown shape) while the second warm component, above the disk, with a temperature of a few KeV, is thought to be responsible for the soft X-ray excess observed in many AGNs (see Sect. 3.3). In principle, if this structure scatters a fraction of the disk radiation, the observed disk luminosity could be dimmer than the intrinsic one, leading to an incorrect mass estimate (i.e., the spectrum peak position could be different from the intrinsic one). Moreover, the soft-excess component could contaminate the 'truncated' disk emission adding further uncertainties.

Disk-Corona emission: AGNSED model

Base on the work of Done et al., 2012, Kubota and Done, 2018 developed the relativistic AD model AGNSED, which takes into account the presence of an X-ray Corona above the disk in a self-consistent way.[8] The authors followed Novikov and Thorne, 1973 to describe the AD emission and divided

[8] As for KERRBB and SLIMBH, the model is implemented in XSPEC.

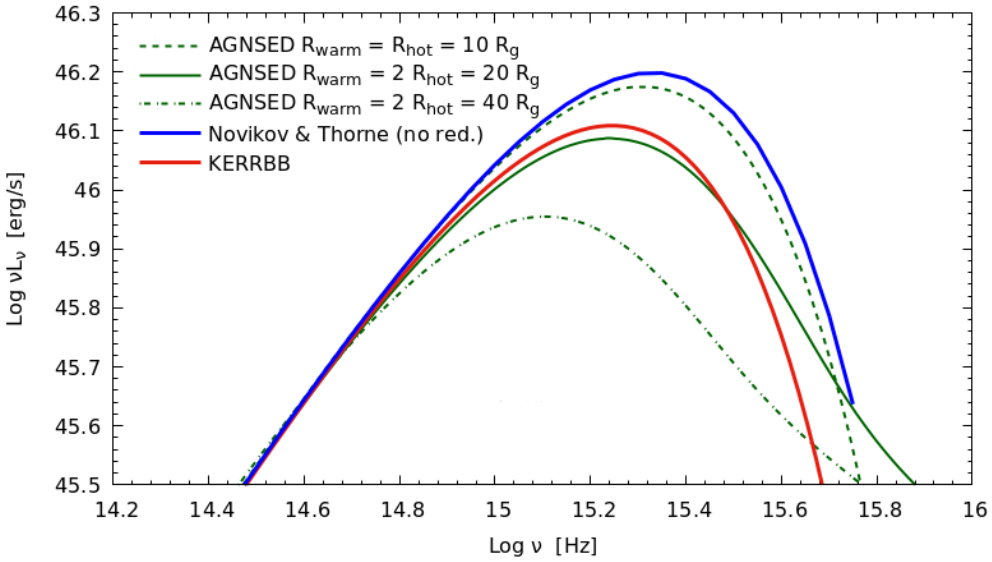

FIGURE 3.13: Same as Fig. 3.12.

the overall SED into three regions: the first is a thin AD model above which a Corona is located; this latter is divided into a hot and warm component, the former one closer to the SMBH with respect to the latter. Both the Corona components cover the disk up to a certain radius, from the ISCO to $R_{\rm warm}$, which is the outer radius of the warm Corona component (the hot component extends from the ISCO to $R_{\rm hot}$): the total Corona luminosity equals the luminosity produced by the disk between the ISCO and $R_{\rm warm}$. The observed disk SED is produced by the uncovered regions, from $R_{\rm warm}$ to $R_{\rm out}$ (which is the outer radius of the disk that can be set manually or computed internally as the *self-gravity radius*; see Laor and Netzer, 1989, Eq. 18).

Given the assumed geometry of a Corona located above the disk at a height H, the author included also the reprocessing of the X radiation: part of the hot Corona component emission is intercepted by the warm component and by the outer region of the disk resulting in an enhanced flux. Both the hot and warm Corona emissions are described by their electron temperature (in keV) and spectral index Γ (see Kubota and Done, 2018 for details).[9]

Figure 3.12 shows the comparison between KERRBB and AGNSED with the same set of parameters and for different Corona sizes (the height is fixed to $100R_{\rm g}$[10]): when only the hot Corona component is present (green dashed line), its luminosity (and so the total X luminosity) correspond to the disk

[9] A simplified version of AGNSED with fewer parameters is called QSOSED, developed by Kubota and Done, 2018 and also implemented in XSPEC.

[10] The other parameters are $k_{\rm B}T_{\rm e,hot} = 100$ keV, $k_{\rm B}T_{\rm e,warm} = 0.2$, $\Gamma_{\rm hot} = 1.7$, $\Gamma_{\rm warm} = 2.7$.

luminosity produced between the ISCO ($6R_g$ for $a = 0$) and $R_{\rm hot}$; the disk SED is slightly affected and its emission is similar to the simple Novikov & Thorne model (blue line) where the gravitational redshift is not included. When the warm Corona component is present, the soft X-ray excess luminosity depends on its size while the disk emission corresponds to the 'truncated' one between $R_{\rm warm}$ and $R_{\rm out}$: the larger $R_{\rm warm}$, the dimmer the disk luminosity, as shown in Fig. 3.13. In this latter, it easy to notice that the AGNSED high-frequency tails are brighter than the KERRBB exponential ones due to the presence of the Corona.

For what concerns the AGNSED code for the disk emission, contrary to KERRBB, such a model does not include important relativistic effects, such as light bending, self-irradiation, and gravitational redshift, that have to be computed numerically: those effects may have a significant weight on both the AD and the Corona emissions even though, they can be negligible for small values of the BH spin a and $\theta_{\rm v}$. Moreover, simultaneous data from Optical to X bands are necessary to perform a proper parameter estimation with such a model. In Sect. 4.3, a comparison between KERRBB and AGNSED results has been made for two low redshift sources.

3.4.3 Disk-wind models

Many observations have been collected by several authors concerting the possibility of associating high-velocity winds with AGN ADs (e.g., Pounds et al., 2003; Reeves, O'Brien, and Ward, 2003; Tombesi et al., 2010; Tombesi et al., 2011). Also, Broad absorption lines (BALs), observed in many objects, provide another strong evidence for material launched from regions close to the SMBH (e.g. Capellupo et al., 2011).

The SED of an AD with a wind outflow should be influenced by the fact that some accreting gas is ejected from the inner regions of the disk, making it dimmer at UV frequencies while the low-frequency SED (related to the outer disk regions) is unaffected by it. Statistical analyses of AGNs have shown a correlation between the presence of BALs and softened Optical-UV spectra (e.g., Ganguly et al., 2007). See Sect. 3.3 for a discussion about the AGN observed spectrum slope.

For what concerns the origin of such winds (possibly ejected from the AD, e.g. King and Pounds, 2003; Proga and Kallman, 2004; Sim et al., 2008), different scenarios have been proposed (radiation driven winds, e.g. Shields, 1977; Proga, Stone, and Kallman, 2000; Risaliti and Elvis, 2010; thermally

driven winds caused by heating of the disc by a central X-ray source, e.g., Begelman, McKee, and Shields, 1983; Krolik and Vrtilek, 1984; Chelouche and Netzer, 2005; Everett and Murray, 2007; magnetically driven winds, e.g. Blandford and Payne, 1982; Contopoulos and Lovelace, 1994; Konigl and Kartje, 1994). Slone and Netzer, 2012 studied in a general way how the presence of winds could affect the AD SED shape and the estimation of parameters (e.g, disk luminosity, accretion rate). Since the properties of such winds (e.g., velocity, geometry) may depend on different factors, all not very well understood, in this thesis I will not consider such models.

As already mentioned before, different methods have been developed to infer the mass and the spin of SMBHs and the theory of accretion have been widely explored through a copious number of models. However, the uncertainties linked to the different approaches are also worsened by a large number of processes and parameters involved in those kinds of estimates: the comparison between different techniques is crucial to strengthen each of them and to set more stringent constraints on the different parameters.

In the next Chapters, I will show the application of the AD models previously presented (i.e., SS, KERRBB, SLIMBH, AGNSED) focusing attention on the uncertainties linked to the fitting procedure and the comparison with other methods to estimate the SMBH masses. The topics and results have been published in refereed journals (Campitiello et al., 2018; Campitiello et al., 2019; Campitiello et al., 2020) and one submitted to A&A (Campitiello et al., 2021).

Chapter 4

AD models for AGNs: mass and spin estimates

"[Science] is not perfect. It can be misused. It is only a tool. But it is by far the best tool we have, self-correcting, ongoing, applicable to everything"
— Carl Sagan, *Cosmos*

Contents

Knowing the mass M and spin a of SMBHs is necessary to better understand their physics and evolution, even in connection with their host galaxies. Despite the huge number of methods and techniques adopted, all of them carry large uncertainties (see Sect. 1.2). For this reason, the comparison between different techniques is crucial to strengthen each of them and to set more stringent constraints on the different parameters.

In this Chapter, I will show the application and the reliability of the AD models to infer the main properties of SMBHs and their accretion in AGNs. I divided this Chapter into three sections:

- Sect. 4.1, I will show the application of the relativistic model KERRBB to 4 sources (for which the viewing angle θ_v is known) and the estimated BH masses compared with the virial ones computed with the SE scaling relations (the work is published in Campitiello et al., 2018).
- Sect. 4.2, I will apply the models KERRBB and SLIMBH to the most distant AGNs ($z > 7$), infer their masses and discuss the possible evolutionary scenarios necessary to build such massive objects when the Universe was only $\sim$ 1 billion years old (the work is published in Campitiello et al., 2019).
- Sect. 4.3, I will show the comparison between the results inferred with the model KERRBB and those estimated with the RM and SE methods for a sample of 28 AGNs, including a discussion about the application and the results obtained with the model AGNSED (the work is published in Campitiello et al., 2020).

In all the works presented here, I adopted a flat cosmology with rounded parameters $H_0 = 68$ km/s/Mpc and $\Omega_M = 0.3$ (see Aghanim et al., 2018).

4.1 Application of KERRBB to radio-loud sources

To decrease the degeneracy between the KERRBB parameters (M, $\dot{M}$, a, θ_v; see Sect. 3.2.3), it is wise to choose sources for which the viewing angle is constrained in a small range. AGNs with relativistic jets pointing towards our line of sight, i.e. blazars, are thought to have a low inclination angle ($\theta_v < 5°$; e.g., Ghisellini et al., 2014). Those sources are radio-loud AGNs and the Radio-mm-FIR emission is dominated by the Synchrotron radiation: this non-thermal emission, if very prominent, could partially contaminate or totally cover the Optical-UV emission coming from the AD. Moreover, the presence of powerful relativistic jets is thought to be connected to large BH spin values (e.g., Blandford and Znajek, 1977; Tchekhovskoy and McKinney,

2012; Garofalo, 2013). However, if the disk emission is very bright, the Synchrotron contribution to the Optical-UV SED could be negligible (see e.g., Ghisellini et al., 2017).

In this Section I will shown the results published in Campitiello et al., 2018 where the authors show the application of the relativistic model KERRBB to four blazars: *S5 0014+813* ($z = 3.366$), studied by Kuhr et al., 1981; Kuhr et al., 1983; Ghisellini et al., 2009; Sbarrato et al., 2016, *SDSS J013127.34-032100.1* (SDSSJ0131, $z = 5.18$), studied by Yi et al., 2014; Ghisellini et al., 2015, and the two sources *SDSS J074625.87+254902.1* (SDSSJ0746, $z = 2.9787$) and *SDSS J161341.06+341247.8* (SDSSJ1613, $z = 1.4$), both from the Sloan Digital Sky Survey (SDSS) and Fermi-LAT catalogs (e.g., Shen et al., 2011; Shaw, Romani, and Cotter, 2012). The sources have a bolometric luminosity $\mathrm{Log}\, L_{\mathrm{bol}}/\mathrm{erg/s} \gtrsim 47$ and a radio-loudness $\mathcal{R} > 100$ (see the reference papers for datails)[1], and the AD emission and its peak are observed and constrained in the Optical - UV band.[2]

For the SED fitting process, the routine implemented in GNUPLOT (i.e., non-linear least-squares Marquardt-Levenberg algorithm) was used to find the best constraints on the peak frequency and luminosity with KERRBB.[3] The disk inclination angle is assumed to be $\theta = 0°$ appropriate for blazars: for larger angles (but still $< 5°$), the KERRBB results do not change significantly. Spectroscopic and photometric data from public archives are collected in order to perform a better fit. The emission at frequencies larger than the Lyman α line ($\mathrm{Log}\, \nu/\mathrm{Hz} = 15.4$) is not considered because a prominent absorption feature is usually present due to intervening inter-galactic clouds absorbing Hydrogen photons at wavelengths < 1216Å, especially for high redshift sources (e.g., Shklovski, 1965; Gunn and Peterson, 1965; Scheuer, 1965). Also, the NIR photometric data points ($\mathrm{Log}\, \nu/\mathrm{Hz} < 14.5$) are not considered probably related to the emission of the dusty torus and/or the Synchrotron non-thermal emission. For more details about the data and their corrections for each source, see the reference papers.

The spectrum peak position (i.e., peak frequency ν_{p} and luminosity $\nu_{\mathrm{p}} L_{\nu_{\mathrm{p}}}$) is estimated by using the curvature given by data at lower frequencies. An

[1] Following Shen et al., 2011 (see also Jiang et al., 2007), the radio-loudness is defined as $\mathcal{R} = F_{6\ \mathrm{cm}}/F_{2500\text{Å}}$, where $F_{6\ \mathrm{cm}}$ and $F_{2500\text{Å}}$ are the flux density at rest-frame wavelength 6 cm and 2500Å, respectively.

[2] For the source S5 0014+813, the bolometric luminosity is estimated from the SED fit (Sbarrato et al., 2016) and the radio-loudness from the available data (following the definition of Shen et al., 2011).

[3] The shape similarity between SS and KERRBB spectra allows the user to constrain the peak position by using one of the models indifferently (see Sect. 3.2.3).

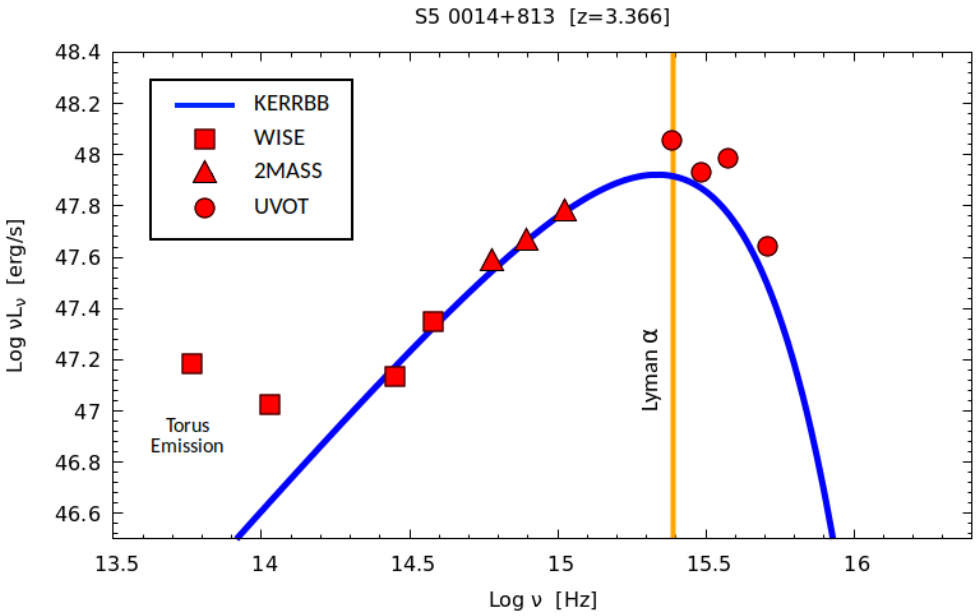

FIGURE 4.1: SED fit of the source S5 0014+813. The orange line shows the Lyman α emission line frequency. At Log ν/Hz < 14.5, photometric data are also associated to the torus emission and/or the Synchrotron emission.

uncertainty on the estimates is still present given the few available data: the average residuals are always less than ~ 0.05 dex with a reduced-$\chi^2 < 0.02$; the peak frequency and luminosity have an uncertainty of ~ 0.05 dex which is reflected on the BH mass (~ 0.10 dex), accretion rate (~ 0.05) and Eddington ratio (~ 0.10 dex) estimates (see Eqs. 3.7 - 3.8).[4]

The results inferred with KERRBB are reported in Table 4.1 and shown in Fig. 4.5 - 4.6 (in terms of BH mass, accretion rate and Eddington ratio).

4.1.1 Sources

S5 0014+813

For this source, the application of the non-relativistic SS model gives Log $M/M_\odot = 9.96$ and $\dot{M}/M_\odot \mathrm{yr}^{-1} = 182.9$, with the spectrum peak in the same position as constrained with the KERRBB model. Sbarrato et al., 2016 inferred a confidence range of Log $M = 9.87 - 10$, using the SS model. By using KERRBB, if the SMBH is associated with a spin $a > 0.9$, the mass is Log $M_{>0.9}/M_\odot \geq 10.04$; if the SMBH is maximally spinning ($a = 0.9982$), the mass is Log $M_{0.9982}/M_\odot = 10.14$; for those spin values, the accretion rates are $\dot{M}_{>0.9} \leq 153.3 M_\odot \mathrm{yr}^{-1}$ and $\dot{M}_{0.9982} = 106.4 M_\odot \mathrm{yr}^{-1}$, respectively (see Fig.

[4]The uncertainties are summed in quadrature.

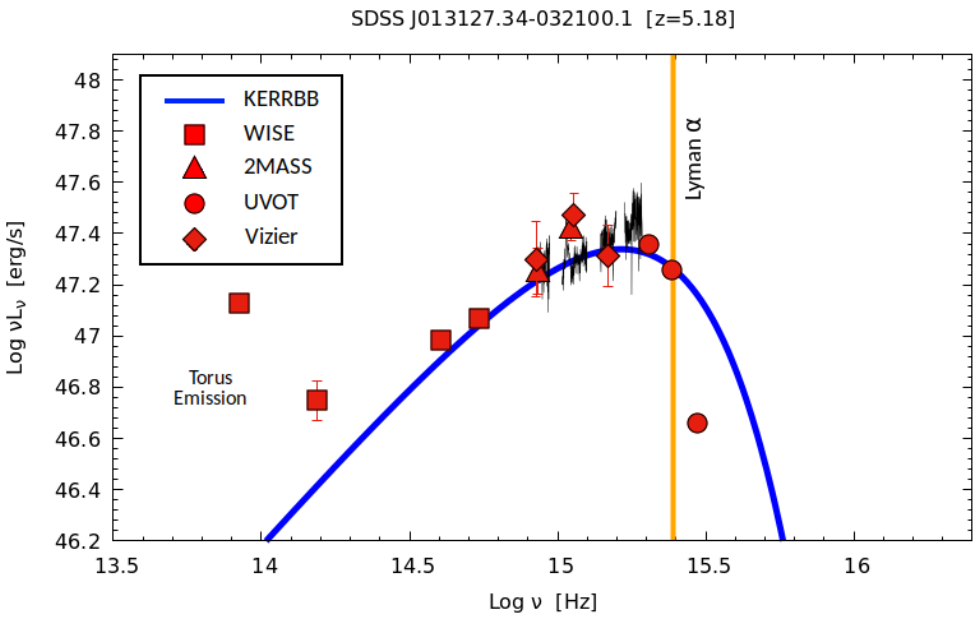

FIGURE 4.2: SED fit of the source SDSSJ013127.34-032100.1. The orange line shows the Lyman α emission line frequency. At Log ν/Hz < 14.5, photometric data are also associated to the torus emission and/or the Synchrotron emission. The spectrum (black line) is taken from Yi et al., 2014.

4.5). The observed disk luminosity (Eq. 3.2) is Log $L_{\rm d}^{\rm obs}$/erg/s $= 48.24$, for all spin values (see Eq. 2.26 and Sect. 3.2.2). In the SED-fitting process, the photometric points at Log ν/Hz ~ 15.4 and Log ν/Hz ~ 15.55 are probably contaminated by the Lyman α and Lyman β emission lines (Fig. 4.1). The Eddington ratio of the source is $\lambda_{\rm Edd} > 0.95$ for all spin values, in contrast with Laor and Netzer, 1989 and the Eddington ratio limit for thin disks (Fig. 4.6; the black dashed line is computed by using Eq. 3.15; see Laor and Netzer, 1989).

SDSS J013127.34-032100.1

The mass and accretion rate inferred with the SS model are Log $M/M_\odot = 9.91$ and $\dot{M}/M_\odot {\rm yr}^{-1} = 47.8$. Ghisellini et al., 2015 found a confidence range of Log $M/M_\odot = 9.95 - 10.11$ using a SS model. Using KERRBB, for $a > 0.9$, the mass is Log $M_{>0.9}/M_\odot > 9.99$ and, if the SMBH is maximally spinning ($a = 0.9982$), the mass is Log $M_{0.9982}/M_\odot = 10.09$; for the same spin values, the accretion rates are $\dot{M}_{>0.9} < 40 M_\odot {\rm yr}^{-1}$ and $\dot{M}_{0.9982} = 27.8 M_\odot {\rm yr}^{-1}$ (Fig. 4.5). The observed disk luminosity is Log $L_{\rm d}^{\rm obs}$/erg/s $= 47.66$. Yi et al., 2014 estimated the virial mass of this blazar using MgII emission line,

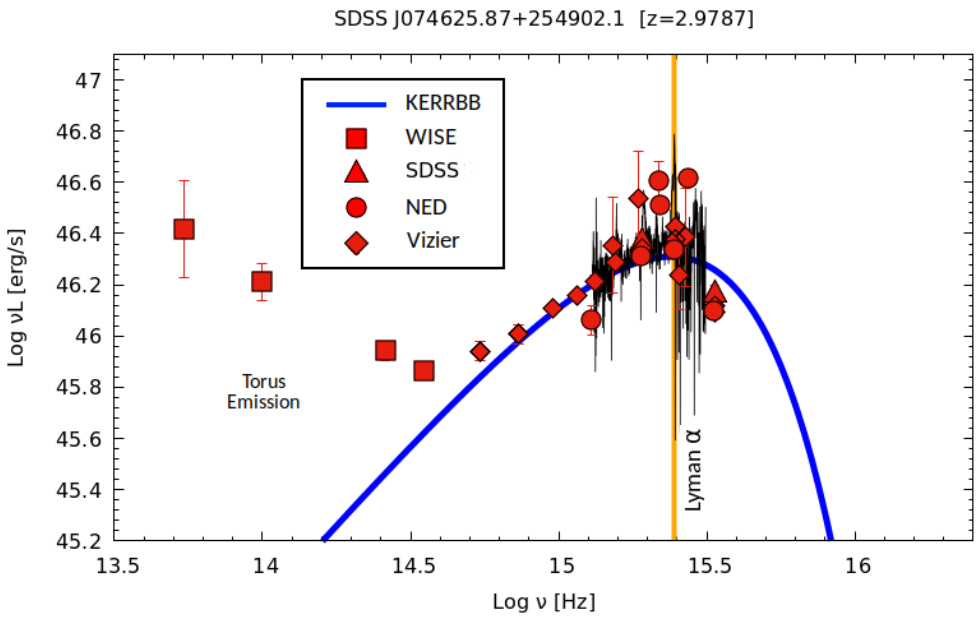

FIGURE 4.3: SED fit of the source SDSSJ074625.87+254902.1. The orange line shows the Lyman α emission line frequency. At Log ν/Hz < 14.5, photometric data are also associated to the torus emission and/or the Synchrotron emission. The spectrum (black line) is taken from the SDSS catalogue.

finding $M_{\rm vir}/M_\odot = 2.7^{+0.5}_{-0.4} \times 10^9$ (Log $M_{\rm vir}/M_\odot = 9.43^{+0.08}_{-0.07}$) with systematic uncertainty of $\sim 0.4 - 0.5$ dex: this estimate is smaller than the SS and KERRBB ones but compatible if the large systematic uncertainty on the virial mass is taken into account. Regarding the Eddington ratio, it is constrained in the range $0.29 < \lambda_{\rm Edd} < 0.59$: following Laor and Netzer, 1989, this source is close the limit of the thin disk reliability (Fig. 4.6). Contrary to what has been done for the photometric data of S5 0014+813 at Log ν/Hz > 15.4 (see Sbarrato et al., 2016), the photometric point at Log ν/Hz ~ 15.5 has not been corrected from the IGM absorption.

SDSS J074625.87+254902.1

The SS model constrains the following SMBH mass and accretion rate, Log $M/M_\odot = 9.07$ and $\dot{M}/M_\odot {\rm yr}^{-1} = 4.5$. The KERRBB model constrains the SMBH in the range Log $M_{>0.9}/M_\odot > 9.15$ for $a > 0.9$, and Log $M_{0.9982}/M_\odot = 9.25$ for $a = 0.9982$. For the same spin ranges, the accretion rates are $\dot{M}_{>0.9} < 3.8 M_\odot {\rm yr}^{-1}$ and $\dot{M}_{0.9982} = 2.6 M_\odot {\rm yr}^{-1}$ respectively (Fig. 4.5). The observed disk luminosity is Log $L_{\rm d}^{\rm obs}$/erg/s $= 46.63$. From the Shen et al., 2011 SDSS catalog, the virial mass of the BH is estimated from the CIV emission line: Log $M_{\rm vir} = 9.59 \pm 0.16$, with systematic uncertainty of $\sim 0.4 - 0.5$ dex; this

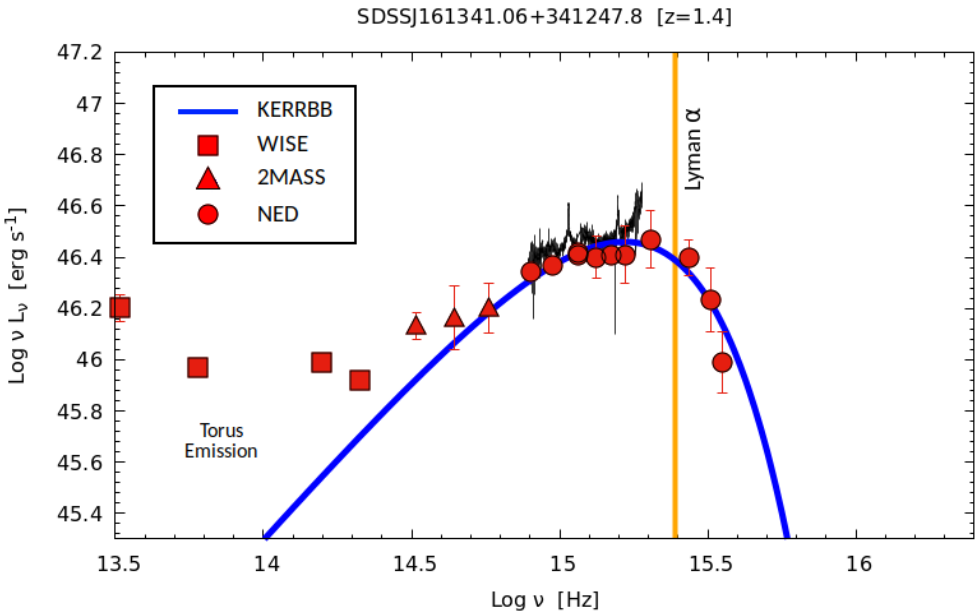

FIGURE 4.4: SED fit of the source SDSSJ161341.06+341247.8. The orange line shows the Lyman α emission line frequency. At Log ν/Hz < 14.5, photometric data are also associated to the torus emission and/or the Synchrotron emission.

estimate is larger than SS and KERRBB results but compatible with them if the systematic uncertainty is taken into account: assuming an uncertainty of 0.5 dex, the BH spin is constrained in the range $a > 0.6$ (taking into account also the uncertainty coming from the SED fit). The Eddington ratio is always $\lambda_{\rm Edd} < 0.38$ and compatible with the Eddington ratio limit from Laor and Netzer, 1989 only for $a < 0.25$ (Fig. 4.6). As the previous source, photometric data at Log ν/Hz > 15.4 has not corrected from the IGM absorption.

SDSS J161341.06+341247.8

For this source, the mass and accretion rate inferred with the SS model are Log $M/M_\odot = 9.45$ and $\dot{M}/M_\odot {\rm yr}^{-1} = 6.3$. Using KERRBB, the BH mass is Log $M_{>0.9}/M_\odot > 9.53$ for $a > 0.9$, and Log $M_{0.9982}/M_\odot = 9.64$ for a maximally spinning BH; the accretion rate are $\dot{M}_{>0.9} < 5.3 M_\odot {\rm yr}^{-1}$ and $\dot{M}_{0.9982} = 3.7 M_\odot {\rm yr}^{-1}$, for the same spin ranges respectively (Fig. 4.5). The observed disk luminosity is Log $L_{\rm d}^{\rm obs}$/erg/s $= 46.78$. From the Shen et al., 2011 SDSS catalog, the virial mass of the BH is estimated from the MgII emission line, Log $M_{\rm vir}/M_\odot = 9.69 \pm 0.02$ with systematic uncertainty of $\sim 0.4 - 0.5$ dex[5]: for this value, the BH spin must be close to maximum

[5]The virial mass has been estimated by using the relation from McLure and Dunlop, 2004. Shen et al., 2011 provided other two virial mass estimates, using the relation from

Source name [1]	ν_p [2]	$\nu_p L_{\nu_p}$ [3]	$M_{0.9}$ [4]	$M_{0.9982}$ [5]
S5 0014+813	15.33	47.92	10.04	10.14
SDSS J013127.34-032100.1	15.21	47.34	9.99	10.09
SDSS J074625.87+254902.1	15.38	46.31	9.15	9.25
SDSS J161341.06+341247.8	15.22	46.46	9.53	9.64
	$\dot{M}_{0.9}$ [6]	$\dot{M}_{0.9982}$ [7]	$\lambda_{\rm Edd,0.9}$ [8]	$\lambda_{\rm Edd,0.9982}$ [9]
S5 0014+813	153.3	106.4	0.99	1.12
SDSS J013127.34-032100.1	40	27.8	0.29	0.33
SDSS J074625.87+254902.1	3.8	2.6	0.19	0.21
SDSS J161341.06+341247.8	5.3	3.7	0.11	0.12

TABLE 4.1: Results from the fit of four blazars. [1] Name of the source; [2] Log of the spectrum peak frequency in Hz; [3] Log of the spectrum peak luminosity in erg/s; [4] [5] Log of the KERRBB BH mass computed for $a = 0.9$ and $a = 0.9982$ in solar masses; [6] [7] Log of the KERRBB accretion rate computed for $a = 0.9$ and $a = 0.9982$ in solar masses per year; [8] [9] the Eddington ratio computed for $a = 0.9$ and $a = 0.9982$. Following Laor and Netzer, 1989, $\lambda_{\rm Edd}$ is above or near the limit of the thin disk reliability ($\lambda_{\rm Edd} \sim 0.3$) for only two sources (se Fig. 4.6).

value $a \sim 0.998$ (without taking into account the systematic uncertainty). The Eddington ratio is $\lambda_{\rm Edd} < 0.23$ for all spin values (Fig. 4.6). For this sources, photometric data at Log ν/Hz > 15.4 does not require any corrections from the IGM absorption (given the low redshift; see e.g., Haardt and Madau, 2012; Castignani et al., 2013).

4.1.2 Caveats

Some structures close to the AD, dust located along the line of sight and/or the geometry of the disk due to its luminosity can lead to incorrect estimates of the peak position and the other parameters of the fit (M, $\dot{M}$, $L_{\rm d}^{\rm obs}$, $\lambda_{\rm Edd}$):

- *High Eddington ratios*: for two sources (S5 0014+813 and SDSSJ0131) and for all spin values, $\lambda_{\rm Edd}$ is larger than the theoretical value for a thin disk (Laor and Netzer, 1989) and another model has to be used (Fig. 4.6). As discussed in Sect. 3.4.1, the relativistic model SLIMBH is more suitable for bright AGNs; however, as shown in Fig. 3.9, the SLIMBH solutions for the BH mass and Eddington ratio as functions of the spin (for a fixed spectrum peak position) are different from the KERRBB ones at most by a factor < 0.1 dex.

Vestergaard and Osmer, 2009 and Shen et al., 2011, Log $M_{\rm vir}/M_\odot = 8.96 \pm 0.04$ and Log $M_{\rm vir}/M_\odot = 9.12 \pm 0.05$, respectively.

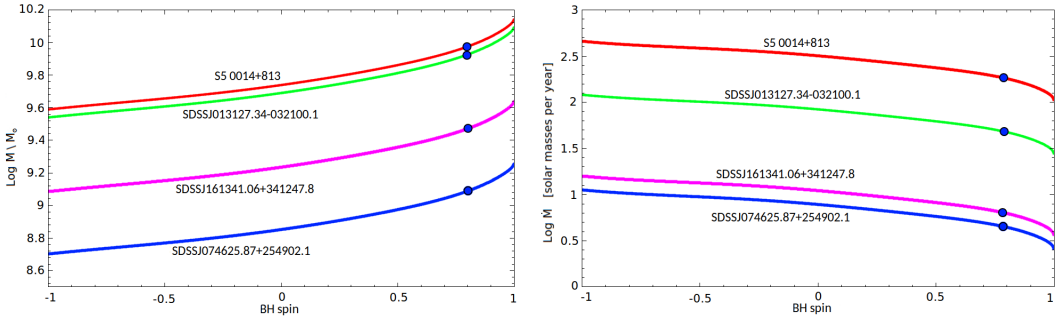

FIGURE 4.5: Mass (left panel) and accretion rate (right panel) as a function of the BH spin for the four blazars studied with KERRBB. The blue dots indicate the corresponding SS solutions. For a fixed spin value, each mass (accretion rate) estimate has an uncertainty of ~ 0.10 (0.05) dex.

- The KERRBB estimates of the observed disk luminosity are smaller with respect to those found by other authors: Yi et al., 2014 found $L_{\rm bol} = 1.1 \times 10^{48}$ erg/s for SDSSJ0131; the SDSS bolometric luminosities for SDSSJ0746 and SDSSJ1613 are Log $L_{\rm bol}/{\rm erg/s} = 46.90$ and Log $L_{\rm bol}/{\rm erg/s} = 47.09$, respectively. Those estimates have been inferred from the monochromatic luminosity at a specific wavelength, using a bolometric correction from Richards et al., 2006 ($L_{\rm bol}$ includes also the IR and the X emissions). As pointed out by Calderone et al., 2013, those estimates are on average larger by a factor of ~ 2 with respect to $L_{\rm d}^{\rm obs}$, inferred from the disk SED fitting procedure.

- *Intrinsic absorption*: dust present in the host galaxy and along the line of sight could in principle reduce the observed flux leading to a wrong parameter estimate. On average, it is generally assumed that the intrinsic reddening in AGNs is small, with an extinction $E_{[\rm B-V]} = 0.05 - 0.1$ mag (Koratkar and Blaes, 1999): this latter does not affect the Optical frequencies but could reduce significantly the UV flux. Using the reddening law derived by Czerny et al., 2004 to correct the observed flux and assuming $E_{[\rm B-V]} < 0.1$ mag, lead to a correction of the peak frequency and luminosity for the four blazars: the BH masses are not modified significantly (< 0.04 dex); however, $\dot{M}$, $L_{\rm d}^{\rm obs}$ and $\lambda_{\rm Edd}$ are larger than the previous results by a factor < 0.25 dex. Since the real amount of dust is unknown, these estimates are only generic; nevertheless, in principle, it is possible to assert that the presence of relativistic jets and large disk luminosities could clear the line of sight: in that case, it could be reasonable to assume a negligible flux extinction.

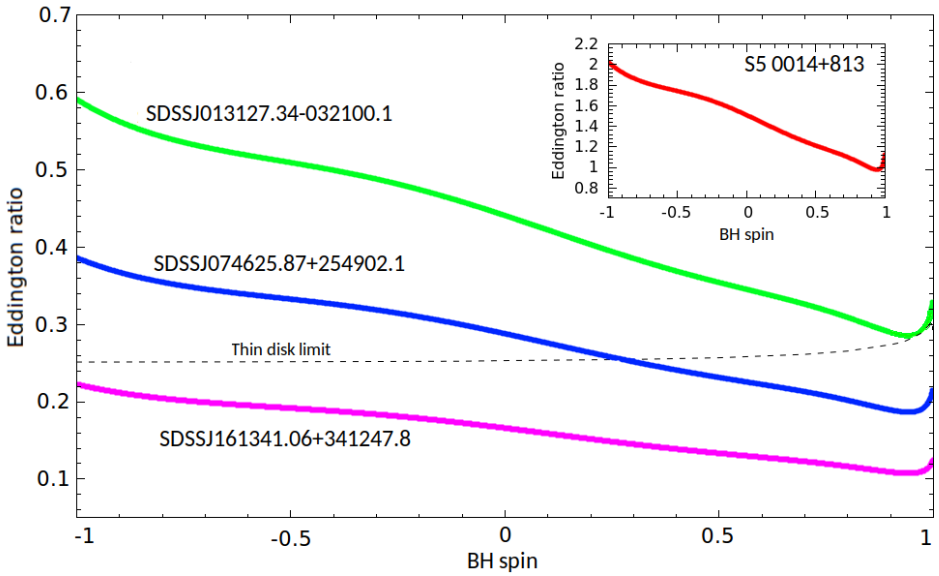

FIGURE 4.6: Eddington ratio as a function of the BH spin for the four blazars studied with KERRBB. The black dashed line is computed by using Eq. 3.15 (see Laor and Netzer, 1989). For a fixed spin value, each Eddington ratio value has an uncertainty of ~ 0.10 dex.

- Structure located close to the disk and/or along the line of sight could reduce the observed disk flux.
  - *BLR*: it is thought to have a disk-like structure rather than spherical (e.g., GRAVITY collaboration; Sturm et al., 2018; Amorim et al., 2020). Given that it is located at $10 - 100$ light days from the SMBH (e.g., Kaspi et al., 2000; Peterson et al., 2004), the peak of the disk emission is unaffected by its presence.
  - *X-ray Corona*: located above the inner region of the disk, could reduce the disk flux (see Sect. 3.4.2). Relations between the X luminosity and the UV or bolometric ones have been found and discussed by several authors (e.g., Risaliti and Lusso, 2019; Duras et al., 2020 and references therein). Assuming that the total X luminosity L_X (hot + warm components) is equal to a fraction of the disk one intercepted and up-scattered by the Corona, it is possible to have an estimate of L_X from the bolometric luminosity, following the work of Duras et al., 2020 (Eq. 2 for Type I AGNs): for the blazars analyzed above, a bolometric luminosity Log $L_{bol}/erg/s >$ 47 corresponds to an X luminosity Log $L_X/erg/s < 45.3$, which is $< 5\%$ of the corresponding L_d^{obs}.[6] This means that the correction of

[6]The X luminosity corresponds to the 2-10 keV band.

the spectrum peak position due to the presence of a Corona above the disk is negligible (< 0.02 dex).

Despite the presence of different sources of uncertainty, the results obtained with the AD SED fitting are rather satisfactory for what concerns the description of the BBB with KERRBB and the estimates of the SMBH masses, comparable with those obtained with the SE scaling relations. Uncertainties are still too large to have constraints on the BH spin, as proposed in Sect. 3.2.3. Moreover, a crucial point to mark is related to the quality and the number of available data: a wide frequency range coverage is crucial for the application of the SED fitting procedure to reduce the fit uncertainties; simultaneity of data is also important to avoid normalization issues between different sets related to different observational epochs (see Sect. 4.3).

4.2 AD models for the most distant AGNs

A growing number of SMBHs with masses $M \sim 10^8 - 10^{10} M_\odot$ have been observed at high redshifts ($z > 6$), showing not only the BBB but also its peak, unaffected by the intervening IGM absorbing material (e.g., Fan et al., 2001; Barth et al., 2003; Willott, McLure, and Jarvis, 2003; Shaw, Romani, and Cotter, 2012; Ai et al., 2017). Since the Universe was less than $\sim$ 1 billion years old, their large masses represent one of the most challenging aspects of such objects and the issue related to their rapid growth is still under debate.

Several authors proposed different evolutionary scenarios (e.g., Haiman and Loeb, 2001; Volonteri and Rees, 2005; Li et al., 2007; Pelupessy, Matteo, and Ciardi, 2007; Tanaka and Haiman, 2009). Two of them can be used in this context to understand the evolution of SMBHs:

1. Merging between two or multiple BHs (e.g., Volonteri, Haardt, and Madau, 2003); this could have led to accelerated growth of the BH mass. The production of gravitational waves is important (e.g. Fig. 2 in Seoane et al., 2013) and the possible recoil effects could have slowed the BH growth down and prevented it from growing to sufficiently large masses (e.g., Haiman, 2004; O'Leary et al., 2006; Volonteri, 2007).[7] A

[7] Yoo and Escude, 2004 showed that the gravitational wave recoil problem can be overcome within certain conditions, making a BH grow quickly without invoking super-Eddington accretion.

large number of BH mergings is required to form a $\sim 10^9 M_\odot$ in a short amount of time and this could happen in a hierarchical process (e.g., Volonteri and Natarajan, 2009; Seoane et al., 2013).

2. Accretion of material onto the BH at a high rate (e.g., Haiman and Loeb, 2001; Ruszkowski and Begelman, 2003; Yoo and Escude, 2004; Koushiappas, Bullock, and Dekel, 2004; Volonteri and Rees, 2005; Li et al., 2007; Pelupessy, Matteo, and Ciardi, 2007; Tanaka and Haiman, 2009; Dotti et al., 2013); this process can happen in two different ways (or a combination of the two): chaotic accretion of "blobs" of matter (this could have led to fast super-Eddington accretion with rapid growth of the BH mass), accretion through a disk-like structure (this scenario leads to the production of the observed thermal UV emission).

Merging and accretion affect both the BH mass and its angular momentum (e.g., Bardeen, 1970): in a BH-BH merging or a chaotic accretion scenario, objects falling onto a central BH from different directions affect its spin amplitude and orientation (e.g. Dotti et al., 2013); if this happens randomly, the expected adimensional spin value is $a \sim 0$. Instead, in the disk-like scenario, an initially non-rotating BH reaches its maximum spin when it has roughly doubled its mass through coherent accretion (Bardeen, 1970; Thorne, 1974).[8] This suggests that high-redshift SMBHs should spin rapidly due to their large mass assembled in less than a Gyr (i.e., at redshift ~ 6); moreover, if a disk-like structure (producing the observed BBB in the UV) is present around a SMBH with a coherent angular momentum for a sufficiently long time, the spin is expected to be large.

Other effects may spin the BH down, like the formation of relativistic jets through the Blandford-Znajek process (e.g., Blandford and Znajek, 1977; Tchekhovskoy, Narayan, and McKinney, 2011): nevertheless some authors showed that even in the presence of such process, the BH spins rapidly with $a > 0.7$ (e.g., Lu et al., 1996; Wang, 1998).

If accretion occurred mainly through a disk, a BH could have reached the maximum spin value in the early stage of its evolution, but this scenario alone could explain the presence of SMBHs at high redshifts only if the BH seed mass is $> 10^7 M_\odot$ and accreting at the Eddington rate (e.g., Li, 2012). This is in contrast with what has been proposed by several authors (e.g., Volonteri and Rees, 2005; Volonteri, 2010; Alexander and Hickox, 2011) who

[8] If the counteracting torque produced by the radiation emitted by the disk is taken into account, the "canonical" equilibrium value for the adimensional black hole spin is $a = 0.9982$ (Thorne, 1974)

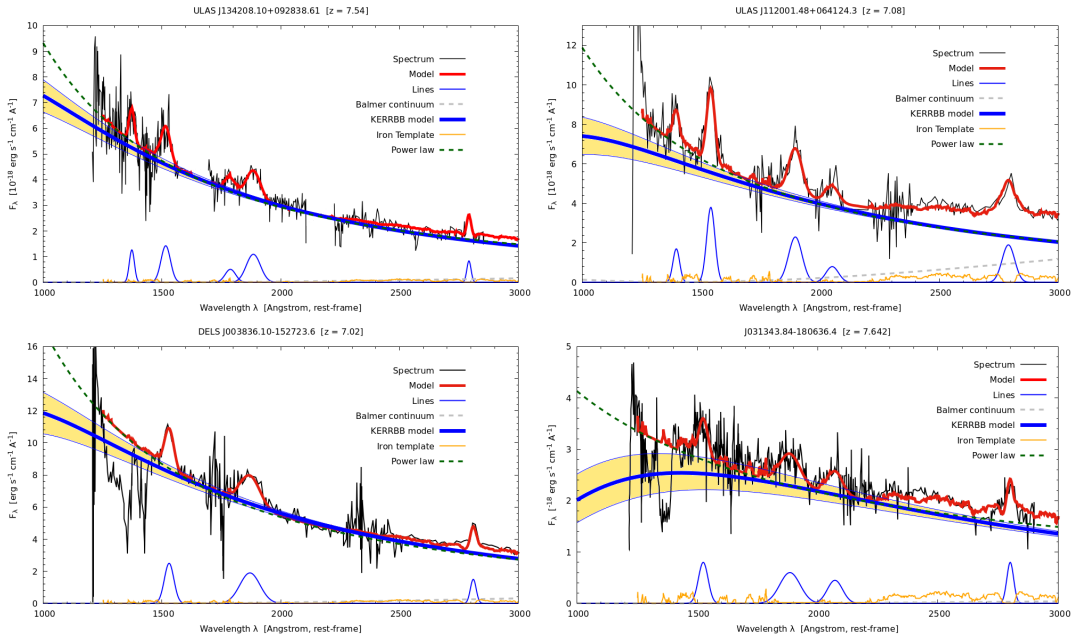

FIGURE 4.7: Fit of the sources J1342, J1120, J0038 and J0313. The KERRBB model (thick blue line) has a confidence interval of ± 0.05 dex (yellow area). See text for details about the fitting procedure.

suggested a smaller seed mass of the order of $\sim 10^2 - 10^5 M_{\odot}$. In the latter case, super-Eddington accretion represents a solution for the rapid growth problem. In this context, Lapi et al., 2014 showed that a BH can grow by accretion in a self-regulated regime with radiative power that can slightly exceed the Eddington limit at high redshifts: in this scenario, the radiative efficiency of the disk is $\eta = 0.15$, large enough to produce a significant luminosity.

Given this discussion, in this Section I will estimate the disk luminosity and the BH mass of the highest redshift QSOs ($z > 7$) known up to 2019 (published in the work Campitiello et al., 2019). Recently, other sources have been discovered at redshift $z > 7$ (e.g, Matsuoka et al., 2019; Wang et al., 2020; Yang et al., 2020): to the analysis presented here, I added the source J031343.84 - 180636.4 (J0313) from the recent work of Wang et al., 2021.

4.2.1 Sources and fitting procedure

I focused on four highest redshift objects: J031343.84 - 180636.4 (J0313) at $z = 7.642$ (Wang et al., 2021), the most distant QSO known up to now, ULAS J134208.10 + 092838.61 (J1342) at $z = 7.54$ (Bañados et al., 2018), ULAS J112001.48 + 064124.3 (J1120) at $z = 7.08$ (Mortlock et al., 2011), and DELS

J003836.10 - 152723.6 (J0038) at redshift $z = 7.02$ (Wang et al., 2018). The second QSO is a source with a radio-loudness $\mathcal{R} = 12.4$ (Venemans et al., 20017), at the border of the radio-loud/quiet divide ($\mathcal{R} = 10$); for the third one, $\mathcal{R} < 0.5 - 4.3$, depending on the assumed radio spectral index (Momjian et al., 2014); no radio detection is available for the first and fourth sources. Given that no constraints on the viewing angle are available, I assume to observe those sources with a viewing angle in the range $0° < \theta_v < 45°$ in order to avoid the absorption from a dusty torus (assumed to have an average aperture angle of $\sim 45°$; see e.g., Calderone, Sbarrato, and Ghisellini, 2012).

To extrapolate information about the observed disk luminosity, the BH mass, spin and Eddington ratio for each source, the Optical-UV BBB is interpreted as the emission produced by an AD around a SMBH: by adapting two relativistic models (i.e., KERRBB and SLIMBH) to the available spectra, the peak frequency ν_p and luminosity $\nu_p L_{\nu_p}$ are estimated (see Chap. 3 for more details on how to extrapolate information from the spectrum peak). The average residuals from the fit are always less than ~ 0.05 dex with a reduced-$\chi^2 < 0.02$, and an average uncertainty of ± 0.05 dex is associated with ν_p and $\nu_p L_{\nu_p}$ defining a strict confidence interval (the propagation of those uncertainties result in confidence intervals for the extrapolated properties of the accretion and SMBHs; see Sect. 4.1).

The fit is performed and shown on the $\lambda - F_\lambda$ and $\nu - \nu L_\nu$ plots (Figs. 4.7 - 4.8): in the fitting procedure, available photometric data and the relative uncertainties are not included because they may be contaminated by some emission lines (e.g. Lyα and MgII, for J1120) and/or affected by absorption (e.g., points at Log ν/Hz > 15.4 for J1342 and J0038). The fit is limited in the rest-frame spectral range $\lambda \sim 1800 - 3000$Å where the uncertainties on the underlying continuum are minimized. The confidence interval of the modeling previously mentioned is thus determined by the range of predicted spectra which does not alter the spectrum in such a spectral range. It is relevant to stress that the location of the spectrum peak can be estimated even if it is slightly outside the frequency range covered by data (i.e. at larger frequencies): this is because it is possible to use the changing curvature of the spectrum at lower frequencies when it is approaching its peak.

The spectra are fitted as a power-law continuum plus the iron complex (Wilkes, 2001; Tsuzuki et al., 2006), the Balmer continuum (e.g., Rosa et al., 2014) and prominent emission lines (modeling them with a Gaussian, e.g. MgII, CIII, CIV, SiIV), using the fitting routine implemented in GNUPLOT (non-linear least-squares Marquardt-Levenberg algorithm). Then the same

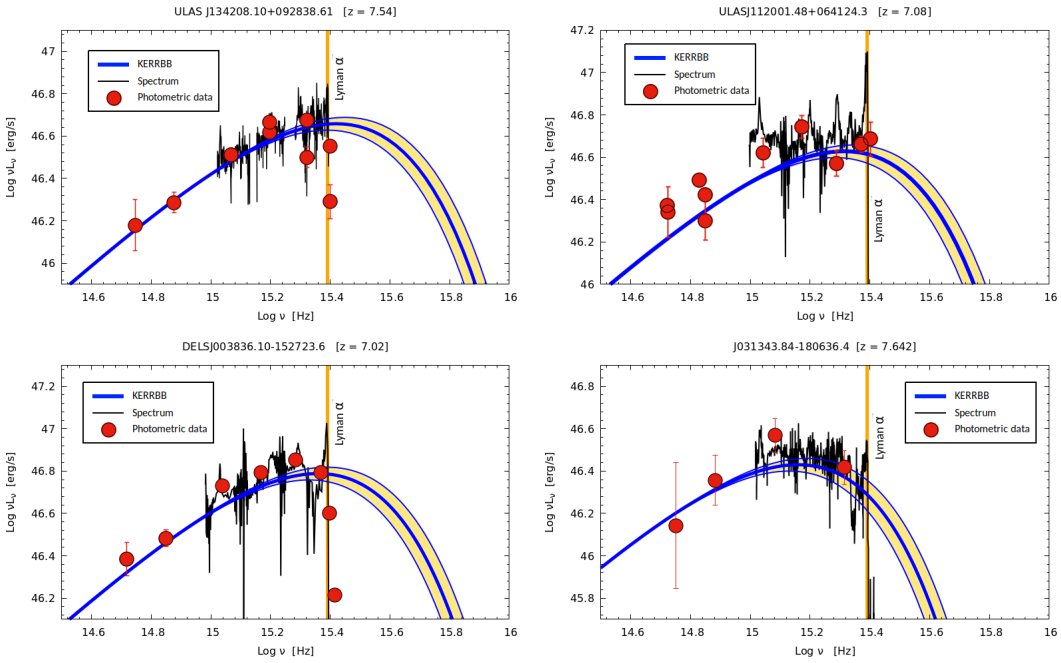

FIGURE 4.8: Fit of the sources J1342, J1120, J0038 and J0313. The KERRBB model (thick blue line) has a confidence interval of ± 0.05 dex (yellow area).

procedure was performed using the KERRBB model to describe the AGN continuum instead of the power-law: as shown in Fig. 4.7, the KERRBB model overlaps well the power law for $\lambda > 1700$Å (the difference at shorter wavelengths is because the accretion disk model is not a power law around the spectral peak). Therefore, when the contributions from lines are subtracted from the total spectrum (and even if uncertainties on the spectrum itself are taken into account)[9], the continuum emission is well reproduced by the KERRBB model inside the confidence interval (yellow area in Fig. 4.7).

4.2.2 Caveats

In the following, I discuss some of the different phenomena which could modify the UV spectrum and have an effect on the goodness of the modeling (as discussed in Sect. 4.1).

- *Intrinsic dust extinction*. Figs. 4.7 - 4.8 show the SED of the four sources without any correction from possible dust absorption: no (strong) dust absorption of the AD emission is expected from the surrounding torus (thought to have an average aperture angle of $\sim 45°$ from the normal to

[9]The spectrum flux uncertainties, shown in the corresponding works, are rather small at 1σ level (the percentage uncertainty is less than $\sim 20\%$).

the disk; see e.g. Calderone, Sbarrato, and Ghisellini, 2012).[10] However, dust extinction could be present at a relatively low level. If corrected for dust, the spectrum becomes harder with a peak shifted at larger frequencies, increasing the disk luminosity, lowering the BH mass and increasing the Eddington ratio estimates. A general analysis of such an effect on the results could be done by considering the extinction curves derived by Czerny et al., 2004: a self-consistency requirement for modeling the spectrum as disk emission is that the slope of the corrected, de-reddened spectrum has to be softer than the theoretical value $\nu L_\nu \propto \nu^{4/3}$ (see Sect. 2.5); this translates into an upper limit for the extinction $E_{[B-V]} < 0.15$ mag. Adopting this correction, the resulting BH masses are not drastically affected (< 0.05 dex); however, the disk luminosity and the Eddington ratio would be larger by a factor < 0.3 dex. It is worth noticing that this correction is rather unrealistic and "extreme" given that, as discussed in Sect. 3.3, the characteristic $1/3$ slope is 'covered' by other emissions (i.e., torus, host galaxy) and it is not expected to be observed in the UV band.

- *Poor sky transparencies*. Regions between the J-H and H-K bands are affected by low sky transparencies (Fig. 4.7). For J1342 these regions are not shown in the original spectrum (Bañados et al., 2018); instead, for the other three sources, these regions are visible but very noisy: they are not included in the fitting procedure; even if they are, the fit would not change significantly because the best model is well determined by the rest of the spectrum.

- *IGM absorption*. The correction of the spectrum from the IGM absorption has been considered for J1342 and J0313 (following the reconstruction of the AGN intrinsic emission shown in Bañados et al., 2018 and the composite spectrum in Wang et al., 2021); such a correction affects only the region around the Lyα line emission without modifying the spectrum at lower frequencies. Therefore, the best fit is not affected significantly and the corrected spectra lie in the defined confidence interval (± 0.05 dex).

[10] The torus emission, mainly produced in the IR band, is characterized by two significant bumps (silicate dust emission at around $\nu \sim 3 \times 10^{13}$ Hz and a hot component at around $\nu \sim 10^{14}$ Hz; Barvainis, 1987; Pier and Krolik, 1993; Mor, Netzer, and Elitzur, 2009; Hönig and Kishimoto, 2010). Therefore, the contribution by such components is not expected to affect the spectral region of the disk emission.

- *Broad Absorption Lines*. The sources J0038 and J0313 show some absorption troughs thought to be associated with fast outflows (see Wang et al., 2018; Wang et al., 2021) that may have caused the high-frequency part of the spectrum to be dimmer. The spectral analysis showed that the fit is not influenced by the absorption features of the spectrum; moreover, the confidence interval (± 0.05 dex) for the spectrum peak is in good agreement with the QSO composite spectra shown in the reference papers and used to described the data.

- *BLR and X-ray Corona*. As shown and discussed in Sect. 4.1.2, these two structures should not affect the results drastically: the distant location of a disk-like BLR from the SMBH and the estimated Corona luminosity ($\mathrm{Log}\, L_X/\mathrm{erg/s} < 45.3$, following Duras et al., 2020) guarantee a general and negligible effect on the results.

As for the first work (Campitiello et al., 2018) shown in Sect. 4.1.2, although the above effects can alter the spectrum, the uncertainties are mostly consistent with the estimated confidence interval of the model (corresponding to the yellow area in Figs. 4.7 - 4.8). The major uncertainty on the spectrum peak position estimates could come from dust absorption, affecting the derived disk luminosity, BH mass and Eddington ratio at most by a factor < 0.3 dex. However, as already discussed, such a strong effect on the visible spectrum is not expected for these sources.

4.2.3 Results

Observed disk luminosities

The observed disk luminosity can be estimated from the spectrum peak luminosity, $L_{\mathrm{d}}^{\mathrm{obs}} \sim 2\nu_{\mathrm{p}} L_{\nu_{\mathrm{p}}}$ (see Sect. 3.2.2): for J1342 $\mathrm{Log}\, L_{\mathrm{d}}^{\mathrm{obs}}/\mathrm{erg/s} = 47.00 \pm 0.05$; for J1120 $\mathrm{Log}\, L_{\mathrm{d}}^{\mathrm{obs}}/\mathrm{erg/s} = 46.95 \pm 0.05$; for J0038 $\mathrm{Log}\, L_{\mathrm{d}}^{\mathrm{obs}}/\mathrm{erg/s} = 47.11 \pm 0.05$ and for J0313 $\mathrm{Log}\, L_{\mathrm{d}}^{\mathrm{obs}}/\mathrm{erg/s} = 46.75 \pm 0.05$ (the uncertainties are related to the uncertainty on the peak luminosity $\nu_{\mathrm{p}} L_{\nu_{\mathrm{p}}}$). These values are smaller than the bolometric luminosities estimated by Bañados et al., 2018; Mortlock et al., 2011; Wang et al., 2018; Wang et al., 2021 because their results are based on a bolometric correction C, i.e. $L_{\mathrm{bol}} = C \times L_a$ (where L_a is the luminosity at the wavelength a) which overestimate the disk luminosity by a factor ~ 2 (Calderone et al., 2013; see also Sect. 2.4).

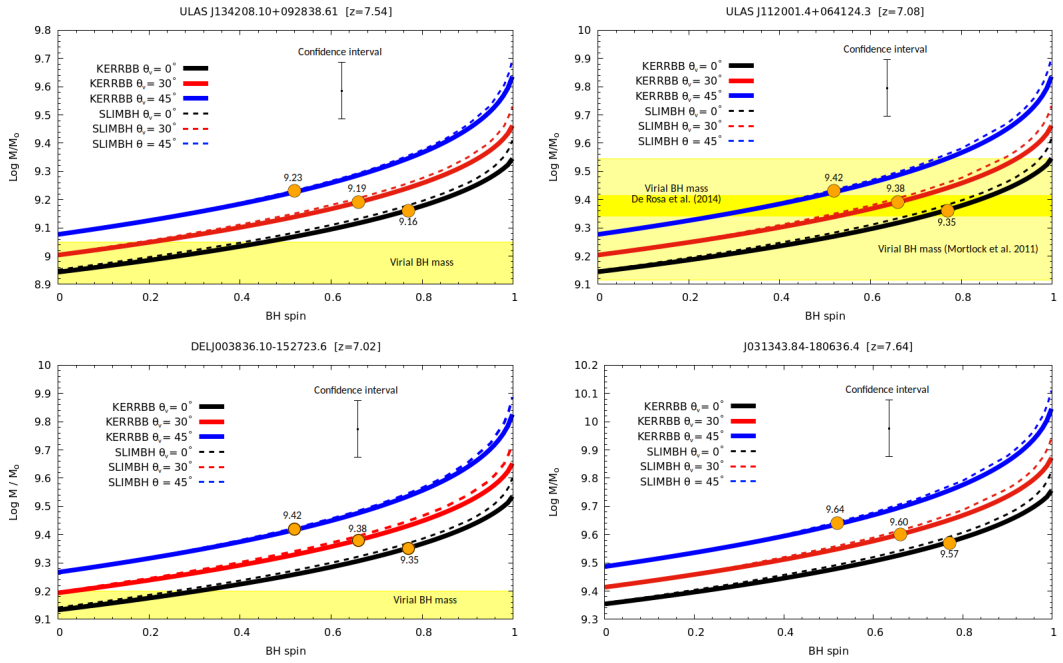

FIGURE 4.9: BH mass of the sources J1342, J1120, J0038 and J0313 as a function of the BH spin. The yellow regions represent the virial BH mass found in literature and the reference works (see text for details). The orange dots represent the SS solutions. The confidence interval of each curve ($\sim$ 0.1 dex) is computed from the uncertainty on the spectrum peak position ($\pm$0.05 dex).

Black hole mass estimates

Figure 4.9 shows the KERRBB BH mass (solid lines) for the four sources as a function of the BH spin, in the cases with $\theta_{\rm v} = 0° - 30° - 45°$ (following Campitiello et al., 2018, it is possible to find analytic expressions for different viewing angles; see Appendix A). These solutions describe the same spectrum with the same peak position (see Sect. 3.2.3). For comparison, the solutions inferred with the classical non-relativistic SS model are shown with orange dots (each estimate corresponds to a particular KERRBB solution with a specific spin value). The SMBH mass estimates for $a = 0 - 0.9982$ are summarized in Table 4.2. In the same Figure, the SE virial mass ranges (from the Mg II line) as estimated by Bañados et al., 2018; Mortlock et al., 2011; Wang et al., 2018; Wang et al., 2021 and Rosa et al., 2014 are shown with yellow areas: on average, the KERRBB results are compatible with the virial masses estimates but with typically smaller uncertainties ($\sim$ 0.1 dex) compared to the systematic $\sim$ 0.4 – 0.5 dex in the local scaling relations for virial estimates (e.g., Vestergaard and Osmer, 2009).

Source	θ_v	M_0			$\lambda_{Edd,0}$			M_1		λ_{Edd1}	
		KBB	SBH	SS	KBB	SBH	SS	KBB	SBH	KBB	SBH
J1342	0°	8.94	8.95	9.16	0.51	0.53	0.26	9.34	9.41	0.38	0.50
	30°	9.00	9.01	9.19	0.49	0.51	0.28	9.46	9.53	0.29	0.37
	45°	9.07	9.08	9.23	0.48	0.48	0.31	9.64	9.70	0.19	0.23
J1120	0°	9.13	9.14	9.35	0.29	0.29	0.16	9.53	9.60	0.22	0.28
	30°	9.19	9.19	9.38	0.28	0.29	0.17	9.65	9.72	0.17	0.21
	45°	9.26	9.26	9.42	0.27	0.28	0.19	9.82	9.89	0.13	0.15
J0038	0°	9.13	9.14	9.35	0.45	0.47	0.23	9.53	9.60	0.34	0.44
	30°	9.19	9.20	9.38	0.44	0.45	0.25	9.65	9.72	0.26	0.33
	45°	9.26	9.27	9.42	0.42	0.42	0.27	9.84	9.89	0.17	0.21
J0313	0°	9.35	9.36	9.57	0.12	0.12	0.06	9.75	9.82	0.09	0.12
	30°	9.41	9.42	9.60	0.12	0.12	0.06	9.87	9.94	0.07	0.09
	45°	9.48	9.49	9.64	0.11	0.11	0.07	10.06	10.11	0.04	0.06

TABLE 4.2: SMBH mass and Eddington ratio for the four sources, computed with the models KERRBB (KBB), SLIMBH (SBH) and Shakura & Sunyaev (SS), for $a = 0$ (M_0, $\lambda_{Edd,0}$) and $a = 0.9982$ (M_1, $\lambda_{Edd,1}$), and different viewing angles. The uncertainty on both M and λ_{Edd} is ~ 0.1 dex.

Black hole spin estimates

Assuming that the virial estimates are reliable measurements of BH masses (with no systematic uncertainties involved), in principle the overlapping between the yellow area (indicating the virial BH mass range) and the KERRBB solutions in Fig. 4.9 could be used to find some constraints on the BH spin (see Sect. 3.2.3): taking the reported virial masses, for the source J1342 the BH spin is constrained to be $a < 0.5$; for J1120, using the virial estimates from Mortlock et al., 2011, an upper limit for the spin is present only for $\theta_v > 0°$ ($a < 0.9$ for $\theta_v = 30°$, $a < 0.75$ for $\theta_v = 45°$); instead, using the virial mass from Rosa et al., 2014, the spin is constrained in the range $0.25 < a < 0.85$; for J0038, the BH spin is $a < 0.3$ and for J0313, the virial mass inferred by Wang et al., 2021 is compatible with KERRBB estimates for negative spin values (not shown on the plot). These ranges would rule out the maximum spin solution but no systematic uncertainties on the virial BH mass estimates (major uncertainty) and the spectrum peak position have been taken into account: if these are considered, no constraints on the BH spin can be derived.

Eddington ratios

Figure 4.10 shows the KERRBB Eddington ratio of the four sources (solid lines) as a function of the BH spin, for different viewing angles ($\theta_v = 0° -$

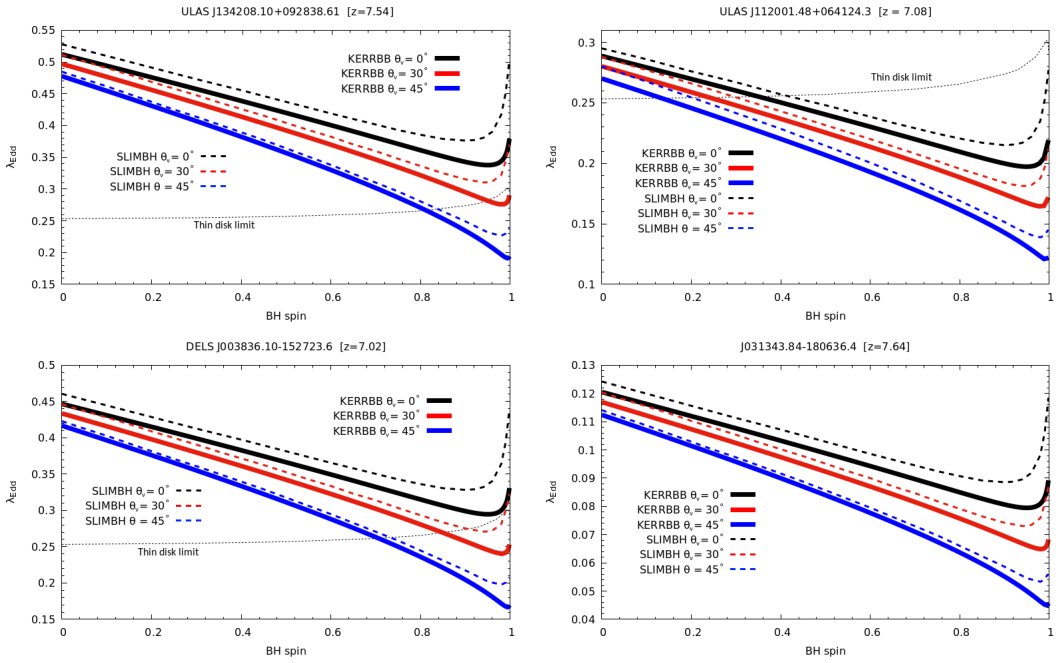

FIGURE 4.10: Eddington ratio of the sources J1342, J1120, J0038 and J0313 as a function of the BH spin. The thin dashed line is the thin disk limit computed following Laor and Netzer, 1989 (see Sect. 3.3). The confidence interval of each curve is ~ 0.1 dex computed from the uncertainty on the spectrum peak position.

$30° - 45°$): the results are summarized in Table 4.2. It is easy to notice that the KERRBB Eddington ratio estimates are smaller than the results found by Bañados et al., 2018 (J1342, $\lambda_{\rm Edd} = 1.5^{+0.5}_{-0.4}$), Mortlock et al., 2011 (J1120, $\lambda_{\rm Edd} = 1.5^{+0.6}_{-0.5}$), Wang et al., 2018 (J0038, $\lambda_{\rm Edd} = 1.25 \pm 0.19$) and Wang et al., 2021 (J0313, $\lambda_{\rm Edd} = 0.67 \pm 0.14$). The reason behind such different results is connected to the bolometric luminosities (larger than those inferred with KERRBB) which lead to a larger value of $\lambda_{\rm Edd}$, at least by a factor of ~ 2 (see the previous section "Observed disk luminosity").

KERRBB versus SLIMBH

On the same plots of Fig. 4.9, KERRBB results are compared with the thin disk limit for $\lambda_{\rm Edd}$, following Laor and Netzer, 1989 (black dotted line; see Sect. 3.2.3): in order to have a geometrically thin disk, the Eddington ratio must be $\lambda_{\rm Edd} < 0.3$;[11] above this value, the results are not consistent with the thin disk assumptions and another model (i.e., slim disk) must be used. The model SLIMBH was used, using the same spectrum peak position, to infer the main SMBH properties: Figs. 4.9 - 4.10 show respectively the BH

[11] Only for J1342 and J0038, the KERRBB estimates are above this limit.

mass and the Eddington ratio for the four sources, computed using SLIMBH (dashed lines), for different spin values and angles; the results, summarized in Table 4.2, are similar for low spin values (i.e., the two models give almost the same results because the disk thickness and relativistic effects are negligible) and slightly different for large ones (by a factor of $\sim 1.2 - 1.3$; see Sect. 3.4.1). Also for what concerns the observed disk luminosity and the BH spin, the results inferred with the SLIMBH are similar to those obtained using KERRBB.

4.2.4 Evolution of the BH mass

In this section, I will describe the possible scenarios for the SMBH growth considering simplified assumptions. The aim of the estimates below is to explore possible evolutionary histories for the considered sources so that they reach their masses via accretion at their observed redshifts. The evolutionary paths are evaluated in terms of accretion parameters, radiative efficiency, seed mass and formation redshift. The procedure is oversimplified as no physically motivated time evolution in the accretion parameters is adopted. Nevertheless, despite the limitations of the procedure, it gives a sense of which range of evolutionary parameters is viable and the possible origin of such massive objects.

Accretion onto a BH changes its mass and spin (Bardeen, 1970; Thorne, 1974). The variation of the BH mass M as a function of time is

$$\frac{dM}{dt} = (1-\eta)\dot{M}.$$

By integrating this expression, it is possible to find the evolution time $t_{\rm ev}$ for a BH, that is, the time it takes to grow from an initial seed mass M_0 to a final mass M (Salpeter time, Salpeter, 1964) assuming a constant Eddington ratio $\lambda_{\rm Edd}$,

$$\frac{t_{\rm ev}}{\rm Gyr} = 0.451 \frac{\eta}{1-\eta} \frac{1}{\lambda_{\rm Edd}} \ln\left[\frac{M}{M_0}\right]. \tag{4.1}$$

Lapi et al., 2014 presented a consistent scenario in which at high redshifts, a SMBH grows in a self-regulated regime with a radiative power slightly super-Eddington ($\lambda_{\rm Edd} < 4$) and a radiative efficiency $\eta = 0.15$. After this phase, a fast decrease of $\lambda_{\rm Edd}$ occurs until the matter reservoir (assumed to surround the SMBH and to accrete onto it) is exhausted (i.e. in a sub-Eddington phase). Figure 20 in Lapi et al., 2014 shows that the fast decrease

of the Eddington ratio lasts less than < 0.1 Gyr while most of the BH evolution occurs during the super-Eddington phase (which lasts longer). Therefore, the BH evolution time can be approximated by Eq. 4.1 with $\lambda_{\rm Edd} \geq 1$. Within such a scenario, the previous estimates of the Eddington ratio for the four sources ($\lambda < 0.5$) would indicate that they have already reached the last phase of their evolution. Therefore, to assess their growth, it is necessary to focus on the previous (super)-Eddington phase.

A first oversimplified assumption is that the observed Eddington ratio and observed accretion rate (defined as $\dot{m} = \dot{M}/\dot{M}_{\rm Edd}$ where $\dot{M}_{\rm Edd} = L_{\rm Edd}/c^2$) describe the whole SMBH evolution. In this case, since for $a > 0$, the Eddington ratio is constrained to be $\lambda_{\rm Edd} < 1$ and an accretion rate $\dot{m} < 10$, a very massive seed (Log $M/M_\odot > 6.5$) is required at redshift $z \sim 40$. In other words, if the SMBH seed had a mass of $10^{2-4} M_\odot$, then a significantly larger $\lambda_{\rm Edd}$ and $\dot{m}$ were necessary during the fast growth phase of super-Eddington accretion. Fig. 4.11 shows the evolutionary tracks (i.e. SMBH mass as a function of redshift with the final mass corresponding to the case with $a = 0$ and $\theta_{\rm v} = 30°$) of the four sources, for different assumptions on the accretion parameters, as described below.[12] These are compared with the equivalent tracks for the radio loud sources SDSS J013127.34-032100.1 (J0131, $z = 5.18$) and S5 0014+813 ($z = 3.36$), studied in Campitiello et al., 2018 using KERRBB, whose masses for non-rotating BHs are Log $M/M_\odot = 9.70$ and Log $M/M_\odot = 9.74$, respectively. For simplicity, the evolution is described in two ways:

1. *Super-Eddington evolution* $\lambda_{\rm Edd} > 1$: given that the radiative efficiency is not easy to estimate, it is fixed to $\eta = 0.1$. This choice is reasonable both in the accretion disk scenario and in the chaotic one. If the disk is in the slim regime during the super-Eddington phase, the SMBH can spin up to the maximum value ($a \sim 1$) and the radiative efficiency is lower than the canonical value ~ 0.3 due to photon trapping; if instead the super-Eddington phase is characterized by a chaotic accretion, the BH spin is thought to be low or ~ 0 (Dotti et al., 2013). In the range of $\dot{m}$ considered in this work, the choice of $\eta = 0.1$ is in agreement with the results of Sadowski, 2009 concerning the super-Eddington accretion through a slim disk. In the case $\lambda_{\rm Edd} = 1$ ($\dot{m} = 10$), a massive seed of $\sim 10^4 M_\odot$ is required at redshift $z \sim 25 - 30$ or larger in order to reach the observed masses (as also obtained by Bañados et al., 2018). For

[12] For the case where $a = 0.9982$, the curves are similar and shifted rigidly to larger masses by a factor of ~ 3.5.

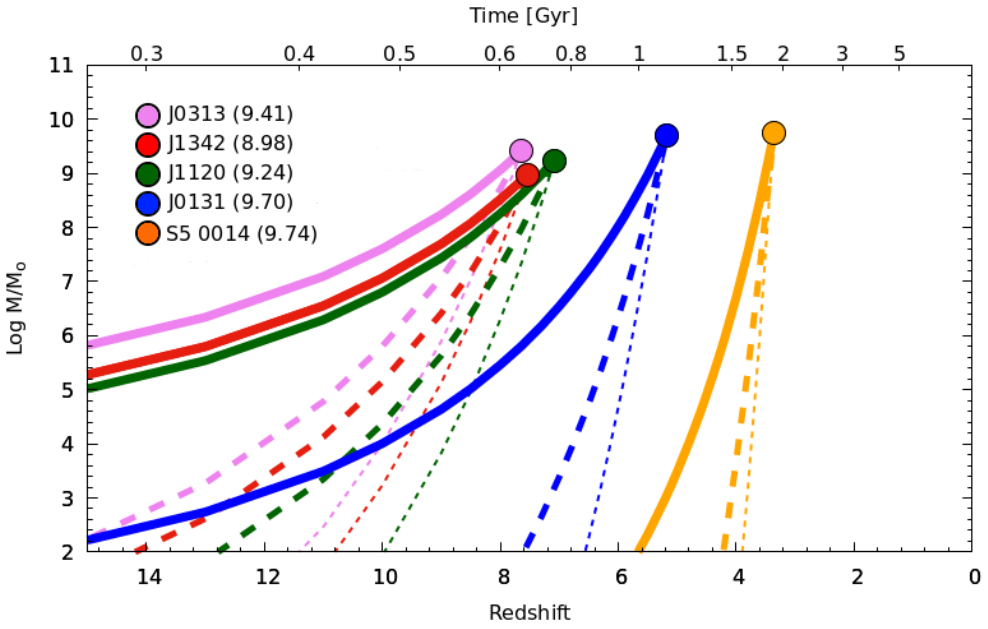

FIGURE 4.11: SMBH mass as a function of z for the four sources (J1120 and J0038 show a similar trend represented with a single curve), compared with those of the sources J0131 and S5 0014+813, studied by Campitiello et al., 2018. The final masses in the brackets correspond to the non-spinning KERRBB solutions $\theta_v = 30°$ (for $a = 0.9982$, the curves are shifted to larger masses by a factor of ~ 3.5). Solid, thick dashed and thin dashed refer to $\lambda_{Edd} = 1 - 2 - 3$, respectively. The radiative efficiency is fixed to $\eta = 0.1$.

J0131 and S5 0014+314 instead, a seed of $\sim 10^2 M_\odot$ could have grown in ~ 0.9 Gyr, starting at redshift $z \sim 15$ and $z \sim 6$, respectively. For larger values of λ_{Edd}, the BH evolution could have begun with a lighter BH seed at smaller redshifts, growing exponentially and reaching the estimated masses in less than ~ 0.4 Gyr: as an example, in the case with $\lambda_{Edd} = 2$, the evolution could have begun with a seed of $\sim 10^2 M_\odot$ at redshift $z \sim 13 - 14$; for $\lambda_{Edd} = 3$, a faster evolution of ~ 0.2 Gyr could have begun at $z \sim 10 - 11$.

2. *Eddington limited evolution* $\lambda_{Edd} \sim 1$: in this case, $\eta\dot{m} \sim 1$. For different values of $\dot{m}$, the evolutionary curves are similar to the ones already shown in Fig. 4.11. For the same value of $\dot{m}$, the evolution is slightly faster because η is smaller due to the previous bound: assuming $\dot{m} = 10$, the radiative efficiency is $\eta = 0.1$ and this case is represented by the solid lines in Fig. 4.11; for $\dot{m} = 20$ (30), the radiative efficiency is $\eta = 0.05$ (0.03) and the evolution curves are similar to the ones described by dashed lines but the growth proceeds slightly faster due to the efficiency < 0.1.

As also noted and discussed by Wang et al., 2021, the most distant QSOs (in this case, J0313, J1342, J1120, J0038) constrain the possible origin of such massive objects in a specific mass range: assuming an Eddington limited evolution ($\lambda_{\rm Edd} \sim 1$), the SMBHs could have grown in $\sim 0.3 - 0.4$ Gyr (from redshift $z \sim 15$) assuming a massive seed of $\sim 10^{5-6} M_{\odot}$, consistent with the mass range related to direct-collapse BHs in pre-galactic dark matter halos (e.g. Begelman, Volonteri, and Rees, 2006). With the same accretion rate, for J0131 and S5 0014+813, the evolution could have last longer ($\sim 0.7 - 0.9$ Gyr) if a different origin is considered (e.g., population III star remnants; e.g., Madau and Rees, 2001).

In this scenario, assuming a constant accretion through a disk, the major uncertainty comes from the radiative efficiency η, linked to the BH spin, which regulates the amount of matter accreted onto the BH: the non-spinning (or slowly-spinning) scenario could be the most compelling since η is smaller with respect to the maximum spin case, resulting in a faster BH growth.

Future works on a large sample of quasars at $z > 7$ could shed light on the possible mass and Eddington ratio distributions and give stronger constraints on the probable BH growth and seed origin. The usage of relativistic accretion disk models (e.g. KERRBB and SLIMBH) could be a viable, alternative (and possibly more accurate) means to infer parameters like BH mass and Eddington ratio and, in principle, well-calibrated alternative mass determinations would constrain BH spins.

4.3 AD fitting versus RM and SE

Different SMBH mass estimate methods carry uncertainties linked to the features of the system, to the parameters of the model involved for the estimates and clearly to the quality of data (see Sect. 1.2). To assess the robustness of the mass estimate, it is necessary to compare the results of the different methods and possibly to calibrate the model-scaling parameters. However, this is not trivial because different approaches are based on different observables and are thus not applicable to all sources.

In this Section, I will compare the results of the AD fitting method with those of RM to test the reliability of AD models as an alternative approach to evaluating SMBH masses in AGNs. Masses estimated through the RM technique are based on direct measurements related to the BLR and it is among the most accurate methods. As a supplementary test, I will also include SE results although the method is calibrated on RM measurements. The results are published in Campitiello et al., 2020.

As already discussed in Sect. 1.2, the RM technique is based on direct measurements related to the BLR response to continuum changes where the SMBH mass can be expressed as

$$M_{\rm BH} = f_{\rm BLR} \underbrace{\frac{c\ \tau_{LT}\ \sigma^2_{\rm line}}{G}}_{=VP}, \tag{4.2}$$

where the *Virial Product* (VP) is a function of $\tau_{\rm LT}$, the light-travel time (i.e., the time related to the emission-line response delayed with respect to changes in the continuum) and $\sigma_{\rm line}$, the line velocity dispersion (or the line Full Width Half Maximum - FWHM). The geometrical factor $f_{\rm BLR}$ is linked to the unknown kinematics and geometry of the BLR, calibrated by comparing BH masses obtained with different approaches (e.g., Bentz and Katz, 2015; Li et al., 2018). SE virial mass estimates are based on RM results which showed a link between the BH mass, the continuum/line luminosity and the $\sigma_{\rm line}$/FWHM of some lines. For both methods, SMBH masses have a systematic uncertainty of $\sim 0.4 - 0.5$ dex (e.g., Peterson et al., 2004; Vestergaard and Peterson, 2006; Shen et al., 2008; Park et al., 2012).

The main source of uncertainty is connected to the unknown factor $f_{\rm BLR}$ and the quality of the fit performed with AD models. Although several issues are connected to this latter (see Sect. 3.3), for a correct description of the AD emission, the more compelling and appropriate models are KERRBB and AGNSED, the former describing a geometrically thin AD including all relativistic effects and the latter taking into account the presence of an X-ray Corona above the disk (see Chap. 3 and Sect. 3.4.2). In this framework, given the large uncertainties on the physical and geometrical properties of the X-ray Corona and the importance of relativistic effects, KERRBB was adopted to estimate the SMBH masses using the analytical expressions found by Campitiello et al., 2018. For two sources with good data coverage in the X band, AGNSED was used and its results were compared with those inferred

with KERRBB. Significant uncertainties on the results also arise from observational issues such as absorption by dust. These possible uncertainties are discussed in the following along with their weight on the mass estimates.

4.3.1 Data selection, Fitting procedure and Caveats

Here I define the AGN sample and describe the AD fitting procedure, illustrating the possible issues related to this approach.

From the AGN Black Hole Mass Database (Bentz and Katz, 2015)[13], a compilation of published spectroscopic RM studies of AGNs, I chose only the sources with clear evidence of BBB. For those sources, I searched for the available and the most recent spectroscopic data (from the NIR to the FUV bands) from the public archives and literature (see Tab. B.1).[14]

I selected 28 sources ($z < 0.3$) with (i) a clear UV bump determined as a power-law continuum $F_\lambda \propto \lambda^\alpha$ with a negative slope in the rest-frame wavelength range $3000 - 5000$Å,[15] (ii) wide spectroscopic coverage especially around the spectral peak, and (iii) limited variability for non-simultaneous spectra (see below). For some sources, the NIR-Optical SED shows contamination by the host galaxy whose emission was taken into account in the SED modeling (see the following Section). For each source, spectroscopic data were corrected for Galactic extinction using the Cardelli, Clayton, and Mathis, 1989 reddening law and $E_{[B-V]}$ from the map of Schlegel, Finkbeiner, and Davis, 1998 with an extinction factor $R_V = 3.1$.

A serious issue concerns non-simultaneous spectroscopic data that could affect the normalization of different spectra. When data did not show the same normalization, I calibrated the different data sets by adopting the following procedure: first, I considered spectroscopic data in the UV wavelength range where the peak of the AD emission should be located; then I calibrated the available FUV and Optical data by matching the flux in the common wavelength range assuming that the spectral shape does not change with flux variation (see also Shang et al., 2005). The same calibration was performed on IR data (when present). In any case, the maximum mismatch amounts to ~ 0.1 dex in flux (leading to an uncertainty on the derived BH mass at most by a factor of ~ 0.05 dex).

[13] See also http://www.astro.gsu.edu/AGNmass/.

[14] I also collected some photometric data (GALEX, Vizier, NED), not taken into account in the fitting procedure because (i) they might be contaminated by emission lines or by some kind of absorption and (ii) their statistical weight in the fit is negligible.

[15] Only two sources (PG1247+267, S50836+71) are at $z \sim 2$. For them, spectroscopic data cover only the spectrum peak position.

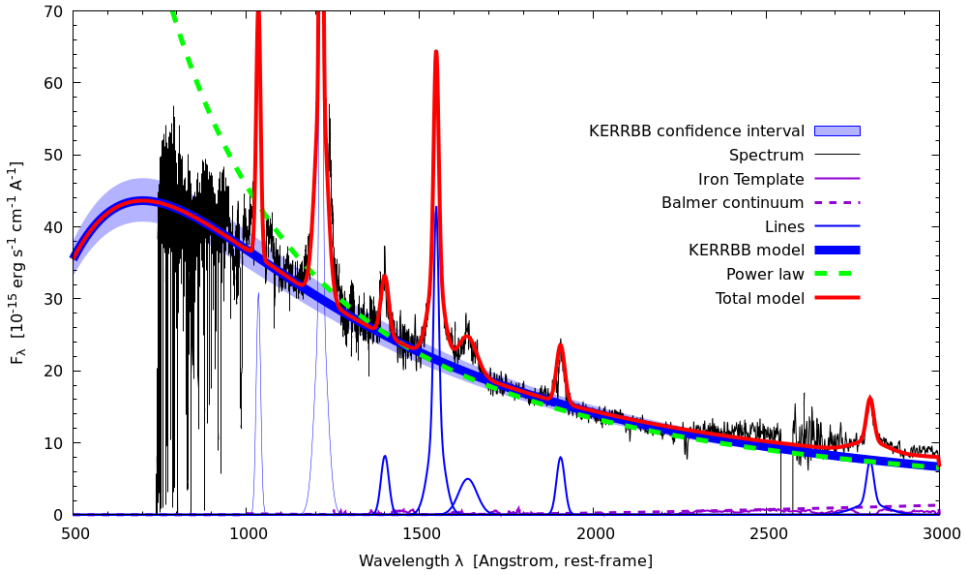

FIGURE 4.12: Example of a fit of the composite FUSE - HST - KPNO spectrum of the source PG0953+414 (from Shang et al., 2005). The KERRBB model (thick blue line) describes the AGN continuum with the iron complex (purple line), the Balmer continuum (purple dashed line) and some prominent emission lines (simple Gaussian profile, blue lines). The red line represents the sum of all these components. The green dashed line is a standard power-law continuum (slope $\alpha = -1.77$). The KERRBB model has an average confidence interval of ~ 0.05 dex (blue shaded area).

Finally, spectroscopic data (especially FUSE and HUT data) were smoothed by averaging the flux in fixed wavelength bins to have a clearer representation of the overall emission. This latter process could have an effect on the fitting procedure and the inferred model parameters (see the following Section).

The following fitting procedure was adopted, using the relativistic thin AD model KERRBB:

- Using GNUPLOT (non-linear least-squares Marquardt-Levenberg algorithm), the rest-frame spectrum ($\lambda - F_\lambda$, Fig. 4.12) was fitted with the KERRBB model to describe the AGN continuum, adding the iron complex (e.g., Wilkes, 2001), some prominent emission lines (MgII, CIII, CIV, SIV and Lyα) modeled with a simple Gaussian profile, a Balmer continuum (e.g., Rosa et al., 2014) and the template for the host-galaxy emission (Manucci et al., 2001) which can contaminate the nuclear spectrum in the NIR-Optical bands.

- As a comparison, a standard fit was also performed using a power-law to describe the AGN continuum. In Fig. 4.12, it is shown an example of both fits. It is clear that the two continua overlap well for $\lambda > 1300$Å

while the AD model turns over around the spectral peak. Even if this latter is not covered by data, it can be constrained using the curvature of the spectrum at larger wavelengths.

- Spectral features, such as strong emission or absorption lines, have no drastic effects on the overall KERRBB fit, even at short wavelengths where the spectrum peak is located (see the following Section).[16]

- Each fit constrains the spectrum peak position which is essential to infer the BH mass (see Sect. 3.2.3): for all sources, the average residuals are always $\lesssim 0.05$ dex with a reduced-$\chi^2 < 0.02$. In the $\nu - \nu L_\nu$ representation, both the peak frequency $\nu_{\rm p}$ and luminosity $\nu_{\rm p} L_{\nu_{\rm p}}$ have an average uncertainty of ~ 0.05 dex (represented with a blue shaded area in Fig. 4.12 and in all the Figures reporting the spectral fits in Appendix B; see also Fig. 4.13). This confidence interval translates to an average uncertainty of ~ 0.1 dex on the BH mass and the Eddington ratio $\lambda_{\rm Edd}$ (for a fixed BH spin and viewing angle - see Fig. 4.13).

Possible absorption by gas or dust along the line of sight could affect the overall AD spectrum shape, leading to different parameter estimates.

- For some ground-based telescopes, the available spectrum can be subjected to absorption due to sky regions with low transparency. Even if these regions are subtracted, our best fit does not change significantly and remains inside the average confidence interval (~ 0.05 dex; as in Campitiello et al., 2019).

- At frequencies Log ν/Hz > 15.4, spectra show some absorption features caused by the Interstellar Medium (ISM): if these blended lines are smoothed or not subtracted from the spectrum appropriately, the AGN continuum can be underestimated, leading to an incorrect evaluation of the spectral peak position (i.e., shifting $\nu_{\rm p}$ to smaller values and leading to an overestimation of the BH mass). To understand if these spectral features have a relevant effect on the results, the same fitting procedure described in the previous Section was performed by choosing only the frequency range Log ν/Hz < 15.4; even if the spectral range is reduced, the curvature of the spectrum at smaller frequencies

[16] As an additional test, two Gaussians were used to fit the broad base of the most prominent lines: no drastic effects were observed on the AGN continuum which remains inside the confidence interval of ~ 0.05 dex.

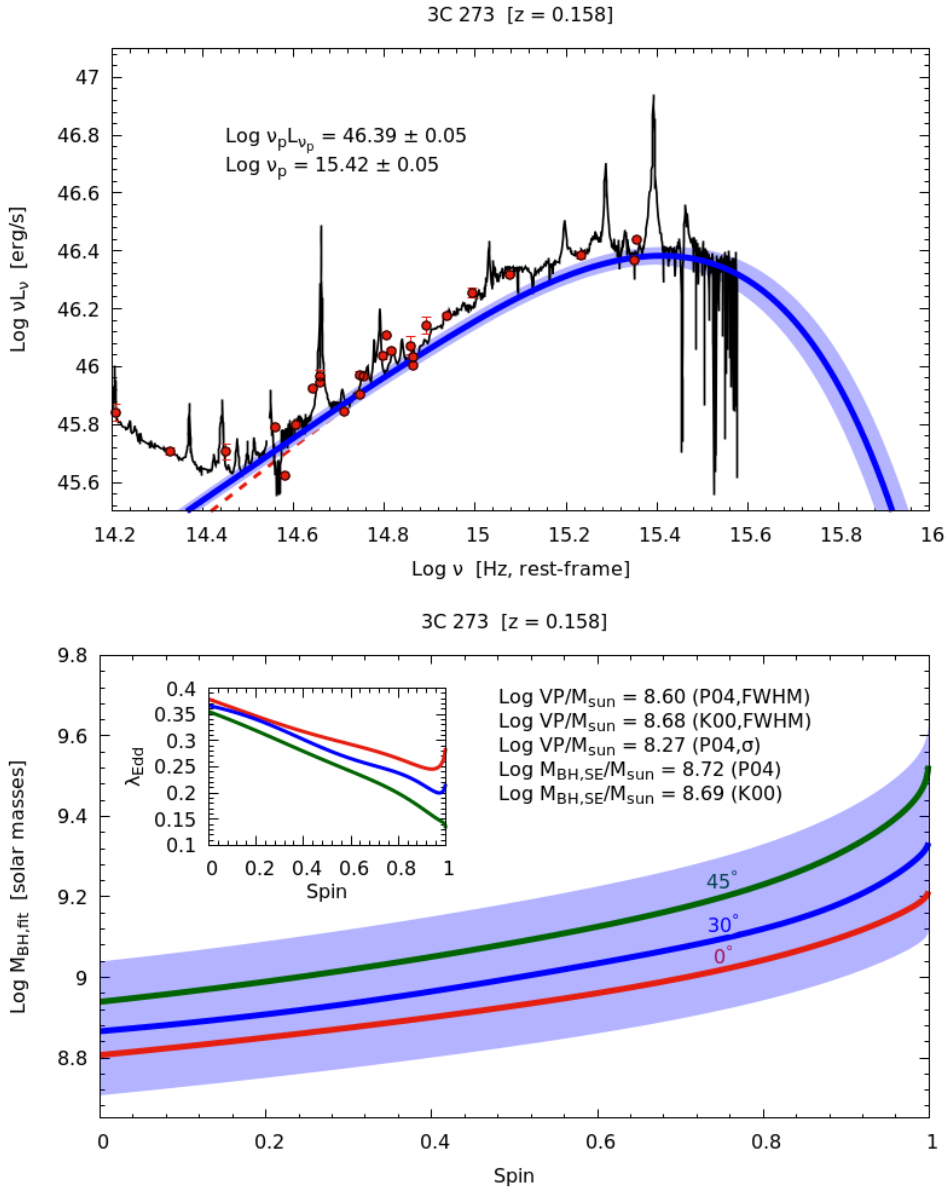

FIGURE 4.13: Top panel: fit of the source 3C273. The rest-frame AGN continuum is described by the KERRBB model (thick blue line) with a blue shaded area ($\sim$ 0.05 dex) defining a confidence interval for the spectrum peak position. Red dots are archival photometric data (GALEX, Vizier, NED) not used in the fitting procedure. The spectroscopic data are listed in Tab. B.1. Bottom panel: KERRBB BH mass and Eddington ratio as a function of the BH spin for different values of the viewing angle θ_v. Different BH mass estimates from different works (listed in the caption of Fig. B.1) are reported on the plot. The blue shaded area ($\sim$ 0.1 dex) defines the confidence interval on each BH mass estimate.

can still be used to constrain the peak position. The new peak frequencies are on average larger than the previous ones (inferred considering the whole available spectral range) but consistent with them within a range of $\sim$ 0.05 dex, while the luminosities are similar. The inferred new BH masses are inside the average confidence interval of $\sim$ 0.1 dex (defined by the spectrum peak uncertainty).

- The IGM could modify the spectrum shape (especially for high-redshift sources) at frequencies $\mathrm{Log}\,\nu/\mathrm{Hz} > 15.4$. For the redshift range spanned by our sample the correction from such a kind of absorption is negligible (see Madau, 1995; Haardt and Madau, 2012; Castignani et al., 2013) except for the two high-redshift sources, PG1247+267 and S50836+71. For these two objects, this correction was performed and the results are shown in Figs. B.23 - B.28, respectively (see Appendix B).

- An important effect that could modify the spectral UV shape concerns dust absorption: if present, this could lead to an incorrect BH mass estimate. The absorption could be caused by the dusty torus surrounding the AD, or dust in the host galaxy ISM.[17]

  Given that our sample is composed of Type 1 QSOs (FWHM $>$ 1000 km/s for the most prominent lines; e.g., Antonucci, 1993), it is not expected any (strong) absorption from the dusty torus which is assumed to have an average aperture angle of $\sim 45°$. For this reason, in order to infer the BH mass, it is assumed that each source is observed with a viewing angle $\theta_v \leq 45°$ (see Tabs. B.2 - B.4 for results). However, the goodness of the fits was checked by considering the possible intrinsic reddening by the host galaxy ISM. To do so, I followed the work by Baron et al., 2016, who found an analytical expression to infer the amount of absorption (in terms of $E_{[B-V]}$) as a function of the rest-frame spectrum slope α in the wavelength range 3000 - 5100Å. For the majority of the sample, the correction is small ($E_{[B-V]} < 0.05$ mag) and could lead to a decrease of the BH mass by a factor < 0.1 dex. This extinction is consistent with what is thought to be the average value for AGNs ($E_{[B-V]} \sim 0.05 - 0.1$ mag; Koratkar and Blaes, 1999).

  For a more complete analysis of the possible UV dust absorption, for each source I used the extinction law of Czerny et al., 2004 and assumed

[17] Recent works (e.g. Leftley et al., 2018) show that $\sim 50 - 80\%$ of the MIR emission originates primarily from polar regions instead of from an equatorial dust distribution. This can affect the observed disk luminosity which would be dimmer with respect to the intrinsic one since part of its radiation is intercepted by the polar dust.

that the slope of the corrected, de-reddened spectrum at wavelength < 2000Å had to be softer than the theoretical value $F_\nu \propto \nu^{1/3}$ (as done in Sect. 4.2). In this way, I found an upper limit for the correction (on average $E_{[B-V]} \sim 0.20$ mag) that leads to a decrease of the BH mass obtained through the SED fitting procedure at most by a factor of ~ 0.3 dex (since the spectrum peak position changes due to the correction).

As also discussed in Sect. 4.2, such a strong UV absorption is not expected because the sample is made of Type 1 QSOs and the $1/3$ slope is not observed in the UV band. Moreover, for what concerns the correction found by Baron et al., 2016 regarding ISM dust absorption, possible deviations from the average continuum slope could be caused by other factors connected to the BH physics, such as the BH mass, the accretion rate, the spin, and the system orientation (e.g., Hubeny et al., 2000; Davis and Laor, 2011). Therefore, I did not consider any correction from dust absorption, confident that the results are inside the estimated BH mass confidence interval (even if the intrinsic extinction is taken into account).

4.3.2 Results

In this section, I show the results coming from the SED fitting procedure and using the analytical KERRBB expressions found by Campitiello et al., 2018 in order to infer the BH mass and the Eddington ratio (reported in Tabs. B.2 - B.4), in the spin range $0 \leq a \leq 0.998$ and for a viewing angle $\theta_v \leq 45°$. As shown by the authors (see also Sect. 3.2.3), the space of KERRBB solutions is degenerate and by using different parameters (M, a and $\dot{M}$) appropriately, it is possible to describe the same set of data. I compare the KERRBB BH masses $M_{\rm fit}$ to those obtained through RM and from SE equations, with a liner fit, i.e., Log $M_{\rm fit}$ = Log $M_{[\rm VP\ or\ SE]}$ + Log$f$, where f can be considered as the geometrical factor $f_{\rm BLR}$ or a simple scaling factor.

Black hole mass uncertainty

The total uncertainty on the KERRBB BH mass inferred from the SED fitting procedure is ~ 0.45 dex (comparable to the systematic uncertainties on the RM and SE estimates, $\sim 0.4 - 0.5$ dex). This uncertainty has to be considered as a *confidence interval* in which the BH mass inferred with KERRBB lies and is connected to different quantities involved in the fitting procedure, namely the BH Spin (in the range $0 \leq a \leq 0.998$), the viewing angle of the system (in

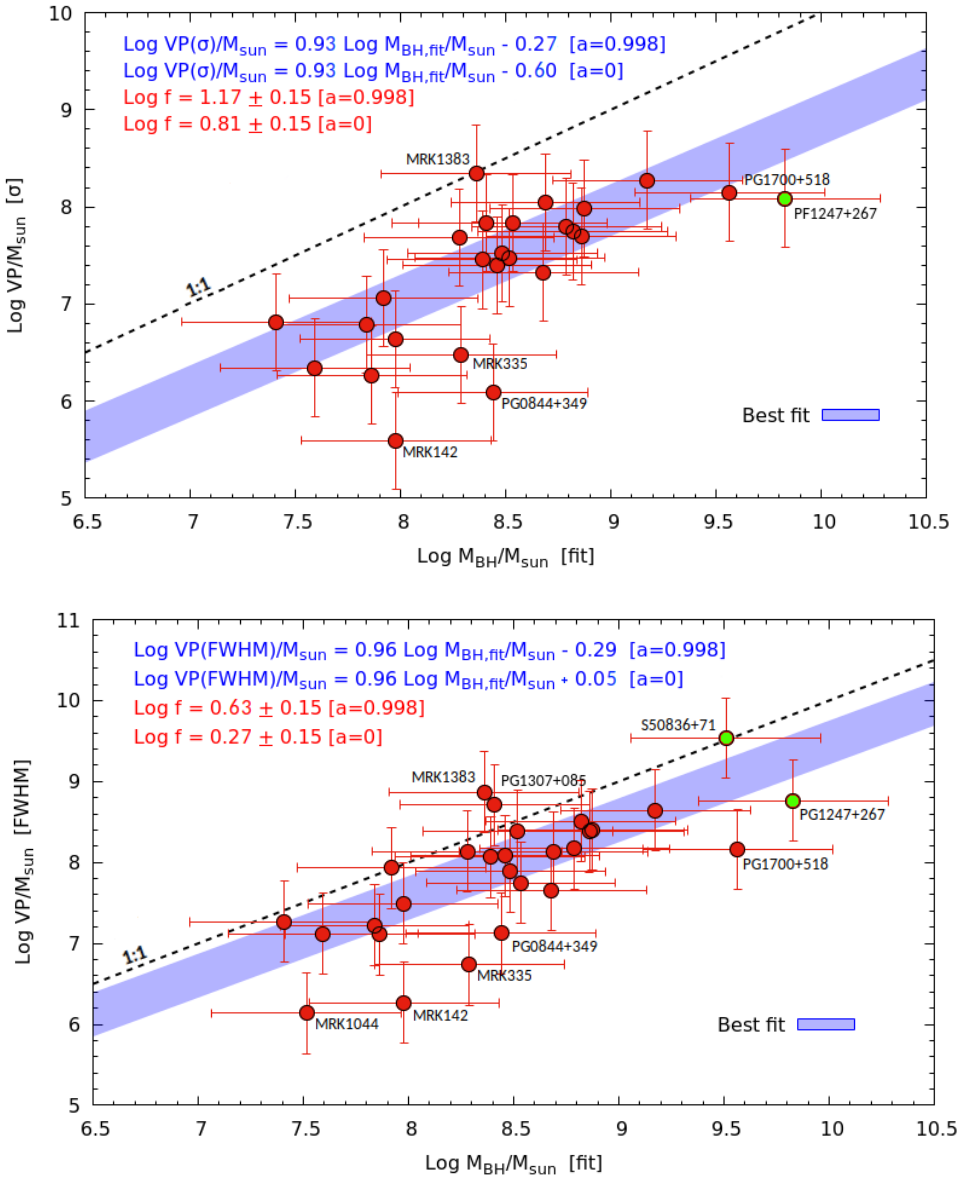

FIGURE 4.14: Comparison between KERRBB BH mass estimates $M_{\rm BH,fit}$ (inferred from the SED fitting procedure; each dot corresponds to the mean value computed using the extreme estimates given by the uncertainties - see text) and the VPs calculated using the Hβ velocity dispersion $\sigma_{\rm line}$ (top panel) and the FWHM (bottom panel). I averaged all the VPs estimates by using data from different authors (see Tabs. B.2 - B.4; PG1247+267 and S50836+71 are marked with green dots). The blue shaded area corresponds to the set of best fits between $M_{\rm BH,Fit}$ and VP after considering all possible spin values between 0 and 0.998 (equations in blue on the plot are the two extreme cases; the uncertainty on the slope is $\sim$ 20%). Assuming that Log $M_{\rm BH,fit}$ = LogVP + Log$f$, the found scale factor f is labeled on the plot in red for the two extreme spin values. Uncertainty bars in both plots are $\sim$ 0.45 dex and $\sim$ 0.5 dex for $M_{\rm BH,fit}$ and VPs respectively, and the black dashed line is the 1:1 line.

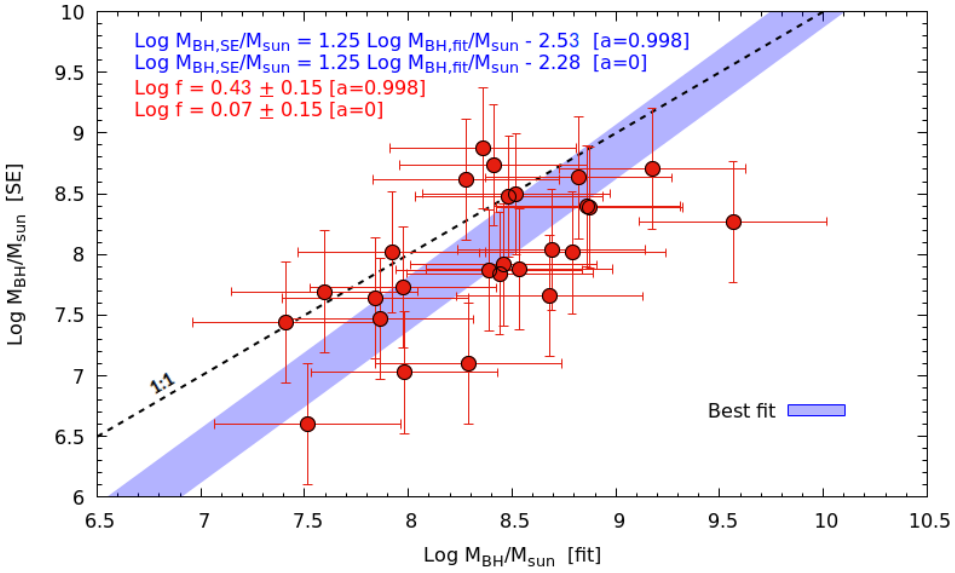

FIGURE 4.15: Comparison between the KERRBB BH mass estimates $M_{\rm BH,fit}$ (inferred from the SED fitting procedure) and the SE BH masses $M_{\rm BH,SE}$ computed using the equation of Vestergaard and Peterson, 2006 and the Hβ line (I excluded the two high-redshift sources, PG1247+267 and S50836+71, for which information are available only on the CIV line; see Tabs. B.2 - B.4). The blue shaded area, the dashed black line, the reported labels, and the uncertainty bars (as also the uncertainty on the best fit slopes) are the same as in Fig. 4.14.

the range $0^\circ \leq \theta_{\rm v} \leq 45^\circ$) and the uncertainty on the spectral peak frequency and luminosity (~ 0.05 dex). Assuming that there is no dust absorption, the BH mass changes by ~ 0.5 dex going from $a = 0$ to $a = 0.998$ (for a fixed viewing angle) and by ~ 0.2 dex going from $\theta_{\rm v} = 0^\circ$ to $\theta_{\rm v} = 45^\circ$ (for a fixed spin). Taking as a reference value the arithmetic mean of the BH mass in both the spin and $\theta_{\rm v}$ ranges, the overall uncertainty is ~ 0.35 dex. Moreover, the confidence interval on the spectral peak position (~ 0.05 dex) leads to an additional uncertainty of ~ 0.1 dex on the BH mass estimate. However, if the spectral peak is well constrained (and/or the viewing angle is known), the mean uncertainty on the AD BH mass estimates can be < 0.3 dex.

Black hole mass comparison

Figure 4.14 shows the comparison between the BH mass estimates inferred from the SED fitting procedure with KERRBB and the VPs computed using the Hβ velocity dispersion $\sigma_{\rm line}$ (top panel) and the FWHM (bottom panel; I excluded PG1247+267 and S5 0836+71 from the fit for consistency since the CIV line was used to computed the VPs). The comparison between the

VP computed using the velocity dispersion and the FWHM is shown because several authors claimed that the ratio FWHM/σ line is not necessarily a constant (e.g., Collin et al., 2006; Peterson, 2011): for the chosen sample, I found FWHM/$\sigma_{\rm line} \sim 2$ with a large dispersion (~ 0.5 dex). Instead, Fig. 4.15 shows the comparison between the KERRBB results and the BH masses computed using the SE relations of Vestergaard and Peterson, 2006. From the analysis of those results, it is easy to notice that both the VPs and the SE estimates are systematically smaller than the KERRBB estimates by a factor f depending on the BH spin. For VP($\sigma_{\rm line}$) and VP(FWHM), assuming a BH spin $a = 0$ (0.998), I found Log $f = 0.81$ $(1.17) \pm 0.15$ and Log $f = 0.27$ $(0.63) \pm 0.15$, respectively. If, in this case, f is identified as the geometrical factor $f_{\rm BLR}$ (Eq. 4.2), the range I found by using VP($\sigma_{\rm line}$) is consistent for example with $f_{\rm BLR} = 5.5 \pm 1.8$ (Onken et al., 2004; see also Li et al., 2018 for other reference values). In both cases, the compatibility is more compelling if, on average, BH spins are assumed to be small.

For SE estimates, I found Log $f = 0.07$ $(0.43) \pm 0.15$, assuming a BH spin $a = 0$ (0.998), partially consistent with the recent work by Marculewicz and Nikolajuk, 2020. This result is similar to the one found for VP(FWHM): the reason is because a geometrical factor $f_{\rm BLR} \sim 1$ and FWHM measurements are used inside the virial equations of Vestergaard and Peterson, 2006, hence SE and VP(FWHM) are almost the same (within uncertainties).

From Fig. 4.14 (bottom panel), it is clear that KERRBB mass estimates are systematically larger than the corresponding VPs: from the fit, a better compatibility is reached if a scale factor of the order of ~ 10 is assumed, in agreement with the recent paper by Nuñez et al., 2019. Nonetheless, the KERRBB results are still compatible with the RM ones if, for these latter, a geometrical factor of less than ten is considered. Assuming that the BH masses estimated through the AD fitting procedure are correct, the geometrical factor must be large (Fig. 4.14) to compensate the differences with the corresponding VPs. Assuming a disk-like BLR (e.g., Collin et al., 2006; Decarli et al., 2008), the geometrical factor related to the VP (computed using the FWHM) is:

$$f_{\rm BLR} = \frac{1}{4\left[(\sin\theta_{\rm v})^2 + (H/r)^2\right]} \tag{4.3}$$

where H/r is the height-to-radius ratio (i.e., thickness) of the BLR. The range

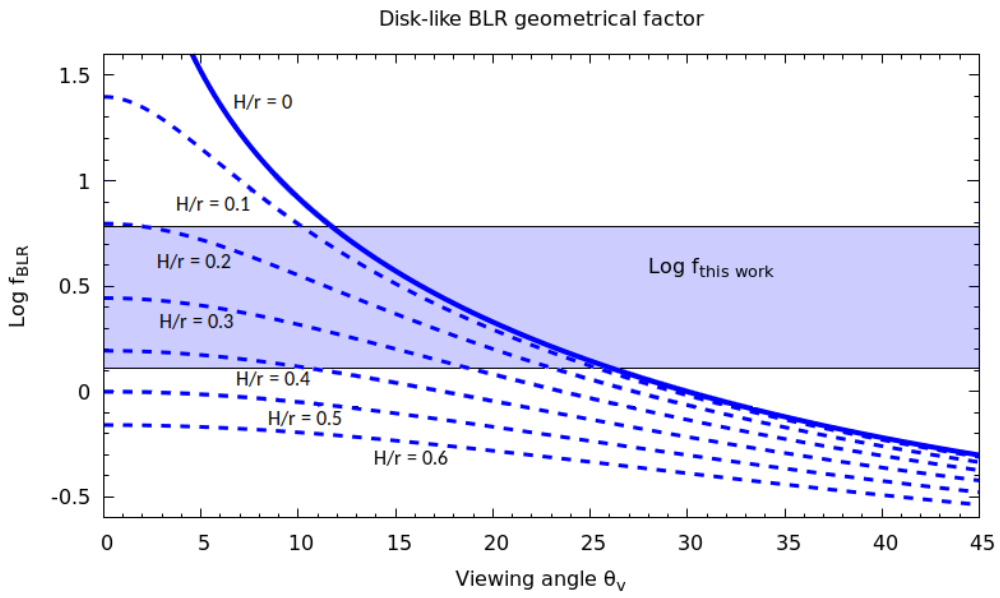

FIGURE 4.16: Geometrical factor $f_{\rm BLR}$ computed using Eq. 4.3 (e.g., Collin et al., 2006; Decarli et al., 2008) as a function of the viewing angle for different BLR thickness H/r. The blue area is the scale factor range found in this work (related to VPs computed using the FWHM; see Fig. 4.14, bottom panel). The comparison leads to a range of $\theta_{\rm v}$ and H/r consistent with the work of Majia-Restrepo et al., 2016.

of scale factors found in this work is consistent with a BLR seen with a viewing angle $< 30°$ (consistent with Type 1 QSOs)[18] and a thickness $H/r < 0.5$ (consistent with the results of Majia-Restrepo et al., 2016; see Fig. 4.16).

Figure 4.17 shows the KERRBB BH estimates compared with the ones from SE and RM (computed using the velocity dispersion $\sigma_{\rm line}$ and different geometrical factors ($f_{\rm BLR} = 2.8 - 5.5$, from Graham et al., 2011; Onken et al., 2004, respectively): about 70% of the sources show a good compatibility between the three results within uncertainties (~ 0.5 dex, on average) favoring smaller KERRBB masses and therefore low spin values.

Spin estimate

Given the large uncertainties involved in each method to infer the BH mass, an estimate of the BH spin is still a hard task. In principle, the comparison of two or more independent BH masses with relativistic AD model results could be an alternative way to constrain the BH spin (see Sect. 3.2.3). For the majority of the sources, the comparison showed that small spin values are

[18] For this range of viewing angles, dust absorption from the torus is not expected (if its aperture angle is considered to be $\sim 45°$).

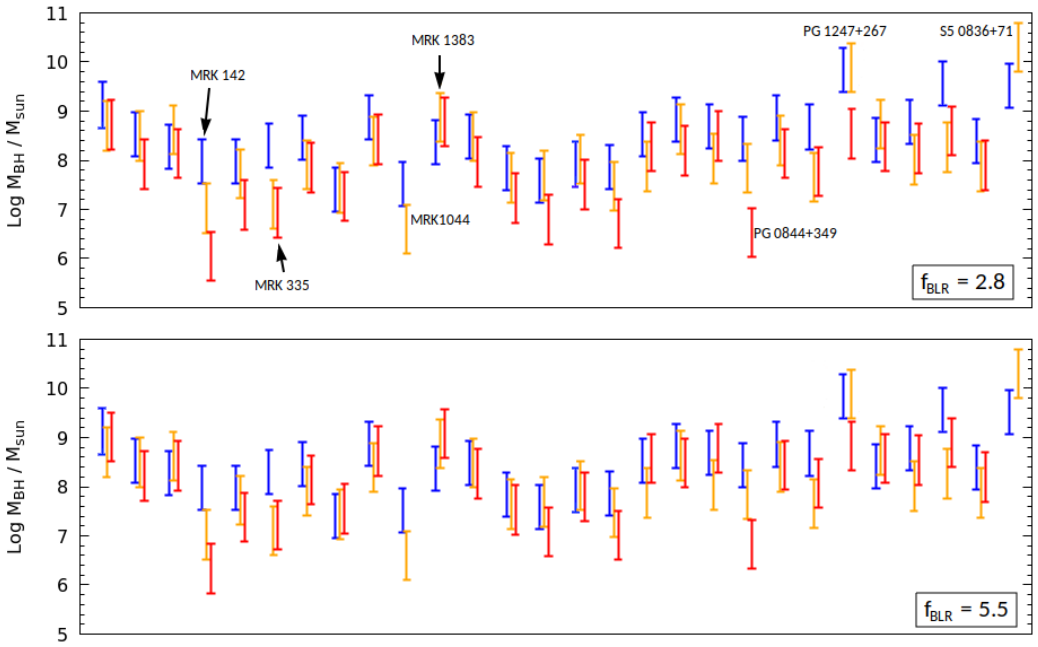

FIGURE 4.17: Comparison between the BH masses computed from the SED fitting procedure with KERRBB (blue) and the SE (orange) and RM estimates (red, inferred with $\sigma_{\rm line}$ and a geometrical factor $f_{\rm BLR} = 2.8 - 5.5$, Graham et al., 2011 top panel and Onken et al., 2004 bottom panel). The average uncertainty for all the measurements is ~ 0.5 dex (the results related to each source are plotted in the same order as listed in the Tabs. B.2 - B.4).

favored. Instead, for a couple of sources (MRK1383, S5 0836+71), the comparison between RM, SE, and KERRBB results (within uncertainties) led to the conclusion that the BH spin must be high (with a lower limit $a > 0.6$). However, as mentioned above, because uncertainties on the fitting procedure, the parameters of the AD and the RM measurements (as well as other methods) are still large, caution is suggested when considering a BH spin estimate based on the comparison of different BH masses.

4.3.3 X-ray Corona above the disk: implications

Estimations of the BH mass using the SED fitting procedure could be affected by the presence of a Corona above the disk: this structure is thought to be compact (e.g., Miniutti and Fabian, 2004; Done et al., 2012; Reis and Miller, 2013; Sazonov et al., 2012; Lusso and Risaliti, 2017) and made of two components: the primary hot one is a plasma of 10-100 keV electrons responsible for hard X-ray emission (with an unknown shape) while the second warm component, above the disk, with a temperature of a few KeV, is thought to

be responsible for the soft X-ray excess observed in many AGNs. In principle, if this structure scatters a fraction of the disk radiation, the observed disk luminosity could be dimmer than the intrinsic one, leading to an incorrect mass estimate (i.e., the spectrum peak position could be different from the intrinsic one, see Sect. 3.4.2).

To check this possibility, I compared the KERRBB results with those of the relativistic model AGNSED (Kubota and Done, 2018), which takes into account also the presence of an X-ray Corona above the disk in a self-consistent way (see Sect. 3.4.2 for a detailed description of the model). It is important to notice that, contrary to KERRBB, AGNSED does not include relativistic effects, such as light bending, self-irradiation, and gravitational redshift, which may have a significant effect on both the AD and the Corona emissions. However, for small values of the BH spin and θ_v, those effects should have a minor weight on the results. For the fitting procedure, I used the sources NGC5548 and MRK509, also studied by Kubota and Done, 2018.

In Kubota and Done, 2018, the authors fitted the UV-X SED of those sources assuming a viewing angle $\theta_v = 45°$ (the other parameters of the model are listed in their Tab. 2, assuming an outer disc emission). As for KERRBB, the modeling with AGNSED of the Optical-to-X SED is degenerate: by changing the model parameters (i.e., BH mass, spin, Eddington ratio, Corona size) appropriately, it is possible to reproduce the same set of data (for some reference values, see Fig. B.29).

For NGC5548, results from both models are compatible while for MRK509, KERRBB BH masses are larger than the AGNSED ones by a factor < 0.2 dex (Fig. B.30). A possible explanation resides in the fact for NGC5548, the absence of relativistic effects in AGNSED is balanced out by modeling a large Corona above the disk, leading to the same BH mass. Instead, for MRK509, the smaller X-ray Corona leads to different results because it does not compensate for the differences between the two models.

In general, the KERRBB observed disk luminosity is dimmer than the intrinsic one because of a compact Corona located in the inner region of the disk, whose presence modifies the AD emission and leads to an overestimated BH mass. If KERRBB disk luminosity is corrected from the Corona coverage, then the same value of the BH mass can be found with both models. I tested this possibility by considering this simple approach:

- I assumed that the observed disk luminosity L_d^{obs} (and so $\nu_p L_{\nu_p}$) is dimmer than the intrinsic one $L_{d,\alpha}$ by a factor $\alpha < 1$: this means that $(1 - \alpha)$

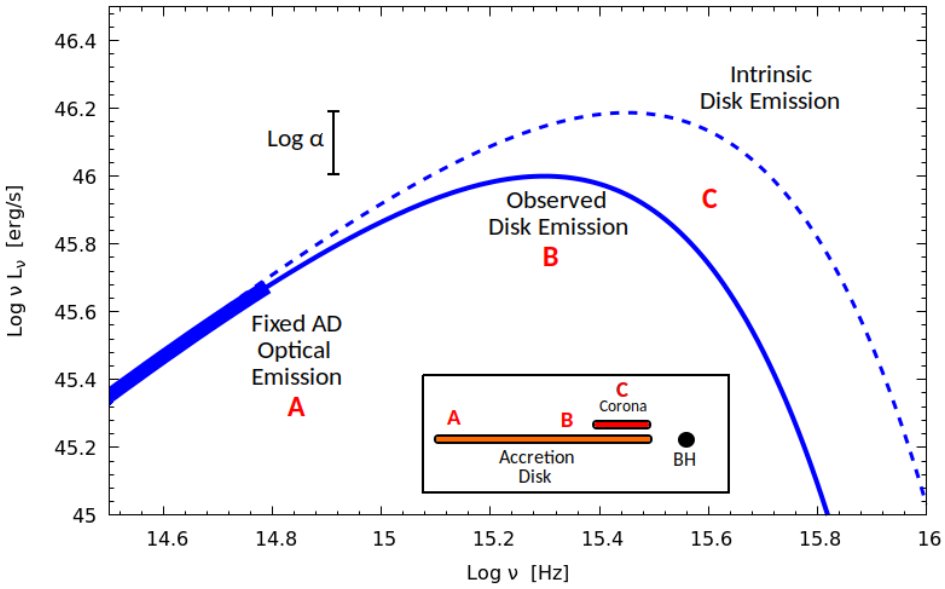

FIGURE 4.18: Scheme used to explain the difference between KERRBB and AGNSED results. The observed AD luminosity is dimmer than the intrinsic one by a factor α because a compact Corona (located in the innermost part of the disk) scatters part of the disk radiation (C). The Optical part of the disk (A, i.e. the emission produced by the most distant annuli of the AD) is fixed because the Corona does not cover its radiation. The peak of the emission (B) is produced by the AD parts closer to the Corona.

of the disk radiation is scattered by the Corona (i.e., the inner disk does not contribute to the observed emission; see Fig. 4.18).

- Assuming that the Corona has a compact structure, the Optical part of the spectrum produced by the outer part of the disk must not change due to the scattering and must keep the same luminosity.

- I found the corrected spectrum luminosity $\nu_{p,\alpha} L_{\nu_{p,\alpha}}$ and frequency $\nu_{p,\alpha}$ by taking into account the correction factor α and by keeping the same luminosity at lower frequencies:

$$\nu_{p,\alpha} L_{\nu_{p,\alpha}} \sim \frac{\nu_p L_{\nu_p}}{\alpha} \qquad \nu_{p,\alpha} \sim \nu_p \, \alpha^{-0.75}$$

where the exponent is derived assuming that the luminosity at Log $\nu/\mathrm{Hz} < 14.8$ is constant.[19] The factor α mimics the actual correction

[19] Following the work of Davis and Laor, 2011, from their Eq. 5, $\nu L_{\nu,\mathrm{opt}} \propto (\dot{M}M)^{2/3}$, where $\nu L_{\nu,\mathrm{opt}}$ is the luminosity at Log $\nu/\mathrm{Hz} \sim 14.8$. By using Eqs. 3.11 - 3.12, it is possible to write $\nu L_{\nu,\mathrm{opt}} \propto (\nu_p L_{\nu_p}) \nu_p^{-4/3}$: this luminosity must be constant before and after the correction with the factor α therefore it is possible to write $(\nu_p L_{\nu_p}) \nu_p^{-4/3} \sim (\nu_{p,\alpha} L_{\nu_{p,\alpha}}) \nu_{p,\alpha}^{-4/3}$. From this latter, the expression $\nu_{p,\alpha} L_{\nu_{p,\alpha}} \sim \nu_p L_{\nu_p} / \alpha$ leads to $\nu_{p,\alpha} \sim \nu_p \alpha^{-3/4}$.

of the disk inner emission when this latter is cut at a certain distance from the SMBH: using the relativistic AD model described by Novikov and Thorne, 1973, as an example, I considered the case with a non-spinning BH where the disk inner boundary is set to $20R_g$ (where R_g is the gravitational radius), similar to the Corona size adopted by Kubota and Done, 2018; I found that the disk peak frequency and luminosity are reduced by a factor of $\sim$ 0.14 and $\sim$ 0.17 dex, respectively; such corrections can be found for $\alpha \sim 0.7$. From Eq. 3.11, the corrected mass is smaller by factor $\sim \alpha$.

- Assuming that the Corona scatters $<$ 30% (i.e. $\alpha \sim 0.7$) of the disk radiation (e.g., Sazonov et al., 2012; Lusso and Risaliti, 2017), the BH mass is reduced by a factor $<$ 0.15 dex. I found that, for MRK509, a correction with $\alpha \sim 0.7$ is needed to make KERRBB results compatible with those found with AGNSED, while for NGC5548, no correction is necessary because the results of both models are already compatible (see Fig. B.30).

The partial compatibility between KERRBB and AGNSED shows that BH masses estimated through the SED fitting procedure clearly depend on the adopted model and their physical background. Nonetheless, despite the rather good results obtained with the α correction, caution is suggested about these findings since additional uncertainties (e.g. Corona geometry and size) could play an important role in estimating BH masses. However, KERRBB results for both sources are still compatible with SE and RM ones within uncertainties (Fig. 4.17) and, moreover, results presented by Kubota and Done, 2018 are compatible with those inferred with KERRBB for what concerns the BH spin: taking their finding for the BH masses as reference values, both the results obtained with the two models favor low values of a.

4.4 Conclusions

Despite the large uncertainties involved in the fitting procedure (i.e., dust absorption, IGM absorption, X-ray Corona) and RM (or SE) measurements (i.e., BLR geometry, geometrical factor f_{BLR}), KERRBB showed a good agreement with data (in all the works presented here - Sects. 4.1-4.2-4.3), strengthening the choice of AD models as an alternative method both to described the observed SEDs and to infer the mass of SMBHs.

For what concerns these latter arguments, the choice of the AD model is crucial even though similar results can be found by using different models (Sect. 4.3). Nonetheless, although few attempts are discussed in previous Sections, the uncertainties involved in these kinds of measurements ($\sim 0.4 - 0.5$ dex for RM and SE) are still too large to have precise information on the BH accretion and spin from the comparison between different methods (see Sect. 3.2.3).

Similarly, the evolution of SMBH though time can be studied only in a general way given the uncertainties connected to the radiative efficiency η and the modality of accretion (i.e., disk-like accretion, chaotic accretion, mergings - Sect. 4.2). Future works on a large sample of AGNs with RM measurements and new discoveries of sources at $z > 7$ could shed light on the possible mass, Eddington ratio and spin distributions, and give stronger constraints on the probable BH growth.

Chapter 5

Disk - torus connection in AGNs

"Innovation is the ability to see change as an opportunity - not a threat"
— Steve Jobs

Contents

The unification paradigm for AGNs assumes the presence of dust surrounding the nuclear regions, causing the apparent differences in the observed broad lines emission as well as X-ray properties (e.g., Antonucci, 1993; Ghisellini, Haardt, and Matt, 1994; Urry and Padovani, 1995).

This dusty and optically thick material would partly "cover" the AD, its X-ray Corona and the BLR surrounding the central SMBH, absorbing a fraction of the total Optical - UV disk luminosity and re-emitting it in the IR band (e.g., Rees et al., 1969; Neugebauer et al., 1979; Barvainis, 1987).

The properties and the geometrical configuration of the dust are still unclear. Several models have been proposed: a smooth/continuous toroidal dust distribution (**torus**) was firstly proposed (e.g., Pier and Krolik, 1993; Granato and Danese, 1994; Schartmann et al., 2005; Fritz, Franceschini, and Hatziminaoglou, 2006); as it was pointed out that such a structure could be unstable, a clumpy distribution was suggested (e.g., Krolik and Begelman, 1988; Tacconi et al., 1994; Nenkova et al., 2008a; Nenkova et al., 2008b; Hönig and Kishimoto, 2010), also supported by observations (e.g., Risaliti, Elvis, and Nicastro, 2002; Jaffe et al., 2004; Tristram et al., 2007; Zhao et al., 2020).

The features of the torus have been recently studied using large samples of AGNs (e.g., Calderone, Sbarrato, and Ghisellini, 2012; Ma and Wang, 2013; Hao et al., 2013; Merloni et al., 2014). One of the simplest approaches to study the geometry of the dust distribution is to consider its *covering factor*, i.e. the fraction of sky covered by the torus as seen from the SMBH. This has been estimated from 1) the numerical ratio of Type 1 vs. Type 2 AGNs, in carefully (unbiased) selected samples (e.g., Lawrence and Elvis, 1982; Lawrence, 1991; Simpson, 2005), 2) detailed physical models of the torus emission (e.g., Ezhikode et al., 2017; Zhuang, Ho, and Shangguan, 2018), 3) the ratio between the bolometric IR and AD luminosities as inferred from SED (e.g., Hatziminaoglou et al., 2008; Alonso-Herrero et al., 2011; Calderone, Sbarrato, and Ghisellini, 2012; Castignani and Zotti, 2015).

More specifically, Calderone, Sbarrato, and Ghisellini, 2012 inferred information on the torus aperture angle θ_T (as measured from the disk normal) by comparing the ratio between the IR and the AD luminosities with that predicted for the AD angular emission pattern by the non-relativistic SS model (see Sect. 2.4). They used a sample of radio-quiet AGNs[1] and found that the torus reprocesses on average $\sim 1/3 - 1/2$ of the disk luminosity, corresponding to $\theta_T \sim 40° - 60°$. Gu, 2013 found a similar result for a sample of low redshift QSOs while, for high redshift ones, the author derived a higher covering factor (~ 1). Similar findings have been inferred by Castignani and Zotti, 2015 for a small sample of bright Flat Spectrum Radio QSOs. The procedure followed by Calderone, Sbarrato, and Ghisellini, 2012 to constrain θ_T assumes a simple $\cos\theta$ radiation pattern for the AD (as expected for the SS model): this is possibly too simplistic since both the relativistic effects and the BH spin modify the radiation pattern, especially in the inner region of the disk, where most of the radiation is produced.

[1]The authors selected a sample of radio-quiet AGNs from the SDSS catalog (York et al., 2000; Schneider et al., 2010; Shen et al., 2011) with redshift in the range $0.56 - 0.73$.

In this Chapter, I will discuss the possibility to infer information on the torus geometry (i.e., its covering factor/aperture angle), and possibly to constrain the BH spin, by comparing the ratio between the torus and disk luminosities, inferred from SEDs, with the predictions for a thin AD around a Kerr BH, as described by the KERRBB model. For this purpose, I considered a sample of Type 1 AGNs selected from the SDSS catalog.[2]

The key point of the work is that, for large spin values, relativistic effects (mostly light-bending) lead to larger AD luminosities at larger viewing angles with respect to the non-relativistic SS case (see e.g., Campitiello et al., 2018; Ishibashi, Fabian, and Reynolds, 2019; see also Sect. 3.2.1). For this reason, the surrounding dusty torus could absorb a higher fraction of the total disk luminosity for a highly spinning BH. The distribution of the ratios between the IR (torus) and the Optical - UV (AD) observed luminosities could provide statistical constraints on the average torus covering factor and possibly on BH spins.[3]

The adopted cosmology is a flat ΛCDM cosmology with rounded parameters $H_0 = 67.4$ km/s/Mpc and $\Omega_M = 0.32$ (Planck Collaboration, 2018).

5.1 Notation and disk radiation pattern

As also discussed in Sect. 2.4 and 3.2, the AD emission is usually described with a small set of observational parameters defined under very general assumptions. The observed disk luminosity L_d^{obs} is a quantity derived from the observed flux integrated over the frequency range in which an AD emits its radiation (i.e., in the Optical-UV bands), i.e. $L_d^{obs} = 4\pi d_L^2 \int F_\nu d\nu$ (where d_L is the luminosity distance and F_ν is the flux density). As noticed in Sect. 2.4, this quantity must not be confused with the bolometric luminosity L_{bol}, normally used in spectroscopic studies (e.g. Shen et al., 2011) to estimate the accretion power output from the monochromatic luminosity at a specific wavelength, using a bolometric correction.

For both the non-relativistic SS model and the relativistic one KERRBB, the AD is not emitting isotropically and the observed flux (and hence L_d^{obs}) strongly depends on the viewing angle θ_v (measured from the disk normal; see Sect. 2.4 and 3.2): this dependence is described by a general function $f(\theta_v, a)$ such that $L_d^{obs} = f(\theta_v, a) L_d(a)$. For a non-relativistic optically thick

[2] The paper has been submitted to A&A, Campitiello et al., 2021.

[3] For this work,I adopted the same fixed parameters reported in Chap. 3.2, i.e. hardening factor $f_{col} = 1$, the inclusion of the returning radiation, no inner torque, and no limb-darkening effect.

and geometrically thin disk described by the SS model, $f(\theta_v) = 2\cos\theta_v$ (corresponding to the Newtonian case; see Sect. 2.4) while for KERRBB $f(\theta_v, a)$ is more complicated since it depends also on the BH spin (Sect. 3.2).

As previously noticed, in the $\nu - \nu L_\nu$ representation, L_d^{obs} can be inferred directly from the spectral UV peak luminosity $\nu_p L_{\nu_p}$ that can be constrained with a disk model: for both the non-relativistic SS model (see Calderone et al., 2013) and the relativistic model KERRBB (see Campitiello et al., 2018), the spectral shape is almost invariant for different combinations of the parameters (i.e., M, $\dot{M}$, a, θ_v) and a good approximation is $L_d^{obs} \sim 2\nu_p L_{\nu_p}$.

The torus intercepts part of the disk radiation depending on its aperture angle θ_T: the *total torus luminosity* L_T depends on θ_T and the BH spin a. Assuming a real toroidal structure, $\theta_T \geq \theta_v$ in order to see the AD. Therefore, this quantity can be defined as:

$$L_T(\theta_T, a) = L_d(a) \underbrace{\int_{\theta_T}^{\pi/2} f(\theta, a) \sin\theta d\theta}_{=\mathcal{I}(\theta_T, a)} \tag{5.1}$$

The integral $\mathcal{I}(\theta_T, a)$ represents the fraction of the total disk luminosity absorbed and re-processed by the torus: for the SS model $\mathcal{I}(\theta_T) = \cos^2\theta_T$ since there is no dependence on a, while for KERRBB the integral must be solved numerically given its dependence on the BH spin. For simplicity, the torus luminosity is assumed to be emitted isotropically thus, the *observed torus luminosity* L_T^{obs} is equivalent to Eq. 5.1.

The crucial quantity that will be investigated in this Chapter is the observed *luminosity ratio* R_{obs}, defined as the ratio between the observed luminosities (inferred from the SED):

$$R_{obs} = \frac{L_T^{obs}}{L_d^{obs}} = \frac{L_T}{L_d^{obs}} = \frac{L_d \mathcal{I}(\theta_T, a)}{L_d\, f(\theta_v, a)} = \begin{cases} \dfrac{\cos^2\theta_T}{2\cos\theta_v} & \text{(SS)} \\ \\ \dfrac{\mathcal{I}(\theta_T, a)}{f(\theta_v, a)} & \text{(KERRBB)} \end{cases} \tag{5.2}$$

Since the IR luminosity is reprocessed radiation produced by the disk, it is expected that $R_{obs} < 1$ always. For the SS case with $\theta_v = 0°$, we have $L_d^{obs} = 2L_d$ therefore the maximum value for R_{obs} is 0.5, corresponding to a torus covering the disk completely (i.e., $\theta_T = 0°$). Instead, the behavior in the KERRBB case is strikingly different: for high spin values ($a > 0.8$), relativistic effects modify the emitted radiation angular pattern significantly,

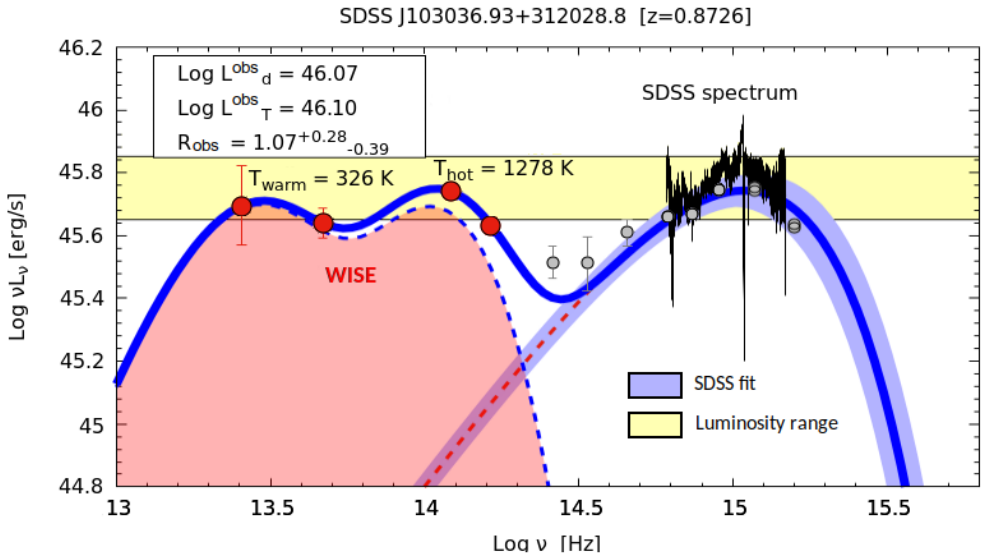

FIGURE 5.1: Example of SED modeling. The continuum of the SDSS spectrum (black line) is described with the relativistic AD model KERRBB (dashed red line) while the torus emission is constrained by using the 4 WISE data (red dots) and two blackbodies (dashed blue line contour) plotted along with the corresponding temperatures. The thick blue line is the overall model (disk + torus). In the plot, I report the observed disk and torus luminosities (in erg/s) and the luminosity ratio $R_{\rm obs}$. Some archival photometric data (2MASS, NED, GALEX - grey dots) are added to the plot. The shaded yellow area is the luminosity range in which $\nu_{\rm p} L_{\nu_{\rm p}}$ lies, obtained by taking into account different uncertainties. For details about the fitting procedure, the uncertainties and the constraints on the $\theta_{\rm T}$ and a, see Sect. 5.3 - 5.4.

more radiation is emitted close to the equatorial plane and less along the disk normal; this makes the torus receive a larger fraction of $L_{\rm d}$ (Fig. 3.3). As an example, Fig. 5.1 shows the IR-to-UV SED modeling on one of the sources analyzed in my work (for details about the fit and the uncertainties, see Sect. 5.3 and 5.4): the observed ratio is $R_{\rm obs} \sim 1.07$ which, for $\theta_{\rm v} = 0°$ and $\theta_{\rm T} = 20°$, corresponds to a maximally spinning BH ($a = 0.9982$).

Figure 5.2 shows the luminosity ratio as a function of the BH spin, for different torus aperture angles (with fixed $\theta_{\rm v} = 30°$): it is easy to notice that the constraints on the BH spin become tighter for large luminosity ratios while, for small values, constraints can be set only for the torus aperture angle. As an examples: a ratio $R_{\rm obs} = 0.6$, can be associated only to aperture angles $< 60°$ since that, for larger angles, the maximum value of $R_{\rm obs}$ is always < 0.6. Instead, a ratio $R_{\rm obs} = 0.8$ can be associated to BH spins $a > 0.95$ (for $\theta_{\rm T} = 30°$) and to $a \sim 0.9982$ (for $\theta_{\rm T} = 45°$). Therefore, in general, the constraints on the BH spin become tighter for larger luminosity ratios while, for small values, constraints can be set only for the torus aperture angle (see Appendix C).

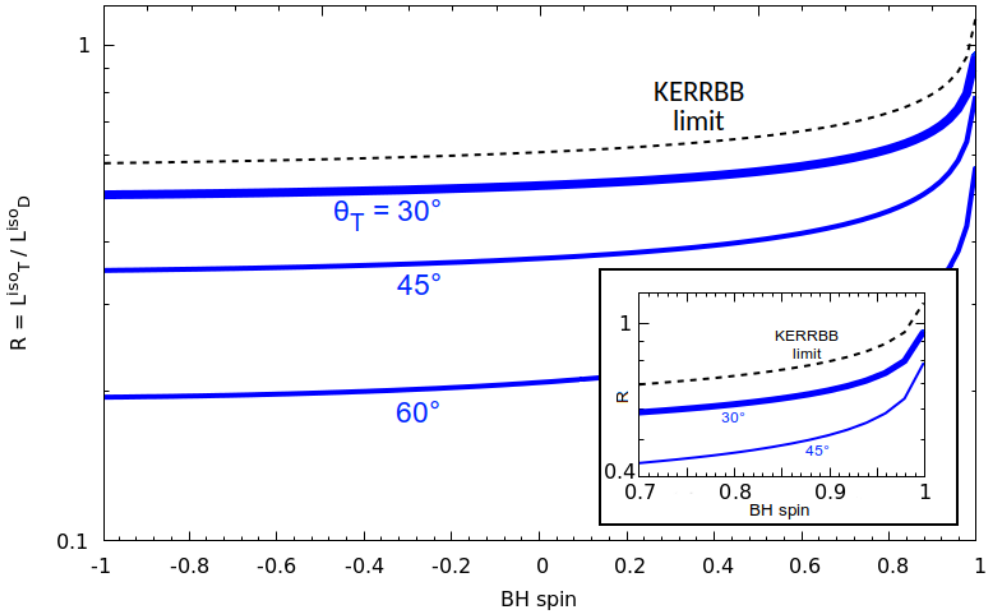

FIGURE 5.2: Luminosity ratio R_{obs} as a function of the BH spin, for different torus aperture angles ($\theta_T = 30° - 45° - 60°$) and $\theta_v = 30°$ (no solution is shown for $\theta_T < \theta_v$; see text). The dashed black line is the KERRBB limit ($\theta_v = \theta_T = 0°$). In the SS case, the ratios (not shown for clarity) are $R_{obs} = 0.43 - 0.29 - 0.14$, respectively. The small plot is the zoom-in of the $a > 0.7$ region.

Close-to-Eddington accretion emission

The strength of the disk radiation is often associated with the Eddington ratio λ_{Edd}: for the non-relativistic SS model, for a fixed viewing angle, M and $\dot{M}$ (and thus L_d and λ_{Edd}) are uniquely found by knowing the spectral peak frequency ν_p and luminosity $\nu_p L_{\nu_p}$ (in a $\nu - \nu L_\nu$ representation; see Sect. 2.6). For KERRBB, the dependence of the spectrum peak position from the BH spin induces a degeneracy in the estimate of M and $\dot{M}$ and thus also the total disk luminosity and the Eddington ratio (see Sect. 3.2.3).

Regarding λ_{Edd}, it is important to mark the fact that for large values ($\lambda_{Edd} > 0.3$), the thin disk approximation implemented in KERRBB is not physically correct (see Sect. 3.3). As shown in Sect. 3.4.1 with the relativistic slim AD model SLIMBH, it is possible to find an expression linking the observed disk luminosity (in the slim regime) to L_d, and thus an expression for L_T and R_{obs}: since the radiation angular pattern shape is similar to the one found for KERRBB (for different a and λ_{Edd}; see Figs. 3.10-3.11), the theoretical values of R_{obs} differ from those found with KERRBB by a factor $< 5\%$ for all angles, spins and Eddington ratios (in the range $0.01 < \lambda_{Edd} < 1$). For this reason, KERRBB was chosen for the next analyses to derive the constraints on the physical parameters.

5.2 The sample

To build a suitable sample, I considered the SDSS catalog (containing 105,783 QSOs) whose continuum and line luminosities have been estimated by Shen et al., 2011. The most prominent emission lines have a Full Width at Half Maximum FWHM > 1000 km/s therefore all QSOs can be classified as Type 1 (e.g., Antonucci, 1993). All spectra are obtained in the observed wavelength range $3800 - 9200$Å. The sample was defined by adopting the following selection criteria:

- The sources must have a measured rest-frame monochromatic luminosity, both at 3000Å and at 5100Å, to estimate the continuum slope. As the AD emission is identified with the BBB, sources with no evidence for it are excluded, by requiring that the spectral slope is positive (in the $\nu - \nu L_\nu$ representation). Given the limited wavelength coverage of the SDSS spectrum, all the selected sources have a redshift in the range $0.35 < z < 0.89$. This criterium set a lower limit for the spectrum peak frequency, Log $\nu_{\rm p}$/Hz > 14.9: sources hosting very massive BHs are possibly neglected. [4]

- A further criterium was imposed to minimize the host galaxy contamination in the FIR - Optical bands. Following Shen et al., 2011, only sources with a SDSS bolometric luminosity $L_{\rm bol} > 10^{46}$ erg/s were selected: for those sources, the SDSS monochromatic luminosity at 5100Å is Log L_{5100}/erg/s > 45 and it is contaminated by the galactic emission by a factor $< 5\%$. At smaller wavelengths, the contamination is negligible. In this way, we reduced the number of components in the fitting procedure by neglecting the contribution of the host galaxy.

- To estimate the dust reprocessed emission in the IR band, the previously selected sources were cross-correlated with the Wide-field Infrared Survey Explorer (WISE; Wright et al., 2010) catalog, selecting only those with a detection in all of the four WISE IR bands (3.4, 4.6, 12 and 22 μm), which have an average flux uncertainty of ~ 0.05 dex.

[4] The average BH mass computed with KERRBB for the whole sample is Log $M/M_\odot = 9.00 \pm 0.20$ and the lower limit for the peak frequency (Log $\nu_{\rm p}$/Hz > 14.9) led to neglect sources with a mass Log $M/M_\odot > 9.5$.

- Finally, to avoid possible contamination of the IR and UV bands from the Synchrotron emission, the cross-correlation between the SDSS catalog and the Faint Images of the Radio Sky at Twenty-centimeter survey (FIRST; Becker, White, and Helfand, 1995) reported by Shen et al., 2011, led to the selection of only radio-quiet sources: following the definition of radio-loudness $\mathcal{R}$ adopted by Shen et al., 2011, only sources with $\mathcal{R} < 10$ (e.g., Kellermann et al., 1989) were selected, including also those observed by FIRST but without a detectable radio flux, still classified as radio-quiet.[5]

The resulting final sample comprises 2922 sources. A further selection criterium will be applied in the next Section to select only sources with a good fit of the SDSS spectrum.

5.3 Accretion disk

Here I will describe the fitting processes adopted to infer $L_{\rm d}^{\rm obs}$ and discuss the possible sources of uncertainty. It is important to stress that the fitting procedure aims only at the determination of $L_{\rm d}^{\rm obs}$ and not to constrain the source physical parameters.

5.3.1 Emission

The AD emission is identified with the BBB component in the Optical-UV band. Given that all sources are Type 1 QSOs, it is assumed that the observed disk luminosity $L_{\rm d}^{\rm obs}$ is free from absorption by the torus. The AGN continuum is modeled by fitting the SDSS spectrum with KERRBB: using the fact that, for different parameters combinations, the KERRBB spectral shape is almost invariant (see Sect. 3.2; Campitiello et al., 2018), the fit is performed using GNUPLOT, using the curvature of the SDSS spectrum to constrain the peak frequency $\nu_{\rm p}$ and luminosity $\nu_{\rm p} L_{\nu_{\rm p}}$ (and thus $L_{\rm d}^{\rm obs}$) even if the peak is not covered by the SDSS data. In the fitting procedure, emission/absorption lines are not included (because those spectral features have no drastic effects on the overall KERRBB fit - e.g. Campitiello et al., 2020; see Sect. 4.3) along with possible available photometric data because they could be contaminated by some emission or absorption lines.

[5] The flux limit of FIRST is ~ 1 mJy at 1.4 GHz (Becker, White, and Helfand, 1995).

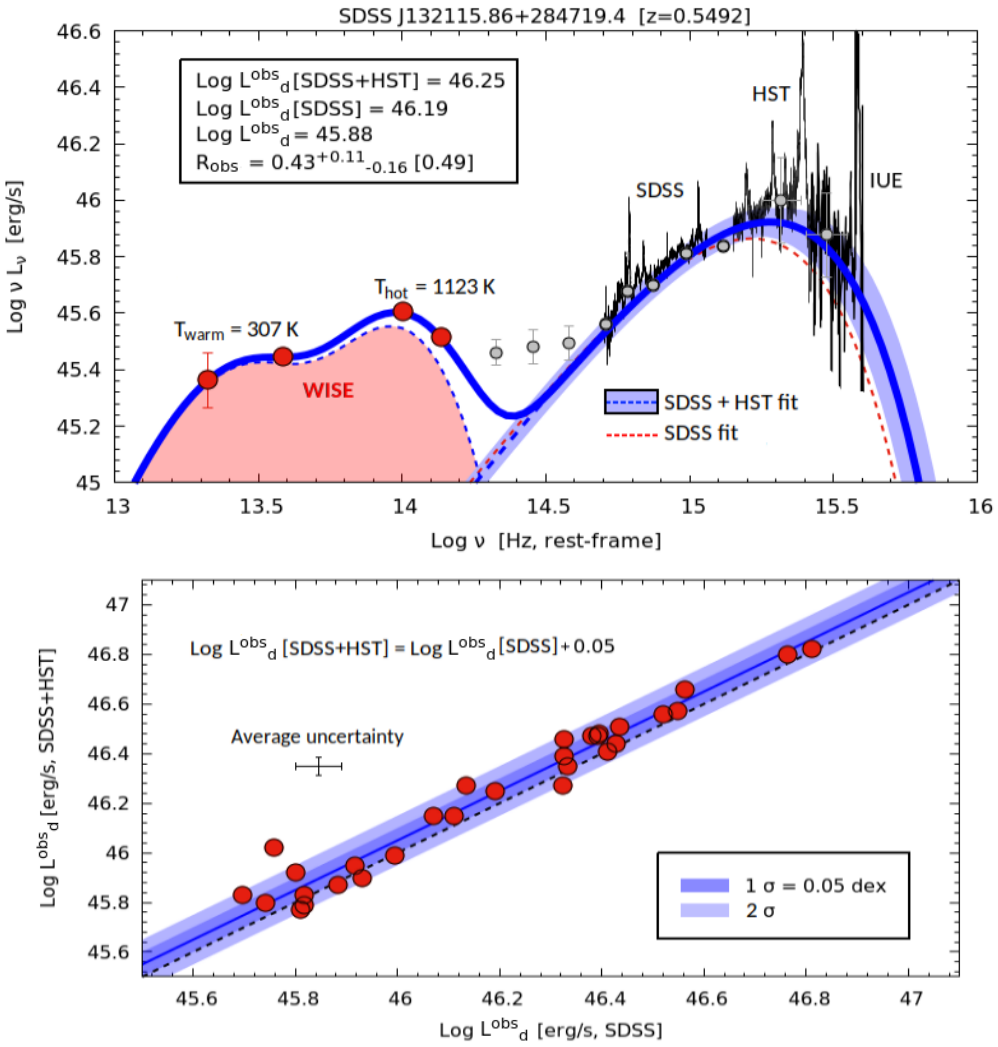

FIGURE 5.3: Top panel: example of fit of the composite SDSS+HST+IUE spectrum (black lines) for one of the sources of the SDSS+HST sample. The disk emission is modeled with KERRBB (dashed blue line), compared with the fit performed only with the SDSS spectrum (dashed red line). The shaded blue area is a confidence interval of ~ 0.05 dex on the spectrum peak. The luminosities inferred from both the fits are reported on the plot (in erg/s) along with the luminosity ratio $R_{\rm obs}$ (the value computed by considering only the SDSS spectrum is reported within brackets). The fit of the 4 WISE data (red dots) is performed with two black-bodies (shaded red area with a dashed line contour) plotted along with the corresponding temperatures. The thick blue line is the overall model (disk + torus). Some archival photometric data (2MASS, NED, GALEX - grey dots) are added to the plot (not used in the fitting process). Bottom panel: comparison between the observed disk luminosities computed from the fit of the SDSS spectrum alone and those computed using also HST data. The average uncertainty from the fit is shown in the plot. The best fit relation (blue line) is reported on the plot along with the 1-2 σ data dispersion (shown with shaded blue areas) and the 1:1 line (dashed black line).

The SDSS spectrum shows a superimposed minor component named "Small Blue Bump" (from Log $\nu/\mathrm{Hz} = 14.9 - 15.1$, rest-frame), caused by the blending of several Iron lines and the Hydrogen Balmer continuum (Wills, Netzer, and Wills, 1985; Berk et al., 2001b), which does not affect the localization of the spectrum peak: even though the SDSS spectral coverage is limited, the curvature of the available spectrum can still be used to constrain the peak (in the frequency range Log $\nu_{\mathrm{p}}/\mathrm{Hz} \sim 15 - 15.5$, rest-frame).

For the analyses performed in the next Sections, only the sources with the best peak position estimation are chosen: for some objects, the SDSS curvature does not constrain the spectral peak precisely and the uncertainty on ν_{p} and $\nu_{\mathrm{p}} L_{\nu_{\mathrm{p}}}$ is > 0.1 dex. Only those sources with an uncertainty on both ν_{p} and $\nu_{\mathrm{p}} L_{\nu_{\mathrm{p}}}$ less than ~ 0.05 dex were selected (corresponding to average residuals less than ~ 0.05 dex with a reduced-$\chi^2 < 0.02$): this criterium reduces the initial sample to 1858 sources (hereafter "*SDSS sample*").

SDSS+HST sample: peak uncertainty

Given its limited spectral coverage, the fit of the SDSS spectrum could lead to a wrong estimate of the spectrum peak. To assess to which degree the spectral curvature at lower frequencies provides significant constraints on ν_{p} and $\nu_{\mathrm{p}} L_{\nu_{\mathrm{p}}}$ (and so on $L_{\mathrm{d}}^{\mathrm{obs}}$), the sample was cross-matched with the Hubble Space Telescope (HST) catalog and a sub-sample of 30 objects (hereafter, "*SDSS+HST sample*") was built with UV spectroscopic data for a wider wavelength range (Log $\nu/\mathrm{Hz} = 14.7 - 15.6$, rest-frame). Also, data from the Far Ultraviolet Spectroscopic Explorer (FUSE) for 5 sources and the International Ultraviolet Explorer (IUE) for 2 sources were found and added.[6] All spectroscopic data were corrected from Galactic extinction using the Cardelli, Clayton, and Mathis, 1989 reddening law and $E_{\mathrm{B-V}}$ from the map of Schlegel, Finkbeiner, and Davis, 1998 with an extinction factor $R_{\mathrm{V}} = 3.1$. When possible, the non-simultaneous spectra were calibrated by matching the flux in their common wavelength ranges, assuming that the spectral shape does not change during flux variations (the maximum flux mismatch found amounts to ~ 0.07 dex).

From the fit of the SDSS+HST sample sources, it was found that $\nu_{\mathrm{p}} L_{\nu_{\mathrm{p}}}$ is on average higher by a factor of ~ 0.05 dex with respect to the one obtained from the fit of the SDSS spectrum alone (Fig. 5.3). Since spectroscopic data in the FUV band were used in the fitting procedure, the results might be

[6] All spectroscopic data were retrieved from the online Mikulski Archive for Space Telescopes (MAST).

affected by the presence of blended interstellar absorption features (at Log $\nu/\mathrm{Hz} > 15.4$) which could reduce the AGN continuum flux: to quantify this effect, the same fitting procedure was performed using only spectroscopic data at Log $\nu/\mathrm{Hz} < 15.4$ (assuming that this frequency range is free from absorption) and found that the new values of $\nu_{\mathrm{p}} L_{\nu_{\mathrm{p}}}$ are consistent with the previous estimates within an interval < 0.05 dex. These values were considered as typical uncertainties for the SDSS sample.

It is crucial to mark that, in this Section, the choices regarding the disk viewing angle or the BH spin are irrelevant since $L_{\mathrm{d}}^{\mathrm{obs}}$ is a mere measurement obtained from the observed SED. However, this argument will be important for the final results since the ratio R_{obs} depends on a and θ_{v} (Eq. 5.2).

5.3.2 Caveats

As also discussed in Chap. 4, some structures close to the AD as well as dust located along the line of sight can lead to incorrect estimates of $\nu_{\mathrm{p}} L_{\nu_{\mathrm{p}}}$ and $L_{\mathrm{d}}^{\mathrm{obs}}$. Here I discuss the main possible sources of uncertainty in order to define a confidence interval for the observed ratio R_{obs}.

- *Dust and Intrinsic absorption*: to estimate the effects of dust absorption, I followed the procedure detailed in Campitiello et al., 2020 (see Chap. 4). For the redshift range spanned by the SDSS sample, the UV attenuation due to the IGM is negligible (see Madau, 1995; Haardt and Madau, 2012; see also Castignani et al., 2013). For what concerns the host galaxy ISM, following Baron et al., 2016, I found that $\sim$ 80% of the sources shows an extinction $E_{[\mathrm{B-V}]} < 0.05$ mag (the average value is ~ 0.03 mag), computed by using the SDSS spectral slope and consistent with what is thought to be the value for Type 1 AGNs ($E_{[\mathrm{B-V}]} < 0.1$ mag; e.g., Koratkar and Blaes, 1999). Consequently, the extinction corrected AD luminosities would be larger (on average) by a factor < 0.1 dex. Given the uncertainties involved in this procedure and since possible changes in the UV slope could be caused by other factors connected to the BH physics (i.e., mass, accretion rate, spin; see e.g., Hubeny et al., 2000; Davis and Laor, 2011), no dust correction was adopted.

- *Broad Line Region*: assumed to have a disk-like structure (see the results for the sources 3C273 and IRAS 09149-6206; Sturm et al., 2018; Amorim et al., 2020), intercepts part of the AD radiation ($< 15\%$; e.g., Baldwin and Netzer, 1978) and re-emits it in form of emission lines. Since the BLR is located at $\sim 10 - 100$ light days from the SMBH (from RM

studies by e.g., Kaspi et al., 2000; Peterson et al., 2004), $L_{\rm d}^{\rm obs}$ (produced mostly by the inner region) is unaffected by its presence. However, a fraction of its radiation can be intercepted by the torus depending on its aperture angle $\theta_{\rm T}$: as shown in Appendix C.2, under the simplified assumption that the BLR emits its radiation isotropically, I found that its presence modifies $L_{\rm T}^{\rm obs}$ and the ratio $R_{\rm obs}$ by a factor < 0.05 dex.

- *X-ray Corona*: this structure up-scatters part of the AD radiation in the X band, resulting in a smaller observed $L_{\rm d}^{\rm obs}$ with respect to the intrinsic one (see Sect. 3.4.2 and Chap. 4). Following the work of Duras et al., 2020 (see also Vasudevan and Fabian, 2009; Lusso, Comastri, Simmons, et al., 2012), the authors found that for sources with a bolometric luminosity $L_{\rm bol} > 10^{46}$ erg/s, the X luminosity is $L_{\rm X} < 0.1 L_{\rm bol}$: assuming that the bolometric luminosity is $L_{\rm bol} \sim 2 L_{\rm d}^{\rm obs}$ (as found by Calderone et al., 2013), the X luminosity is $L_{\rm X} < 0.2 L_{\rm d}^{\rm obs}$ on average. If this latter fraction (< 0.2) corresponds to the fraction of disk radiation up-scattered by the Corona in the X band, the intrinsic $L_{\rm d}^{\rm obs}$ would be larger at most by a factor ~ 0.08 dex. Such modifications of $L_{\rm d}^{\rm obs}$ and $R_{\rm obs}$ can be considered as average upper limits. To quantify the real effect of the X-ray Corona on the UV emission, sophisticated broad-band models has to be used (e.g., AGNSED; see Sect. 3.4.2). For the sample analyzed here, all sources have a limited data coverage which cannot allow to use those models appropriately; moreover, simultaneous data are necessary to perform a proper parameter estimation.

- *Variability*: disk flux changes could modify both $L_{\rm d}^{\rm obs}$ and $L_{\rm T}^{\rm obs}$ given that this latter is proportional to the disk luminosity. In this context, the time-lag between the AD and the torus is important: for bright sources ($L_{\rm bol} > 10^{46}$ erg/s), the sublimation radius of the torus is located at a few parsecs from the SMBH (e.g., Barvainis, 1987) therefore IR flux variations are expected to occur after a few years after the disk ones (e.g., Lyu, Rieke, and Smith, 2019). For this reason, in variable sources and in short time intervals, only the disk luminosity can be observed to change while the torus one remains constant. Assuming a flux variability of 0.1 dex, the disk luminosity would change by the same amount. However, from a statistical point of view, only a few sources are expected to vary by a significant amount and in large samples, this effect can be negligible. Therefore, in this work, I did not consider any disk variability.

5.4 Torus

In this Section, I will describe the assumptions and the procedure adopted to estimate the observed torus luminosity $L_{\rm T}^{\rm obs}$ and quantify the involved uncertainties.

5.4.1 Emission

The torus emission is estimated based on the following simple assumptions: a) the dust is distributed with a symmetric, equatorial structure with an aperture angle $\theta_{\rm T} \geq \theta_{\rm v}$ (for the disk to be visible), b) the disk radiation intercepted by the torus is re-processed and totally re-emitted isotropically (see Sect. 5.1), c) the torus is assumed to have a continuous dust distribution even though the possible clumpiness (confirmed by observations) could affect the observed torus flux (which results in an anisotropic emission as also shown by several numerical models; see e.g., Nenkova et al., 2008a; Nenkova et al., 2008b). A discussion about the effects of an angle-dependent torus emission on the results is present in Sect., a discussion is present in the next Sect. 5.4.2.

The torus emission is estimated from the SED in the frequency range Log $\nu/{\rm Hz} \sim 13 - 14.5$ (rest-frame), as constrained by the 4 WISE data points. Given that only its luminosity is necessary for the next analysis, two simple independent black-body emissions were used to describe the torus SED, instead of sophisticated numerical models (e.g., CLUMPY, Nenkova et al., 2008a; Nenkova et al., 2008b; or CAT3D, Hönig and Kishimoto, 2010). In this procedure, an isotropic emission is assumed even though several numerical torus models show and angle and frequency-dependent IR emission (also depending on some dust parameters). Given that those models fail to describe the FIR emission (peaking at Log $\nu/{\rm Hz} \sim 14$),[7], in this statistical work, I adopted the simplest model(i.e., isotropic emission, two black-bodies).

The temperature of the two black-bodies is set to be $T < 2000$ K (i.e., dust sublimation temperature; see e.g., Hernán-Caballero et al., 2004; Calderone, Sbarrato, and Ghisellini, 2012; Collinson et al., 2016). Two components were used to be consistent with the scenario where dust is located at different distances from the SMBH: a hotter component originates from hot (graphite) dust close to the sublimation temperature and facing the disk (e.g., Barvainis, 1987; Gallagher et al., 2006; Mor, Netzer, and Elitzur, 2009) while a warm

[7] This peak probably originates from the hot dust closer to the SMBH, which is described with ad additional black-body (e.g, Deo et al., 2011; Mor and Netzer, 2012; Leipski, Meisenheimer, Walter, et al., 2014; Krogager, Geiser, Fynbo, et al., 2015; Zhuang, Ho, and Shangguan, 2018).

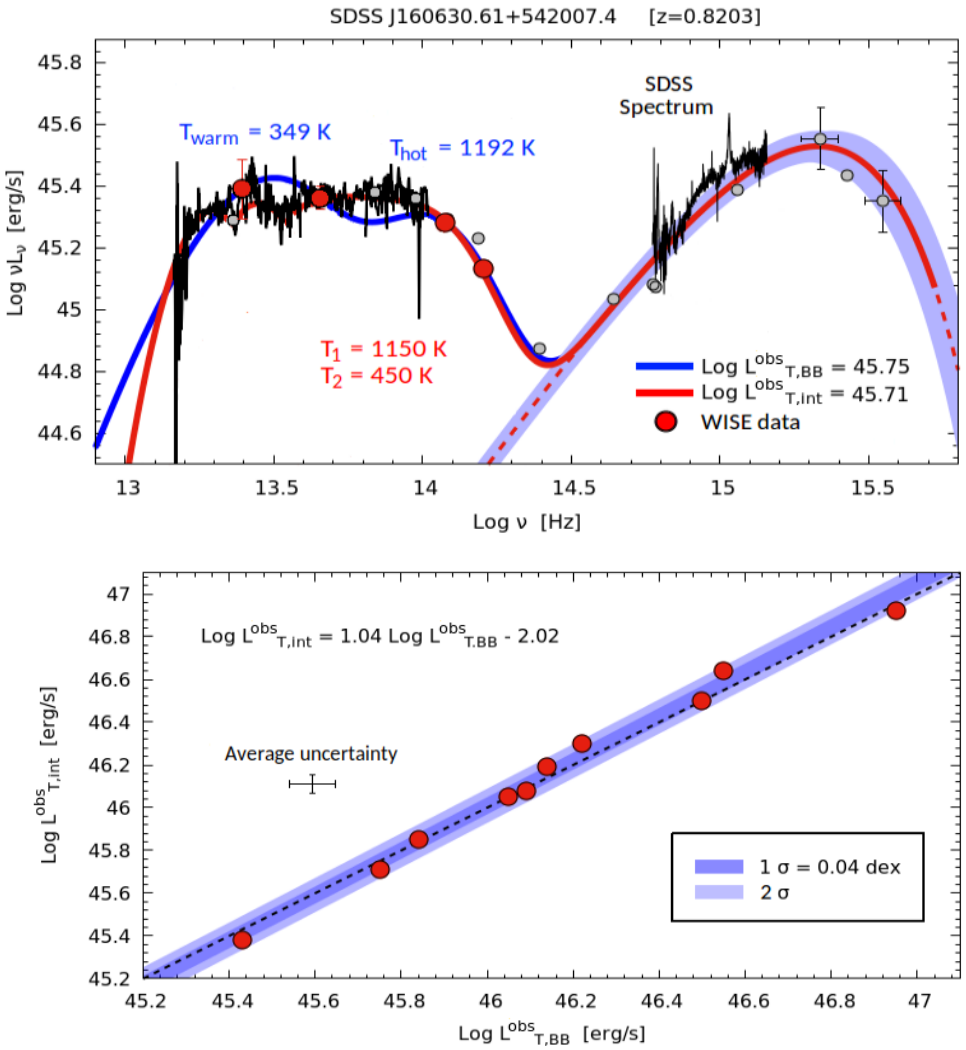

FIGURE 5.4: Top panel: example of fit of the SDSS Optical - UV and SPITZER IR spectra (black lines). The thick blue line is the fit performed with two black-bodies (whose temperatures, $T_{\rm warm}$ and $T_{\rm hot}$, are reported on the plot) using the 4 WISE data (red points) for the IR emission, and KERRBB for the disk emission (dashed red line with a shaded blue area, representing the confidence interval for the spectrum peak). The thick red line is the fit performed with two parabolas and two black-bodies (whose temperatures, T_1 and T_2, are reported on the plot; see text for details) to describe the SPITZER emission, and KERRBB for the disk emission. Both the integrate luminosities ($L^{\rm obs}_{\rm T,BB}$ and $L^{\rm obs}_{\rm T,int}$) are reported on the plot (in erg/s). Archival photometric data (2MASS, NED, GALEX) are shown with grey dots. Bottom panel: comparison between $L^{\rm obs}_{\rm T,BB}$ and $L^{\rm obs}_{\rm T,int}$ for the sources with SPITZER IR data. The average uncertainty from the fit is shown in the plot. The best-fit equation is reported along with the 1-2σ data dispersion (shaded blue areas) and the 1:1 line (dashed black line).

component from the outer region of the torus. This latter emission (characterized by a black-body temperature of $\sim 200 - 400$ K) does not correspond to the cold dust heated by stars (with a temperature < 100 K; e.g., Bendo et al., 2003; Boselli et al., 2010; Dale et al., 2012), located at larger distances from the disk and peaking around Log ν/Hz ~ 12.7 (e.g., Pearson, Eales, Dunne, et al., 2013; see also the next Section). Finally, $L_{\rm T}^{\rm obs}$ is obtained as the sum of the luminosities of those two frequency-integrated black-bodies.[8]

SPITZER test

To check the goodness of the two black-body approximation, I performed a further analysis by cross-matching the SDSS sample with the SPITZER catalog. I found 10 sources with IR spectroscopic data in the rest-frame frequency range Log ν/Hz $= 13 - 14$, compatible with the WISE photometric data. The SPITZER spectrum was described with two parabolas, one in the rest-frame range Log ν/Hz $\sim 13 - 13.4$ (describing the cold bump peaking at Log ν/Hz ~ 13.3), one in the rest-frame range Log ν/Hz $\sim 13.4 - 13.6$ (corresponding to the silicate emission peaking at Log ν/Hz ~ 13.5 - see e.g., Hönig and Kishimoto, 2010 and references therein), and two black-bodies in the range Log ν/Hz $\sim 13.6 - 14.5$. The choice of using a parabola-like emission instead of a black-body one was adopted in order to vary the width of the peak emission and perform a better fit of the SPITZER data in the range Log ν/Hz $\sim 13 - 13.4$. The colder black-body was used to have a better description of the spectrum in the range Log ν/Hz $\sim 13.5 - 14$. The SPITZER torus luminosity $L_{\rm T,int}^{\rm obs}$ is obtained by integrating all these components in the corresponding frequency ranges and summing up their contributions.

Figure 5.4 (top panel) shows an example of fit: the modeling with two black-bodies overestimates part of the IR luminosity at Log ν/Hz < 13.5 and underestimates it for Log ν/Hz $\sim 13.5 - 14$; on average, these two effects balance out resulting in a torus luminosity similar to the one computed by integrating the SPITZER spectrum. Figure 5.4 (bottom panel) shows the comparison between the two luminosities: although the sample is rather small, the best fit is consistent with the 1:1 line with a small 1σ data dispersion of ~ 0.04 dex.

[8] The mean temperatures of the hot and warm black-bodies are $T_{\rm hot} = 1277$ K and $T_{\rm warm} = 309$ K, similar to those found by other authors (e.g., Hernán-Caballero et al., 2004; Calderone, Sbarrato, and Ghisellini, 2012; Collinson et al., 2016). The two black-body luminosities are linked by the relation Log $L_{\rm T,warm}^{\rm obs} =$ Log$L_{\rm T,hot}^{\rm obs} + 0.11$, with a 1σ data dispersion of ~ 0.17 dex. If this relation holds for all sources, I derived Log $L_{\rm T}^{\rm obs} \approx$ Log$L_{\rm T,hot}^{\rm obs} + \beta$, with $\beta \sim 0.36$ and a dispersion of ~ 0.1 at 1σ.

5.4.2 IR contamination and torus anisotropy

Here I discuss the possible sources of contamination that could affect the estimates of $L_{\rm T}^{\rm obs}$ and so the value of the ratio $R_{\rm obs}$.

- *Galaxy emission*. A strong contamination of the torus luminosity is not expected from this emission due to the criterium adopted to build the SDSS sample (Sect. 5.2). However, the effects on $L_{\rm T}^{\rm obs}$ was quantified by using the galaxy template from Manucci et al., 2001: by requiring that L_{5100} is contaminated at most by a factor of $\sim 5\%$, I found that the host galaxy SED leads to a modification of $L_{\rm T}^{\rm obs}$ by a negligible factor (< 0.01 dex).

- *Cold dust emission*, related to dust heated by stars with an associated black-body temperature < 100 K (e.g., Bendo et al., 2003; Boselli et al., 2010; Dale et al., 2012), located at larger distances from the AD with respect to the torus. In principle, it could contaminate the cold part of the torus emission leading to an overestimation of $L_{\rm T}^{\rm obs}$. I used the SED of the starburst galaxy M82 (Kennicutt et al., 2003) to quantify its effect. Fig. 5.5 (top panel) shows the case in which the cold dust peak luminosity is chosen arbitrarily to be twice the AD one (as an extreme case). I subtracted its contribution to the WISE data flux, fitted the new data with two black-bodies and found that $L_{\rm T}^{\rm obs}$ is overestimated by a factor of ~ 0.1 dex, leading to a similar modification for the intrinsic $R_{\rm obs}$. A further test was conducted using the extinction law found by Calzetti et al., 2000 for a sample of local galaxies: the basic assumption is that the galaxy emission in the NIR - Optical bands is attenuated by the host galaxy cold dust; the amount of absorbed radiation is emitted in the FIR band as a modified black-body. Using the law found by Calzetti et al., 2000 (their Eqs. 2-3-4) with an intrinsic reddening $E_{[\rm B-V]} = 0.1$ mag leads to a cold dust emission in the FIR which has a negligible effect on the torus emission (< 0.01 dex). It is important to notice that those tests are generic analyses due to uncertainties related to modeling of the cold dust emission and the lack of data in the corresponding frequency range for almost the whole sample.

- *Polar dust*: recent works (e.g., Asmus, Hönig, and Gandhi, 2016; López-Gonzaga et al., 2016; Leftley et al., 2018; Lyu and Rieke, 2018) have

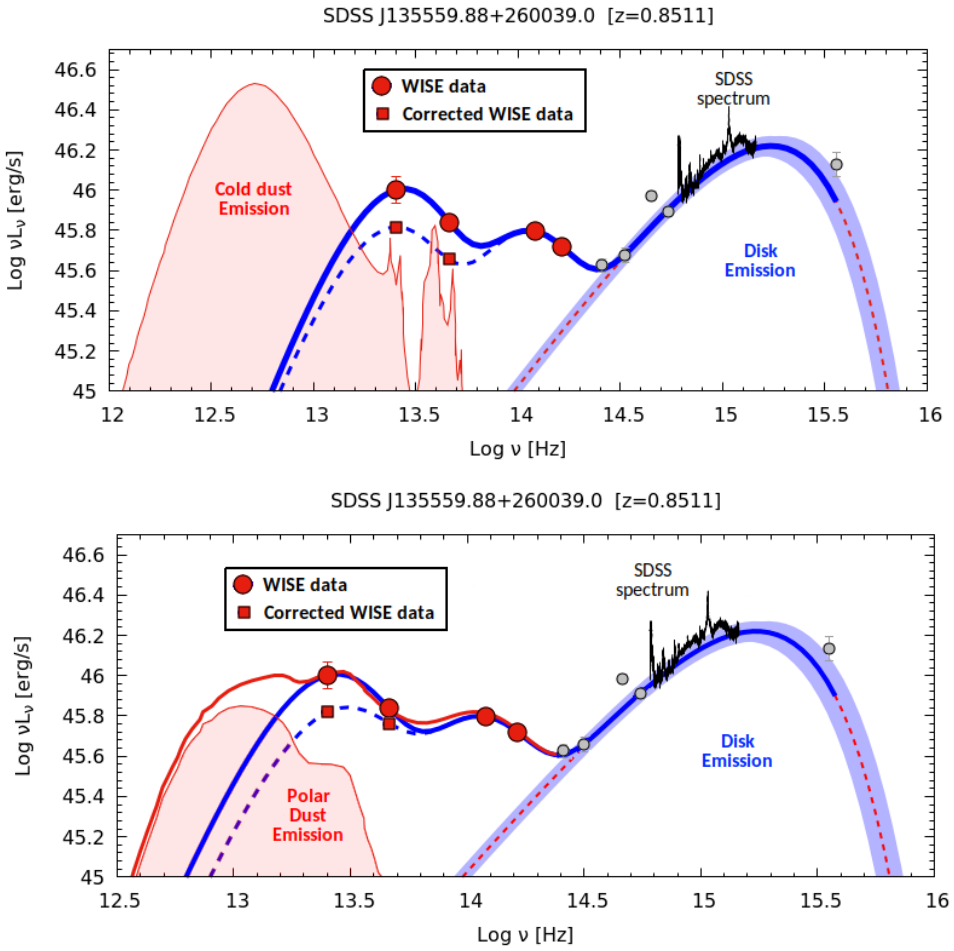

FIGURE 5.5: Example of flux correction from cold dust (top panel) and polar dust (bottom panel) of the WISE data, using the template of the starburst galaxy M82 (Kennicutt et al., 2003, red line, assuming a peak luminosity twice larger than the AD one) and the mean polar dust template as found by Lyu and Rieke, 2018 (assuming that its contribution to the MIR emission is $\sim$ 50%, as found by Asmus, Hönig, and Gandhi, 2016; Lyu and Rieke, 2018). In both plots, the AD emission is described by KERRBB (dashed red line). The thick blue line is the disk-torus model related to the uncorrected WISE data and the SDSS spectrum (black line). The dashed blue line is the new fit performed after the correction of the WISE data flux from the contamination. For the cold dust, the uncorrected and corrected luminosity ratios are $R_{\rm obs} = 0.55$ and $R_{\rm obs} = 0.44$, respectively; for the polar dust, $R_{\rm obs} = 0.55$ and $R_{\rm obs} = 0.39$, respectively: the presence of polar dust leads to a smaller ratio since it also modifies the disk luminosity (not shown on the plot; see text). Some archival photometric data (2MASS, NED, GALEX) are plotted with grey dots (not used in the fitting process).

shown that part of the MIR emission originates from polar regions instead of from an equatorial dusty torus with a characteristic dust temperature of $\sim$ 110 K (Lyu and Rieke, 2018). In this case, the disk luminosity would be partly absorbed, while the torus would produce less MIR radiation than observed. Assuming that half of the MIR emission (Log ν/Hz $\sim 13 - 13.5$) of all sources is due to the possible presence of polar dust (as found on average by Asmus, Hönig, and Gandhi, 2016), on average the intrinsic torus luminosity would be dimmer by a factor of $\sim$ 0.10 dex with respect to the observed one; moreover, if the polar dust luminosity comes from a reprocessed fraction of the disk luminosity, this latter would be brighter by a factor of $\sim$ 0.05 dex with respect to the observed one, leading to an overall modification of the ratio $R_{\rm obs}$ at most by a factor of $\sim$ 0.15 dex (Fig. 5.5, bottom panel).

- *Torus anisotropy*. Some numerical models show the dependence of the torus luminosity from $\theta_{\rm v}$ (e.g., Nenkova et al., 2008a; Hönig and Kishimoto, 2010; Stalevski et al., 2016), depending also on the dust distribution and its possible clumpiness, even though they cannot fit properly the IR bump peaking at Log ν/Hz $\sim$ 14. Castignani and Zotti, 2015 quantify the torus anisotropy though an analytical expression, using the numerical model CAT3D (Hönig and Kishimoto, 2010): their Eq.1 represents the angle-dependent flux density from which it is possible to find that the observed luminosity is larger by a factor $a + b\cos\theta_{\rm v}$ (where $a = 0.56$ and $b = 0.88$; see Appendix C.3) with respect to the intrinsic one. Assuming that the intrinsic torus luminosity is equal to $L_{\rm T}$ (i.e., the fraction of disk radiation absorbed by the torus; Eq. 5.1), the luminosity ratio (Eq. 5.2) becomes

$$R_{\rm obs} = \frac{L_{\rm T}^{\rm obs}}{L_{\rm d}^{\rm obs}} = \frac{\mathcal{I}(\theta_{\rm T}, a)(a + b\cos\theta_{\rm v})}{f(\theta_{\rm v}, a)} \tag{5.3}$$

Adopting this correction with $\theta_{\rm v} = 30^{\circ}$, the KERRBB curves plotted in Fig. 5.2 would be shifted towards larger values of $R_{\rm obs}$ by a factor of $\sim$ 1.3 ($\sim$ 0.11 dex). As already mentioned before, the approximation found by Castignani and Zotti, 2015 depends on the model CAT3D which cannot fit properly the IR bump at Log ν/Hz $\sim$ 14 therefore I did not considered this correction in the next Sections.

5.4.3 Luminosity ratio: total uncertainty

To define an average confidence interval for the main observables used in this work, I chose to neglect possible intrinsic dust absorption (see Sect. 5.3.2) and assuming no disk variability and an isotropic torus emission. Given that the estimations of all those previous sources of uncertainty (discussed in Sects. 5.3.2-5.4.2) are independent and uncorrelated, I defined a confidence interval for $L_{\rm d}^{\rm obs}$, $L_{\rm T}^{\rm obs}$ and $R_{\rm obs}$ by summing up in quadrature the uncertainties coming from the spectrum peak $\nu_{\rm p} L_{\nu_{\rm p}}$, the torus luminosity estimated from WISE data (taking into account the analysis performed with the SPITZER data), the effect of the X-ray Corona, the polar and cold star-heated dust on the IR and UV emissions, as discussed in the previous Sections. This procedure led to a confidence interval for the disk luminosity of $^{+0.10}_{-0.10}$ dex, and for the torus luminosity of $^{+0.05}_{-0.15}$ dex, resulting in a final average confidence interval for Log $R_{\rm obs}$ of $^{+0.10}_{-0.20}$ dex (corresponding to a 1σ uncertainty).

For illustration, Fig. 5.1 shows the IR-UV SED modeling of one of the SDSS-sample sources (SDSS J103036.93+312028.8, $z = 0.8726$): for a fixed viewing angle $\theta_{\rm v} = 30°$, the observed luminosity ratio ($R_{\rm obs} = 1.07^{+0.28}_{-0.39}$) sets a constraint on the BH spin ($a > 0.9$) and on the torus aperture angle ($\theta_{\rm T} < 50°$; see Appendix C.1 for details on how to find such constraints from $R_{\rm obs}$). For comparison, the SS model fails to explain the high observed ratio $R_{\rm obs}$ (see Sect. 5.1). For this object, even if all the main sources of uncertainty are taken into account for estimating the interval of $R_{\rm obs}$, a large BH spin is required to explain the high torus luminosity with respect to the disk one.

Given the importance of the involved uncertainties in this work, the reader is warned about the confidence interval defined above and the results shown and discussed in the next Section: in the worst-case scenario, a direct combination (not in quadrature) of all the previously discussed sources of contamination and their uncertainties could lead to an even larger observed ratio with respect to the intrinsic one; the correction of such a measurement could result is a ratio smaller than the one given by the 1σ lower limit of its confidence interval by a factor of ~ 2, leading to poor or even unavailable estimates of $\theta_{\rm T}$ and a.

5.5 Results

In this section, I will show the statistical analysis performed on the SDSS sample. Since $R_{\rm obs}$ depends also on the viewing angle of the system (see

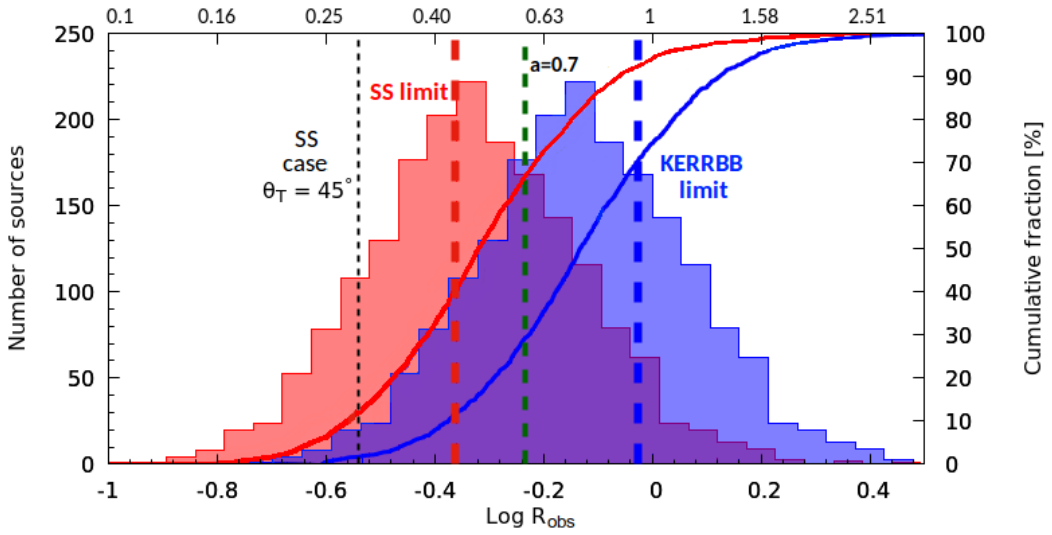

FIGURE 5.6: Logarithmic distribution of the luminosity ratio $R_{\rm obs}$ (blue histogram; mean logarithmic value $\langle \mathrm{Log}\ R_{\rm obs} \rangle = -0.13 \pm 0.20$). The red histogram is the distribution assuming that $R_{\rm obs}$ is given by its lower limit (from uncertainties - see Sect. 5.4.3). The blue and red lines are the cumulative functions related to the two histograms. The thick dashed blue line is the KERRBB limit ($R = 0.94$) assuming $\theta_{\rm v} = 30°$, while the maximum SS value ($R = 0.43$) is represented with a dashed red line for the same viewing angle (the thin dashed black line represents the SS case with $\theta_{\rm T} = 45°$ and $\theta_{\rm v} = 30°$). Sources, whose luminosity ratio $R_{\rm obs}$ is larger than the one shown with a dashed green line, have a BH spin $a > 0.7$ (see Sect. 5.1). The top x-axis shows the linear value of $R_{\rm obs}$.

Sect. 5.1), it is fixed to an average $\theta_{\rm v} = 30°$. This choice does not influence the final results drastically: on average, for a different viewing angle in the range $0° < \theta_{\rm v} < 45°$, BH spin and torus aperture angle estimates would differ by a factor $< 20\%$ from the results reported in the following Section.

5.5.1 Distribution of $R_{\rm obs}$

The mean logarithmic value of the luminosity ratio with its standard deviation is $\langle \mathrm{Log} R_{\rm obs} \rangle = -0.13 \pm 0.20$ (the mean linear value is $\langle R_{\rm obs} \rangle = 0.83 \pm 0.41$) which is larger than the SS limit ($R_{\rm obs} = 0.5$; see Sect. 5.1). The distribution of $R_{\rm obs}$ is shown in Fig. 5.6: if the 1σ lower limit of $R_{\rm obs}$ (given by its average uncertainty; see Sect. 5.4.3) is considered, about 60% of the sources show a ratio larger than the SS limit and, for an average torus aperture angle $\theta_{\rm T} = 45°$, almost 80% of the observed ratios cannot be explained with the SS model. Instead, taking into account the relativistic effects related to large BH spin values and the 1σ lower limit of $R_{\rm obs}$ (red histogram), almost 95% of the luminosity ratios can be explained with the KERRBB model. For the

SDSS+HST sample, the mean luminosity ratio does not change significantly with respect to the SDSS sample with a slight difference < 0.05 dex.

5.5.2 Black hole spin and torus aperture angle

The mean values, $\langle \mathrm{Log}R_{\mathrm{obs}} \rangle$ and $\langle R_{\mathrm{obs}} \rangle$ (related to the blue histogram in Fig. 5.6) set a constraint on the BH spin: if only the central value is considered, the average BH spin must be $a > 0.95$. If the lowermost limit of R_{obs} is considered, no constraints on the BH spin can be found (see Fig. 5.2). Given that the sample is made of radio-quiet sources, the result of such a statistical analysis seems to be in contrast with the idea that all radio-quiet AGNs host slow rotating BHs (due to the lack of relativistic jets - e.g., Urry and Padovani, 1995) and in agreement with the assumption that coherent gas accretion (proved by the presence of the BBB in the Optical-UV bands) through a disk causes the majority of BHs to have large spins (e.g., Elvis, Risaliti, and Zamorani, 2002; Sikora, Stawarz, and Lesota, 2007 and references therein).

As discussed in Campitiello et al., 2018; Campitiello et al., 2019, an independent BH mass estimate (i.e., virial mass) can be used to constrain a which can be compared with the spin inferred from the luminosity ratios. I performed such an analysis and found no correlation between the two spin estimates and this results is due to two reasons:

1. Different virial equations lead to different BH mass estimates (e.g., the analysis of Shen et al., 2011 showed that, with differences up to 1 order of magnitude) therefore, more precise independent mass estimates have to be used to perform such a study;

2. The virial BH mass estimates have a systematic uncertainty up to $\sim$ 0.5 dex (e.g., Vestergaard and Osmer, 2009) which leads to poor spin estimates.

For what concerns the torus aperture angle, both the SDSS and the SDSS+HST samples pose little constraints on θ_{T}, with an average range $30^{\circ} < \theta_{\mathrm{T}} < 70^{\circ}$ (at 2σ), consistent with the common picture of a torus with an average aperture angle of 45°, and with the results of Calderone, Sbarrato, and Ghisellini, 2012. Using the SS model, the mean luminosity ratios of both samples can be explained only if the average torus aperture angle is smaller than 40° (at 2σ), which disagrees with the commonly accepted scenario.

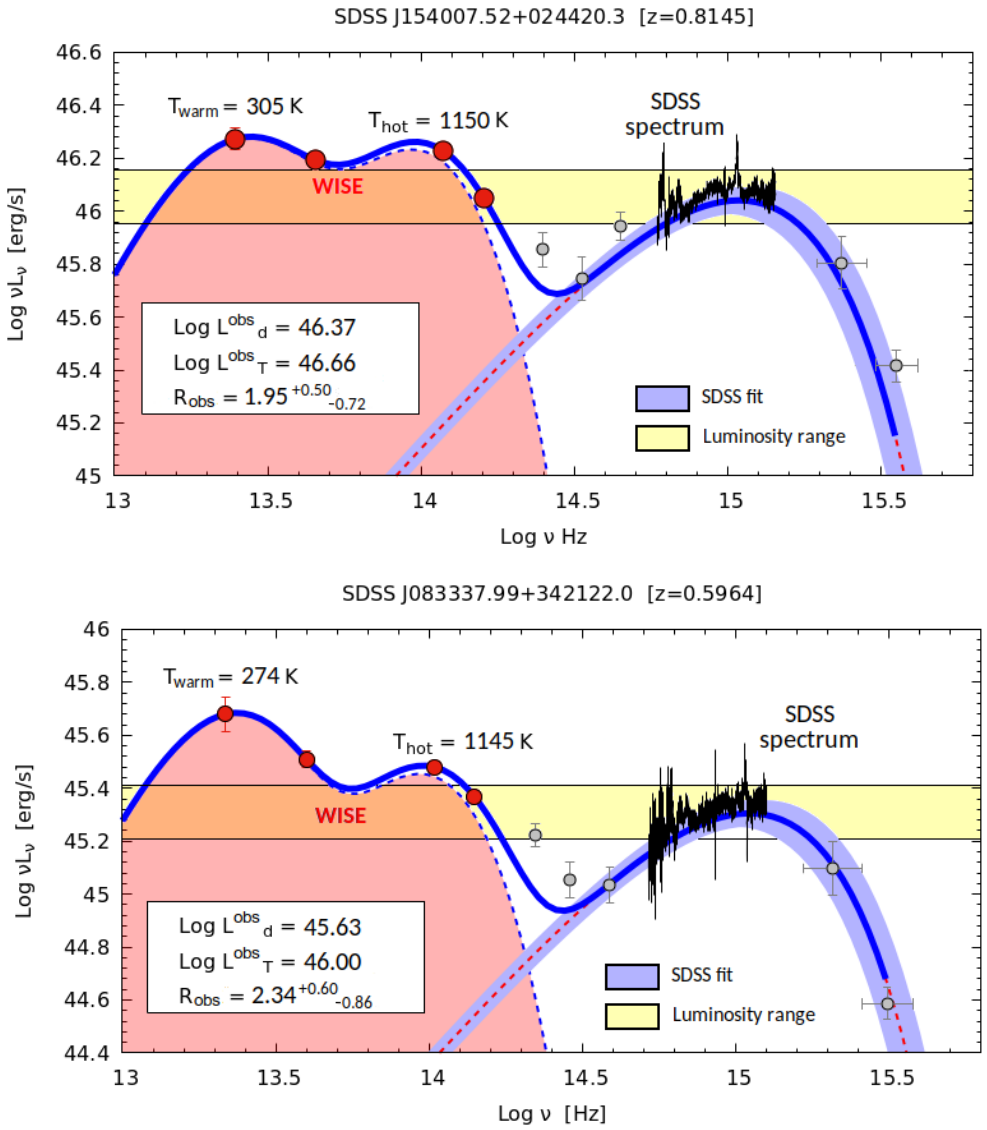

FIGURE 5.7: Fit of two sources with a large luminosity ratio that cannot be explained with the KERRBB radiation pattern. The SDSS spectrum (black line) continuum is described with KERRBB (dashed red line, with a shaded blue area representing a confidence interval given by the uncertainty on the spectrum peak; see Sect. 5.3.1) while the torus emission is constrained with the 4 WISE data (red dots) and two black-bodies (shaded red area with a dashed blue line contour) plotted along with the corresponding temperatures. The thick blue line is the overall model (disk + torus). On each plot, the observed disk and torus luminosities (in erg/s) are reported along with the corresponding luminosity ratio $R_{\rm obs}$ and its uncertainty (see Sect. 5.4.3). Some archival photometric data (2MASS, NED, GALEX - grey dots) are added to both plots. The yellow shaded area is the luminosity range in which $\nu_{\rm p} L_{\nu_{\rm p}}$ lies, obtained by taking into account different uncertainties (Sect. 5.4.3).

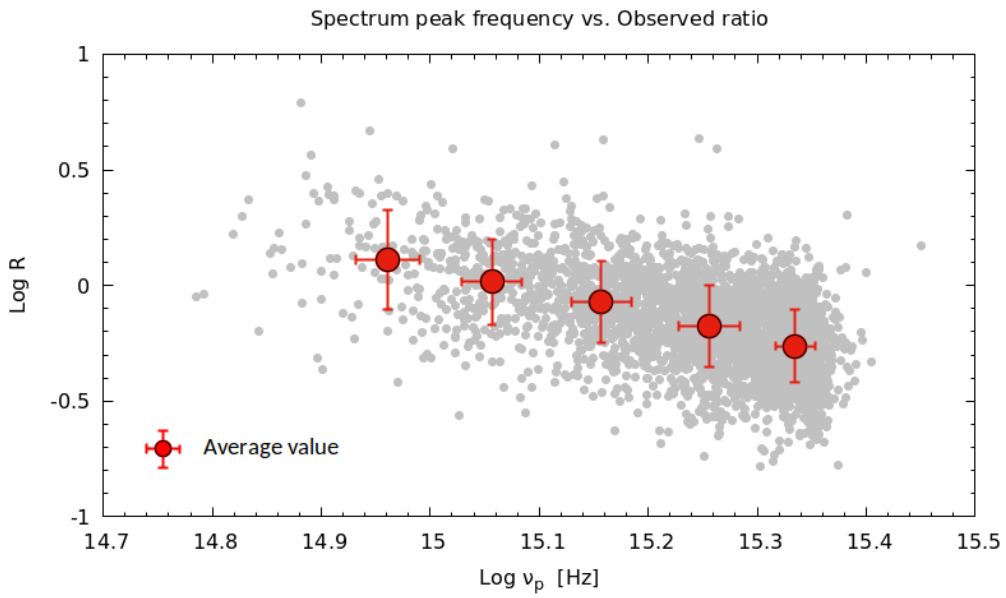

FIGURE 5.8: Luminosity ratio R_{obs} as a function of the spectrum peak frequency ν_p. The grey dots represent the SDSS sample. The red dots are the average values of R_{obs} ins fixed frequency bins (with 1σ error bars).

5.5.3 Sources with large R_{obs}

Considering the entire 1σ range of R_{obs} (given by its uncertainty; Sect. 5.4.3), $\sim 1/3$ of the sources of the SDSS sample shows a luminosity ratio $R_{obs} > 0.6$ for which the BH spin is constrained to be $a > 0.7$ (for a fixed viewing angle $\theta_v = 30°$; Fig. 5.6). Moreover, for the most extreme values, θ_T must be close to the viewing angle of the system. Almost 5% of the SDSS sample sources shows a ratio at 1σ above the KERRBB limit ($\sim 1\%$ at 2σ; Fig. 5.6) as the two shown as examples in Fig. 5.7.

All those sources were checked to understand the possible causes of those large luminosity ratios: no strong conclusion was drawn given the lack of data in the mm and FIR bands (where the peak of the other possible contaminating emissions is located; see Sect. 5.4.2) and the results have to be taken statistically. Dust absorption along the line of sight (e.g. from polar dust) could be one of the possible explanations for those large ratios, along with the contamination of the IR and the absorption of the UV emissions stronger than the average values discussed and shown in Sect. 5.3.2 and 5.4.2.

5.5.4 Torus geometry versus Eddington ratio

Several authors suggested that the key parameter determining the torus covering factor is the Eddington ratio (e.g., Lawrence, 1991; Ueda et al., 2003;

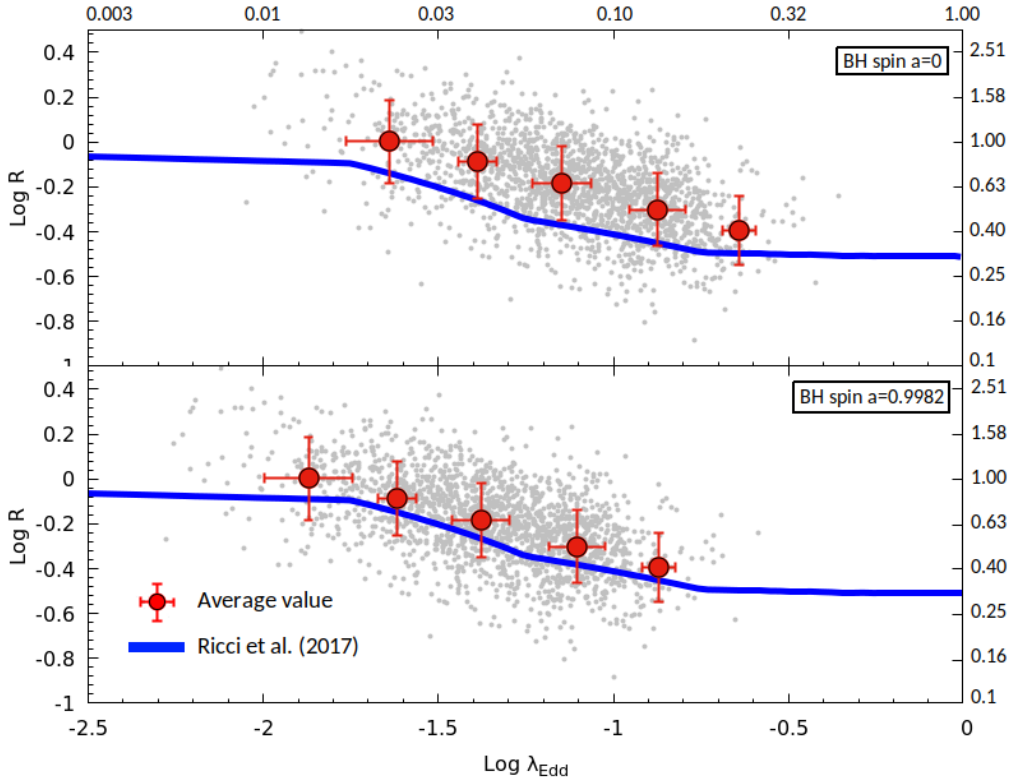

FIGURE 5.9: Luminosity ratio $R_{\rm obs}$ as a function of the Eddington ratio $\lambda_{\rm Edd}$ for the SDSS sample (grey dots), assuming non-spinning SMBHs (top panel) and maximally spinning SMBHs (bottom panel), for a fixed $\theta_{\rm v} = 30°$. The thick blue line represents the results of Ricci et al., 2017 (their Fig. 4, assuming the covering factor $\approx$ luminosity ratio $R_{\rm obs}$; see text). Red dots represent the average values of $R_{\rm obs}$ computed in fixed Eddington ratio bins (with 1σ error bars). The top x-axis and side y-axis show the linear value of $\lambda_{\rm Edd}$ and $R_{\rm obs}$, respectively.

Treister, Krolik, and Dullemond, 2008; Burlon et al., 2011; Buchner and Bauer, 2017; Ezhikode et al., 2017; Ricci et al., 2017). The $\lambda_{\rm Edd} - R_{\rm obs}$ anti-correlation (i.e., receding torus) could be due to different causes discussed by several authors (e.g., Lawrence, 1991; Lamastra, Perola, and Matt, 2006; Menci et al., 2008; Fabian et al., 2009; Wada, 2015; Ricci et al., 2017).

Given the spectral shape similarity between KERRBB models and the degeneracy between the parameters (a, M, $\dot{M}$), once the BH spin is fixed, it is possible to constrain the BH mass and the accretion rate and hence $\lambda_{\rm Edd}$ (see Sect. 3.2.3). However, in this study, both $\lambda_{\rm Edd}$ and $R_{\rm obs}$ depend on the same variable (i.e., the peak luminosity $\nu_{\rm p} L_{\nu_{\rm p}}$) even though in a different manner ($\sqrt{\nu_{\rm p} L_{\nu_{\rm p}}}$ vs. $1/\nu_{\rm p} L_{\nu_{\rm p}}$, respectively). I chose instead to study the relation between the peak frequency $\nu_{\rm p}$ and $R_{\rm obs}$ since they are independent measurements: I found an anti-correlation between the two quantities as shown in Fig. 5.8 (the best fit is Log $R_{\rm obs} \approx -1.01$Log $\nu_{\rm p} + 15.28$, with 1σ data dispersion of ~ 0.15 dex). Assuming that no strong dust absorption is present in

those sources (causing an apparent shift of the peak frequency to lower values; see the discussion in Sect. 5.3.2), from this plot, two simple conclusions can be drawn:

- Large values of ν_p are related to small BH masses (given the dependence $M \propto 1/\nu^2$; see Chaps. 2-3), therefore large Eddington ratios are expected for those sources, linked to small observed ratios.
- On the contrary, small values of ν_p, are related to large BH masses, therefore large values of R_{obs} corresponds to small Eddington ratios.

These conclusions are in agreement with the receding torus scenario and with the work of Ricci et al., 2017 who studied a local sample of AGNs (median redshift $z \approx 0.037$). In order to visualize these results, I plotted the observed ratios as a function of λ_{Edd} (Fig. 5.9) for two fixed BH spins ($a = 0 - 0.9982$) and $\theta_v = 30°$, although, as discussed before, the two quantities are biased by the spectrum peak luminosity.[9]. An anti-correlation is visible and comparable with the results of Ricci et al., 2017 (blue lines). For such a comparison, I removed the effect of a possible X-ray corona above the disk that can reduce the value of L_d^{obs} (and thus λ_{Edd} and R_{obs}) following the work of Duras et al., 2020 and the discussion in Sect. 5.3.2, adn assuming that the covering factor shown by Ricci et al. in their Figure 4 corresponds to the luminosity ratio R_{obs}.[10]

Although the KERRBB estimates lie above the results of Ricci et al., it is easy to notice the remarkable resemblance of the slopes in the same Eddington ratio range. As shown in Figs. 5.8-5.9, the compatibility between the two works is more evident in the case with maximally spinning SMBHs, while in the case with $a = 0$, the compatibility is marginal. Moreover, also the recent results by Toba et al., 2021 are partially compatible with the reported results although their anti-correlation (shown in their Figure 7, not shown here for clarity) is 'flatter'. The discrepancy between the results presented here and those from Ricci et al., 2017 could be caused by 1) the different luminosity ranges of the two samples, 2) the different redshift ranges related to the sources in the two works and 3) the fact that the high-z sources show a larger λ_{Edd} (e.g., Lusso, Comastri, Simmons, et al., 2012.

[9] For different values of θ_v in the range $0° < \theta_v < 45°$, the estimated λ_{Edd} would differ by a factor $< 20\%$ from the reported ones.

[10] Even though the two quantities do not necessarily coincide, the thick blue lines in Fig. 5.9 must be considered only as an indicative representation of the relationship between them and not a general function.

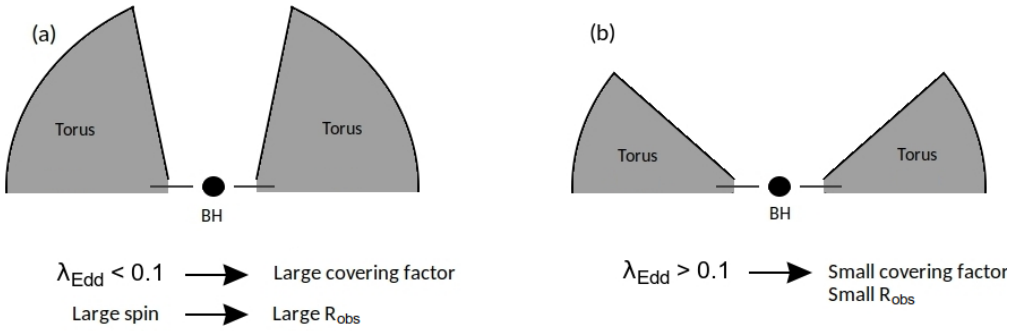

FIGURE 5.10: Cartoons representing the different results inferred in this work. Despite the value of the BH spin, if the Eddington ratio is low ($\lambda_{\rm Edd} < 0.1$), the torus can survive almost in all direction resulting in a large covering factor (*a*); on the contrary, for larger $\lambda_{\rm Edd}$, the torus survives only on the equatorial plane with a small covering factor and luminosity ratio $R_{\rm obs}$ (*b*). For a very large ratio ($R_{\rm obs} \sim 1$), the torus covering factor must be large and it intercepts almost all the radiation coming from the disk. Moreover, such a large $R_{\rm obs}$ can be explained only if the BH is rapidly spinning (Sect. 5.1).

The results of this comparison suggest that large Eddington ratios ($\lambda_{\rm Edd} > 0.1$) result in small luminosity ratios and, for a fixed spin value, in small covering factors (i.e., large $\theta_{\rm T}$): the torus survives only on the equatorial plane. On the contrary, smaller Eddington ratios ($\lambda_{\rm Edd} < 0.1$) result plausibly in a large $R_{\rm obs}$ and a large covering factor: the AGN is not able to remove dust in all direction efficiently which forms a more extended structure with a small $\theta_{\rm T}$ (Fig. 5.10), in agreement with the picture of Ricci et al., 2017 (see also Kawakatu and Ohsuga, 2011; Lyu, Rieke, and Shi, 2017). These results are in an overall agreement with the suggestions by Ishibashi, Fabian, and Reynolds, 2019 (see also Ishibashi, 2020): the authors discuss the possibility that the radiation pattern of the AD might shape the surrounding structures, depending on the BH spin. For low spin values, dust can be cleared out in the face-on direction while it may survive at higher inclination angles; for high spin values, dust can be removed from most directions, except in the equatorial plane (resulting in a smaller covering factor with respect the low spin case). However, for $\sim 1/3$ of our sample, the large luminosity ratios can be explained only if both the torus covering factor and the BH spin are large (see Sect. 5.5.3).

5.5.5 Hot dust covering factor

Dust distribution can play an important role in describing the IR emission properly. Hönig, 2019 reconsiders the torus structure and emission based on observational constraints: the author states that the IR emissions in different

bands are due to different regions of the dust distribution, in particular, the NIR emission is due to a disk-like structure with a covering factor $\sim 0.2-0.3$ (see also Mor and Netzer, 2012; Landt et al., 2011 who found an average covering factor of ~ 0.1), corresponding to $\theta_T \sim 70^\circ - 80^\circ$. Given that the NIR torus luminosity estimate is free from the possible contamination related to the cold and polar dust (see Sect. 5.4.2 and Fig. 5.5), I used the hot blackbody emission $L^{obs}_{T,hot}$ as a proxy of the NIR luminosity to compute the NIR luminosity ratio, defined as $R_{obs,NIR} = L^{obs}_{T,hot}/L^{obs}_{d}$: for the SDSS sample, I found $\langle \mathrm{Log}R_{obs,NIR}\rangle = -0.48 \pm 0.20$ (the mean linear value is $\langle R_{obs,NIR}\rangle = 0.37 \pm 0.18$).[11] This result is consistent with the one described by Hönig, 2019 only if the BH spin is $a > 0.95$ at 1σ ($a > 0.5$ at 2σ). Using the SS model, the NIR luminosity ratio constrains the torus aperture angle in the range $\theta_T < 60^\circ$ at 2σ, inconsistent with the average NIR covering factor.

[11] For the SDSS+HST sample, I obtained $\langle \mathrm{Log}R_{obs,NIR}\rangle = -0.58 \pm 0.22$ (the linear mean is $\langle R_{obs,NIR}\rangle = 0.29 \pm 0.15$).

Chapter 6

Conclusions and Future works

"I never think of the future. It comes soon enough"
— Albert Einstein

In this thesis, I discussed the possibility to have reliable estimates of the main SMBH and accretion properties through relativistic AD models, comparing the results with other independent measurements. Moreover, I explored the potentiality of using the relativistic AD angular pattern to study the surrounding environment close to the AD, inferring information on the SMBH spin. In this work, an extended analysis of the involved uncertainties has been conducted to define a suitable confidence interval for the results.

The main results of my work are summarized below:

- In Campitiello et al., 2018, I built an analytic approximation of the numerical model KERRBB, developed for X-ray binaries and accounting for all the relativistic effects (Li et al., 2005). With this approach, I managed to extend its use to SMBHs. The presence of relativistic effects makes the space of solution degenerate for the main disk parameters (i.e., mass, accretion rate, spin, viewing angle) so it is crucial to fix one of them to constrain the others (Sect. 3.2.3).

- Both the non-relativistic SS and KERRBB models rely upon the assumption of a geometrically thin and optically thick disk. Therefore, the KERRBB disk emission scales with BH mass and accretion rate as in the SS case (Calderone et al., 2013). In general, only the spectrum peak (frequency ν_p and luminosity $\nu_p L_{\nu_p}$) are necessary to find all the solutions for different spin values (Fig. 3.6).

- As shown in Campitiello et al., 2018; Campitiello et al., 2019; Campitiello et al., 2020, all sources show a good match between data and the

modeling with KERRBB which led to a relatively good estimate of the spectrum peak position (i.e., peak frequency and luminosity) with a small uncertainty (~ 0.05 dex on average). If the viewing angle is fixed in the range $0° < \theta_v < 45°$ (assuming the presence of a torus with an aperture angle of 45°), the total uncertainty related to the AD BH mass estimates is ~ 0.45 dex, which is connected to the unknown BH spin (in the range $0 < a < 0.998$), the viewing angle and the uncertainty on the peak position from the fitting procedure. If the quality of the data is high and either the spectral peak or the viewing angle of the system are well constrained (with an uncertainty $< 10\%$), the mean uncertainty is reduced to < 0.3 dex, which is smaller than the systematic uncertainties on RM (or SE) estimates ($0.4 - 0.5$ dex);

- In Campitiello et al., 2018, I applied the analytical method to 4 well-known high-redshift blazars (fixed θ_v) to derive a new estimate of their BH mass and accretion rate, and to the most distant QSOs known up to 2019 (Campitiello et al., 2019). For these last high-redshift sources, I found that they emit radiation at a sub-Eddington rate, contrary to what other authors found. Such a sub-Eddington regime I inferred for the observed accretion suggests the need for a previous (super-Eddington?) phase during which most of the BH mass was quickly assembled (e.g., Lapi et al., 2014). In both a super or Eddington-limited evolution, the evolutionary tracks (i.e. mass versus time) show that a high accretion rate and a low radiative efficiency ($\sim 10\%$) are necessary to reach the estimated masses at the observed redshifts, starting the evolution from a $\sim 10^{2-4} M_\odot$ BH seed at redshift $z \sim 10 - 20$ (see Sect. 4.2.4).

- I studied how the observed luminosity L_d^{obs} of the AD depends on the viewing angle and the BH spin. I obtained a phenomenological function $f(\theta_v, a)$ that approximates the variation of the observed luminosity at different θ_v and a values (Sect. 3.2.1). The availability of an analytic expression for the observed luminosity related to a spinning BH can be extremely useful in the analysis of the disk emission features. The radiation pattern shows the following:

  - A larger spin implies a larger observed luminosity. The increase of luminosity and the strength of the relativistic effects on the pattern are more pronounced for $a > 0.8$;

  - At a fixed viewing angle, there is a KERRBB model equivalent to a SS one with the same parameters (mass and accretion rate). At $\theta_v = 0°$, the equivalent KERRBB has spin $a \sim 0.8$. To emit the same luminosity, the KERRBB emission must have a larger efficiency, hence a larger BH spin value. At larger viewing angles, the KERRBB model is brighter because of the strong relativistic effects;
  - Relativistic effects modifies the pattern at different viewing angles: the simple $\cos\theta_v$-law (followed by the SS model) is no longer valid, mostly due to light-bending. Hence the maximum observed luminosity is no longer at $\theta_v = 0°$ but at larger viewing angles for larger spin values (see Tab. 3.1);

- In principle, it is possible to use the analytical AD expressions to find the BH spin once a reliable estimate of the BH mass is available (as done in Campitiello et al., 2019). Currently, the virial BH masses have an average uncertainty of $0.4 - 0.5$ dex, which leads only to a poor constraint on a. However, when more precise BH mass estimates are available, the method will provide robust spin estimates and thus new insights into BH physics.

- In Campitiello et al., 2020, I compared the KERRBB AD mass results with those inferred with the RM technique and SE equations finding that the AD estimates are systematically larger, with a scale factor Log $f < 1.2$ (depending on the BH spin; Fig. 4.14). Despite these findings, assuming a geometrical factor in the range $f_{BLR} = 2.8 - 5.5$, I find a good compatibility between RM, SE, and KERRBB results for $\sim 70\%$ of the sources (Fig. 4.17). I also checked the possibility that the presence of an X-ray Corona above the disk could affect the AD mass estimates. For this reason, I compared KERRBB results with those from the relativistic model AGNSED (Kubota and Done, 2018) that accounts also for the X-ray emission in a self-consistent way, finding that two models are compatible only for particular sizes of the Corona (Sect. 4.3.3)

- In Sect. 5 (Campitiello et al., 2021), I discussed the possibility to apply the relativistic radiation patterns to constrain the torus geometry and possibly the BH spin. I inferred the IR torus and UV disk luminosities from the WISE and SDSS data, respectively, analyzing all the main possible sources of uncertainties (Sects. 5.3 - 5.4) and studied the distribution of the observed luminosity ratio R_{obs}, defined as the ratio between the observed torus and disk luminosities (Sect. 5.1). The mean

logarithmic value of the luminosity ratio distribution is $\langle \mathrm{Log}R_{\mathrm{obs}} \rangle = -0.13 \pm 0.20$ that, for an average viewing angle $\theta_{\mathrm{v}} = 30^{\circ}$, corresponds to a torus aperture angle in the range $30^{\circ} < \theta_{\mathrm{T}} < 70^{\circ}$.

- If only the central value of the mean luminosity ratio is considered, the BH spin must be on average $a > 0.95$. Even though all the main sources of contamination of the IR and UV luminosities are taken into account, $\sim 1/3$ of the sources shows a large value of R_{obs} that can be explained only if relativistic effects are very strong, i.e, the SMBH is rapidly spinning with $a > 0.7$. The same conclusion can be drawn by using the hot black-body emission as a proxy of the NIR luminosity which is thought to be due to a disk-like structure with a covering factor $\sim 0.2 - 0.3$.

- Although our sample has been built by choosing only radio-quiet sources, our statistical results suggest that a fraction of the sources must have a rapidly spinning SMBH, in contrast with the view that those AGNs host slow rotating BHs (e.g., e.g., Antonucci, 1993; Urry and Padovani, 1995. The implications of such findings (that clearly require further investigations to assess their robustness) are the following:

  - Despite their radio-nature, the accretion mode is the same for the majority of AGNs, i.e. a coherent gas accretion that spins the BHs up to the maximum value (following the accretion disk theory of e.g., Thorne, 1974);
  - If relativistic jets are thought to be linked to rapidly spinning SMBHs, the radio-quiet nature of some sources could be due to the different inclination angle of the system or to the jet dissipation region (see e.g., Ghisellini and Tavecchio, 2015);
  - If relativistic jets are present only in radio-loud sources, their production could be linked to some other features of the system and not only to the BH spin.

- The evolution of the hole could play an important role for both the spin and the shape of the surrounding environment. Several studies suggest that the slower spinning SMBHs should be the more massive ones because a lower radiative efficiency (linked to a small value of a) favors a fastest growth of the BH, despite the nature of the accretion (chaotic vs. coherent; see e.g. Campitiello et al., 2019; Subovas and King, 2019 and references therein). Moreover, such a conclusion is suggested also

by the available spin measurements (see e.g. Reynolds, 2020 and references therein) even though it is extrapolated from a very small sample. In this work, I found no significant correlation between the BH mass (virial and from the fitting procedure) and the observed ratio (or high BH spin values constrained from R_{obs}). Given the involved uncertainties for both the mass and the spin estimates, I could not make a proper comparison with the referred studies and draw any conclusions. However, given the average virial BH mass of the sample (Log $M/M_{\odot} \sim 9$), my results indicating the presence of highly spinning SMBHs agree with the work of Trakhtenbrot, 2014 that, contrary to those previously mentioned, found that very massive BHs have large radiative efficiencies (i.e., large spins). Given that these arguments are still under debate, I suggest caution regarding the conclusions presented here.

- It is well known that the accretion history of the BH and its accretion rate are crucial to understand its evolution and the link between the different features: in this context, other variables must be taken into account which are not completely understood and/or are very hard to constrain (e.g., the exact BH accretion mode evolution - coherent or chaotic -, the BH system - isolated or binary -,...). The presence of the BBB in the Optical-UV bands for the sources analyzed in this work suggest that the accretion mode is coherent and can be described by an AD around the SMBH: despite that and the evolution of the spin in such a scenario (which lead it to the maximum value $a \sim 1$; Thorne, 1974), the growth of the BH is linked to $\dot{M}$ and its possible changes during its accretion history (e.g., via gas or BH-BH mergings). Given the uncertainties involved in such studies, thes latter arguments suggest to be careful in considering the possible relation discussed in the previous bullet (mass vs. spin).

- My results suggest an anti-correlation between the luminosity ratio R_{obs} and the Eddington ratio λ_{Edd}, as also suggested by several authors and comparable with the results of Ricci et al., 2017 (Fig. 5.9). A larger λ_{Edd} leads to smaller ratios R_{obs} and, for a fixed spin value, to smaller covering factors (i.e., the torus survives only on the equatorial plane). On the contrary, a smaller Eddington ratio results in a larger R_{obs} and a larger covering factor (partially in agreement with the works of Ishibashi, Fabian, and Reynolds, 2019; Ishibashi, 2020).

Given the current works described here, the following topics can be investigated to improve the general understanding of AGN physics:

- *Spin in Radio-loud & Radio-quiet sources*

  The application of the continuum fitting method with relativistic AD models to Radio-quiet and Radio-loud sources could lead to a more precise classification based on the SMBH spin: this latter can be inferred by the comparison between the masses obtained with an AD model and SE scaling relations (Campitiello et al., 2018; Campitiello et al., 2019 - see Sect. 3.2.3). If accretion has been coherent for all sources, a large spin value is expected despite the radio nature (e.g., Thorne, 1974).

- *Torus luminosity at high-redshifts*

  The study of IR torus luminosity with respect to the disk one (as shown in Chap. 5) could lead to strong constraints on the AGNs environment for high-redshift sources when the Universe was younger. Large Eddington ratios and IR luminosities are expected (e.g., Lusso, Comastri, Simmons, et al., 2012; Magdis et al., 2012), implying large torus covering factors that can lead to precise constraints on the BH spin. However, dust could also absorb the disk UV light drastically and a careful analysis must be conducted.

- *Comparison between independent BH spin estimates*

  In Chap. 4 and 5, I discussed the possibility to infer the BH spin by comparing different and independent estimates of the SMBH mass and through the study of the observed IR-to-UV luminosity ratio. The comparison between different spin estimates (e.g., Iron line shape modification in the strong gravity regime; see Sect. 1.2) is important to strengthen the usage of relativistic models for studying the AD surrounding environment. A careful SED analysis is required to separate the different AGN emissions properly.

- *Comparison between water megamaser BH mass estimates and AD ones*

  As discussed in Sect. 1.2, BH masses estimated from such Keplerian disks are free from systematic uncertainties and represent one of the most precise BH mass measurements. Such a constraint can be used along with AD models which have to be applied assuming a viewing

angle close to the AD equatorial plane ($\theta_v \sim 90°$): this implies that the disk emission is obscured by the dusty torus and a careful AGN emission component analysis must be performed in order to isolate the disk emission.

- *Relativistic radiation angular pattern for BLR*

  As done for the torus, the disk radiation angular pattern can be used to constraints the BLR geometry (in terms of its covering factor) and possibly the SMBH spin. Given the latest results of the GRAVITY collaboration (e.g., Sturm et al., 2018) and the improvement of the RM technique to study the environment close to SMBHs (e.g., Grier et al., 2017), it is possible to compare the results to set tighter constraints on the BLR geometry and the SMBH spin and to strengthen the application of the relativistic radiation angular pattern.

- *Disk emission variability*

  Several studies have been conducted to explain this phenomenon, possibly related to the presence of an X-ray Corona above the disk (e.g, Lohfink, Reynolds, Vasudevan, et al., 2014; Ricci et al., 2020). Simultaneous data at different epochs and different frequencies are necessary o study one of the possible causes related to variations of the disk accretion rate (e.g., Gu and Li, 2013) which can be inferred with relativistic disk models.

Appendix A

KERRBB and SLIMBH equations

A.1 Observed disk luminosity

In Sect. 3.2, I showed that an analytic expression that approximates the KERRBB observed disk luminosity $L_{\rm d}^{\rm obs}$ can be written as Eq. 3.2 with the function $f(\theta_{\rm v}, a)$ (Eq. 3.3) expressed as:

$$f(\theta_{\rm v}, a) = A\cos\theta[1-(\sin\theta_{\rm v})^C]^B[1-E(\sin\theta_{\rm v})^F]^D$$

This latter is defined by the parameters A, B, C, D, E, F that are functions only of the BH spin a. To find the expression for $L_{\rm d}^{\rm obs}$, given a value of the spin a, a set of viewing angles $\theta_{\rm v}$ has been chosen (from 0° to 85°) and the integrals over frequency of the KERRBB spectra have been computed. Each of the parameters has the following form (Eq. 3.4):

$$\mathcal{F}(a) = \alpha + \beta x_1 + \gamma x_1^2 + \delta x_1^3 + \epsilon x_1^4 + \iota x_1^5 + \kappa x_1^6$$

Figure A.1 shows $L_{\rm d,Kerr}^{\rm obs}$ as a function of the viewing angle, for spin $a = -1, -0.6, 0.6$ and 0.998 (red dots), and the fitting functions (blue lines). In the cases $a = -1$, -0.6 and 0.6, the observed disk luminosity between the cases 0° and 85° decreases by a factor of ~ 7, 6.6 and 4.4, respectively[1]. In the case with $a = 0.998$, the strong relativistic effects cause the luminosity to reach a maximum value at $\sim 64°$ (see Tab. 3.1) and then make it drop at larger viewing angles. The cases with 0° and 85° have almost the same luminosity (see also Fig. 3.4), contrary to the small-spin cases.

Figure A.2 shows the parameters A, B, C, D, E, F for different values of the BH spin: for what concern the common fitting equation (blue line), the

[1] In the case with no relativistic effects (i.e., SS model), there would have been a factor of ~ 11.5 between the cases 0° and 85°.

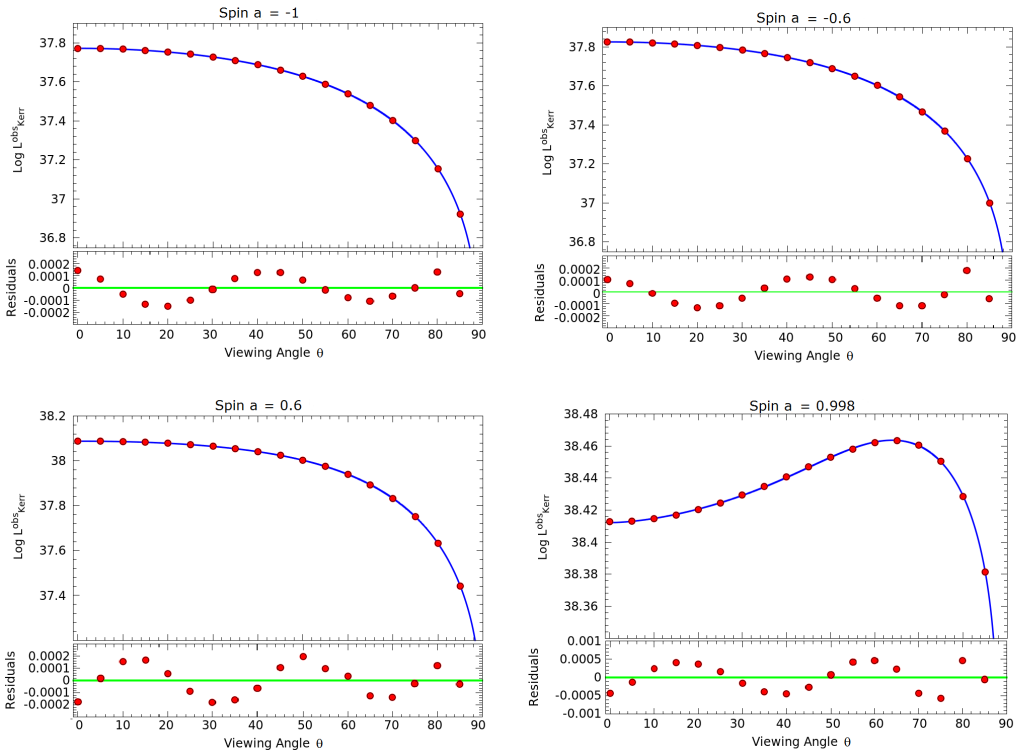

FIGURE A.1: KERRBB observed disk luminosity (in units of erg/s) as a function of the viewing angle of the disk, in the cases with $a = -1$, $a = -0.6$, $a = 0.6$ and $a = 0.998$, with $\dot{M} = 10^{18}$ g/s.

values of α, β, γ, δ, ϵ, ι and κ are listed Tab. A.1. The residuals are always of the order of 1% (or less), except for F (on the order of $\sim 10\%$).

A.2 Polynomial approximation of $L^{\rm obs}_{\rm d,Kerr}$

Once a, $\dot{M}$ and θ are fixed, Eq. 3.2 needs 37 parameters for the description of $L^{\rm obs}_{\rm d,Kerr}$ with an accuracy of $< 1\%$. Another approximation for this quantity can be expressed with the following polynomial function:

$$\mathrm{Log}L^{\rm obs}_{\rm d,Kerr,2}(a,\theta) = \mathrm{Log}[\dot{M}c^2] + \sum_{i=0}^{3} a^i(\alpha_i + \beta_i\theta + \gamma_i\theta^2) \qquad \text{(A.1)}$$

which have 12 parameters listed in Tab. A.2. The function is valid for $a \in [-1 : 0.998]$ and $\theta \in [0^\circ : 80^\circ]$. The accuracy of this polynomial approximation is $\sim$ 10%, less accurate than the previous eequations (differences growing with spin, larger for $\theta > 70^\circ$), but still good enough to obtain $L^{\rm obs}_{\rm d,Kerr}$ for a wide range of spins and angles (Fig. A.3). However, because of its accuracy, this approximation does not allow the user to study the emission pattern precisely, as Eq. 3.2 does (see Fig. 3.2).

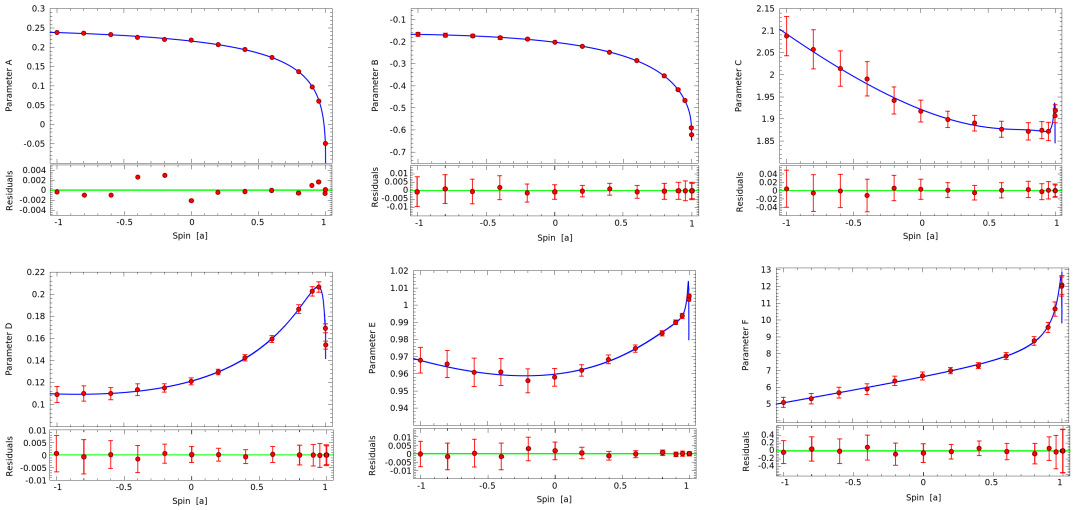

FIGURE A.2: Parameters A, B, C, D, E, F of Eq. 3.3 as functions of the BH spin a. The fitting function (blue line) has the general form of Eq. 3.4. The residuals are always on the order of 1% (or less), except for F (on the order of $\sim$ 10%). Red bars are associated with the uncertainties on the parameter values from the fit of the $L^{\rm obs}_{\rm d,Kerr}$ for different viewing angles (Fig. A.1.)

Par of Eq. 3.4	α	β	γ	δ	ϵ	ι	κ
Log A	0.21595	0.09107	−0.05037	−0.02739	−0.00361	0	0
B	−0.20229	0.17538	−0.14390	−0.14534	−0.04544	−0.00480	0
C	1.92161	0.27712	0.67368	0.81327	0.48946	0.13591	0.01373
D	0.12120	−0.07852	0.08995	0.12746	0.04556	0.00510	0
E	0.95973	−0.02003	0.09341	0.16775	0.11440	0.03367	0.00351
F	6.62190	−3.84845	−3.11662	−3.61394	−1.54083	−0.19834	0

TABLE A.1: Parameter values of Eq. 3.4 from Eq. 3.3.

i	α_i	β_i	γ_i
0	-1.054	0.00443	-0.000132
1	0.159	0.000559	-3.63e-6
2	0.148	-0.000929	4.08e-5
3	0.145	-0.00155	5.47e-5

TABLE A.2: Parameter values of Eq. A.1, which represents a less accurate ($\sim$ 10%) but still good approximation of $L^{\rm obs}_{\rm d,Kerr}$.

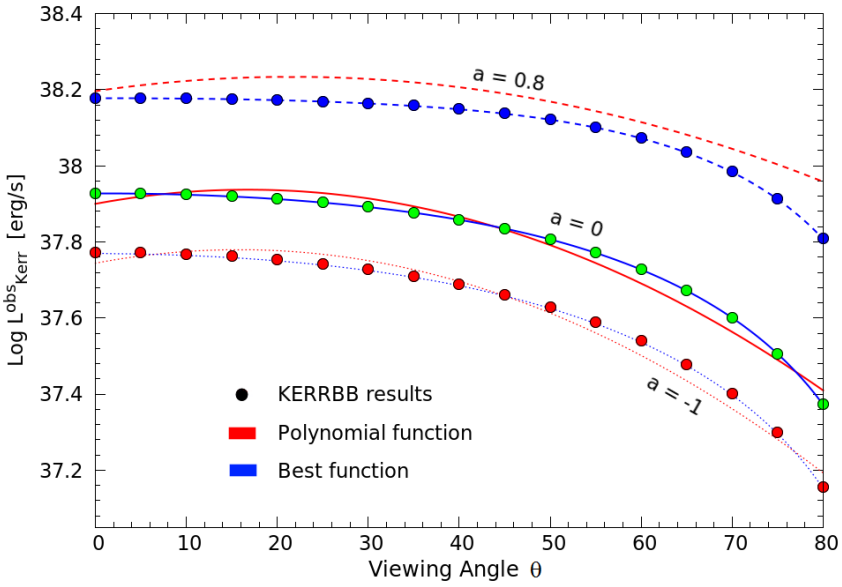

FIGURE A.3: KERRBB observed disk luminosity as a function of the viewing angle of the disk, fitted by the best function given by Eq. 3.2 (blue lines) and the polynomial function given by Eq. A.1 (red lines) for different spin values. Dots represent the KERRBB results with $\dot{M} = 10^{18}$ g/s.

θ_v		α_g	β_g	γ_g	δ_g	ϵ_g	ζ_g	ι_g	κ_g
0°	g_1	1001.3894	-0.06174	-381.6494	8282.0773	-40453.436	66860.089	-34974.154	0
	g_2	2003.6451	-0.16661	-737.3402	16310.060	-80127.144	132803.24	-69584.315	0
30°	g_1	-6238.2428	-0.12968	-926.6079	37153.527	-319409.16	983173.49	-1228407.6	532213.70
	g_2	-9332.6548	-0.30891	-1356.532	54978.793	-474342.12	1462740.0	-1829629.7	793292.22
45°	g_1	-12431.613	-0.20298	-1797.017	73606.043	-636017.89	1961099.2	-2451848.7	1062521.6
	g_2	-16314.313	-0.41098	-2325.942	95651.404	-828227.38	2557278.0	-3200363.0	1387917.3

TABLE A.3: KERRBB parameter values of Eq. 3.9 for the equations g_1 and g_2, for the viewing angles $\theta_v = 0° - 30° - 45°$.

A.3 Shifting Equations

In Sect. 3.2.2, the peak frequency and luminosity are expressed as functions of the BH mass, accretion rate, viewing angle and BH spin (Eqs. 3.7 - 3.8). The dependence on θ_v and a is described by the two functions g_1 and g_2, that can be written as polynomials (Eq. 3.9)

$$g_i(a, \theta_v = 0°) = \alpha_g + \beta_g y_1 + \gamma_g y_2 + \delta_g y_3 + \epsilon_g y_4 + \zeta_g y_5 + \iota_g y_6 + \kappa_g y_7$$

Table A.3 reports the different parameters for g_1 and g_2 for the viewing angles $\theta_v = 0° - 30° - 45°$.

θ_v		$\bar{a}$	$\bar{b}$	$\bar{c}$	$\bar{d}$	$\bar{e}$	$\bar{f}$
0°	$\alpha_{1,s}$	1.37528	-0.03581	0.21458	-0.35971	0.16821	0
	$\beta_{1,s}$	-0.69241	0.21439	-0.57440	0.75878	-0.31345	0
	$\gamma_{1,s}$	-0.28949	0.33854	-1.10213	1.27581	-0.48471	0
	$\delta_{1,s}$	-0.02094	0.20299	-0.65531	0.69134	-0.24475	0
	$\epsilon_{1,s}$	0.00538	0.04041	-0.12718	0.12852	-0.04411	0
	$\alpha_{2,s}$	9.917034	-3.22512	17.89987	-41.84139	41.27971	-14.78658
	$\beta_{2,s}$	3.51987	-2.44127	13.36609	-29.61009	29.12455	-10.46037
	$\gamma_{2,s}$	0.72886	-4.09764	21.16717	-46.66724	46.53742	-16.81675
	$\delta_{2,s}$	0.39809	-2.70631	14.15261	-31.93365	32.12041	-11.63591
	$\epsilon_{2,s}$	0.10769	-0.52470	2.79254	-6.40072	6.46561	-2.34359
30°	$\alpha_{1,s}$	1.43631	-0.04881	0.29277	-0.47116	0.22691	0
	$\beta_{1,s}$	-0.79532	-0.01997	0.33520	-0.75650	0.53158	0
	$\gamma_{1,s}$	-0.22587	-0.02063	0.09107	-0.69291	0.63651	0
	$\delta_{1,s}$	0.02389	0.02883	-0.15739	-0.10901	0.22802	0
	$\epsilon_{1,s}$	0.01253	0.01160	-0.05570	0.01933	0.02243	0
	$\alpha_{2,s}$	10.35255	-3.29155	18.23667	-42.38302	41.68164	-14.90491
	$\beta_{2,s}$	2.98930	-2.42948	12.92896	-28.15866	27.60484	-9.89120
	$\gamma_{2,s}$	0.59669	-4.53087	22.72740	-49.83698	49.55957	-17.85179
	$\delta_{2,s}$	0.48252	-3.02872	15.50716	-34.91153	35.02577	-12.65587
	$\epsilon_{2,s}$	0.13420	-0.58612	3.06804	-7.02543	7.08401	-2.56372
45°	$\alpha_{1,s}$	1.50731	-0.07421	0.44310	-0.66183	0.30977	0
	$\beta_{1,s}$	-0.94113	0.04156	0.22037	-0.66194	0.48374	0
	$\gamma_{1,s}$	-0.13063	-0.33330	1.96527	-3.88455	2.23797	0
	$\delta_{1,s}$	0.06519	-0.16637	1.16515	-2.43971	1.43194	0
	$\epsilon_{1,s}$	0.01540	-0.02046	0.19603	-0.44262	0.26763	0
	$\alpha_{2,s}$	11.07996	-3.55277	19.73825	-45.64546	44.84619	-16.02576
	$\beta_{2,s}$	2.34516	-2.75232	14.20309	-30.41746	29.43857	-10.38000
	$\gamma_{2,s}$	0.65369	-5.59958	27.68371	-60.66151	59.68996	-21.22119
	$\delta_{2,s}$	0.71299	-3.70302	18.84159	-42.43550	42.23110	-15.11877
	$\epsilon_{2,s}$	0.18732	-0.70811	3.69829	-8.47710	8.49652	-3.05447

TABLE A.4: SLIMBH parameter values of Eq. 3.18 for the viewing angles $\theta_v = 0° - 30° - 45°$. The subscript i $= 1, 2$ specifies the equations $g_{1,s}$ and $g_{2,s}$ (see Eqs. 3.16 - 3.17).

$\lambda_{\rm Edd}$		$\alpha_{\rm slim}$	$\beta_{\rm slim}$	$\gamma_{\rm slim}$	$\delta_{\rm slim}$	$\epsilon_{\rm slim}$	$\zeta_{\rm slim}$
0.15	$\mathcal{M}_{\rm s}$	0.09216	-0.09172	-0.00476	-0.01228	0.01878	0.00711
	$\mathcal{N}_{\rm s}$	2.07731	-0.43140	-0.17963	-0.80959	-0.74089	-0.15899
	$\mathcal{O}_{\rm s}$	-0.15253	1.57266	-0.08590	2.29891	1.86426	0.36146
	$\mathcal{P}_{\rm s}$	-0.80658	-0.76583	-0.50436	-3.43981	-2.22829	-0.38868
	$\mathcal{Q}_{\rm s}$	0.40216	0.18023	0.48616	1.55637	0.88679	0.14490
0.35	$\mathcal{M}_{\rm s}$	0.09344	-0.10071	-0.02655	-0.03928	0.00713	0.00552
	$\mathcal{N}_{\rm s}$	2.09345	-0.39421	0.03348	-0.53567	-0.63088	-0.14509
	$\mathcal{O}_{\rm s}$	-0.17944	1.54913	-0.55926	1.73870	1.66778	0.34067
	$\mathcal{P}_{\rm s}$	-0.79669	-0.74036	-0.05316	-2.99626	-2.10762	-0.38134
	$\mathcal{Q}_{\rm s}$	0.40178	0.16699	0.34007	1.44161	0.86920	0.14662
0.95	$\mathcal{M}_{\rm s}$	0.10614	-0.13017	-0.06530	-0.11203	-0.04067	-0.00354
	$\mathcal{N}_{\rm s}$	2.15366	-0.38033	0.20774	0.04626	-0.29432	-0.08926
	$\mathcal{O}_{\rm s}$	-0.44957	1.88900	-1.28991	-0.07013	0.79772	0.21638
	$\mathcal{P}_{\rm s}$	-0.60744	-1.13639	1.24831	-0.77179	-1.18243	-0.26440
	$\mathcal{Q}_{\rm s}$	0.35570	0.27729	-0.28986	0.55978	0.53766	0.10882

TABLE A.5: SLIMBH parameter values related to Eqs. 3.20 - 3.21 - 3.22.

A.4 SLIMBH equations

As for KERRBB, similar equations describing the disk emission can be found for the SLIMBH model (Sect. 3.4.1). The peak frequency and luminosity can be expressed as a function of the BH spin and viewing angle by defining to different equations, $g_{1,\rm s}$ and $g_{2,\rm s}$, that have a polynomial form (Eq. 3.18):

$$g_{\rm i,s}(a,\theta_{\rm v},\lambda_{\rm Edd}) = \alpha_{\rm i,s} + \beta_{\rm i,s} y_1(a) + \gamma_{\rm i,s} y_1^2(a) + \delta_{\rm i,s} y_1^3(a) + \epsilon_{\rm i,s} y_1^4(a)$$

where each parameter is a function of the Eddington ratio and is expressed as (Eq. 3.19)

$$\chi_{\rm i,s}(\theta_{\rm v},\lambda_{\rm Edd}) = \bar{a} + \bar{b}\lambda_{\rm Edd} + \bar{c}\lambda_{\rm Edd}^2 + \bar{d}\lambda_{\rm Edd}^3 + \bar{e}\lambda_{\rm Edd}^4 + \bar{f}\lambda_{\rm Edd}^5$$

The value of each coefficient is reported in Tab. A.4. Also the observed disk luminosity can be described analytically: as shown in Sect. 3.4.1, the disk radiation angular pattern depends on BH spin but also on the Eddington ratio. The new function $f_{\rm s}(\theta_{\rm v}, a, \lambda_{\rm Edd})$ is expressed as (Eq. 3.21)

$$f_{\rm s}(\theta_{\rm v},a,\lambda_{\rm Edd}) = \mathcal{M}_{\rm s} + \mathcal{N}_{\rm s}\mathcal{Z}(\theta_{\rm v}) + \mathcal{O}_{\rm s}\mathcal{Z}(\theta_{\rm v})^2 + \mathcal{P}_{\rm s}\mathcal{Z}(\theta_{\rm v})^3 + \mathcal{Q}_{\rm s}\mathcal{Z}(\theta_{\rm v})^4$$

where the coefficient are expressed as (Eq. 3.22):

$$\mathcal{R}(a) = \alpha_{\rm slim} + \beta_{\rm slim} y_1(a) + \gamma_{\rm slim} y_1^2(a) + \delta_{\rm slim} y_1^3(a) + \epsilon_{\rm slim} y_1^4(a) + \zeta_{\rm slim} y_1^5(a)$$

The value of each parameter is reported in Tab. A.5 for different Eddington ratios ($\lambda_{\rm Edd} = 0.15 - 0.35 - 0.95$).

Appendix B

AD vs. RM and SE: tables and plots

B.1 Data and Results

Here I report the fits of the individual SEDs, performed by adapting the KERRBB model to the rest-frame spectrum (spectroscopic data are summarized in Tab. B.1), whose results are listed in Tabs. B.2 - B.4. When necessary, a host-galaxy template (from Manucci et al., 2001) is added to the KERRBB model to obtain a better fit in the NIR-Optical range. For a few sources, IUE data were used instead of the most recent HST ones because the former covers a wider wavelength range. Red dots are archival photometric data (GALEX, Vizier, NED) not used in the fitting procedure because they might be contaminated by emission lines or some kind of absorption. A confidence interval for the spectrum peak position is shown with a blue shaded area (~ 0.05 dex).

For the two sources PG0844+349 and PG1211+143, spectra were corrected from possible dust absorption (following Czerny et al., 2004) to have a better compatibility between the data and KERRBB: for PG1211+143, correcting the spectrum from dust leads to a satisfactory fit even without including the host-galaxy emission. Despite this correction, BH masses do not change drastically (< 0.1 dex). For the two high-redshift sources PG1247+267 and S50836+71 ($z \sim 2$), data were corrected from the IGM absorption, following Madau, 1995, Haardt and Madau, 2012 and Castignani et al., 2013, showing the corrected results in the corresponding plots.

The BH mass and the Eddington ratio inferred with KERRBB are shown as a function of the BH spin for different values of the viewing angle θ_v; on each plot, I report different BH mass estimates from different works (listed in the caption of Fig. B.1); a blue shaded area (~ 0.1 dex) defines the confidence interval on each BH mass estimate.

Name	Redshift	Telescope	Observation Date	Name	Redshift	Telescope	Observation Date
3C273	0.158	FUSE	2000 Apr 23 [a]	NGC5548	0.017	HUT	1995 Mar 14
		HST	2000 Mar 16 [a]			IUE	1995 May 16
		KPNO	2000 Feb 25-26 [a]			KPNO	1985 - 1989 [l]
		IRTF	2007 Jan 25 [b]				
Ark120	0.033	FUSE	2000 Dic 31	NGC7469	0.016	FUSE	2002 Dic 14
		HST	1994 Sep - 1995 Jul			IUE	1991 Nov 29
		IRTF	2007 Jan 26 [b]			KPNO	1985 - 1989 [l]
						IRTF	2003 Oct 23 [f]
Fairall9	0.047	HUT	1995 Mar 11	PG0026+129	0.142	HST	[c]
		HST	1993 Jan 21 [c]			KPNO	1990 Oct 11 [e]
		AGN Watch	1994 - 1995 [d]			GNIRS	2011 Aug 3 [m]
MRK142	0.045	EUVE	1998 May 04	PG0052+251	0.154	FUSE	1999 Oct 03 [a]
		IUE	1983 Jun 02			HST	1999 Oct 01 [a]
		SDSS 2007	2007			KPNO	1999 Oct [a]
						GNIRS	2011 Aug 03 [m]
MRK290	0.029	FUSE	2007 Mar 17	PG0804+761	0.100	FUSE	2002 Feb 09
		IUE	1985 Jan 22			IUE	1986 Mar 01
		SDSS 2007	2007			KPNO	1991 Mar [j]
						IRTF	2007 Jan 24 [b]
MRK335	0.026	FUSE	2000 Nov 21	PG0844+349	0.064	FUSE	2000 Feb 20 [a]
		IUE	1993 Set 05			HST	1999 Oct 21 [a]
		IRTF	2007 Jan 25 [b]			KPNO	2000 Feb [a]
						IRTF	2007 Jan 24 [f]
MRK509	0.034	FUSE	1999 Nov 06 [a]	PG0953+414	0.234	FUSE	1999 Dec 30 [a]
		HST	1992 Jun 21 [a]			HST	2000 Feb 05 [a]
		KPNO	1999 Dec 11 [a]			KPNO	2000 Feb 26 [a]
		IRTF	2004 Jun 01 [f]				
MRK590	0.026	IUE	1991 Jan 15	PG1211+143	0.081	HUT	1995 Mar 15
		SDSS 2007	2007			HST	[c]
						KPNO	1991 Mar [j]
MRK877	0.112	IUE	1993 May	PG1247+267	2.038	HST	[c]
		KPNO	1990 Feb 20 [e]			SDSS 2016	
MRK1044	0.016	FUSE	2004 Jan 01	PG1307+085	0.155	FUSE	1980 May 04
		IUE	1995 Dic 21			IUE	2000 Jun 12
		UKST	2001 - 2006 [g]			KPNO	1991 Mar [j]
			2012 - 2013 [h]			GNIRS	2011 Aug 11
MRK1383	0.086	FUSE	2001 Mar 10	PG1411+442	0.089	FUSE	2000 May 11
		IUE	1985 Mark 03 [i]			HST	[n]
		Steward Obs.	1991 Mar [j]				
MRK1501	0.089	IUE	1984 Jun 12	PG1700+518	0.292	HST	1992 Aug - Dec
		KPNO	1990 Set 18 [e]			INT	1984 May - Jun [p]
						KPNO	1991 Mar [j]
NGC3783	0.010	FUSE	2004 May 05	PG2130+099	0.063	FUSE	2004 Nov 01
		IUE	1992 Jul 30			IUE	1985 Dic
		UKST	2001 - 2006 [g]			KPNO	1991 Mar [j]
		IRTF	2002 Apr 25 [f]				
NGC4151	0.003	FUSE	2002 Jun 01	S50836+71	2.172	Palomar 200in	[o]
		IUE	1996 Jun 09				
		Palomar 200in	1984 Feb 15 [k]				
		IRTF	2002 Apr 23 [f]				

TABLE B.1: Public Spectroscopic data for each of the sources used in Sect. 4.3 (collected in the online Mikulski Archive for Space Telescopes - MAST). Here I report the name of the source, the redshift, the telescope, the date of observation and a reference work ([a] Shang et al., 2005; [b] Landt et al., 2011; [c] Bechtold et al., 2002; [d] Castelló-Mor and Kaspi, 2016; [e] Boroson and Green, 1992; [f] Riffel et al., 2006; [g] Jones et al., 2009; [h] Wang et al., 2014; [i] Kinney, 1991; [j] Kaspi et al., 2000; [k] Ho, Filippeko, and Sargent, 1999; [l] Kennicutt, 1992; [m] Landt et al., 2013; [n] Shang et al., 2011; [o] Lawrence et al., 1996; [p] Pettini and Boksenberg, 1984).

TABLE B.2: AGN sample used in Campitiello et al., 2020 (Sect. 4.3). (1) Name of the source ($_a$ from Kaspi et al., 2000; $_b$ from Peterson et al., 2004; $_c$ from Grier et al., 2012; $_d$ from Bentz et al., 2009; $_e$ from Wang et al. 2014; $_f$ from Bentz et al., 2014; $_g$ from Denney et al., 2010; $_h$ from Trevese et al., 2014; $_i$ from Kaspi et al., 2007); (2) (3) Log value of the spectrum peak frequency $\nu_{\rm p}$ in Hz and luminosity $\nu_{\rm p}L_{\nu_{\rm p}}$ in erg/s (from the SED fit). (4) (5) BH mass and Eddington ratio $\lambda_{\rm Edd}$ (from the SED fit). (6) (7) velocity dispersion and FWHM in km/s related to the Hβ line (for PG 1247+267 and S5 0836+71, these measurements are related to the CIV line). (8) Light travel time in the rest-frame expressed in days. (9) (10) Virial Product computed using the velocity dispersion and the FWHM; the uncertainties are connected to $\tau_{\rm LT}$ and $\sigma_{\rm line}$ (or FWHM). (11) (12) Continuum luminosity at 5100 and 1350 in erg/s as reported in the corresponding reference papers. (13) (14) BH mass computed using the Hβ (or CIV) line FWHM and the luminosity at 5100 (1350) as reported in the reference papers, through the SE relations described in Vestergaard and Peterson, 2006. When a lower error is absent, the measurement has only an upper limit.

Source Name	Log $\nu_{\rm p}$	Log $\nu_{\rm p}L_{\nu_{\rm p}}$	Log $M_{\rm BH,fit}$	$\lambda_{\rm Edd,FIT}$	σ	FWHM	τ_{LT}	Log VP$_\sigma$	Log VP$_{\rm fwhm}$	L_{5100}	L_{1350}	Log $M_{\rm BH,Hfi}$	Log $M_{\rm BH,CIV}$
	[Hz]	[erg/s]	[$M_\odot$]		[km/s]	[km/s]	[lt. days]	[$M_\odot$]	[$M_\odot$]	[erg/s]	[erg/s]	[$M_\odot$]	[$M_\odot$]
(1)	(2)	(3)	(4)	(5)	(6)	(7)	(8)	(9)	(10)	(11)	(12)	(13)	(14)
3C273 $_a$	15.42	46.39	9.175 ± 0.450	0.26 ± 0.12	-	2742 ± 58	$329.9^{+101.0}_{-82.9}$	-	$8.683^{+0.134}_{-0.144}$	45.810	-	8.691	-
$_b$					1777 ± 150	2598 ± 299	$306.8^{+68.5}_{-90.9}$	$8.275^{+0.158}_{-0.229}$	$8.605^{+0.182}_{-0.259}$	45.960	-	8.719	-
Ark120 $_a$	15.28	44.52	8.520 ± 0.450	0.016 ± 0.007	-	5850 ± 480	$38.6^{+5.3}_{-6.5}$	-	$8.409^{+0.124}_{-0.154}$	44.140	-	8.514	-
$_b$					1959 ± 109	5536 ± 297	$47.1^{+8.2}_{-12.4}$	$7.546^{+0.117}_{-0.182}$	$8.448^{+0.115}_{-0.181}$	44.230	-	8.511	-
$_b$					1884 ± 48	5284 ± 203	$37.1^{+4.8}_{-5.4}$	$7.408^{+0.075}_{-0.091}$	$8.304^{+0.086}_{-0.102}$	44.230	-	8.471	-
Fairall9 $_a$	15.42	44.60	8.280 ± 0.450	0.033 ± 0.015	-	5900 ± 650	$17.1^{+3.5}_{-8.0}$	-	$8.063^{+0.172}_{-0.375}$	44.140	-	8.522	-
$_b$					3787 ± 197	6901 ± 707	$17.4^{+3.2}_{-4.3}$	$7.686^{+0.117}_{-0.170}$	$8.207^{+0.158}_{-0.217}$	44.250	-	8.713	-
MRK142 $_d$	15.40	43.92	7.980 ± 0.450	0.014 ± 0.006	859 ± 102	1368 ± 379	$2.74^{+0.73}_{-0.83}$	$5.594^{+0.200}_{-0.267}$	$5.998^{+0.315}_{-0.438}$	43.540	-	6.952	-
$_e$					-	1647 ± 69	$6.4^{+0.8}_{-2.2}$	-	$6.528^{+0.087}_{-0.220}$	43.520	-	7.103	-
MRK290 $_g$	15.41	43.95	7.975 ± 0.450	0.015 ± 0.007	1606 ± 47	4270 ± 157	$8.72^{+1.21}_{-1.02}$	$6.640^{+0.081}_{-0.080}$	$7.490^{+0.088}_{-0.087}$	43.110	-	7.726	-
MRK335 $_a$	15.32	44.22	8.290 ± 0.450	0.014 ± 0.006	-	1260 ± 120	$16.8^{+5.2}_{-3.3}$	-	$6.715^{+0.196}_{-0.182}$	43.790	-	7.006	-
$_b$					917 ± 52	1629 ± 145	$16.8^{+4.8}_{-4.2}$	$6.439^{+0.157}_{-0.176}$	$6.938^{+0.183}_{-0.206}$	43.860	-	7.264	-
$_b$					948 ± 113	1375 ± 357	$12.5^{+6.6}_{-5.5}$	$6.339^{+0.282}_{-0.362}$	$6.662^{+0.385}_{-0.513}$	43.860	-	7.117	-
$_c$					1293 ± 64	1025 ± 35	$14.1^{+0.4}_{-0.4}$	$6.661^{+0.054}_{-0.057}$	$6.459^{+0.041}_{-0.043}$	43.700	-	6.781	-
$_e$					-	1997 ± 265	$10.6^{+1.7}_{-2.9}$	-	$6.915^{+0.173}_{-0.262}$	43.640	-	7.331	-
MRK509 $_a$	15.35	44.68	8.460 ± 0.450	0.026 ± 0.012	-	2860 ± 120	$79.3^{+6.5}_{-6.2}$	-	$8.100^{+0.070}_{-0.073}$	44.170	-	7.908	-
$_b$					1276 ± 28	2715 ± 101	$79.6^{+6.1}_{-5.4}$	$7.401^{+0.051}_{-0.050}$	$8.057^{+0.064}_{-0.063}$	44.280	-	7.918	-

TABLE B.3: Same as Table B.2

Source Name (1)	Log ν_p [Hz] (2)	Log $\nu_p L_{\nu_p}$ [erg/s] (3)	Log $M_{BH,fit}$ [$M_\odot$] (4)	$\lambda_{Edd,FIT}$ (5)	σ [km/s] (6)	FWHM [km/s] (7)	τ_{LT} [lt. days] (8)	Log VP_σ [$M_\odot$] (9)	Log VP_{fwhm} [$M_\odot$] (10)	L_{5100} [erg/s] (11)	L_{1350} [erg/s] (12)	Log $M_{BH,Hfi}$ [$M_\odot$] (13)	Log $M_{BH,CIV}$ [$M_\odot$] (14)
MRK590 *a*	15.50	43.18	7.410 ± 0.450	0.009 ± 0.004	-	2170 ± 120	$20.5^{+4.5}_{-3.0}$	-	$7.273^{+0.133}_{-0.118}$	43.710	-	7.438	-
b					789 ± 74	1675 ± 587	$20.7^{+3.5}_{-2.7}$	$6.399^{+0.146}_{-0.146}$	$7.052^{+0.329}_{-0.435}$	43.810	-	7.263	-
b					1935 ± 52	2566 ± 106	$14.0^{+8.5}_{-8.8}$	$7.008^{+0.229}_{-0.454}$	$7.253^{+0.241}_{-0.467}$	43.810	-	7.634	-
b					1251 ± 72	2115 ± 575	$29.2^{+4.9}_{-5.0}$	$6.948^{+0.116}_{-0.133}$	$7.404^{+0.276}_{-0.357}$	43.810	-	7.466	-
b					1201 ± 130	1979 ± 386	$28.8^{+3.6}_{-4.2}$	$6.907^{+0.140}_{-0.168}$	$7.341^{+0.206}_{-0.257}$	43.810	-	7.408	-
MRK877 *a*	15.20	44.91	8.875 ± 0.450	0.017 ± 0.008	-	3880 ± 650	$70.1^{+27.0}_{-36.8}$	-	$8.312^{+0.276}_{-0.483}$	44.370	-	8.273	-
b					2626 ± 211	4718 ± 991	$71.5^{+29.6}_{-33.7}$	$7.981^{+0.218}_{-0.350}$	$8.490^{+0.316}_{-0.482}$	44.480	-	8.498	-
MRK1044 *e*	15.50	43.39	7.515 ± 0.450	0.012 ± 0.006	-	1211 ± 48	$4.8^{+7.4}_{-3.7}$	-	$6.136^{+0.439}_{-0.675}$	43.050	-	6.601	-
MRK1383 *b*	15.56	45.32	8.360 ± 0.450	0.145 ± 0.067	3442 ± 308	6323 ± 1295	$95.0^{+29.9}_{-37.1}$	$8.340^{+0.193}_{-0.296}$	$8.868^{+0.281}_{-0.414}$	44.720	-	8.872	-
MRK1501 *c*	15.34	44.69	8.485 ± 0.450	0.026 ± 0.012	3321 ± 107	5054 ± 145	$15.5^{+2.2}_{-1.8}$	$7.521^{+0.085}_{-0.082}$	$7.886^{+0.082}_{-0.079}$	44.320	-	8.477	-
NGC3783 *a*	15.40	43.64	7.840 ± 0.450	0.010 ± 0.005	-	4100 ± 1160	$4.5^{+3.6}_{-3.1}$	-	$7.167^{+0.472}_{-0.796}$	43.250	-	7.761	-
b					1753 ± 141	3093 ± 529	$10.2^{+3.3}_{-2.3}$	$6.785^{+0.189}_{-0.184}$	$7.278^{+0.259}_{-0.274}$	43.260	-	7.521	-
NGC4151 *a*	15.20	42.35	7.595 ± 0.450	0.001 ± 0.000	-	5230 ± 920	$3.0^{+1.8}_{-1.4}$	-	$7.203^{+0.345}_{-0.441}$	42.860	-	7.777	-
b					1914 ± 42	4248 ± 516	$3.1^{+1.3}_{-1.3}$	$6.344^{+0.171}_{-0.255}$	$7.036^{+0.252}_{-0.349}$	42.880	-	7.606	-
NGC5548 *a*	15.33	43.52	7.920 ± 0.450	0.006 ± 0.003	-	5500 ± 400	$21.6^{+2.4}_{-0.7}$	-	$8.104^{+0.107}_{-0.080}$	43.430	-	8.106	-
b					1687 ± 56	4044 ± 199	$19.7^{+1.5}_{-1.5}$	$7.037^{+0.060}_{-0.064}$	$7.797^{+0.074}_{-0.078}$	43.510	-	7.879	-
b					2026 ± 68	5706 ± 357	$16.4^{+1.2}_{-1.1}$	$7.117^{+0.059}_{-0.060}$	$8.016^{+0.083}_{-0.086}$	43.510	-	8.178	-
d					4270 ± 292	11177 ± 2266	$4.18^{+0.86}_{-1.30}$	$7.170^{+0.139}_{-0.223}$	$8.006^{+0.242}_{-0.359}$	42.620	-	8.317	-
g					1822 ± 35	4849 ± 112	$12.40^{+2.74}_{-3.85}$	$6.903^{+0.103}_{-0.178}$	$7.753^{+0.107}_{-0.182}$	42.660	-	7.611	-
NGC7469 *a*	15.40	43.69	7.865 ± 0.450	0.011 ± 0.005	-	3220 ± 1580	$5.0^{+0.6}_{-1.1}$	-	$7.003^{+0.396}_{-0.694}$	43.740	-	7.796	-
b					1456 ± 207	2169 ± 459	$4.5^{+0.7}_{-0.8}$	$6.268^{+0.178}_{-0.218}$	$6.614^{+0.230}_{-0.292}$	43.720	-	7.443	-
e					-	1722 ± 30	$24.3^{+4.0}_{-4.0}$	-	$7.146^{+0.081}_{-0.093}$	43.560	-	7.162	-
PG0026+129 *a*	15.47	45.31	8.535 ± 0.450	0.095 ± 0.044	-	1358 ± 91	$109.5^{+25.4}_{-31.6}$	-	$7.594^{+0.147}_{-0.208}$	44.850	-	7.601	-
b					1773 ± 285	1719 ± 495	$111.0^{+24.1}_{-28.3}$	$7.831^{+0.215}_{-0.280}$	$7.804^{+0.305}_{-0.423}$	45.020	-	7.891	-
e					-	2544 ± 56	$111.0^{+24.1}_{-28.3}$	-	$8.145^{+0.104}_{-0.147}$	44.840	-	8.141	-
PG0052+251 *a*	15.35	45.40	8.820 ± 0.450	0.060 ± 0.028	-	4550 ± 270	$85.6^{+26.0}_{-26.8}$	-	$8.537^{+0.165}_{-0.216}$	44.810	-	8.631	-
b					1783 ± 86	4165 ± 381	$89.8^{+24.5}_{-24.1}$	$7.744^{+0.146}_{-0.179}$	$8.481^{+0.181}_{-0.219}$	44.960	-	8.629	-

TABLE B.4: Same as Tables B.2 - B.3

Source Name (1)	Log $\nu_{\rm p}$ [Hz] (2)	Log $\nu_{\rm p} L_{\nu_{\rm p}}$ [erg/s] (3)	Log $M_{\rm BH,fit}$ [$M_\odot$] (4)	$\lambda_{\rm Edd,FIT}$ (5)	σ [km/s] (6)	FWHM [km/s] (7)	τ_{LT} [lt. days] (8)	Log VP$_\sigma$ [$M_\odot$] (9)	Log VP$_{\rm fwhm}$ [$M_\odot$] (10)	L_{5100} [erg/s] (11)	L_{1350} [erg/s] (12)	Log $M_{\rm BH,Hfi}$ [$M_\odot$] (13)	Log $M_{\rm BH,CIV}$ [$M_\odot$] (14)
PG0804+761 $_a$	15.40	45.34	8.690 ± 0.450	0.071 ± 0.033	-	2430 ± 42	$137.3^{+23.6}_{-21.8}$	-	$8.197^{+0.084}_{-0.090}$	44.820	-	8.091	-
$_b$					1971 ± 105	2012 ± 845	$146.9^{+18.8}_{-18.9}$	$8.045^{+0.097}_{-0.107}$	$8.063^{+0.357}_{-0.533}$	44.940	-	7.987	-
PG0844+349 $_a$	15.44	45.00	8.440 ± 0.450	0.058 ± 0.027	-	2830 ± 120	$12.2^{+13.2}_{-10.3}$	-	$7.278^{+0.355}_{-0.845}$	44.240	-	7.934	-
$_b$					1448 ± 79	2148 ± 612	$3.0^{+12.4}_{-10.0}$	$6.087^{+0.757}_{-}$	$6.430^{+0.928}_{-}$	44.350	-	7.749	-
$_e$					-	2694 ± 58	$32.3^{+13.7}_{-13.4}$	-	$7.658^{+0.172}_{-0.252}$	44.150	-	7.846	-
PG0953+414 $_a$	15.45	45.88	8.860 ± 0.450	0.167 ± 0.077	-	2723 ± 62	$150.9^{+21.8}_{-26.6}$	-	$8.337^{+0.078}_{-0.104}$	45.080	-	8.320	-
$_b$					1306 ± 144	3002 ± 398	$150.1^{+21.6}_{-22.6}$	$7.697^{+0.149}_{-0.172}$	$8.420^{+0.167}_{-0.194}$	45.220	-	8.475	-
PG1211+143 $_a$	15.37	45.20	8.680 ± 0.450	0.053 ± 0.024	-	1479 ± 66	$94.9^{+29.5}_{-40.5}$	-	$7.606^{+0.155}_{-0.281}$	44.690	-	7.595	-
$_b$					1080 ± 102	1317 ± 138	$93.8^{+25.6}_{-42.1}$	$7.328^{+0.183}_{-0.345}$	$7.500^{+0.191}_{-0.355}$	44.750	-	7.524	-
$_e$					-	2012 ± 37	$93.8^{+25.6}_{-42.1}$	-	$7.868^{+0.121}_{-0.275}$	44.660	-	7.847	-
PG1247+267 $_h$	15.39	47.58	9.830 ± 0.450	0.895 ± 0.414	2104 ± 540	4568 ± 1338	$142.0^{+26.0}_{-25.0}$	$8.087^{+0.271}_{-0.342}$	$8.760^{+0.296}_{-0.385}$	-	47.590	-	9.882
PG1307+085 $_a$	15.55	45.38	8.410 ± 0.450	0.148 ± 0.069	-	5260 ± 270	$93.5^{+39.8}_{-93.5}$	-	$8.701^{+0.197}_{-}$	44.720	-	8.712	-
$_b$					1820 ± 122	5058 ± 524	$105.6^{+36.0}_{-46.6}$	$7.832^{+0.184}_{-0.313}$	$8.720^{+0.213}_{-0.348}$	44.880	-	8.758	-
PG1411+442 $_a$	15.24	44.90	8.790 ± 0.450	0.020 ± 0.009	-	2740 ± 110	$108.4^{+66.1}_{-65.2}$	-	$8.199^{+0.241}_{-0.435}$	44.510	-	8.040	-
$_b$					1607 ± 169	2398 ± 353	$124.3^{+61.0}_{-61.7}$	$7.795^{+0.260}_{-0.394}$	$8.143^{+0.293}_{-0.436}$	44.630	-	7.985	-
PG1700+518 $_a$	15.04	45.65	9.565 ± 0.450	0.019 ± 0.009	-	1970 ± 150	$88.2^{+190.4}_{-88.2}$	-	$7.823^{+0.563}_{-}$	45.430	-	8.214	-
$_b$					1700 ± 123	1846 ± 682	$251.8^{+45.9}_{-38.8}$	$8.150^{+0.133}_{-0.138}$	$8.222^{+0.346}_{-0.473}$	45.630	-	8.257	-
$_e$					-	2252 ± 85	$251.8^{+45.9}_{-38.8}$	-	$8.395^{+0.105}_{-0.106}$	45.440	-	8.335	-
PG2130+099 $_a$	15.39	44.70	8.390 ± 0.450	0.032 ± 0.015	-	3010 ± 180	$177.2^{+128.2}_{-25.4}$	-	$8.494^{+0.287}_{-0.121}$	44.330	-	8.032	-
$_b$					1623 ± 86	2912 ± 231	$158.1^{+29.8}_{-18.7}$	$7.908^{+0.120}_{-0.102}$	$8.416^{+0.141}_{-0.126}$	44.460	-	8.068	-
$_c$					1825 ± 65	2097 ± 102	$15.5^{+2.2}_{-1.8}$	$7.001^{+0.088}_{-0.085}$	$7.122^{+0.099}_{-0.097}$	44.150	-	7.628	-
$_e$					-	2450 ± 188	$31.0^{+4.0}_{-4.0}$	-	$7.558^{+0.117}_{-0.129}$	44.130	-	7.753	-
S50836+71 $_i$	15.46	47.22	9.510 ± 0.450	0.816 ± 0.377	-	9700 ± 0	$188.0^{+27.0}_{-37.0}$	-	$9.536^{+0.058}_{-0.095}$	-	47.050	-	10.250

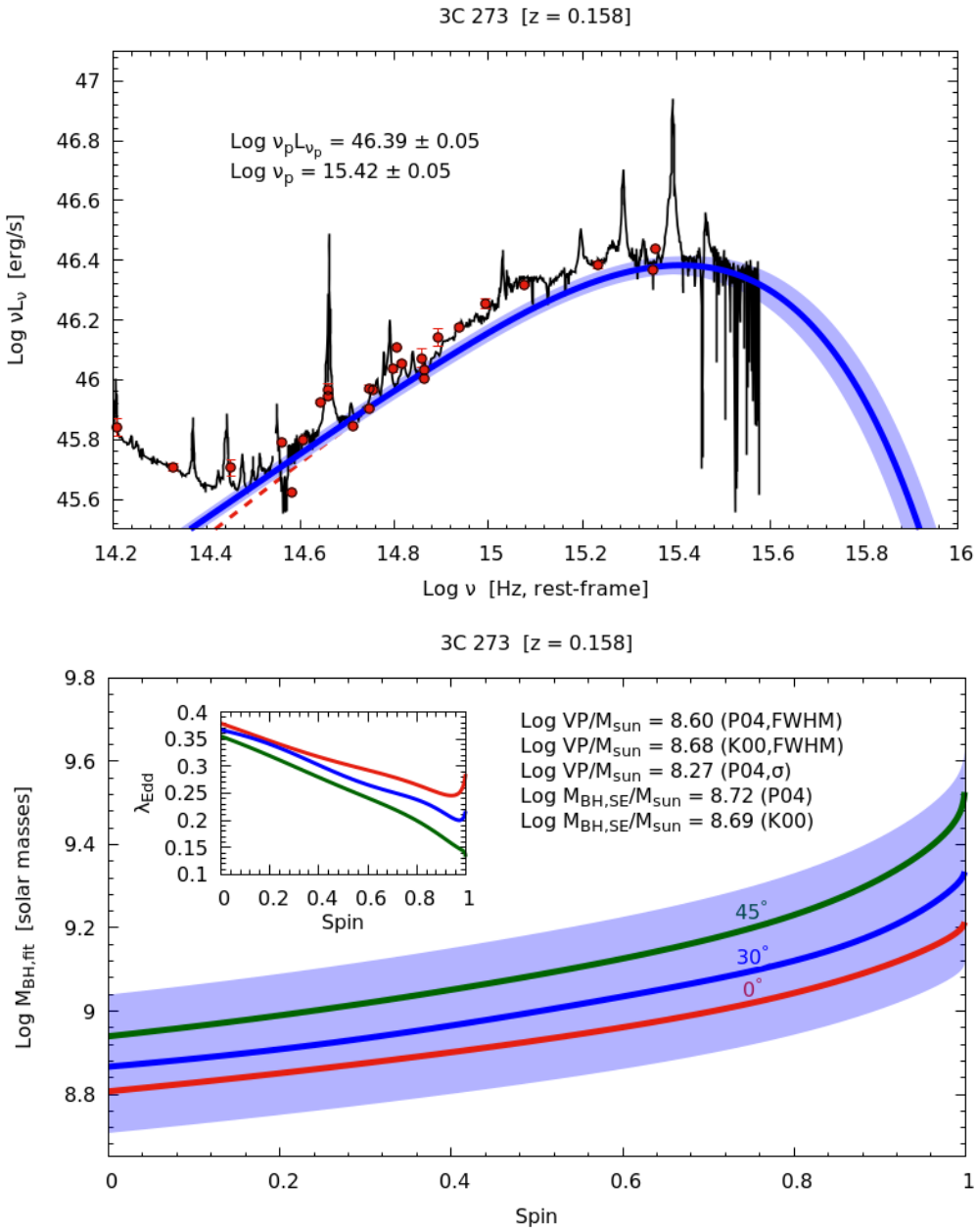

FIGURE B.1: Other recent BH mass estimates for 3C273 are from Sturm et al., 2018 (Log $M/M_\odot = 8.41^{+0.16}_{-0.23}$) and Zhang et al., 2019 (Log VP(FWHM)$/M_\odot = 8.50^{+0.04}_{-0.06}$). On each of the following plots, different BH mass estimates are reported: VPs computed using the $\sigma_{\rm line}$ and FWHM, and SE estimates computed using the equations of Vestergaard and Peterson, 2006 and line data from different works (K00 for Kaspi et al., 2000; P04 for Peterson et al., 2004; G12 for Grier et al., 2012; B09 for Bentz et al., 2009; W14 for Wang et al., 2014; B14 for Bentz et al., 2014; D10 for Denney et al., 2010; T14 for Trevese et al., 2014; K07 for Kaspi et al., 2007).

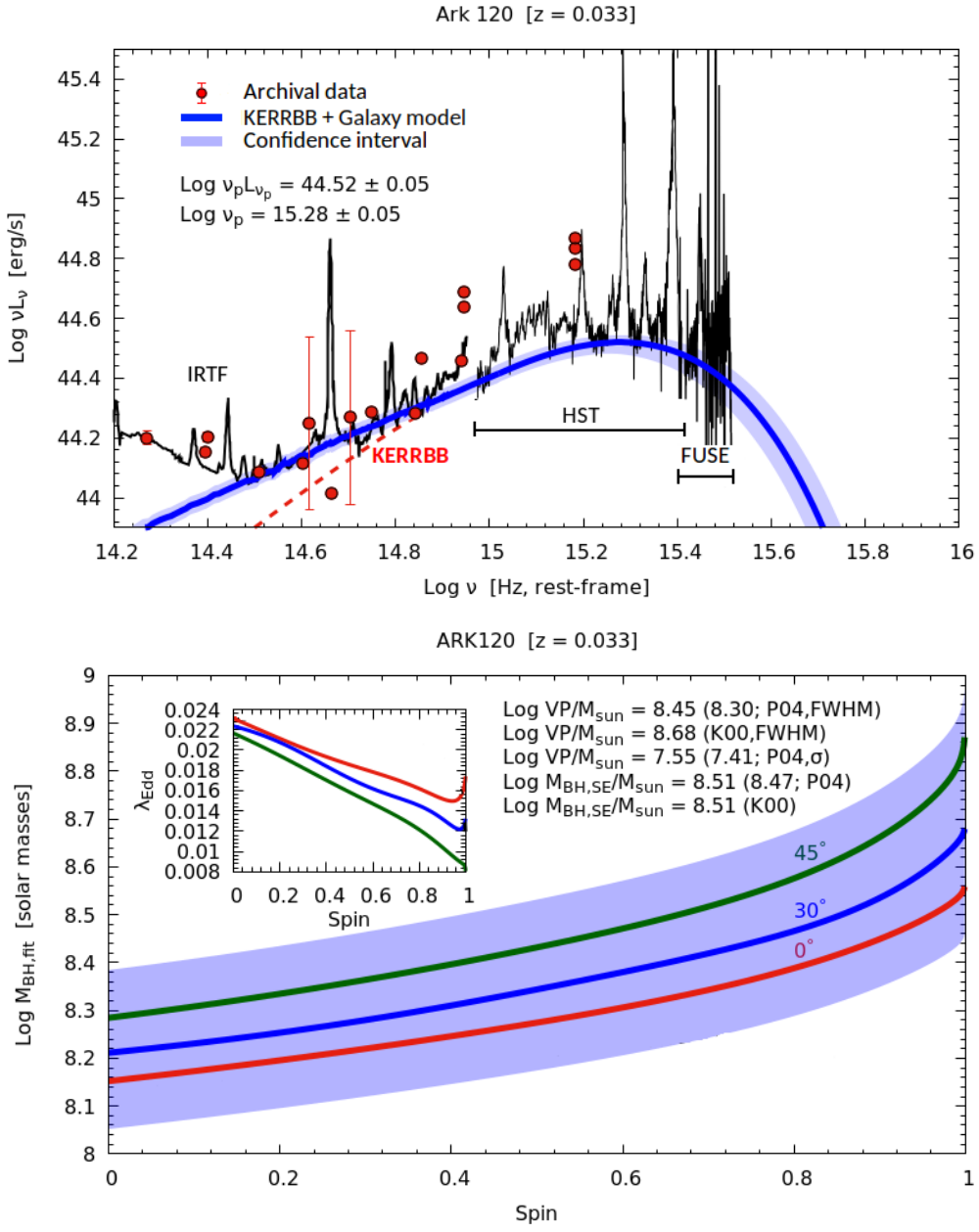

FIGURE B.2: Other BH mass estimates are from Haas et al., 2011 (Log $\mathrm{VP}(\sigma_{\mathrm{line}})/M_{\odot} = 7.53^{+0.13}_{-0.19}$) and Du et al., 2018 (Log $\mathrm{VP(FWHM)}/\mathrm{M}_{\odot} = 8.12^{+0.08}_{-0.09}$). The galaxy emission is necessary to obtain a satisfactory fit at Log $\nu/\mathrm{Hz} = 14.4 - 14.8$. The spectrum rise at Log $\nu/\mathrm{Hz} < 14.5$ is caused by the IR emission of the dusty torus.

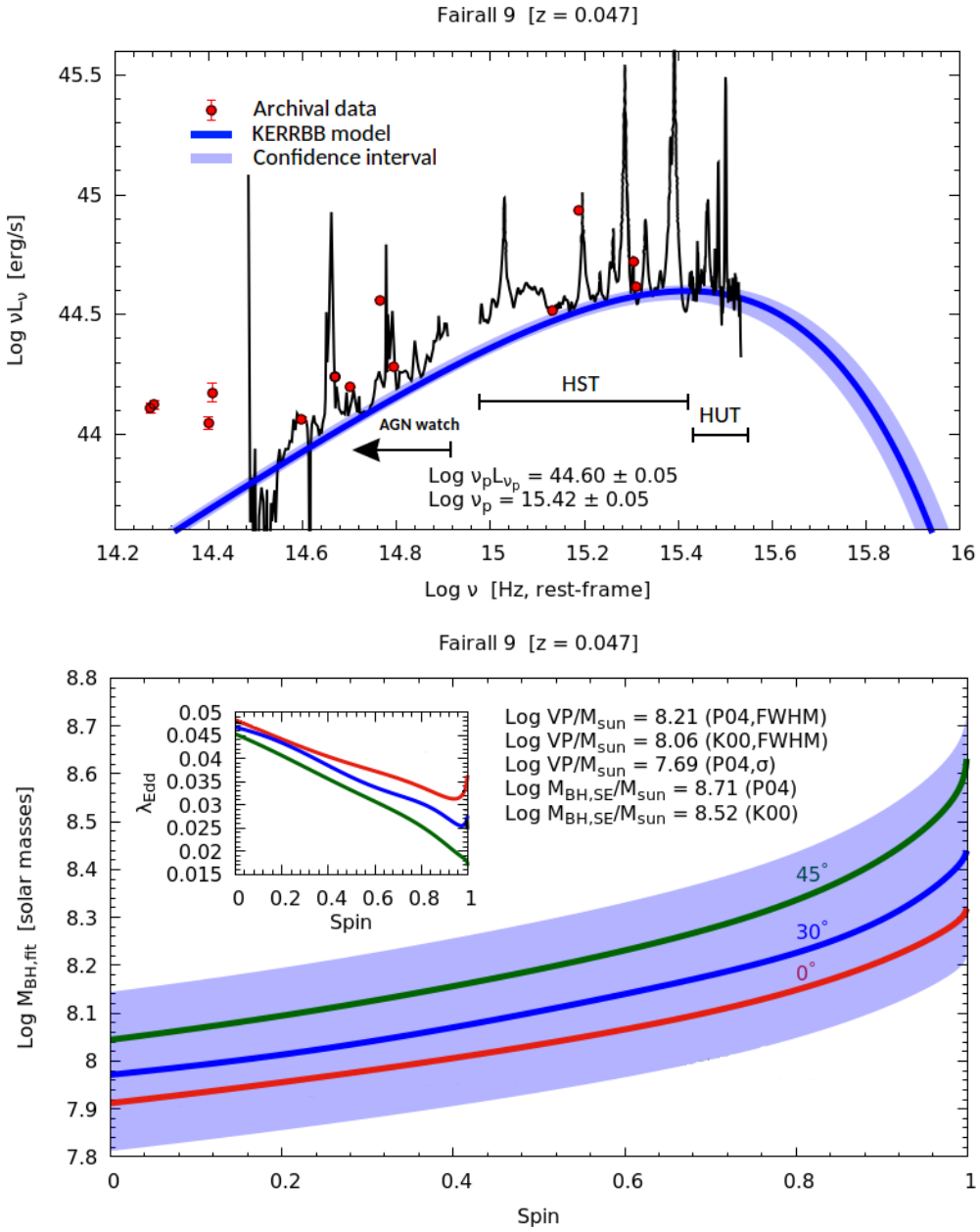
Fairall 9 [z = 0.047]
Archival data
KERRBB model
Confidence interval
HST
HUT
AGN watch
Log νpLνp = 44.60 ± 0.05
Log νp = 15.42 ± 0.05
Log νLν [erg/s]
Log ν [Hz, rest-frame]
Fairall 9 [z = 0.047]
Log VP/Msun = 8.21 (P04,FWHM)
Log VP/Msun = 8.06 (K00,FWHM)
Log VP/Msun = 7.69 (P04,σ)
Log MBH,SE/Msun = 8.71 (P04)
Log MBH,SE/Msun = 8.52 (K00)
λEdd
Spin
45°
30°
0°
Log MBH,fit [solar masses]
Spin

FIGURE B.3

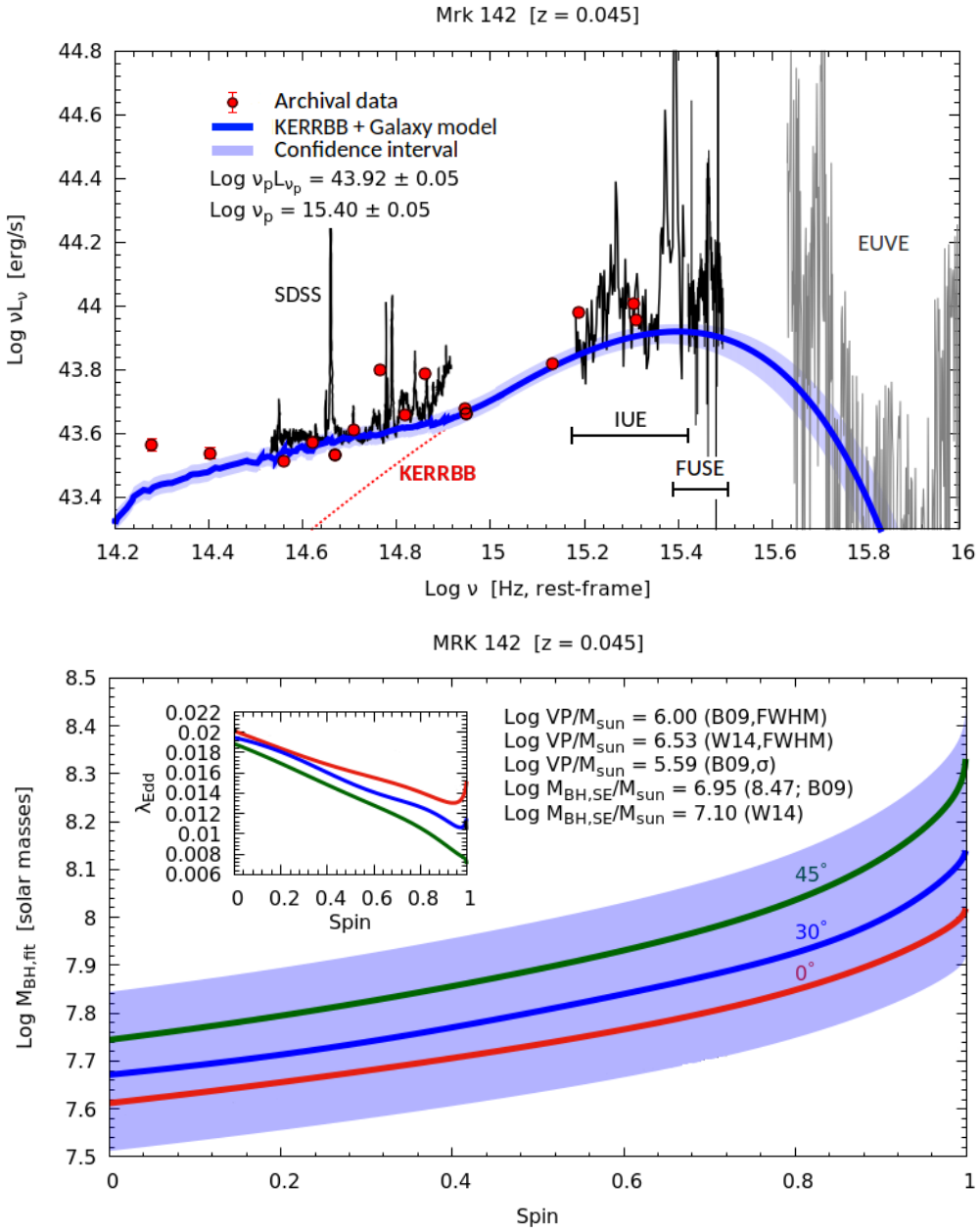

FIGURE B.4: Spectroscopic data in the EUV region are very noisy and represented in gray to give an idea of the emission at large frequencies. Another BH mass estimate is from Li et al., 2018 (Log $\mathrm{VP}(\sigma_{\mathrm{line}})/M_{\odot} = 6.23^{+0.26}_{-0.45}$).

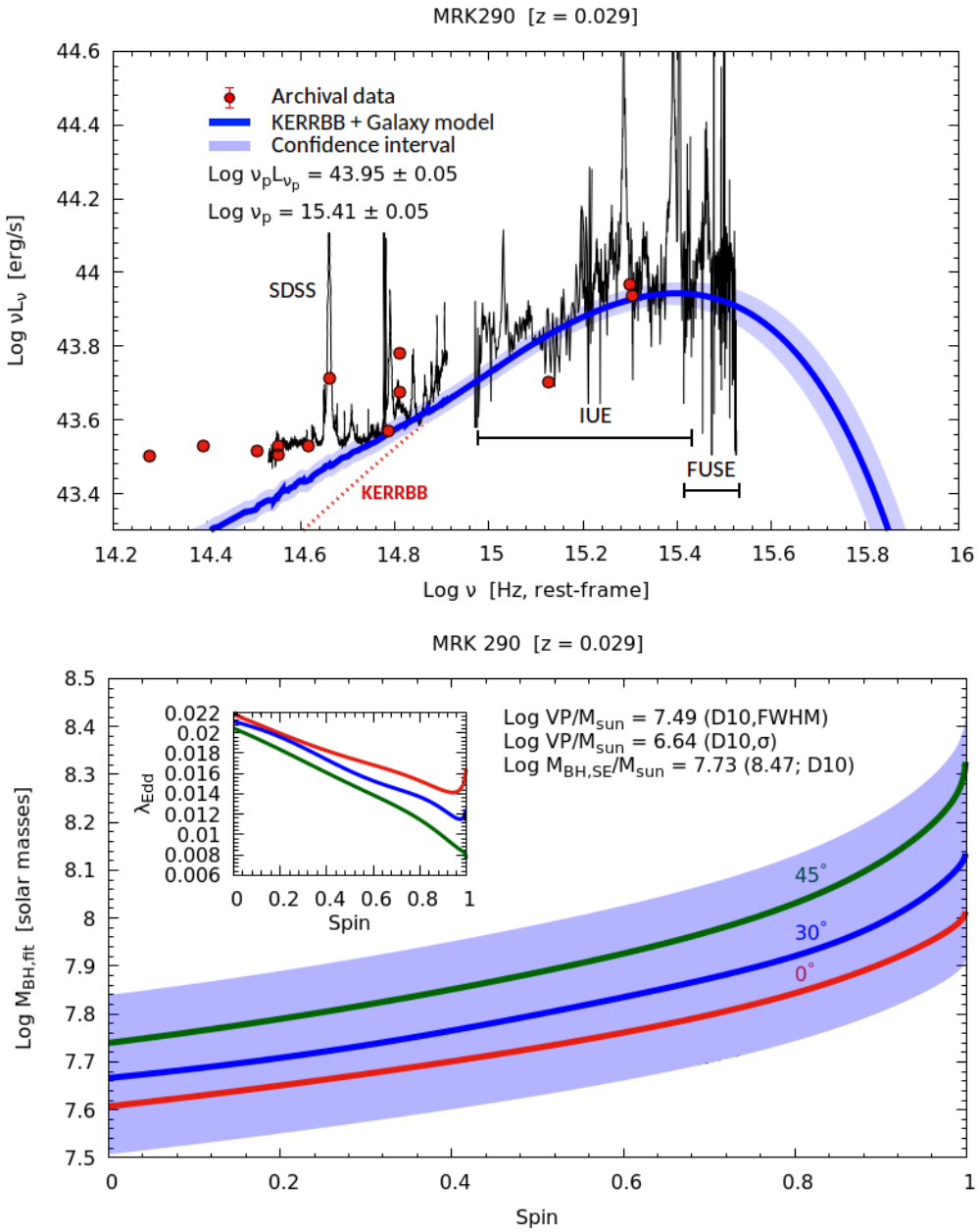

FIGURE B.5: Spectrum rise at Log ν/Hz < 14.5 is caused by the IR emission of the dusty torus.

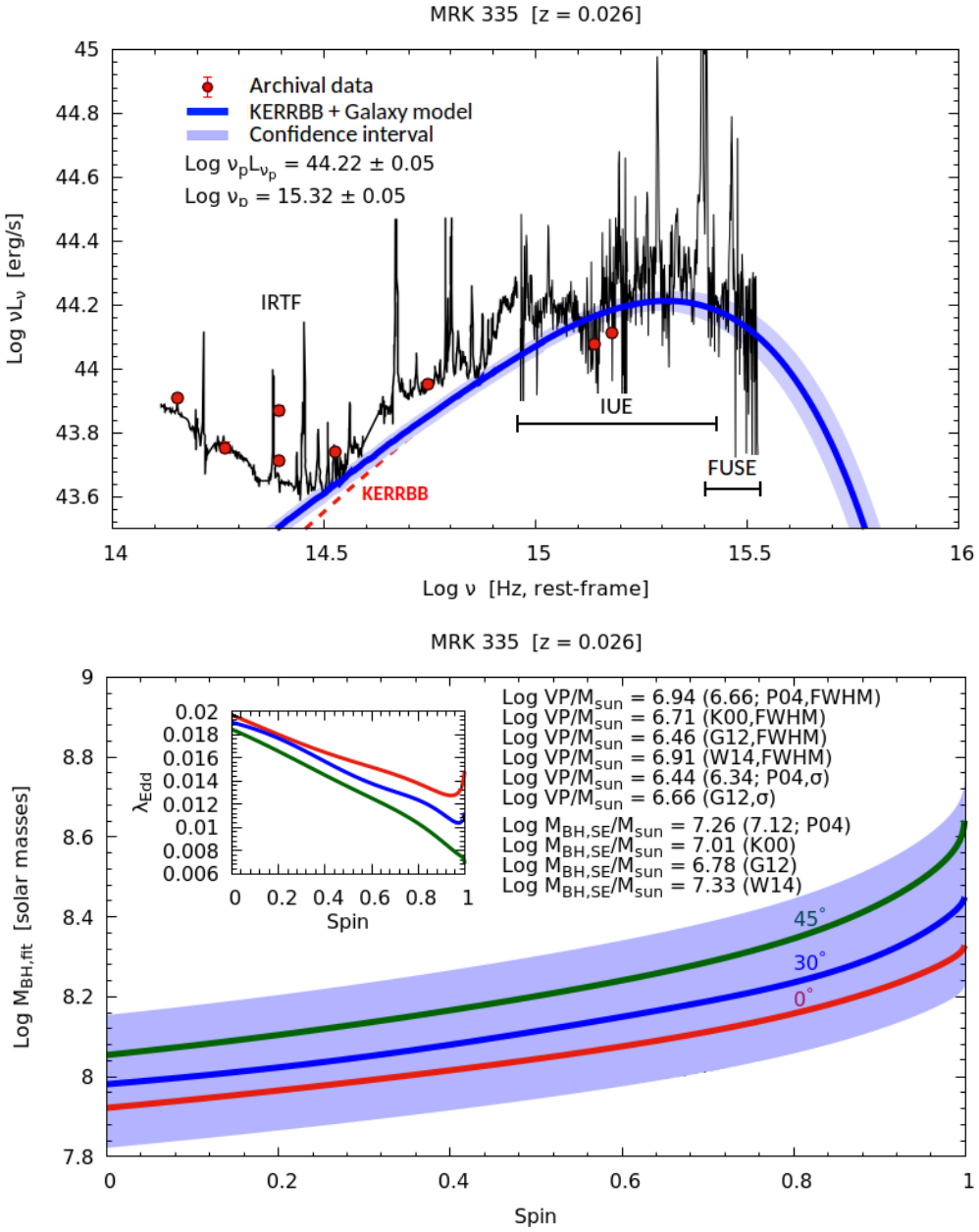

FIGURE B.6: HST data around the Lyα-CIV region are also available, in good agreement with IUE data. The spectrum rise at Log ν/Hz < 14.4 is caused by the IR emission of the dusty torus. Other BH mass estimates are from Haas et al., 2011 (Log $M/M_\odot = 6.45^{+0.14}_{-0.22}$) and Grier et al., 2017 (Log $M/M_\odot = 7.25 \pm 0.10$).

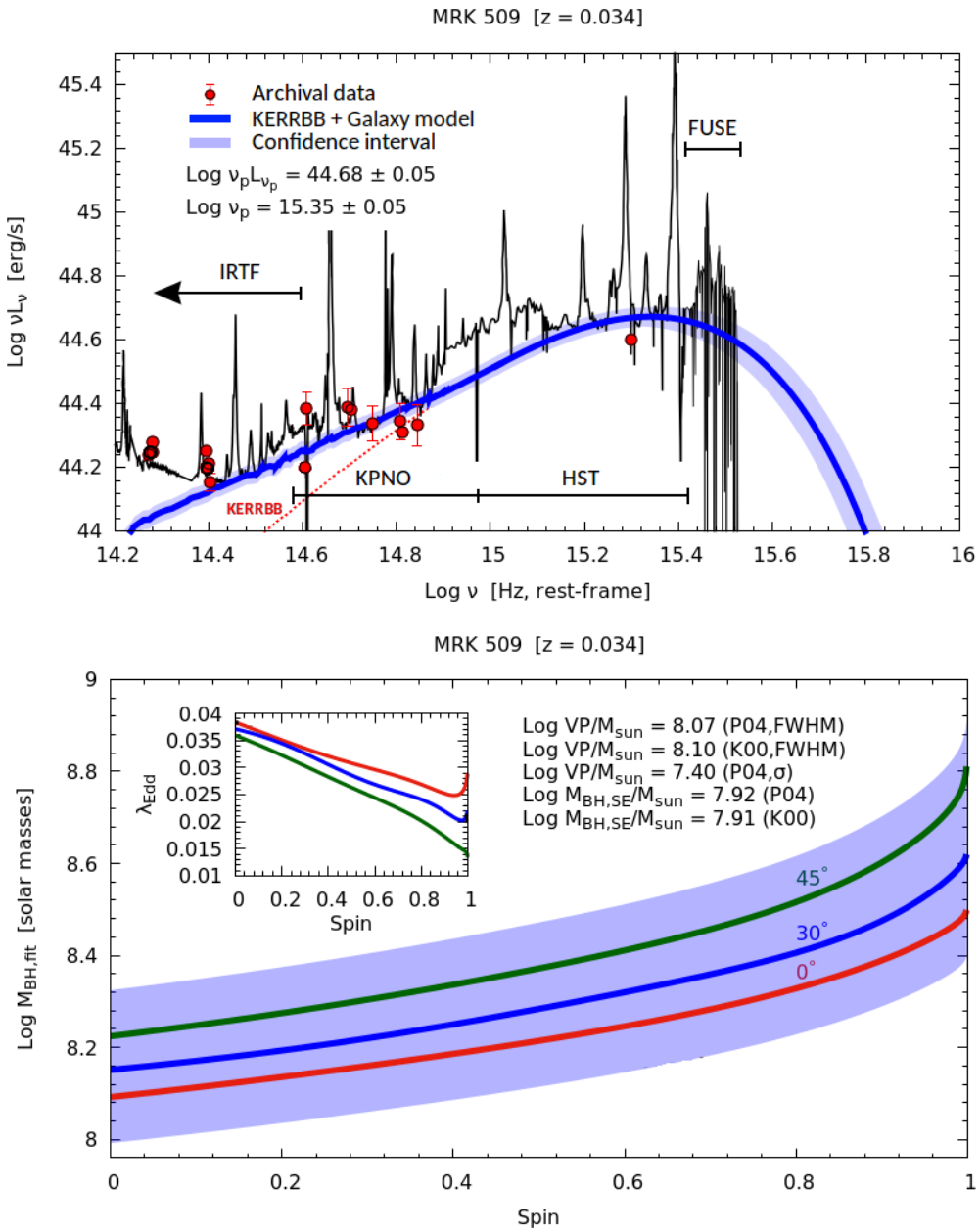

FIGURE B.7: Spectrum rise at Log ν/Hz < 14.5 is caused by the IR emission of the dusty torus.

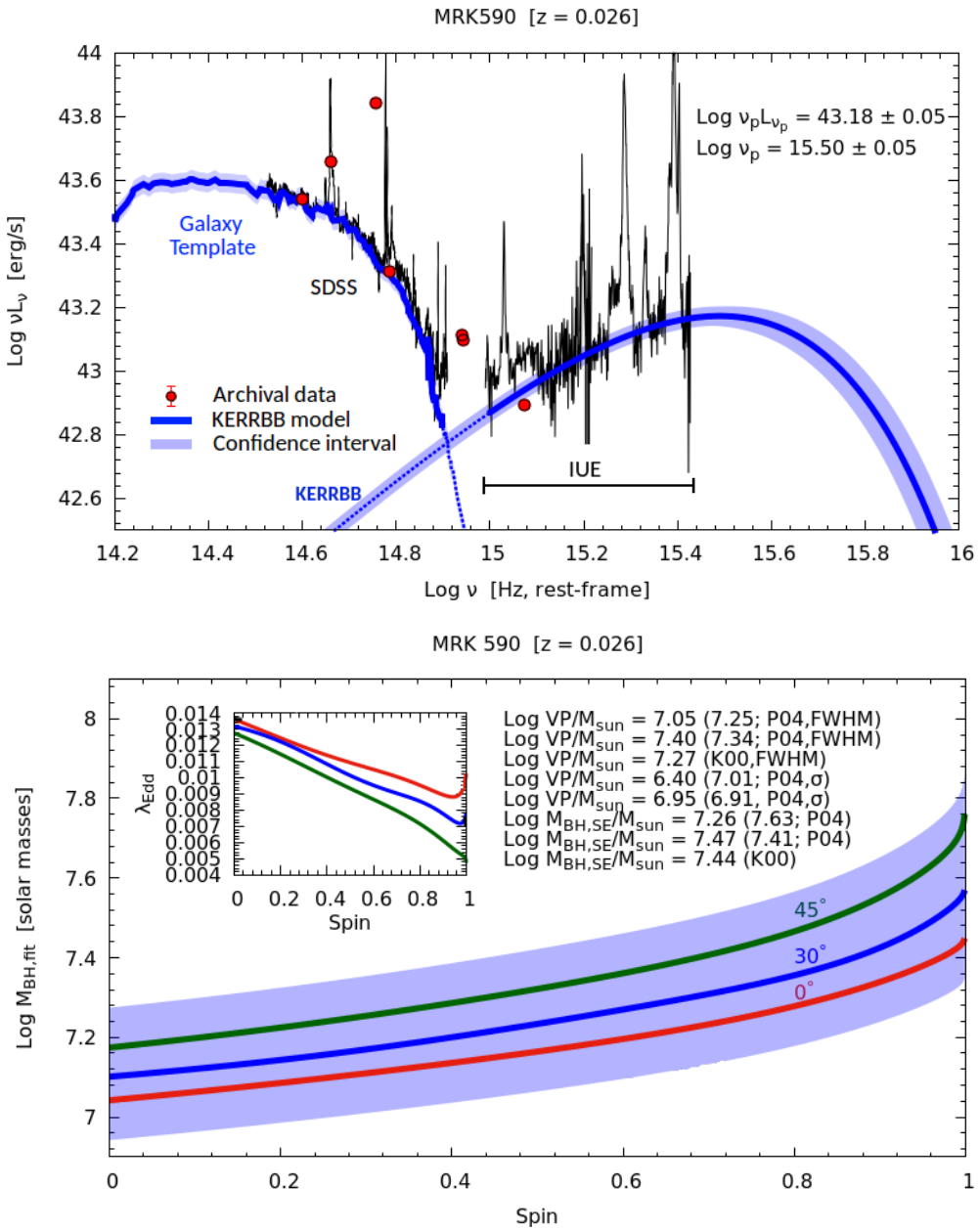

FIGURE B.8: A prominent host-galaxy emission is required in the fitting procedure; for a satisfactory fit, the AD emission has to be cut at around Log ν/Hz $\sim$ 15 (i.e., the AD size is smaller than $10^6 R_g$ as implemented in KERRBB by default). In the range Log ν/Hz $= 14.9 - 15$, the Balmer continuum can describe the rise of spectroscopic data (not represented for clarity). For this source, the peak is not visible but the curvature at smaller frequencies was used to obtain an estimate of the position.

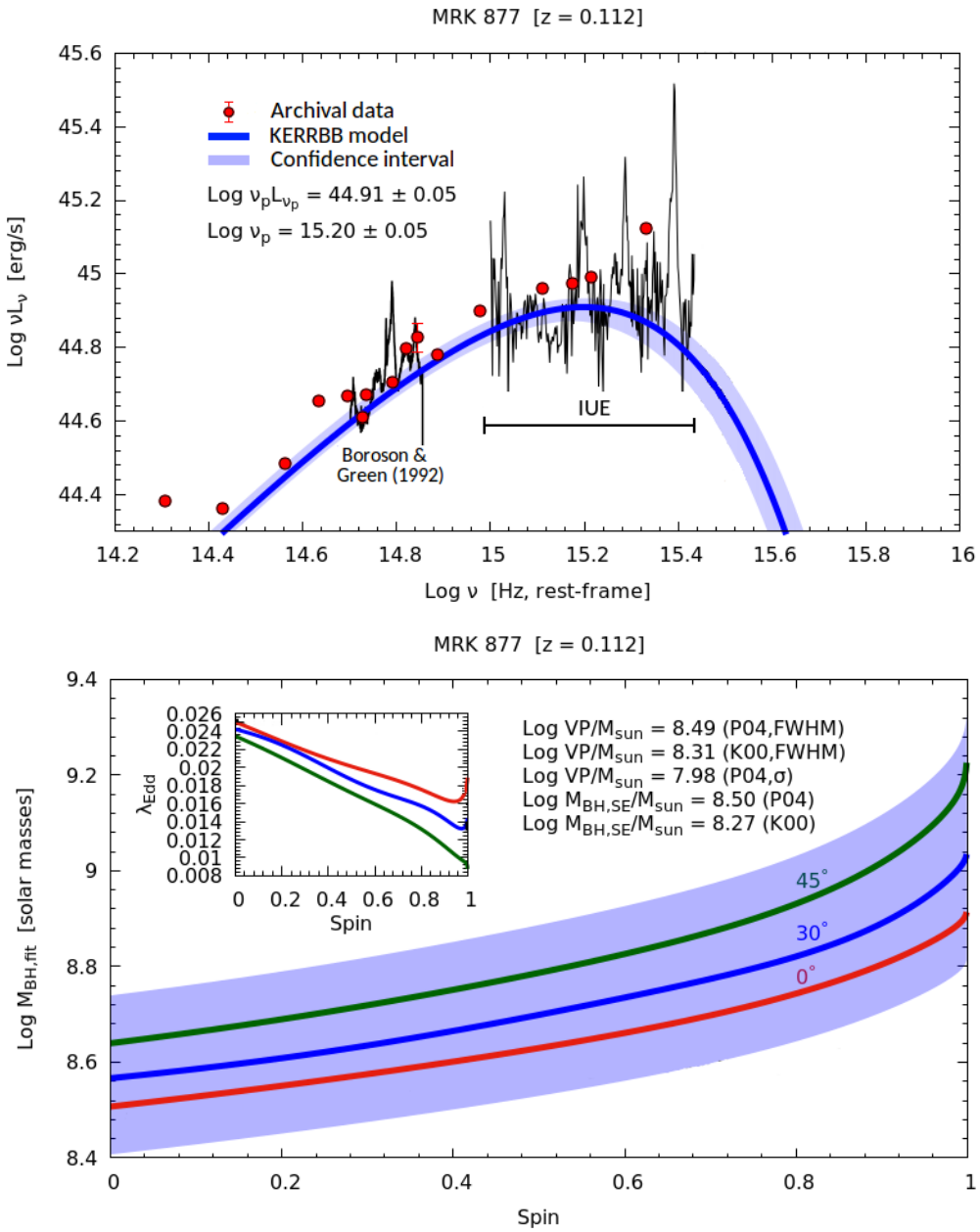

FIGURE B.9: Some absorption features are present at Log ν/Hz $\sim$ 15.1 $-$ 15.2; nevertheless, they do not interfere with the fitting procedure.

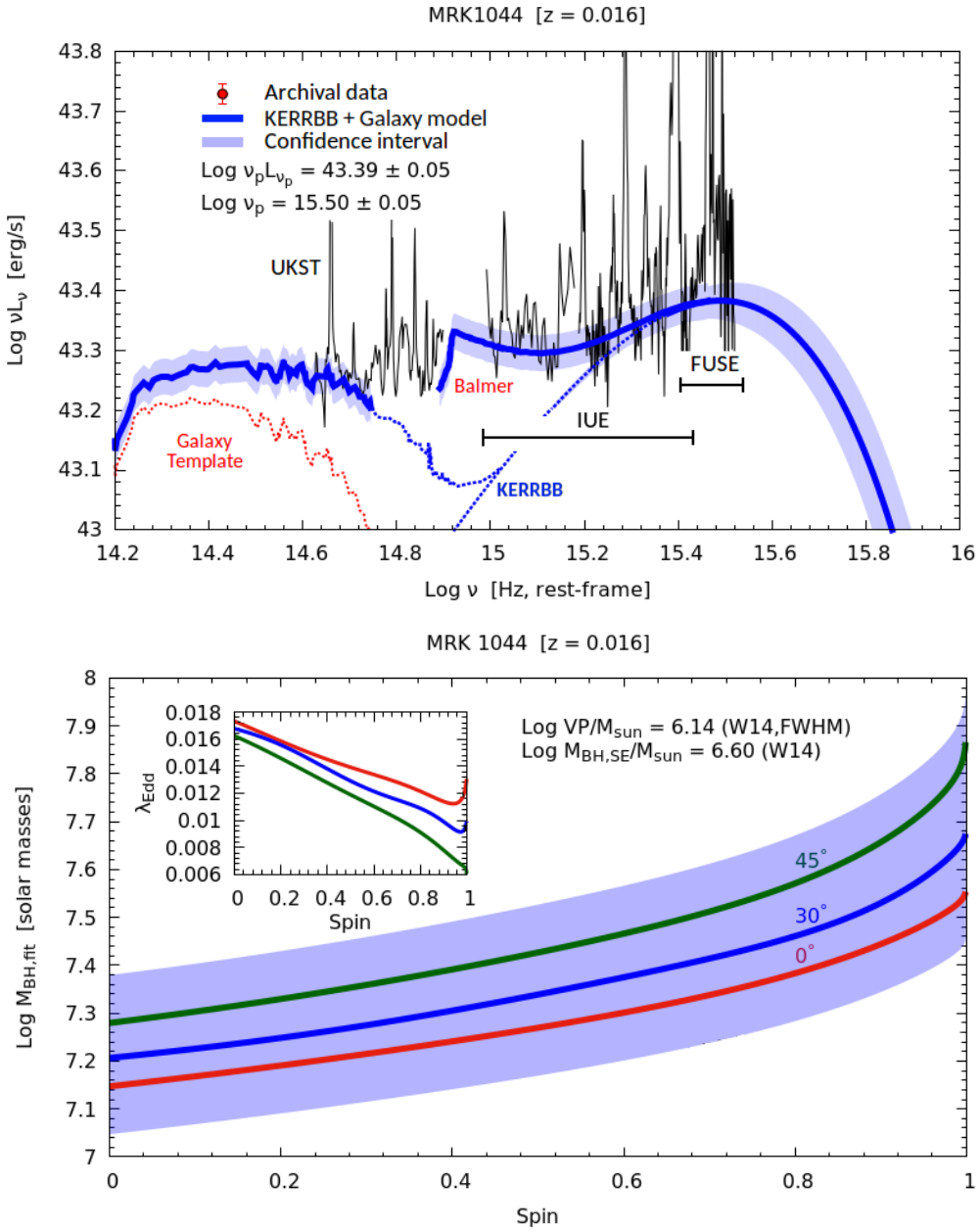

FIGURE B.10: The quality of spectroscopic data is low but nonetheless, the fit was rather satisfactory. The Balmer continuum is shown to visualize the rise in the spectrum at Log ν/Hz $\sim$ 15.

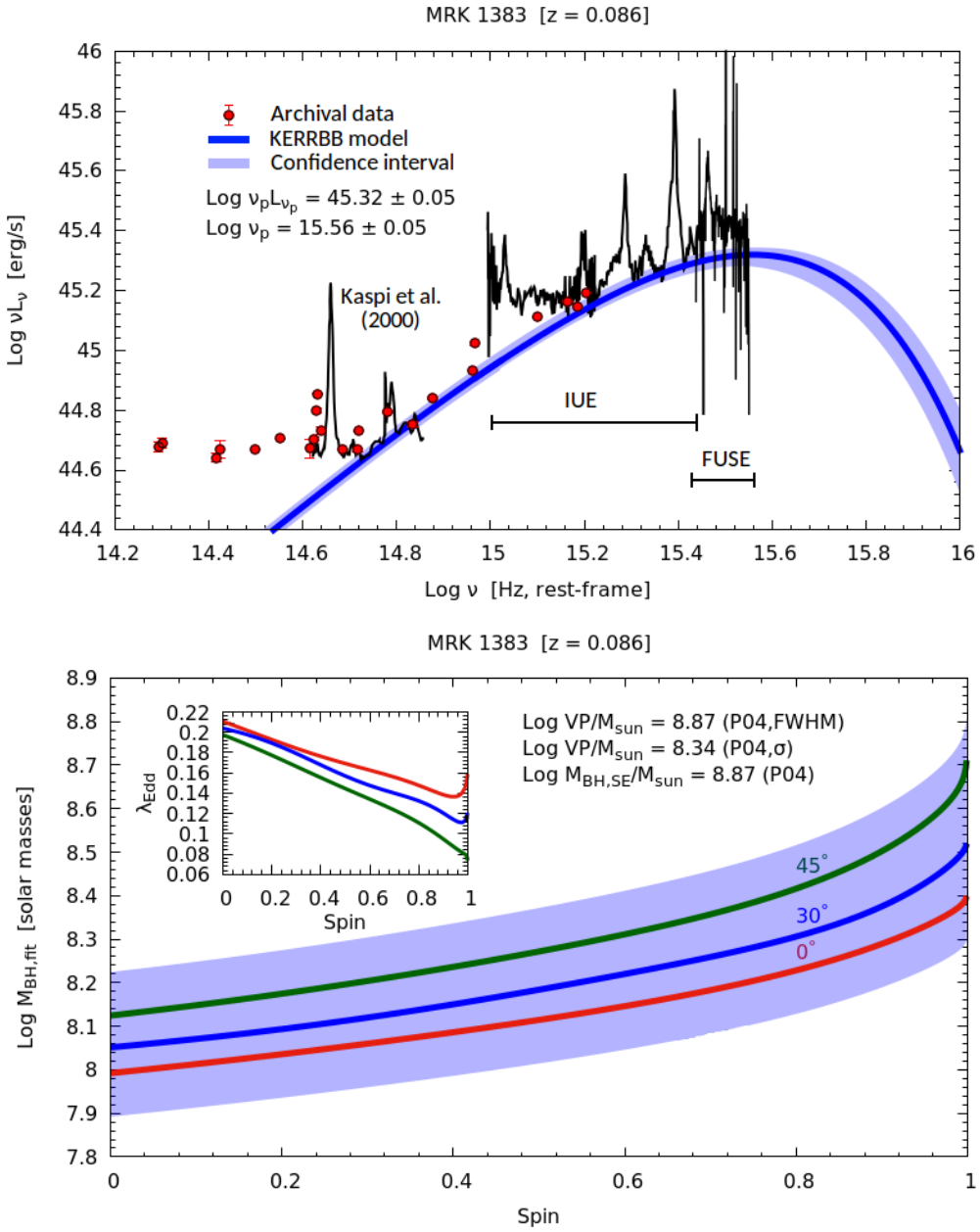
MRK 1383 [z = 0.086]
Archival data
KERRBB model
Confidence interval
Log $\nu_p L_{\nu_p}$ = 45.32 ± 0.05
Log ν_p = 15.56 ± 0.05
Kaspi et al. (2000)
IUE
FUSE
Log νL$_\nu$ [erg/s]
Log ν [Hz, rest-frame]
MRK 1383 [z = 0.086]
Log VP/M$_{sun}$ = 8.87 (P04,FWHM)
Log VP/M$_{sun}$ = 8.34 (P04,σ)
Log M$_{BH,SE}$/M$_{sun}$ = 8.87 (P04)
45°
30°
0°
λ$_{Edd}$
Spin
Log M$_{BH,fit}$ [solar masses]
Spin

FIGURE B.11

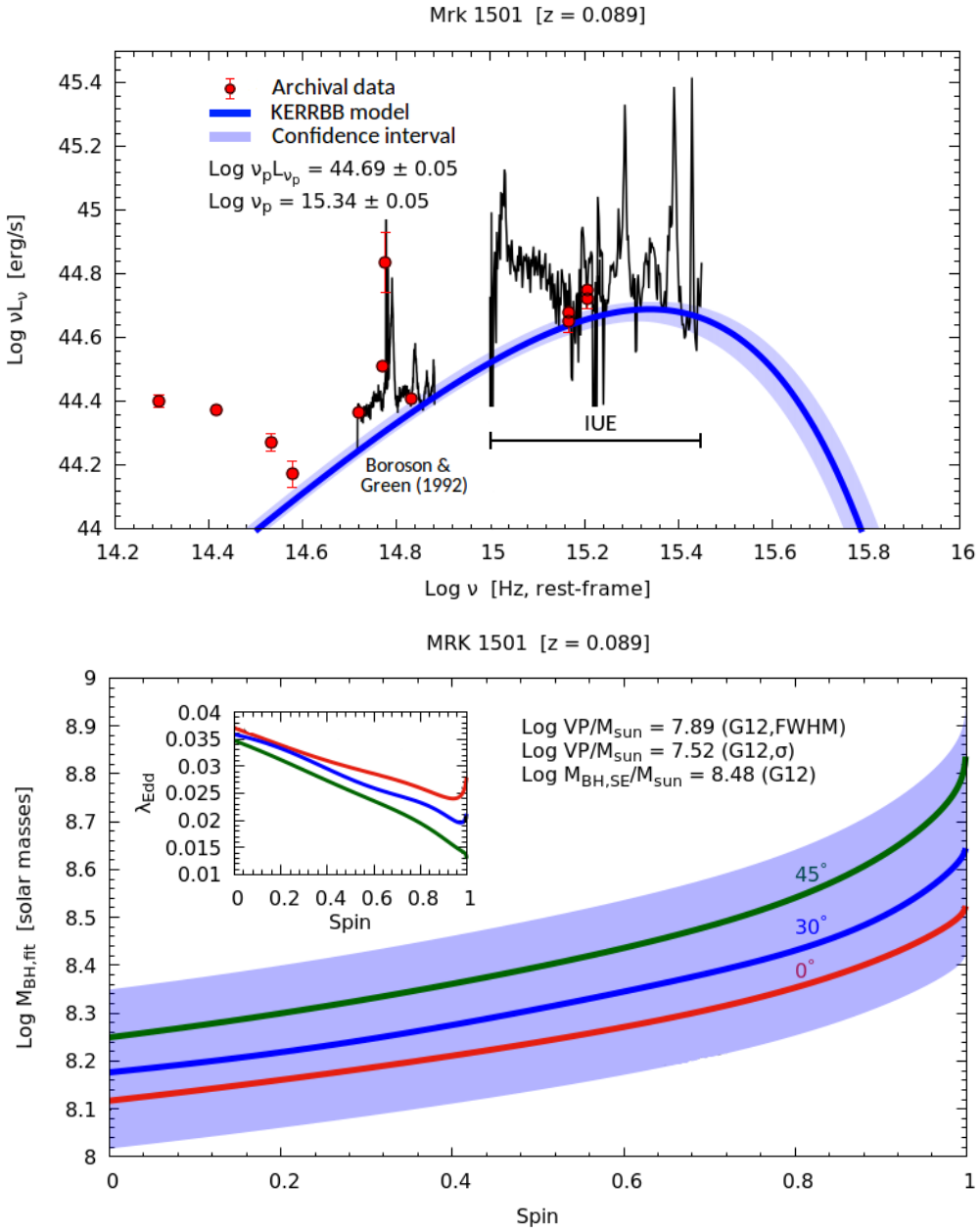

FIGURE B.12: Spectroscopic data are not excellent but are good enough to localize the spectrum peak. The other BH mass estimate shown is from Grier et al., 2017 (Log $M/M_{\odot} = 7.84^{+0.14}_{-0.19}$).

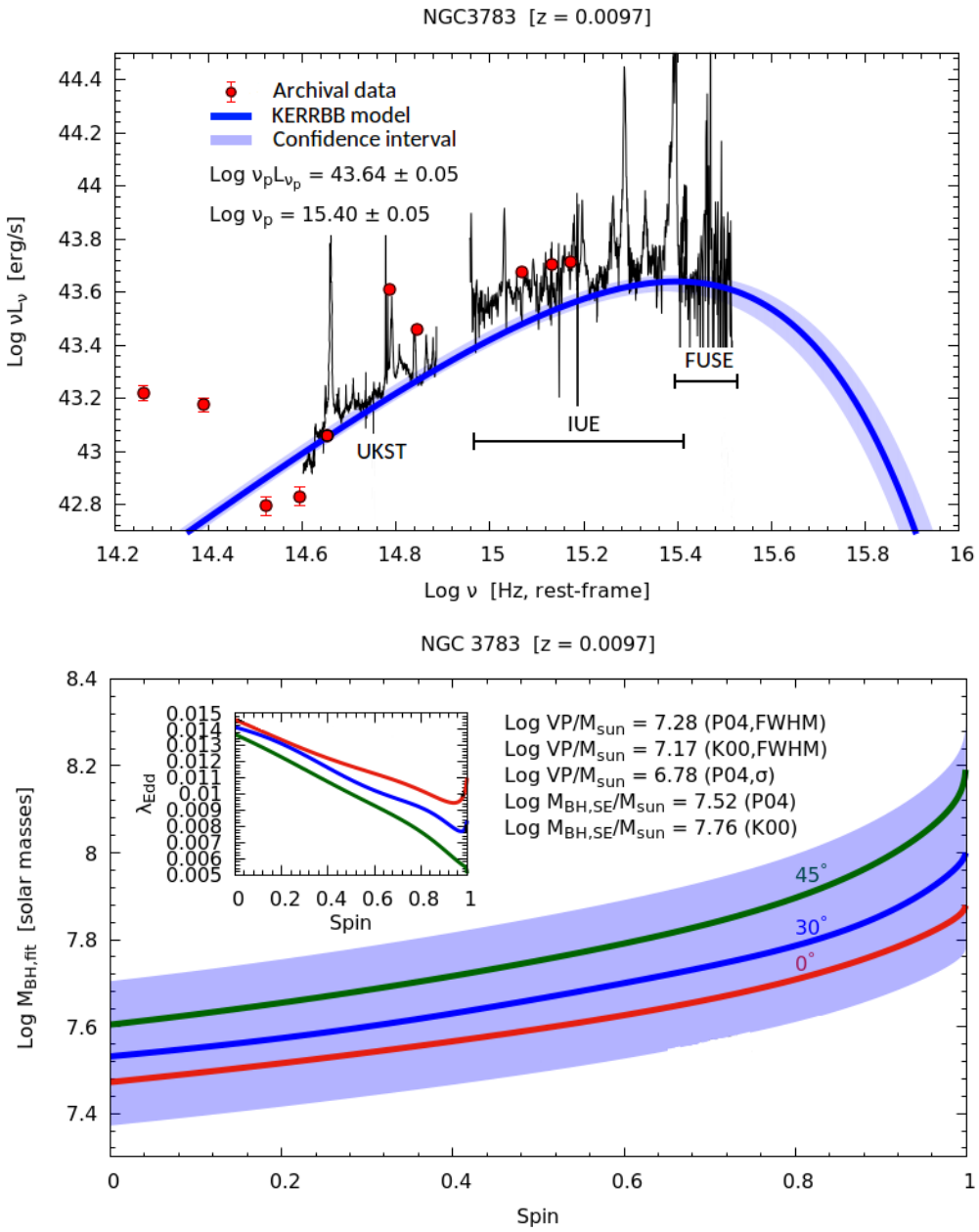

FIGURE B.13: Another BH mass estimate from Kollatschny and Zetzl, 2013 (Log $M/M_{\odot} = 7.47$).

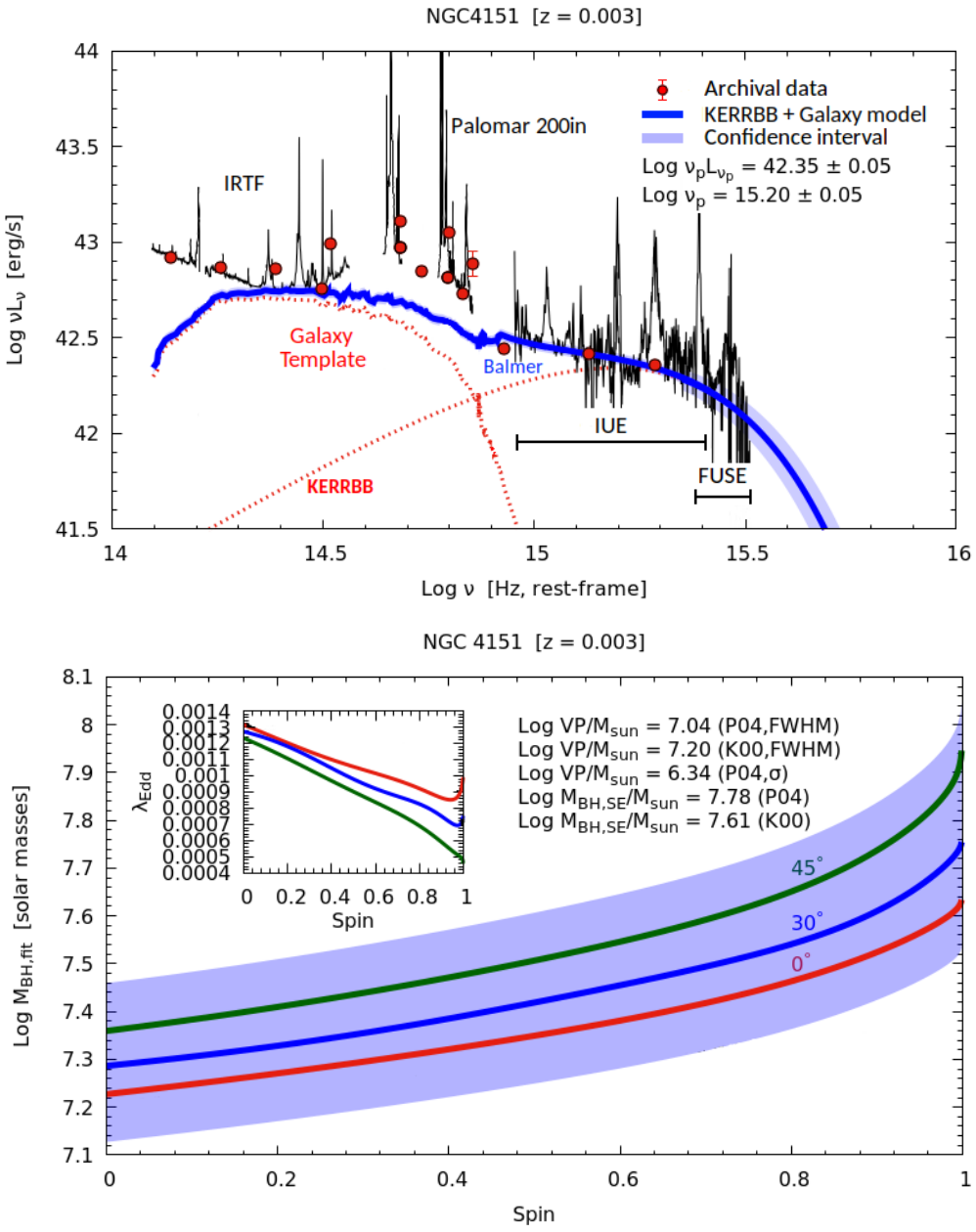

FIGURE B.14: The Balmer continuum is added to obtain a better visualization of the best fit. Spectrum rise at Log ν/Hz < 14.3 caused by the IR emission of the dusty torus.

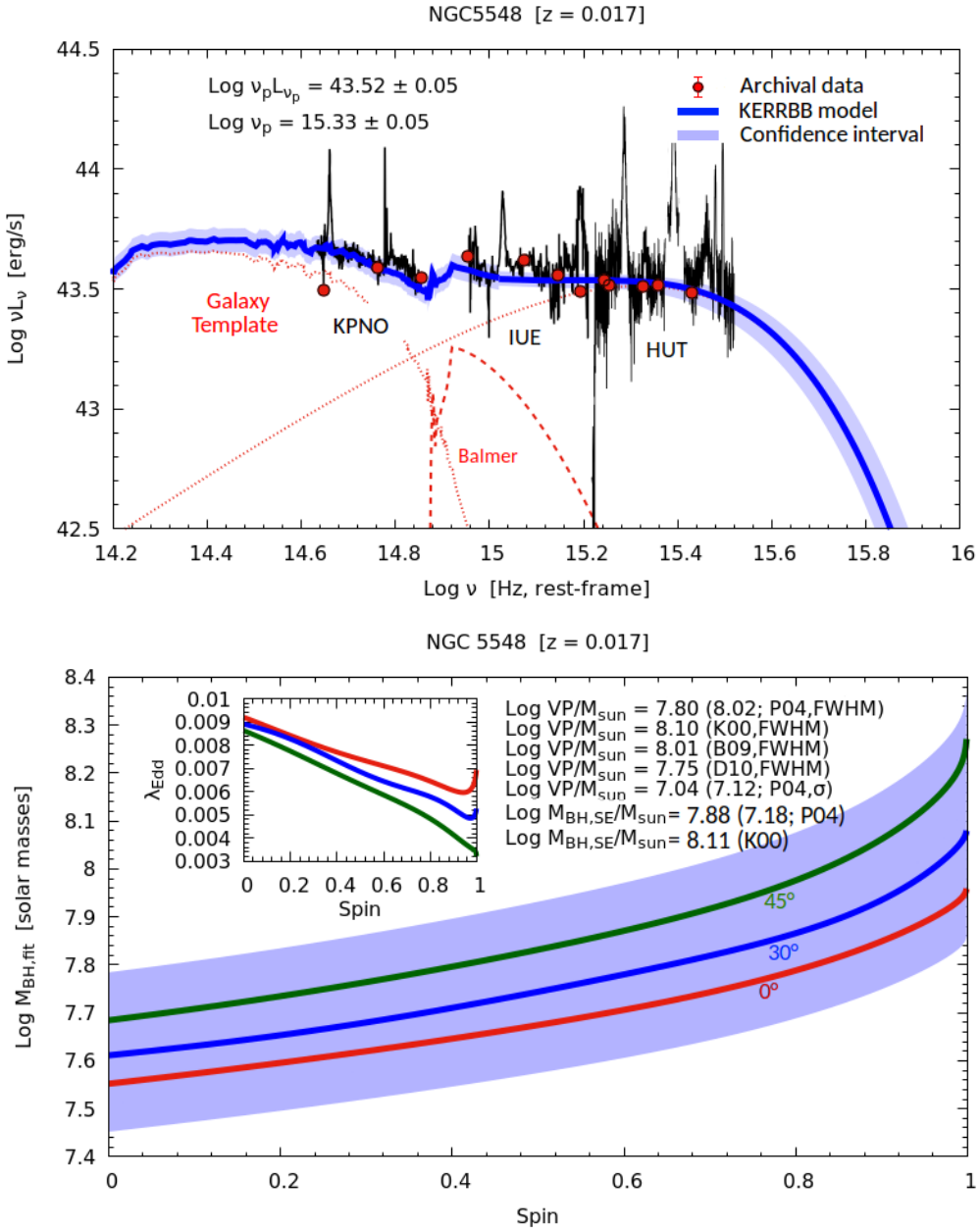

FIGURE B.15: The Balmer continuum is added to obtain a better visualization of the best fit. IUE, HST, and HUT data were smoothed in order to have a clearer spectrum. Other BH mass estimates are from Rosa et al., 2018 (Log VP$(\sigma_{\rm line})/M_\odot = 6.74 \pm 0.06$) and Kollatschny and Zetzl, 2013 (Log $M/M_\odot = 7.83$).

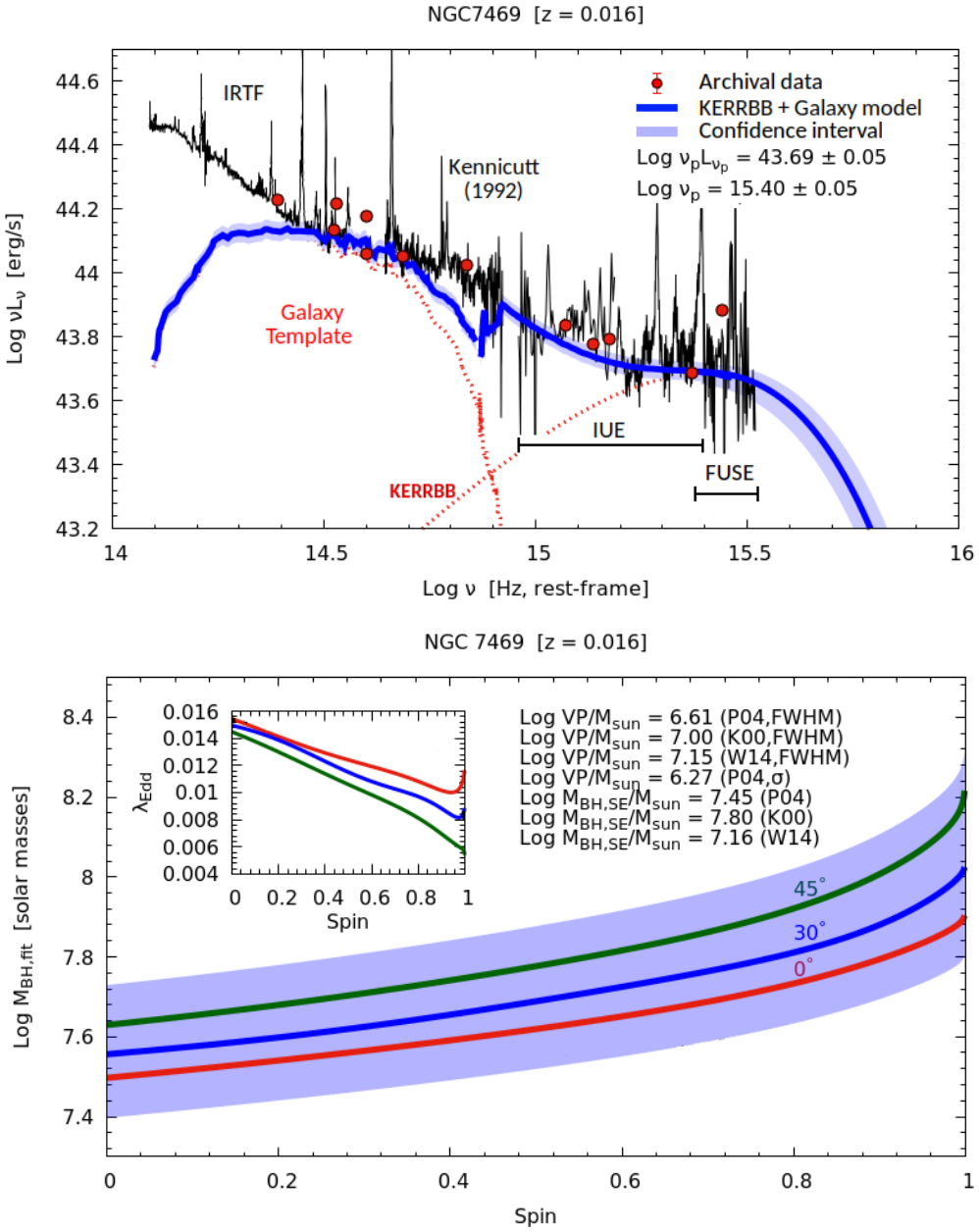

FIGURE B.16: The Balmer continuum is added to obtain a better visualization of the best fit. Spectrum rise at Log $\nu/\mathrm{Hz} < 14.5$ is caused by the IR emission of the dusty torus. Another BH mass estimate is from Kollatschny and Zetzl, 2013 (Log $M/M_{\odot} = 7.09$).

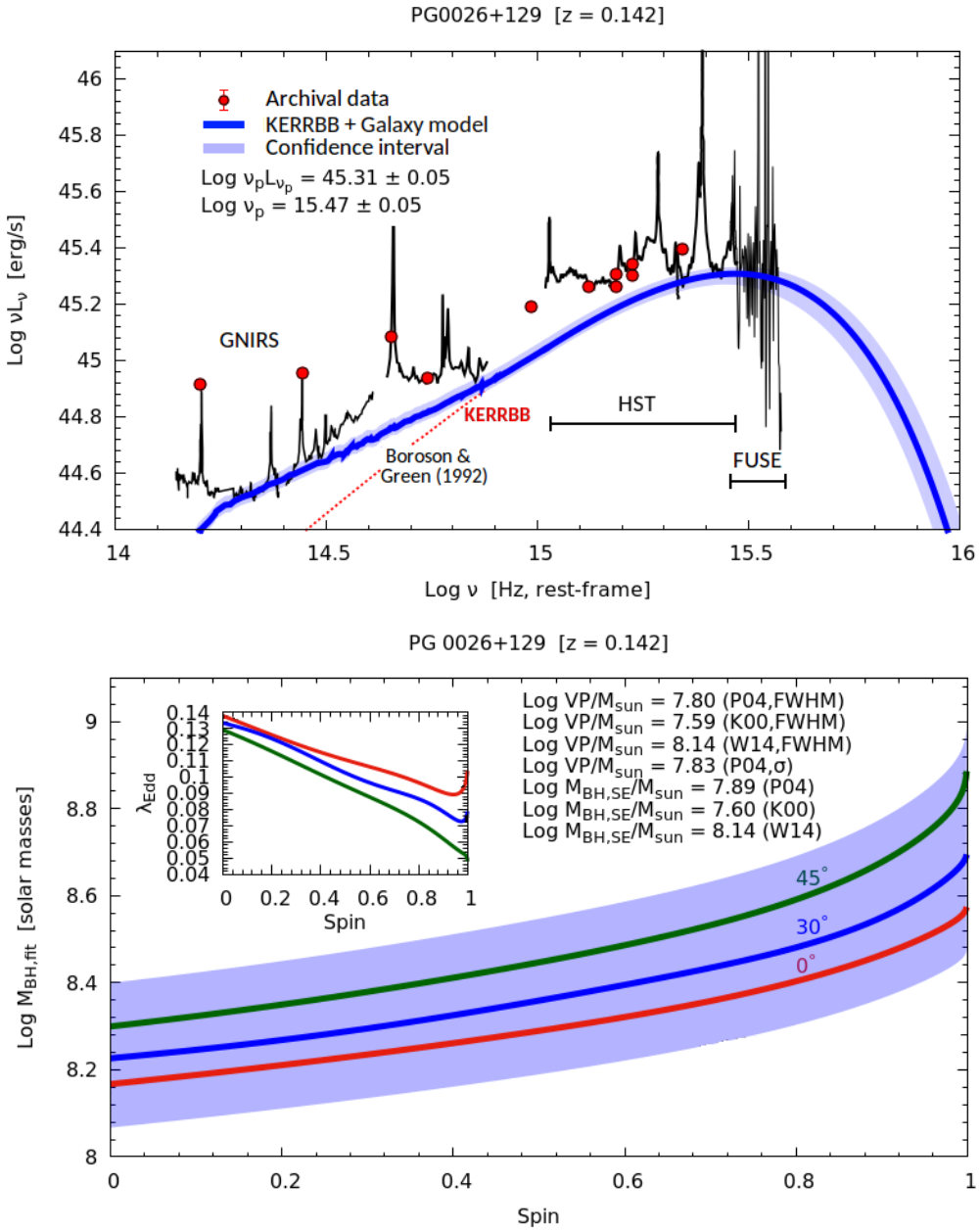
PG0026+129 [z = 0.142]
Archival data
KERRBB + Galaxy model
Confidence interval
Log $\nu_p L_{\nu_p}$ = 45.31 ± 0.05
Log ν_p = 15.47 ± 0.05
GNIRS
KERRBB
Boroson & Green (1992)
HST
FUSE
Log νL$_\nu$ [erg/s]
Log ν [Hz, rest-frame]
PG 0026+129 [z = 0.142]
Log VP/M$_{sun}$ = 7.80 (P04,FWHM)
Log VP/M$_{sun}$ = 7.59 (K00,FWHM)
Log VP/M$_{sun}$ = 8.14 (W14,FWHM)
Log VP/M$_{sun}$ = 7.83 (P04,σ)
Log M$_{BH,SE}$/M$_{sun}$ = 7.89 (P04)
Log M$_{BH,SE}$/M$_{sun}$ = 7.60 (K00)
Log M$_{BH,SE}$/M$_{sun}$ = 8.14 (W14)
45°
30°
0°
λ$_{Edd}$
Spin
Log M$_{BH,fit}$ [solar masses]
Spin

FIGURE B.17

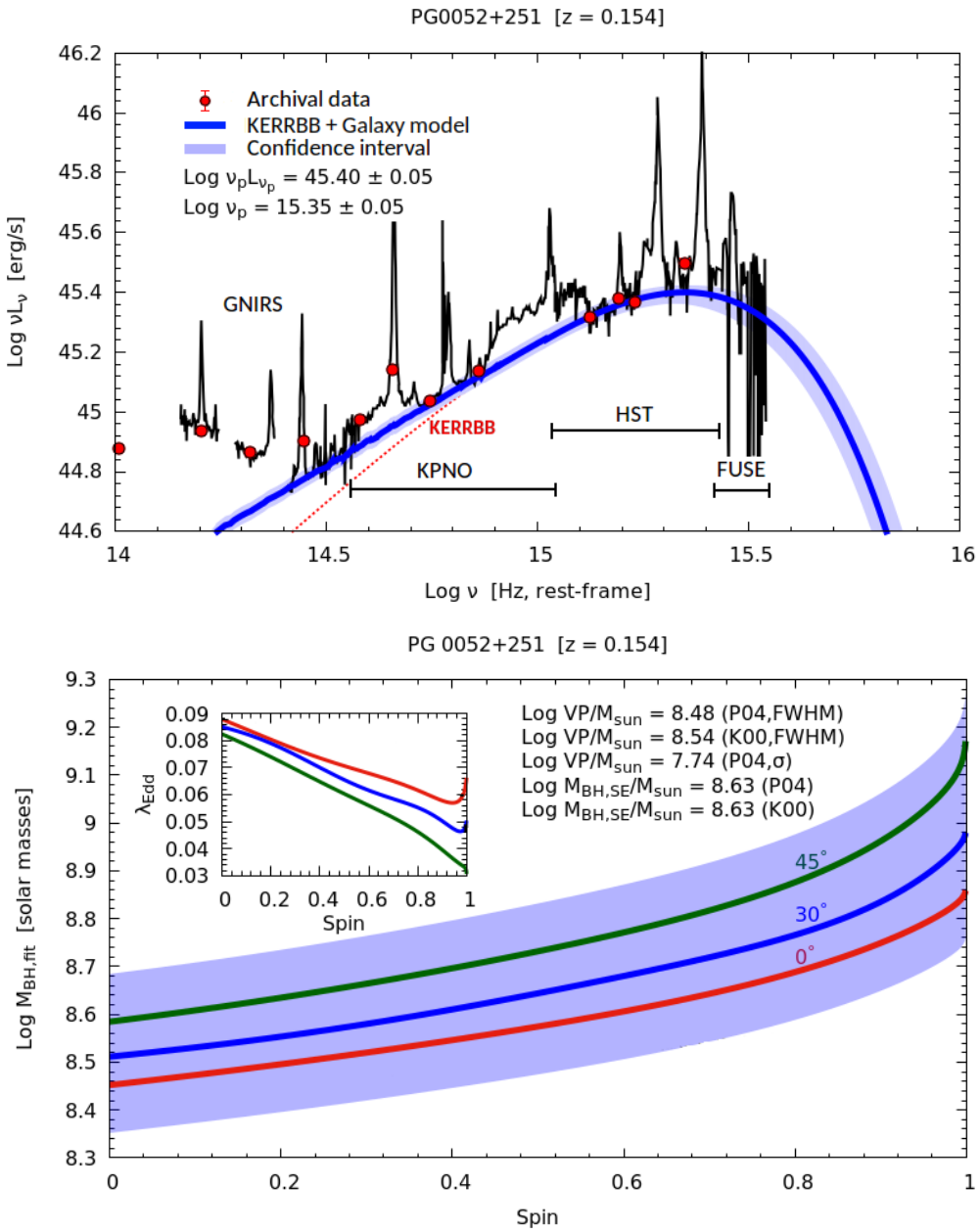

FIGURE B.18: Spectrum rise at Log ν/Hz < 14.5 is caused by the IR emission of the dusty torus.

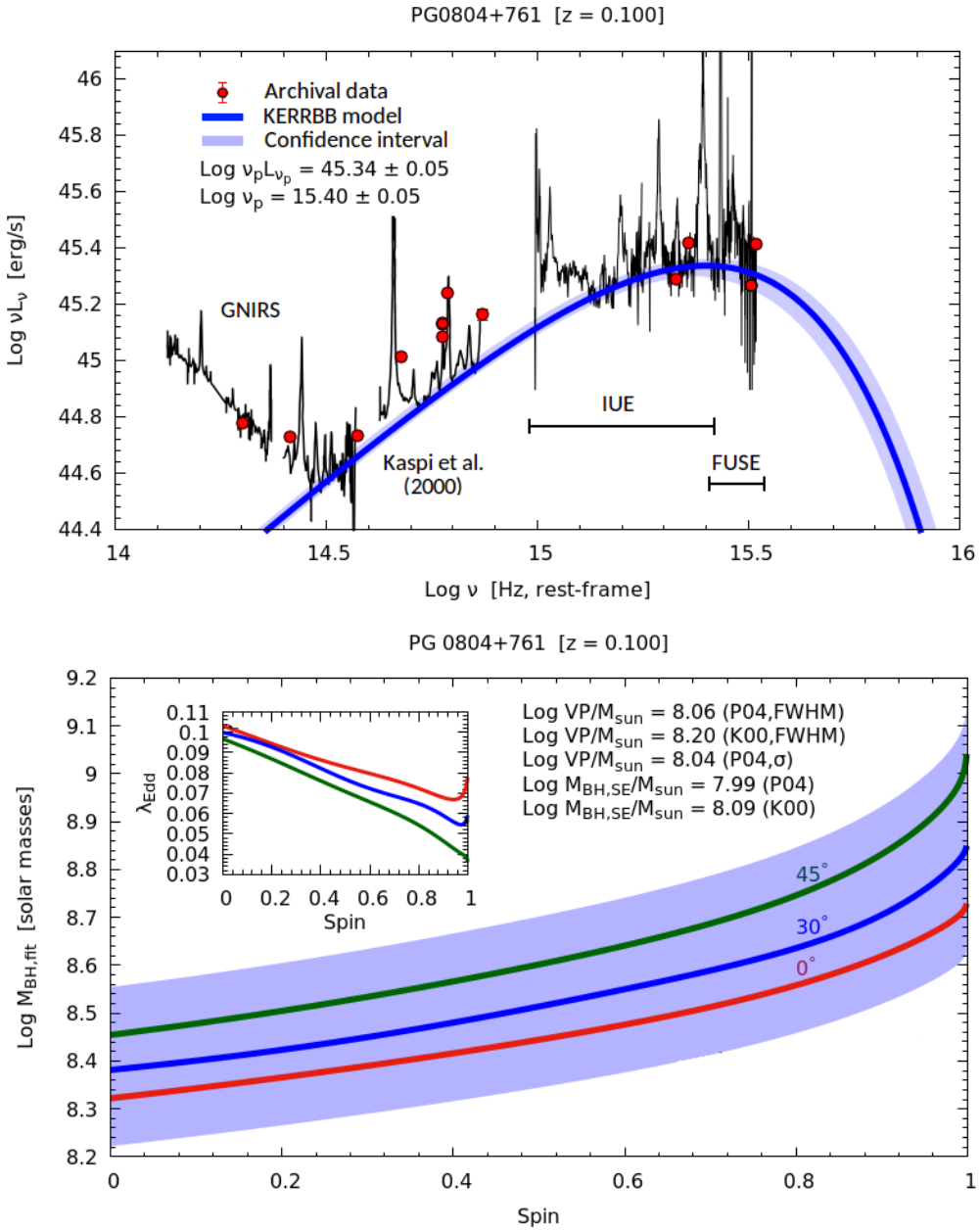

FIGURE B.19: Spectrum rise at Log ν/Hz < 14.5 is caused by the IR emission of the dusty torus.

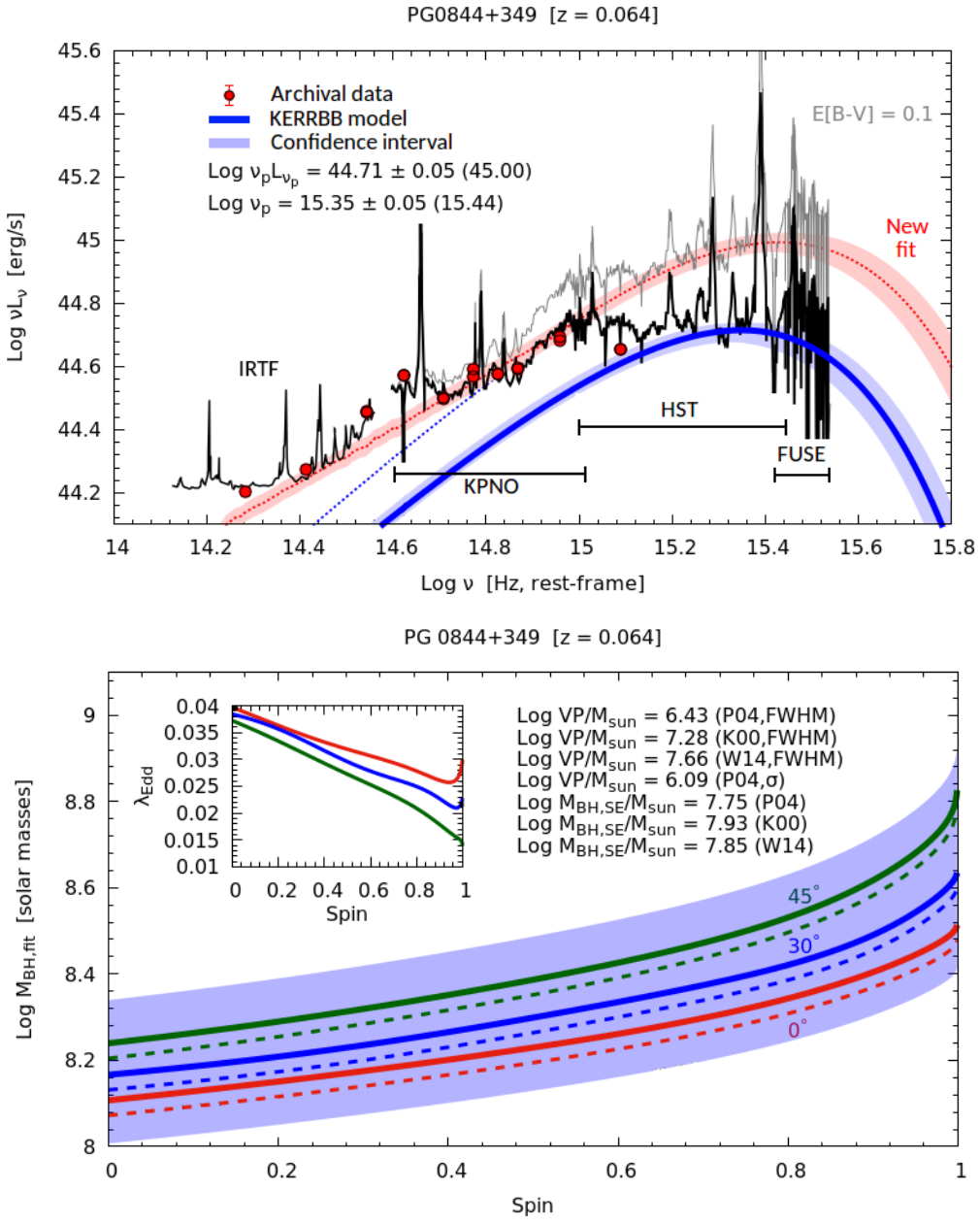

FIGURE B.20: For this source, adding a galaxy template to the blue line fit or a prominent Balmer continuum does not lead to a satisfactory fit. Instead, assuming an intrinsic reddening of the source (corrected by assuming $E[B-V] = 0.1$ mag), the new fit (red line) describes the AGN continuum for Log $\nu > 14.8$ (for smaller frequencies, I added the host-galaxy emission). Bottom panel: thick lines correspond to the first fit (blue line on the top panel), dashed lines to the second one (red line on the top panel).

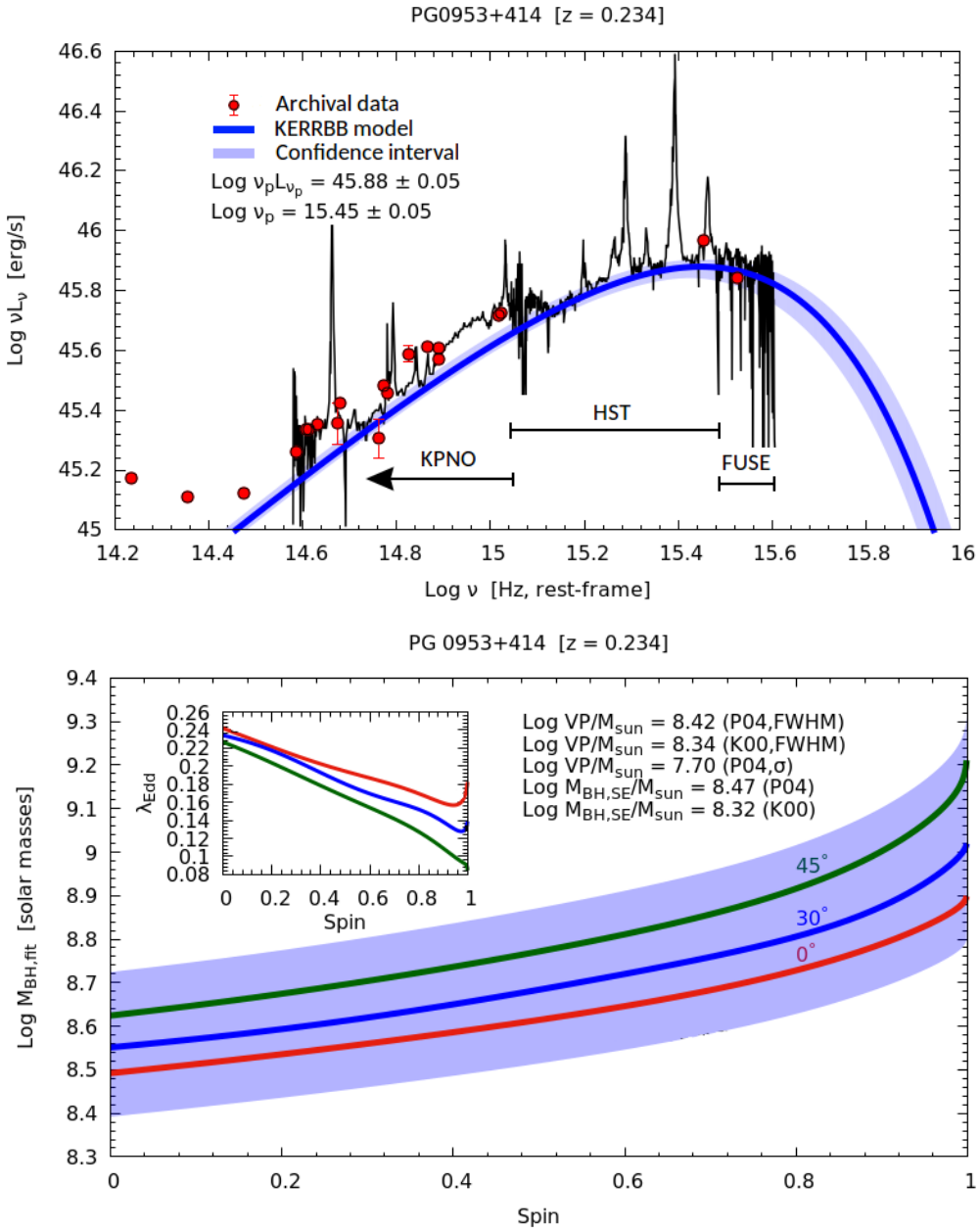
PG0953+414 [z = 0.234]
Archival data
KERRBB model
Confidence interval
Log $\nu_p L_{\nu_p}$ = 45.88 ± 0.05
Log ν_p = 15.45 ± 0.05
HST
KPNO
FUSE
Log νL$_\nu$ [erg/s]
Log ν [Hz, rest-frame]
PG 0953+414 [z = 0.234]
Log VP/M$_{sun}$ = 8.42 (P04,FWHM)
Log VP/M$_{sun}$ = 8.34 (K00,FWHM)
Log VP/M$_{sun}$ = 7.70 (P04,σ)
Log M$_{BH,SE}$/M$_{sun}$ = 8.47 (P04)
Log M$_{BH,SE}$/M$_{sun}$ = 8.32 (K00)
45°
30°
0°
λ$_{Edd}$
Spin
Log M$_{BH,fit}$ [solar masses]
Spin

FIGURE B.21

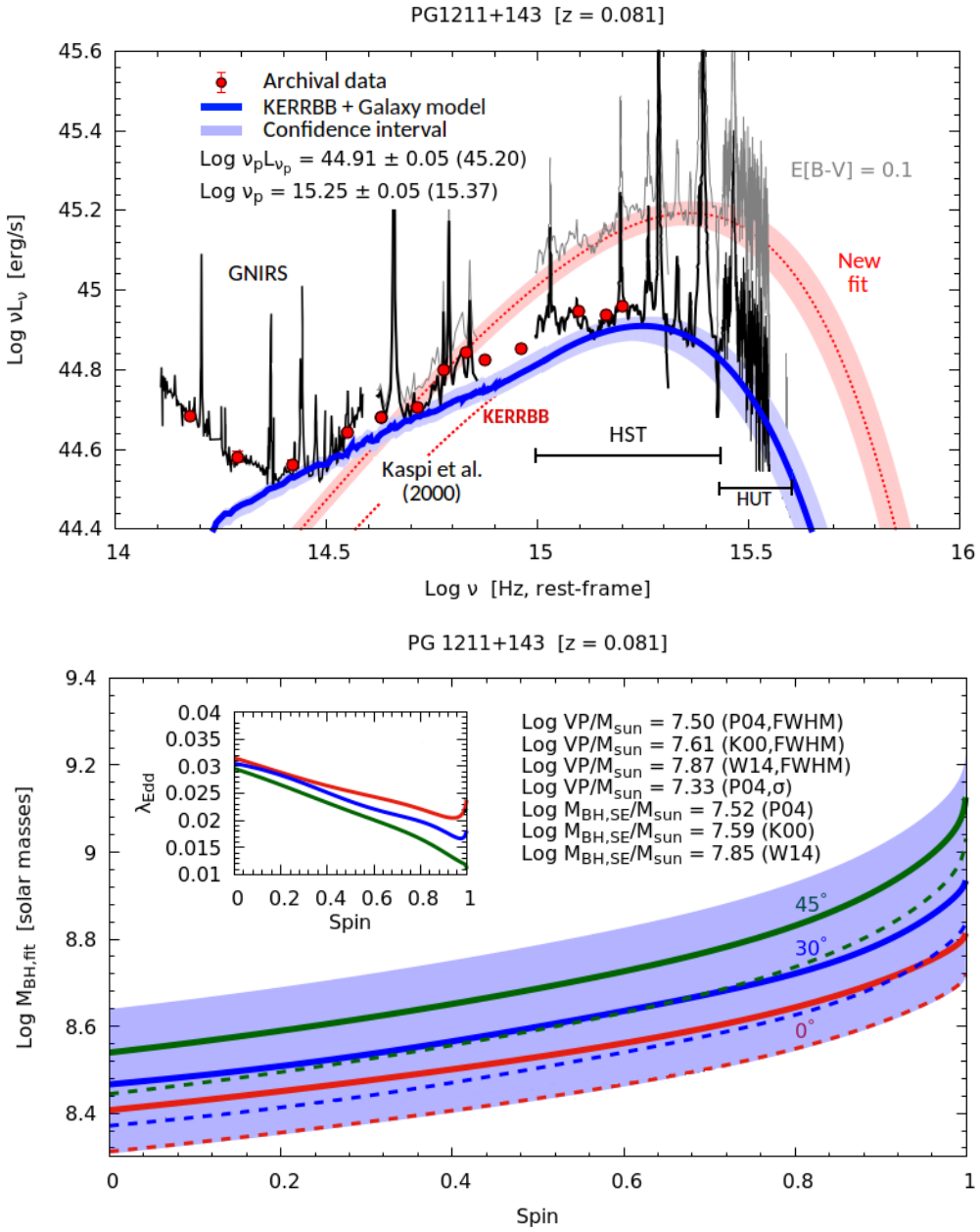

FIGURE B.22: For this source, the first satisfactory fit (blue line) is given by KERRBB+host galaxy. The spectrum rise at Log ν/Hz < 14.5 is caused by the IR emission of the dusty torus. Assuming an intrinsic reddening of the source (corrected by assuming $E[B-V] = 0.1$ mag), the new fit (red line) describes the AGN continuum for Log $\nu > 14.8$, with no need for the host-galaxy emission. Bottom panel: thick and dashed lines correspond to the first and second fits, respectively (blue and red lines on the top panel, respectively).

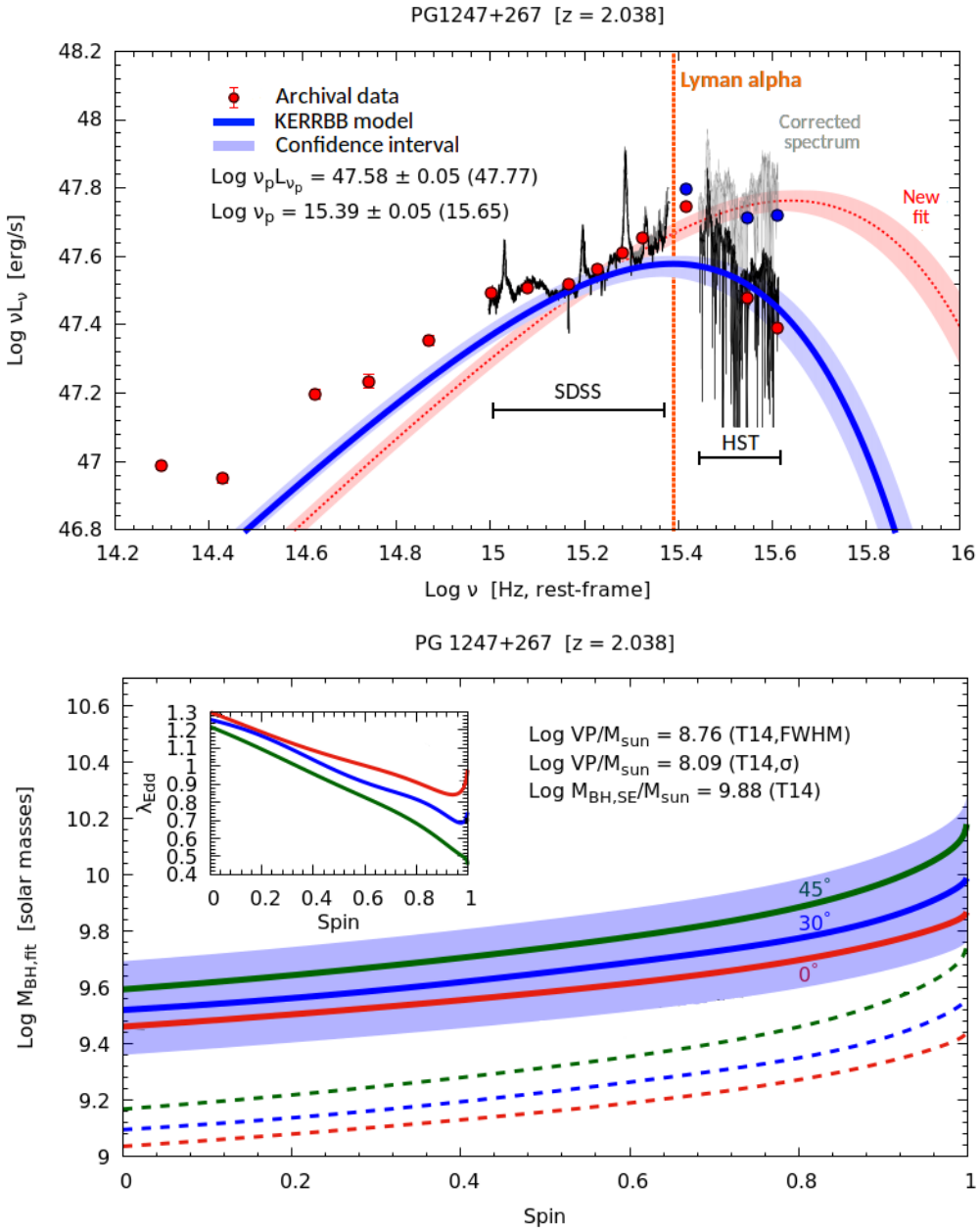

FIGURE B.23: For this source, the spectrum emission was corrected from the Intergalactic Medium absorption at large frequencies by following Madau, 1995 and Haardt and Madau, 2012. Bottom panel: thick and dashed lines correspond to the first and second fits, respectively (blue and red lines on the top panel, respectively).

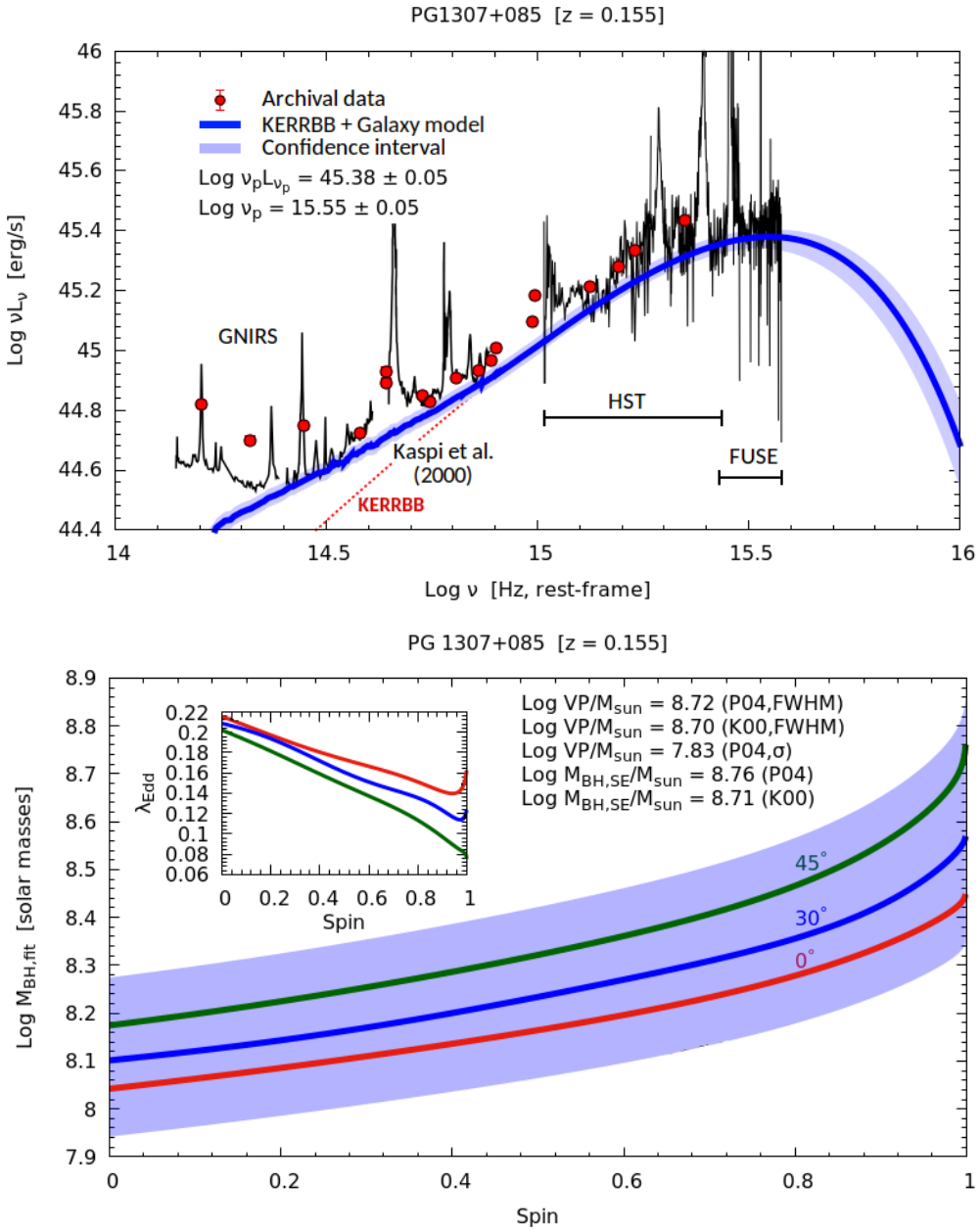
PG1307+085 [z = 0.155]
Archival data
KERRBB + Galaxy model
Confidence interval
Log νpLνp = 45.38 ± 0.05
Log νp = 15.55 ± 0.05
GNIRS
HST
FUSE
Kaspi et al. (2000)
KERRBB
Log νLν [erg/s]
Log ν [Hz, rest-frame]
PG 1307+085 [z = 0.155]
Log VP/Msun = 8.72 (P04,FWHM)
Log VP/Msun = 8.70 (K00,FWHM)
Log VP/Msun = 7.83 (P04,σ)
Log MBH,SE/Msun = 8.76 (P04)
Log MBH,SE/Msun = 8.71 (K00)
45°
30°
0°
λEdd
Spin
Log MBH,fit [solar masses]
Spin

FIGURE B.24

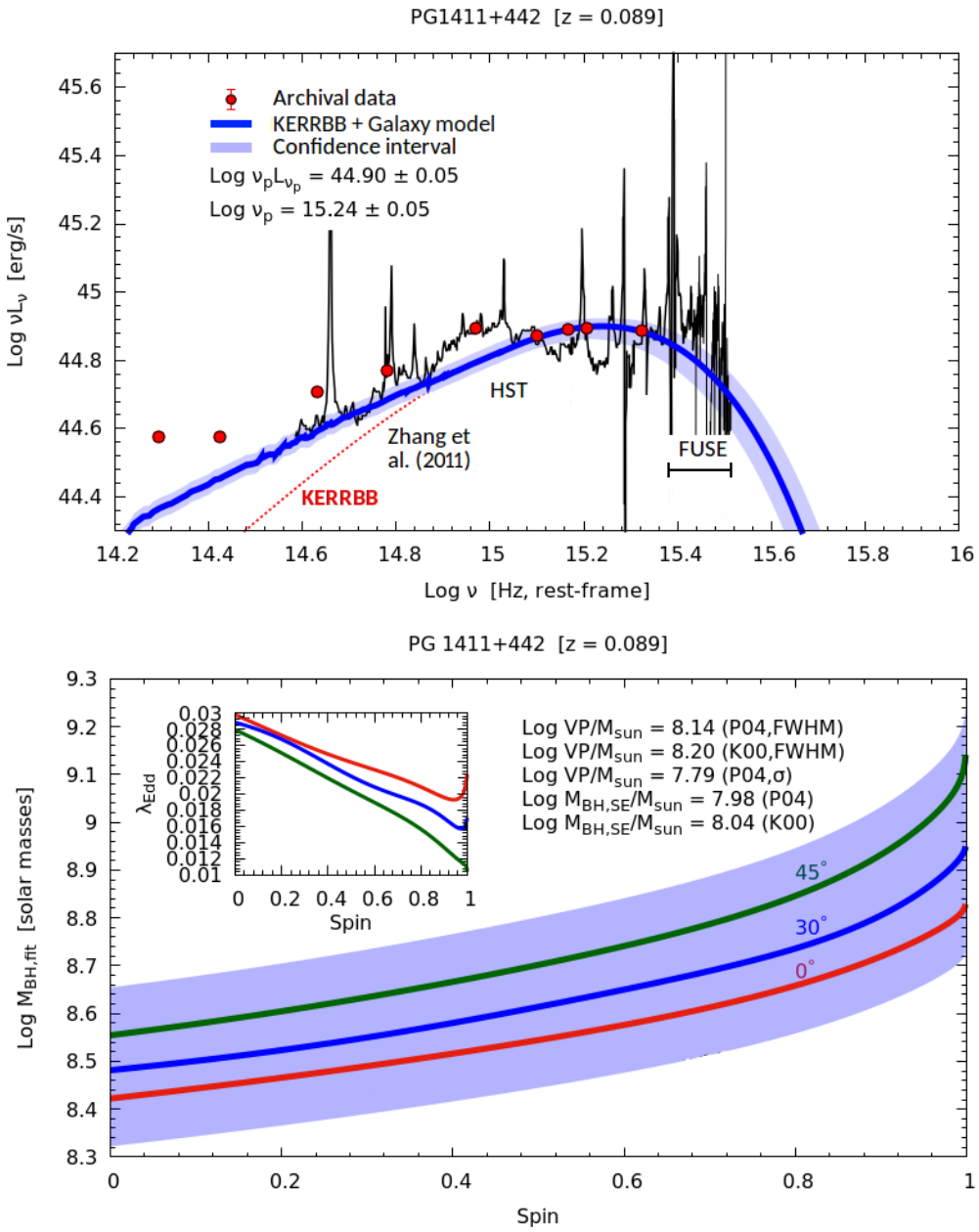

FIGURE B.25: Some intrinsic absorption is present in the data but does not affect the fit.

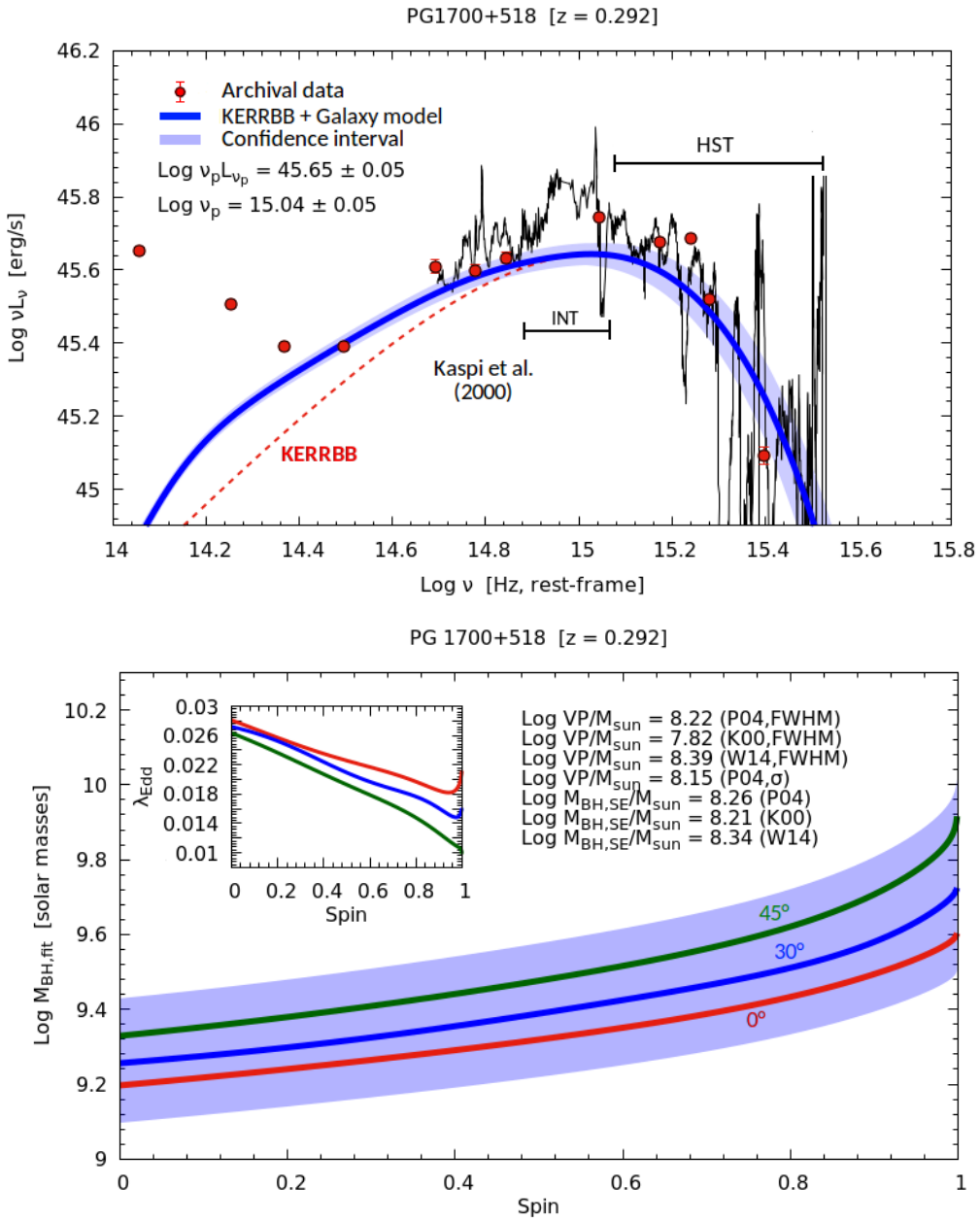

FIGURE B.26: The quality of spectroscopic data at large frequencies is low; a larger mass is inferred by a factor of $\sim$ 10 with respect to RM and SE. Dust absorption could be the cause of the decreasing flux at Log ν/Hz > 15. The galaxy emission was added to the fit to obtain a better description of the Optical continuum.

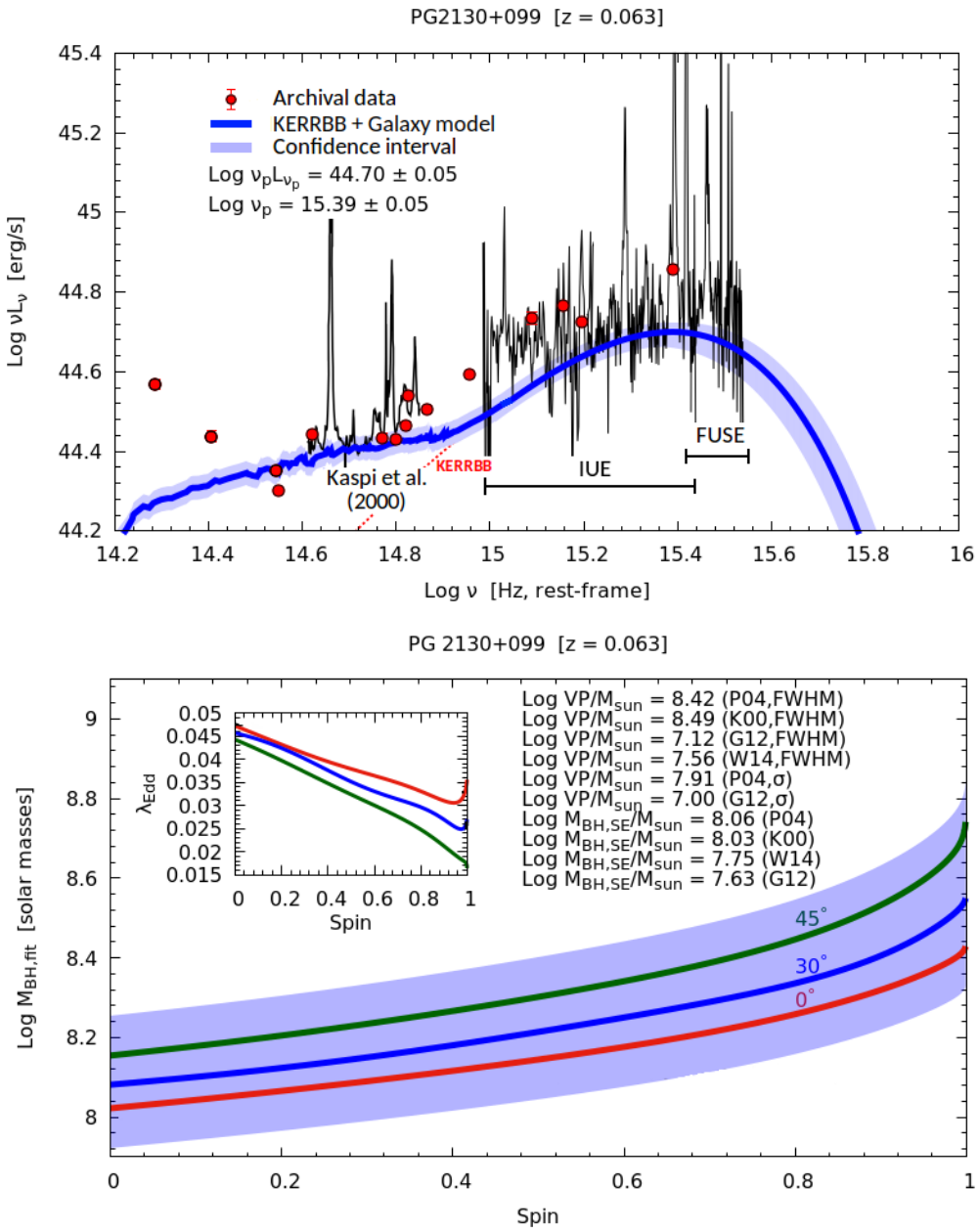

FIGURE B.27: Another BH mass estimate is obtained by Grier et al., 2017 (Log $M/M_{\odot} = 6.92^{+0.24}_{-0.23}$).

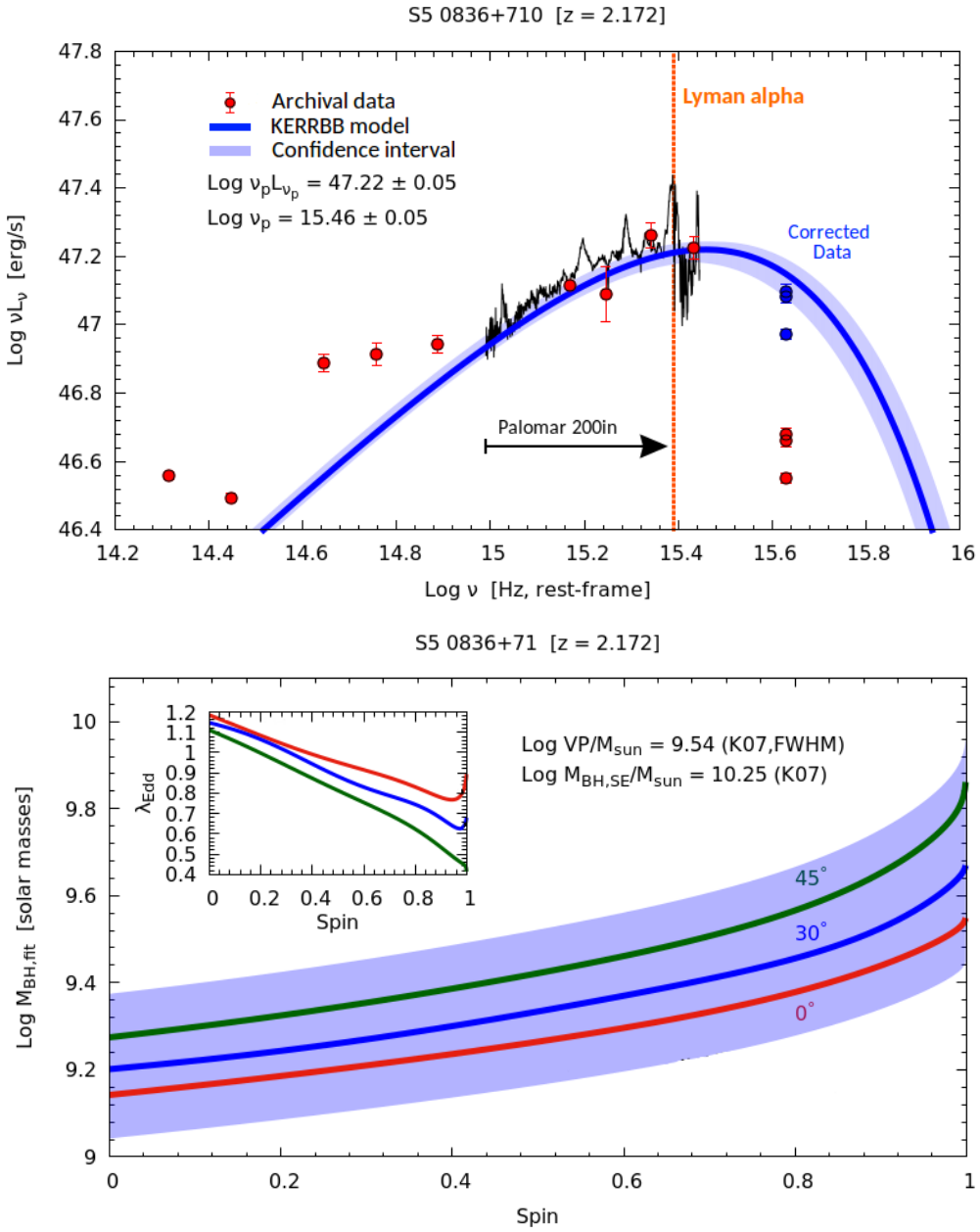

FIGURE B.28: As done for PG1247+267, photometric data were corrected from the IGM absorption at large frequencies by following Madau, 1995 and Haardt and Madau, 2012; new data (blue dots) are consistent with the best fit.

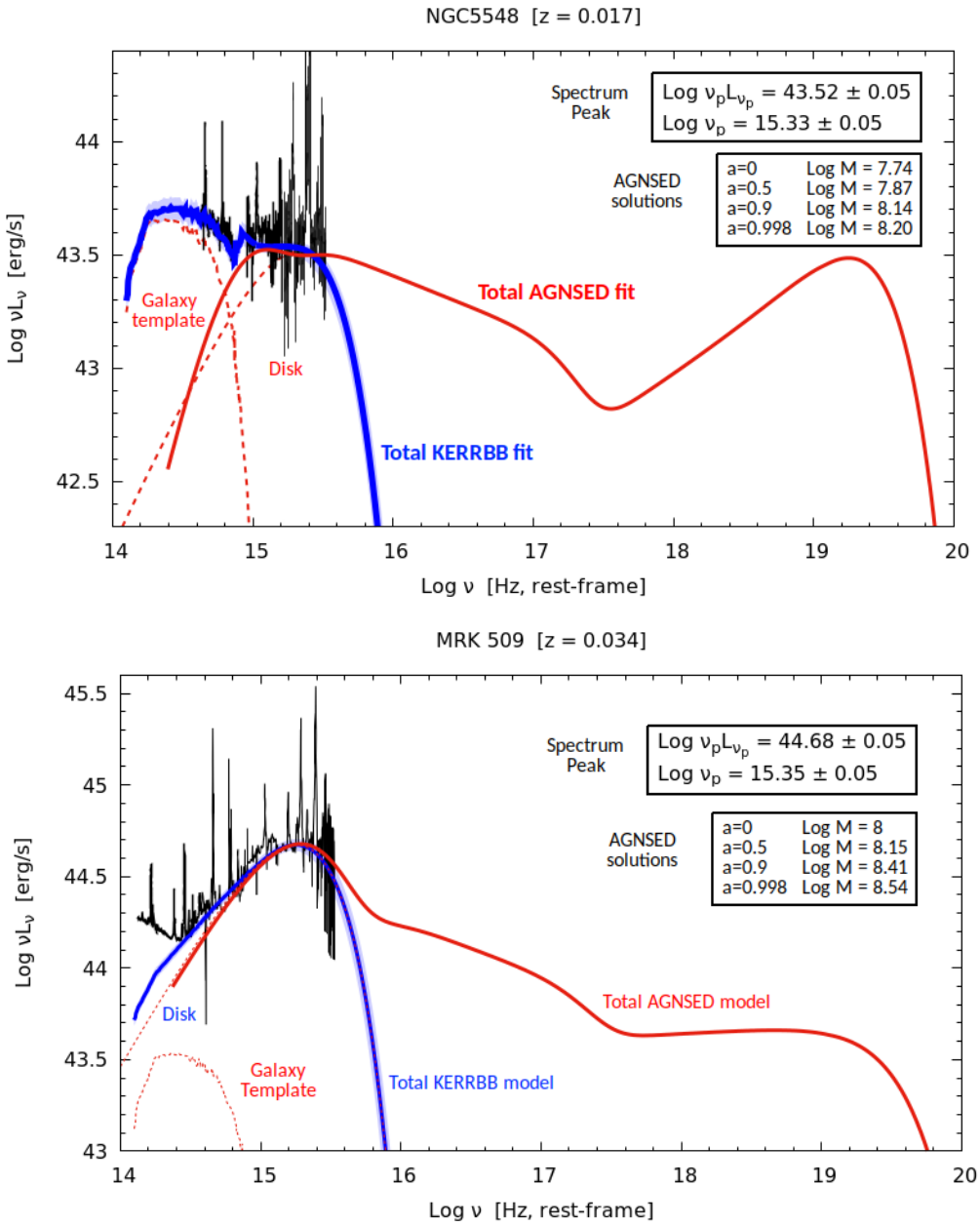

FIGURE B.29: SED modeling of the sources NGC5548 (top panel) and MRK509 (bottom panel). The red line is the modeling from Kubota and Done, 2018 (disk + Corona) and the blue line is the modeling adopted by Campitiello et al., 2020 (disk + Galaxy). As KERRBB, the AGNSED modeling is degenerate and by changing some of its parameters (i.e., BH mass, spin, Eddington ratio, X-ray Corona size) appropriately, it is possible to reproduce the same SED (keeping the Corona slopes constant as reported in Kubota and Done, 2018): on the plot, some AGNSED BH mass solutions (in solar masses) are reported for different spin values, along with the spectrum peak position (frequency and luminosity, in Hz and erg/s respectively).

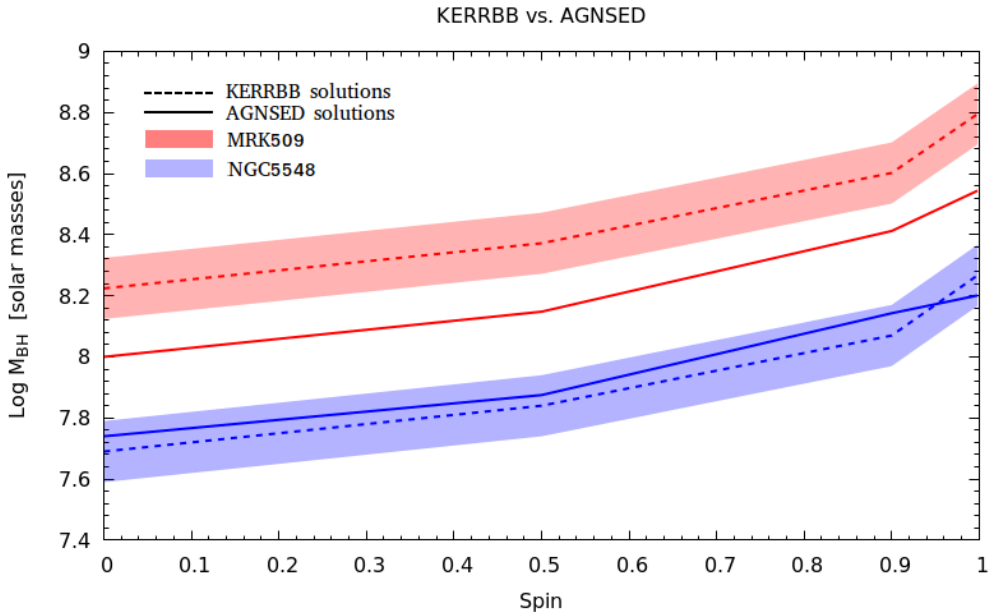

FIGURE B.30: Comparison between AGNSED BH mass solutions (thick lines) as a function of the spin, and KERRBB ones (dashed lines) for NGC5548 (blue) and MRK509 (red). All these solutions describe the same SED plotted in Fig. B.29 for $\theta_v = 45°$. For NGC5548, the results of both models are consistent while for MRK509, masses differ by a factor < 0.2 dex. The shaded area represents the uncertainty of ~ 0.1 dex (on average) linked to the spectrum peak position (see Sect. 4.3.3).

Appendix C

Disk-torus correction

C.1 Constrain θ_T and a from R_{obs}

Following the results shown in Chap. 5 and in Tab. C.1, it is possible to find constraint on the torus aperture angle θ_T and the BH spin a, given a certain value of the luminosity ratio R_{obs}, defined as the ratio between the observed torus and disk luminosities. Here I describe the three possible cases related to a disk - torus system with a viewing angle $\theta_v = 0°$ (for some illustrative examples, see Fig. C.1):

- $R_{obs} < 0.57$: for this range, it is possible to constrain the torus aperture angle with two limiting values, corresponding to $a = -1$ and $a = 0.9982$. For example (using Tab. C.1): the ratio $R_{obs} = 0.4$ can be explained only if the viewing angle is $35° < \theta_T < 70°$ because, for the other cases, the possible observed ratios are larger (for $\theta_v < 35°$) or smaller (for $\theta_v > 70°$) than 0.4; in this case, it is not possible to have any constraint on the BH spin since all the range of possible values is covered. Given R_{obs}, the torus aperture angle range can be found by looking at the first and last row of Tab. C.1.

- $0.57 < R_{obs} < 1.12$: in this case, it is possible to constrain both the BH spin (with a lower limit) and the torus aperture angle. Looking at Fig. C.1 (and Tab. C.1), each curve increases monotonically with the BH spin a (for a fixed aperture angle) and it decreases monotonically with θ_T (for a fixed spin value); the maximum value is when $\theta_T = 0°$: the comparison between the observed R_{obs} with the maximum value of the ratio (for a given a) gives a lower limit for the spin. For example (using Tab. C.1): if $R_{obs} = 0.8$, this value can be explained only if $a > 0.9$ because for lower spin values the possible ratios are always < 0.8. This can be graphically seen in Fig. C.1: all the possible solutions for $R_{obs} = 0.8$ lie above the $a = 0.9$ curve (dashed blue line); as an example, the

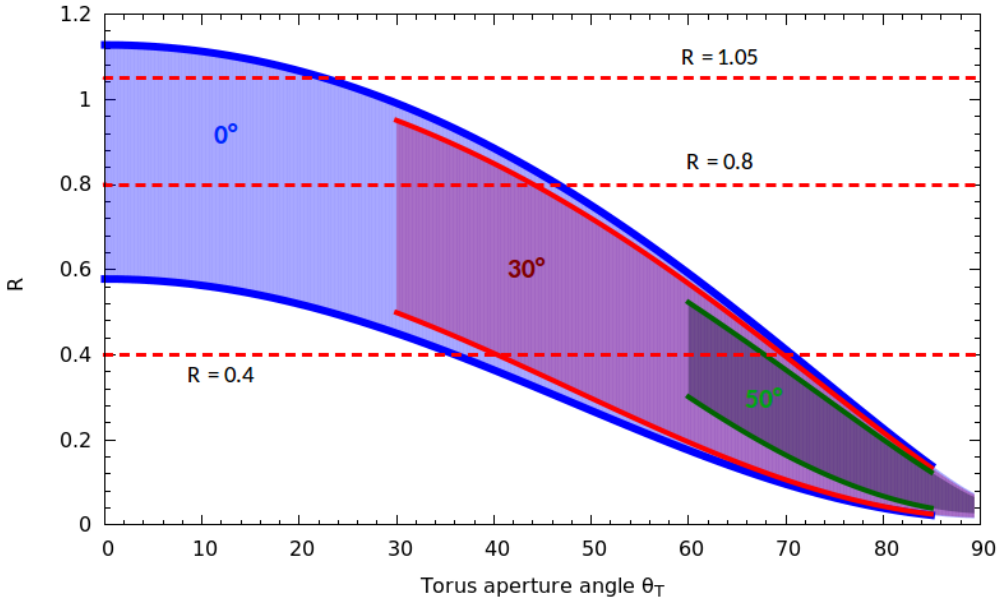

FIGURE C.1: Examples of observed ratios and the possible constraints for the torus aperture angle θ_T and the BH spin a, for different viewing angles $\theta_v = 0° - 30° - 60°$ (see Appendix C.1 for more details).

case $a = 0$ has to be rejected since the maximum value is ~ 0.6. For what concerns the torus aperture angle, an upper limit can be found that corresponds to the maximum spin value case. Given R_{obs}, the BH spin lower limit can be found by looking at the 0° column in Tab. C.1 and the aperture angle upper limit can be found by looking at the last row.

- $R_{obs} > 1.12$: for these observed ratios, the approach with the relativistic AD luminosity pattern fails since no solution is allowed. Possible explanations are linked to the main sources of uncertainty discussed in Chap. 5.

For viewing angles larger than 0°, the procedure is the same, assuming $\theta_v \leq \theta_T$ (i.e. avoiding partial/complete absorption of the disk emission by the torus). For example: in the case with $\theta_v = 30°$, as before, by looking at the first and last value in the 30° column of Tab. C.2, for $R_{obs} < 0.49$ only the torus aperture angle can be constrained; for $0.49 < R_{obs} < 0.94$, also the BH spin can be constrained with a lower limit; no solutions are allowed for $R_{obs} > 0.94$ (see also Fig. C.1).

Spin [a]	θ_T 0°	5°	10°	15°	20°	25°	30°	35°	40°	45°	50°	55°	60°	65°	70°	75°	80°	85°
-1	0.567	0.563	0.552	0.533	0.508	0.476	0.439	0.398	0.353	0.306	0.258	0.210	0.165	0.123	0.085	0.053	0.029	0.012
-0.8	0.571	0.568	0.556	0.538	0.512	0.481	0.444	0.402	0.357	0.310	0.262	0.214	0.168	0.125	0.087	0.055	0.030	0.013
-0.6	0.577	0.573	0.562	0.543	0.518	0.486	0.449	0.407	0.362	0.314	0.266	0.217	0.171	0.128	0.089	0.056	0.031	0.014
-0.4	0.583	0.580	0.568	0.550	0.524	0.492	0.455	0.413	0.368	0.320	0.271	0.222	0.175	0.131	0.092	0.058	0.032	0.015
-0.2	0.592	0.588	0.576	0.558	0.532	0.500	0.463	0.421	0.375	0.327	0.277	0.228	0.180	0.135	0.095	0.061	0.034	0.016
0.0	0.602	0.598	0.587	0.568	0.543	0.511	0.473	0.431	0.385	0.336	0.285	0.235	0.186	0.141	0.099	0.064	0.036	0.017
0.05	0.605	0.601	0.590	0.571	0.546	0.514	0.476	0.434	0.387	0.338	0.288	0.237	0.188	0.142	0.101	0.065	0.037	0.017
0.1	0.608	0.605	0.593	0.575	0.549	0.517	0.479	0.437	0.390	0.341	0.290	0.240	0.190	0.144	0.102	0.066	0.037	0.018
0.15	0.612	0.608	0.597	0.578	0.553	0.521	0.483	0.440	0.394	0.344	0.293	0.242	0.193	0.146	0.103	0.067	0.038	0.018
0.2	0.616	0.612	0.601	0.582	0.556	0.524	0.487	0.444	0.397	0.348	0.296	0.245	0.195	0.148	0.105	0.068	0.039	0.019
0.25	0.620	0.616	0.605	0.586	0.561	0.529	0.491	0.448	0.401	0.351	0.300	0.248	0.198	0.150	0.107	0.070	0.040	0.019
0.3	0.625	0.621	0.610	0.591	0.565	0.533	0.495	0.452	0.405	0.355	0.303	0.251	0.201	0.153	0.109	0.071	0.041	0.020
0.35	0.630	0.626	0.615	0.596	0.570	0.538	0.500	0.457	0.410	0.360	0.308	0.255	0.204	0.155	0.111	0.073	0.042	0.020
0.4	0.635	0.632	0.620	0.602	0.576	0.544	0.506	0.462	0.415	0.364	0.312	0.259	0.207	0.158	0.113	0.074	0.043	0.021
0.45	0.642	0.638	0.627	0.608	0.582	0.550	0.512	0.468	0.421	0.370	0.317	0.264	0.211	0.162	0.116	0.077	0.045	0.022
0.5	0.649	0.645	0.634	0.615	0.589	0.557	0.519	0.475	0.427	0.376	0.323	0.269	0.216	0.166	0.119	0.079	0.046	0.023
0.55	0.657	0.653	0.642	0.623	0.597	0.565	0.527	0.483	0.435	0.383	0.330	0.275	0.221	0.170	0.123	0.082	0.048	0.024
0.6	0.666	0.662	0.651	0.632	0.607	0.574	0.536	0.492	0.443	0.391	0.337	0.282	0.228	0.175	0.127	0.085	0.050	0.025
0.65	0.677	0.673	0.662	0.643	0.617	0.585	0.546	0.502	0.453	0.401	0.346	0.290	0.235	0.181	0.132	0.089	0.053	0.027
0.7	0.690	0.686	0.675	0.656	0.630	0.598	0.559	0.515	0.465	0.413	0.357	0.300	0.244	0.189	0.138	0.093	0.056	0.029
0.75	0.706	0.702	0.691	0.672	0.646	0.614	0.575	0.530	0.480	0.427	0.370	0.312	0.255	0.198	0.146	0.099	0.060	0.031
0.8	0.727	0.723	0.712	0.693	0.667	0.634	0.595	0.550	0.499	0.445	0.388	0.328	0.269	0.211	0.156	0.107	0.066	0.035
0.85	0.754	0.750	0.739	0.720	0.694	0.661	0.622	0.576	0.525	0.470	0.411	0.350	0.288	0.228	0.170	0.118	0.073	0.039
0.9	0.794	0.791	0.779	0.760	0.734	0.701	0.661	0.615	0.563	0.507	0.446	0.383	0.318	0.254	0.192	0.135	0.086	0.047
0.92	0.817	0.813	0.802	0.783	0.757	0.724	0.683	0.637	0.585	0.527	0.466	0.401	0.335	0.269	0.204	0.145	0.093	0.052
0.94	0.847	0.843	0.832	0.813	0.786	0.753	0.713	0.666	0.613	0.555	0.492	0.426	0.358	0.289	0.222	0.159	0.103	0.058
0.96	0.888	0.884	0.873	0.854	0.828	0.794	0.754	0.706	0.653	0.593	0.529	0.461	0.390	0.318	0.247	0.179	0.118	0.068
0.98	0.956	0.952	0.941	0.922	0.895	0.861	0.820	0.772	0.718	0.657	0.591	0.520	0.445	0.368	0.290	0.215	0.145	0.085
0.99	1.015	1.011	0.999	0.980	0.954	0.920	0.878	0.830	0.775	0.713	0.645	0.572	0.494	0.413	0.330	0.249	0.171	0.103
0.995	1.063	1.059	1.047	1.028	1.002	0.968	0.926	0.877	0.822	0.759	0.690	0.615	0.536	0.452	0.365	0.278	0.195	0.118
0.9982	1.120	1.116	1.105	1.086	1.059	1.025	0.983	0.934	0.878	0.814	0.744	0.668	0.586	0.498	0.408	0.315	0.224	0.138

TABLE C.1: Value of the observed ratio R_{obs} for different spin a and torus aperture angle θ_T, assuming a viewing angle $\theta_v = 0°$.

Spin [a]	θ_T 0°	5°	10°	15°	20°	25°	30°	35°	40°	45°	50°	55°	60°	65°	70°	75°	80°	85°
-1	-	-	-	-	-	-	0.487	0.441	0.391	0.339	0.286	0.233	0.183	0.136	0.094	0.059	0.032	0.014
-0.8	-	-	-	-	-	-	0.490	0.444	0.395	0.342	0.289	0.236	0.185	0.138	0.096	0.060	0.033	0.014
-0.6	-	-	-	-	-	-	0.494	0.448	0.399	0.346	0.293	0.240	0.188	0.141	0.098	0.062	0.034	0.015
-0.4	-	-	-	-	-	-	0.500	0.454	0.404	0.351	0.297	0.244	0.192	0.144	0.101	0.064	0.035	0.016
-0.2	-	-	-	-	-	-	0.506	0.460	0.410	0.357	0.303	0.249	0.197	0.148	0.104	0.067	0.037	0.017
0.0	-	-	-	-	-	-	0.514	0.468	0.418	0.365	0.310	0.256	0.203	0.153	0.108	0.070	0.039	0.018
0.05	-	-	-	-	-	-	0.517	0.471	0.420	0.367	0.312	0.258	0.204	0.154	0.109	0.071	0.040	0.019
0.1	-	-	-	-	-	-	0.519	0.473	0.423	0.370	0.315	0.260	0.206	0.156	0.110	0.072	0.041	0.019
0.15	-	-	-	-	-	-	0.522	0.476	0.426	0.372	0.317	0.262	0.208	0.158	0.112	0.073	0.041	0.020
0.2	-	-	-	-	-	-	0.525	0.479	0.429	0.375	0.320	0.264	0.210	0.160	0.113	0.074	0.042	0.020
0.25	-	-	-	-	-	-	0.528	0.482	0.432	0.378	0.323	0.267	0.213	0.162	0.115	0.075	0.043	0.021
0.3	-	-	-	-	-	-	0.532	0.486	0.435	0.382	0.326	0.270	0.216	0.164	0.117	0.076	0.044	0.021
0.35	-	-	-	-	-	-	0.536	0.490	0.439	0.386	0.330	0.274	0.219	0.166	0.119	0.078	0.045	0.022
0.4	-	-	-	-	-	-	0.541	0.494	0.444	0.390	0.334	0.277	0.222	0.169	0.121	0.080	0.046	0.023
0.45	-	-	-	-	-	-	0.546	0.499	0.449	0.394	0.338	0.281	0.226	0.172	0.124	0.082	0.048	0.023
0.5	-	-	-	-	-	-	0.551	0.505	0.454	0.400	0.343	0.286	0.230	0.176	0.127	0.084	0.049	0.024
0.55	-	-	-	-	-	-	0.558	0.511	0.461	0.406	0.349	0.291	0.235	0.180	0.130	0.086	0.051	0.025
0.6	-	-	-	-	-	-	0.565	0.519	0.468	0.413	0.356	0.298	0.240	0.185	0.134	0.089	0.053	0.027
0.65	-	-	-	-	-	-	0.574	0.528	0.476	0.421	0.364	0.305	0.247	0.191	0.139	0.093	0.055	0.028
0.7	-	-	-	-	-	-	0.584	0.538	0.487	0.431	0.373	0.314	0.255	0.198	0.144	0.097	0.059	0.030
0.75	-	-	-	-	-	-	0.597	0.551	0.499	0.444	0.385	0.325	0.265	0.206	0.152	0.103	0.062	0.033
0.8	-	-	-	-	-	-	0.614	0.567	0.515	0.459	0.400	0.339	0.277	0.217	0.161	0.110	0.068	0.036
0.85	-	-	-	-	-	-	0.636	0.589	0.537	0.481	0.421	0.358	0.295	0.233	0.174	0.120	0.075	0.040
0.9	-	-	-	-	-	-	0.669	0.622	0.570	0.513	0.451	0.387	0.322	0.257	0.194	0.136	0.087	0.048
0.92	-	-	-	-	-	-	0.688	0.641	0.588	0.531	0.469	0.404	0.337	0.270	0.206	0.146	0.093	0.052
0.94	-	-	-	-	-	-	0.712	0.665	0.612	0.554	0.492	0.426	0.357	0.289	0.221	0.159	0.103	0.058
0.96	-	-	-	-	-	-	0.747	0.700	0.647	0.588	0.524	0.457	0.387	0.315	0.244	0.177	0.117	0.067
0.98	-	-	-	-	-	-	0.803	0.756	0.703	0.643	0.579	0.509	0.436	0.360	0.284	0.210	0.142	0.084
0.99	-	-	-	-	-	-	0.853	0.806	0.753	0.693	0.627	0.556	0.480	0.401	0.321	0.241	0.166	0.100
0.995	-	-	-	-	-	-	0.894	0.847	0.793	0.733	0.666	0.594	0.517	0.436	0.353	0.269	0.188	0.114
0.9982	-	-	-	-	-	-	0.944	0.897	0.843	0.782	0.715	0.641	0.562	0.479	0.391	0.303	0.215	0.132

TABLE C.2: Value of the observed ratio R_{obs} for different spin a and torus aperture angle θ_T, assuming a viewing angle $\theta_v = 30°$.

C.2 X-ray Corona & Broad Line Region

In Chap. 5, I discussed the possibility that the presence of an X-ray Corona above the AD or the BLR could affect both the disk and the torus luminosity. Both structures intercept part of the disk radiation leading to a wrong estimate of $L_{\rm d}^{\rm obs}$; nonetheless, due to their geometry, also $L_{\rm T}^{\rm obs}$ could be influenced by their presence.

- **X-ray Corona**

  An X-ray Corona could affect only the AD luminosity (if its structure is assumed to be lamp post-like - e.g., Miniutti and Fabian, 2004) or both the torus and the AD luminosities (if it is assumed as an extended slab or spherical - e.g., Petrucci et al., 2017; Chainakun et al., 2019). In both cases, the Corona covers the inner part of the AD w.r.t. a distant observer (leading to a dimmer $L_{\rm d}^{\rm obs}$ with respect to the intrinsic one) while the torus can absorb part of the Corona radiation along with the one of the uncovered disk (without exceeding the total disk luminosity). Assuming that the whole Corona (hot + warm components) scatters $< 20-30\%$ of the disk radiation (e.g., Sazonov et al., 2012; Lusso and Risaliti, 2017), the intrinsic $L_{\rm d}^{\rm obs}$ ($R_{\rm obs}$) is larger (smaller) by a factor of $< 0.10-0.15$ dex.

- **Broad Line Region**

  The BLR emits a fraction $f_{\rm BLR}$ of the total AD radiation in the range 0.002 and 0.35 (Baldwin and Netzer, 1978), but preferentially < 0.15 (Smith et al., 1981). In principle, this emission can be assumed to be emitted isotropically (in the spherical case) or anisotropically (in the disk-like case; e.g., Wills and Browne, 1986; Kollatschny, 2003; Decarli et al., 2008).

  In general, the BLR total luminosity is defined as a fraction of the total disk luminosity, i.e. $L_{\rm BLR} = f_{\rm BLR} L_{\rm D}$. In the isotropic case, the flux is independent of $\theta_{\rm v}$ and therefore $L_{\rm BLR} \equiv L_{\rm BLR}^{\rm obs}$. If the BLR is assumed to be a disk-like structure (see e.g., Sturm et al., 2018; Amorim et al., 2020) a reasonable assumption is that its emission is anisotropic and similar to Eq. 2.17, i.e. $L_{\rm BLR}^{\rm obs} \approx 2\cos\theta_{\rm v} L_{\rm BLR}$, even though a possible angle-dependence is unknown and has not been observed.[1] The torus intercepts part of the BLR radiation depending on its aperture angle $\theta_{\rm T}$.

[1] About this topic, see the work by Rudge and Raine, 2000.

As for a disk, this luminosity fraction $L^{\rm obs}_{\rm T,BLR}$ can be written as:

$$L^{\rm obs}_{\rm T,BLR} = \int_{\theta_{\rm T}}^{\pi/2} L^{\rm obs}_{\rm BLR}(\theta_{\rm v}) \sin\theta d\theta$$

For an isotropic emission, it is possible to find $L^{\rm obs}_{\rm T,BLR}(\theta_{\rm T}) = L_{\rm BLR}\cos\theta_{\rm T}$; instead, in the anisotropic case $L^{\rm obs}_{\rm T,BLR}(\theta_{\rm T}) = L_{\rm BLR}\cos^2\theta_{\rm T}$. The $\theta_{\rm T}$-dependence can be defined as $\mathcal{H}(\theta_{\rm T})$ and the observed torus luminosity can be written as

$$L^{\rm obs}_{\rm T}(\theta_{\rm T}, a) = (1 - f_{\rm BLR})L_{\rm d}\mathcal{I}(\theta_{\rm T}, a) + f_{\rm BLR}L_{\rm d}\mathcal{H}(\theta_{\rm T})$$

where the first term is the fraction of the AD radiation not intercepted by the BLR. When $f_{\rm BLR} = 0$, it is possible to find the ideal case with no BLR (as Eq. 5.2). So, assuming that the observed disk luminosity is unaffected by the presence of the BLR, the observed luminosity ratio is

$$R_{\rm obs,BLR}(\theta_{\rm v}, \theta_{\rm T}, a) = \frac{L^{\rm obs}_{\rm T,BLR}(\theta_{\rm T}, a)}{L^{\rm obs}_{\rm d}(\theta_{\rm v}, a)} = \frac{(1 - f_{\rm BLR})\mathcal{I}(\theta_{\rm T}, a) + f_{\rm BLR}\mathcal{H}(\theta_{\rm T})}{f(\theta_{\rm v}, a)}$$

Assuming $f_{\rm BLR} = 0.15$, the differences with respect to the ideal case without a BLR, both in the isotropic and anisotropic case, are small ($<$ 0.05 dex) for all angles.

C.3 Torus anisotropy

Possible changes of $R_{\rm obs}$ can occur if a torus anisotropic emission is considered. From the numerical model CAT3D (Hönig and Kishimoto, 2010), Castignani and Zotti, 2015 quantify the torus anisotropy (their Eq. 1)[2]: using that approximation and the same disk equation (Eq. 2.15) applied to the torus emission, it is possible to write:

$$\begin{aligned} L_{\rm T}(\theta_{\rm v}) &= \int_{\nu}\int_{\Omega} F^{\rm obs}_{\nu,{\rm T}}(\theta_{\rm v}) d^2_{\rm L} d\nu\, d\Omega \\ &\approx 2 \times \int_0^{\pi/2} 2\pi F^{\rm obs}_{\rm T}(0^\circ) d^2_{\rm L} \frac{a + b\cos\theta}{a + b} \sin\theta d\theta \\ &= L^{\rm obs}_{\rm T}(\theta_{\rm v}) \Big[\frac{1}{a + b\cos\theta_{\rm v}}\Big] \end{aligned} \tag{C.1}$$

[2]Notice that this numerical model does not fit properly the NIR emission (e.g.. Deo et al., 2011; Mor, Netzer, and Elitzur, 2009; Zhuang, Ho, and Shangguan, 2018).

where $F_{\rm T}^{\rm obs}(0^\circ)$ is the observed torus flux in a face-on configuration w.r.t. a distant observer, $a = 0.56$ and $b = 0.88$. Using this approximation, the observed luminosity ratio is modified with an extra term

$$R_{\rm obs}(\theta_{\rm v}, \theta_{\rm T}, a) = \frac{L_{\rm T}^{\rm obs}(\theta_{\rm v}, \theta_{\rm T}, a)}{L_{\rm d}^{\rm obs}(\theta_{\rm v}, a)} = \frac{\mathcal{I}(\theta_{\rm T}, a)[a + b\cos\theta_{\rm v}]}{f(\theta_{\rm v}, a)}$$

For $\theta_{\rm v} = 30^\circ$, the ratio is larger by a factor of ~ 0.12 dex with respect to the isotropic case (~ 0.16 dex for $\theta_{\rm v} = 0^\circ$).

Bibliography

Abramowicz, M. A., M. Calvani, and L. Nobili (1983). In: Nature, 302. 597-599.

Abramowicz, M. A. and W. Kluzniak (2001). In: Astronomy and Astrophysics, 374, L19.

Abramowicz, M. A. et al. (1988). In: The Astrophysical Journal, 332, 646-658.

Afanasiev, V. L. and L. C. Popovic (2015). In: The Astrophysical Journal, 800, L35.

Aghanim, N. et al. (2018). In: Planck Collaboration, arXiv:1807.06209.

Agol, E. and J. K. Krolik (2000). In: The Astrophysical Journal, 528, 161.

Ai, Y. L. et al. (2017). In: Monthly Notices of the Royal Astronomical Society, 470, 1587-1592.

Alexander, D. M. and R. C. Hickox (2011). In: arXiv:1112.1949.

Alonso-Herrero, A. et al. (2011). In: The Astrophysical Journal, 736, 82.

Alton, W. et al. (2016). In: Astronomische Nachrichten, 337(4-5),417-422.

Amorim, A. et al. (2020). In: Collaboration, GRAVITY, Accepted for publication in Astronomy & Astrophysics, arXiv:2009.08463.

Antonucci, R. (1993). In: Annual Review of Astronomy and Astrophysics, 31, 473.

Arnaud, K. A. (1996). In: Astronomical Data Analysis Software and Systems V. ASP Conference Series, Vol. 101, eds. G. H. Jacoby and J. Barnes, p. 17.

Asmus, D., S. F. Hönig, and P. Gandhi (2016). In: The Astrophysical Journal, 822, 109.

Baldwin, J. A. and H. Netzer (1978). In: The Astrophysical Journal, 226, 1.

Bañados, E. et al. (2018). In: Nature, 553.7689, 473.

Bardeen, J. M. (1970). In: The Astrophysical Journal, 162, 71.

Bardeen, J. M., W. H. Press, and S. A. Teukolsky (1972). In: The Astrophysical Journal, 178, 347.

Baron, D. et al. (2016). In: The Astrophysical Journal, 832(1), 8.

Barth, A. J. et al. (2003). In: The Astrophysical Journal, 594, L95.

Barvainis, R. (1987). In: The Astrophysical Journal, 320, 537.

Bechtold, J. A. et al. (2002). In: The Astrophysical Journal Supplements Series, 140, 143.

Becker, R. H., R. L. White, and D. J. Helfand (1995). In: The Astrophysical Journal, 450, 559.

Begelman, M. C. (1978). In: Monthly Notices of the Royal Astronomical Society, 184, 53.

Begelman, M. C., R. D. Blandford, and M. J. Rees (1984). In: Rev. Mod. Ph, 56, 255.

Begelman, M. C., C. F. McKee, and G. A. Shields (1983). In: The Astrophysical Journal, 271, 70.

Begelman, M. C., M. Volonteri, and M. J. Rees (2006). In: Monthly Notices of the Royal Astronomical Society, 370, 289.

Beifiori, A. et al. (2012). In: Monthly Notices of the Royal Astronomical Society, 419, 2497.

Belloni, T. M., A. Sanna, and M. Mendez (2012). In: Monthly Notices of the Royal Astronomical Society, 426(3), 1701-1709.

Bendo, G. J. et al. (2003). In: The Astrophysical Journal, 125, 2361.

Bentz, M. C. and S. Katz (2015). In: The Publications of the Astronomical Society of the Pacific, 127 (947), 67.

Bentz, M. C. and E. Manne-Nicholas (2018). In: The Astrophysical Journal, 864, 146.

Bentz, M. C. et al. (2009). In: The Astrophysical Journal, 697, 160.

Bentz, M. C. et al. (2014). In: The Astrophysical Journal, 796(1), 8.

Berk, D. E. V. et al. (2001a). In: The Astrophysical Journal, 122, 549.

Berk, D. E. Vande et al. (2001b). In: The Astrophysical Journal, 122, 549.

Blandford, R. D. and C. F. McKee (1982). In: The Astrophysical Journal, 255, 419.

Blandford, R. D. and D. G. Payne (1982). In: Monthly Notices of the Royal Astronomical Society, 199, 883.

Blandford, R. D. and R. L. Znajek (1977). In: Monthly Notices of the Royal Astronomical Society, 179, 433-456.

Bondi, H. (1952). In: Monthly Notices of the Royal Astronomical Society, 112, 195.

Bonning, E. W. et al. (2007). In: The Astrophysical Journal, 659, 211.

Boroson, T. A. and R. F. Green (1992). In: The Astrophysical Journal Supplement Series, 80, 109-135.

Boselli, A. et al. (2010). In: Astronomy & Astrophysics, 518, L61.

Broderick, A. E. et al. (2011). In: The Astrophysical Journal, 738(1), 38.

Buchner, J. and F. E. Bauer (2017). In: Monthly Notices of the Royal Astronomical Society, 465, 4348-4362.

Burlon, D. et al. (2011). In: The Astrophysical Journal, 728, 58.

Caballero-Garcia, M. D. et al. (2019). In: arXiv:1901.04357.

Calderone, G., T. Sbarrato, and G. Ghisellini (2012). In: Monthly Notices of the Royal Astronomical Society, 425, L41.

Calderone, G. et al. (2013). In: Monthly Notices of the Royal Astronomical Society, 431, 210.

Calzetti, D. et al. (2000). In: The Astrophysical Journal, 533(2), 682.

Campitiello, S. et al. (2018). In: Astronomy & Astrophysics, 612, A59.

Campitiello, S. et al. (2019). In: Astronomy & Astrophysics, 625, A23.

— (2020). In: Astronomy & Astrophysics, 640, A39.

— (2021). In: submitted to Astronomy & Astrophysics.

Capellupo, D. M. et al. (2011). In: Monthly Notices of the Royal Astronomical Society, 413, 908.

Capellupo, D. M. et al. (2015). In: Monthly Notices of the Royal Astronomical Society, 446, 3427-3446.

Capellupo, D. M. et al. (2016). In: Monthly Notices of the Royal Astronomical Society, 460, 212-226.

Cardelli, J. A., G. C. Clayton, and J. S. Mathis (1989). In: The Astrophysical Journal, 345, 245.

Castelló-Mor, N. and H. Netzer S. Kaspi (2016). In: Monthly Notices of the Royal Astronomical Society, 458(2), 1839-1858.

Castignani, G. and G. De Zotti (2015). In: Astronomy & Astrophysics, 573, A125.

Castignani, G. et al. (2013). In: Astronomy & Astrophysics, 560, A28.

Chainakun, P. et al. (2019). In: Monthly Notices of the Royal Astronomical Society, 487(1), 667-680.

Chandrasekhar, S. (1950). In: "Radiative Transfer", Oxford: Oxford Univ. Press).

Chelouche, D. and H. Netzer (2005). In: The Astrophysical Journal, 625, 95.

Chen, M. A. Abramowicz X. et al. (1995). In: The Astrophysical Journal Letters, 438, L37-L39.

Collaboration, Event Horizon Telescope (2019). In: The Astrophysical Journal Letters, 875(1), L6.

Collin, S. et al. (2006). In: Astronomy & Astrophysics, 456, 75.

Collinson, J. S. et al. (2016). In: Monthly Notices of the Royal Astronomical Society, stw2666.

Contopoulos, J. and R. V. E. Lovelace (1994). In: The Astrophysical Journal, 429, 139.

Crummy, J. et al. (2006). In: Monthly Notices of the Royal Astronomical Society, 365(4), 1067-1081.

Cunningham, C. T. (1975). In: The Astrophysical Journal, 202, 788.

— (1976). In: The Astrophysical Journal, 208, 534.

Czerny, B. et al. (2004). In: Monthly Notices of the Royal Astronomical Society, 348(3), L54-L57.

Czerny, B. et al. (2011). In: Monthly Notices of the Royal Astronomical Society, 415(3), 2942-2952.

Dai, X. et al. (2010). In: The Astrophysical Journal, 709, 278.

Dale, D. A. et al. (2012). In: The Astrophysical Journal, 745, 95.

Davies, R. I. (2006). In: The Astrophysical Journal, 646(2), 754.

Davis, S. W. and S. El-Abd (2019). In: The Astrophysical Journal, 874(1), 23.

Davis, S. W. and A. Laor (2011). In: The Astrophysical Journal, 728, 98.

Davis, S. W. et al. (2007). In: The Astrophysical Journal, 668, 682.

Decarli, R. et al. (2008). In: Monthly Notices of the Royal Astronomical Society, 386, L15-L19.

Denney, K. D. et al. (2010). In: The Astrophysical Journal, 721(1), 715.

Deo, R. P. et al. (2011). In: The Astrophysical Journal, 729, 108.

Done, C. et al. (2012). In: Monthly Notices of the Royal Astronomical Society, 420, 1848.

Dotti, M. et al. (2013). In: The Astrophysical Journal, 762, 68.

Du, P. et al. (2018). In: The Astrophysical Journal, 869(2), 142.

Duras, F. et al. (2020). In: Astronomy & Astrophysics, 636, A73.

Ebisawa, K., K. Mitsuda, and T. Hanawa (1991). In: The Astrophysical Journal, 367, 213.

Elvis, M., G. Risaliti, and G. Zamorani (2002). In: The Astrophysical Journal Letters, 565(2), L75.

Everett, J. E. and N. Murray (2007). In: The Astrophysical Journal, 656, 93.

Ezhikode, S. H. et al. (2017). In: Monthly Notices of the Royal Astronomical Society, 472, 3492.

Fabian, A. C. et al. (1989). In: Monthly Notices of the Royal Astronomical Society, 238, 729-736.

Fabian, A. C. et al. (2009). In: Monthly Notices of the Royal Astronomical Society, 394, L89-L92.

Fabian, A. C. et al. (2015). In: Monthly Notices of the Royal Astronomical Society, 451, 4375.

Fan, X. et al. (2001). In: The Astrophysical Journal, 122, 2833.

Fanton, C. et al. (1997). In: Publications of the Astronomical Society of Japan, 49, 159.

Fausnaugh, M. M. et al. (2017). In: The Astrophysical Journal, 840, 97.

Ferrarese, L. and D. Merrit (2000). In: The Astrophysical Journal, 539, L9.

Franck, J., A. King, and D. Raine (2002). In: "Accretion Power in Astrophysics", 3rd edn., Cambridge University Press.

Fritz, J., A. Franceschini, and E. Hatziminaoglou (2006). In: Monthly Notices of the Royal Astronomical Society, 366, 767.

Gallagher, S. C. et al. (2006). In: The Astrophysical Journal, 644, 709.

Gammie, C. F. (1999). In: The Astrophysical Journal, 522, L57.

Ganguly, R. et al. (2007). In: The Astrophysical Journal, 665, 990.

Gao, F. et al. (2017). In: The Astrophysical Journal, 834, 52.

Gardner, E. and C. Done (2018). In: Monthly Notices of the Royal Astronomical Society, 473(2), 2639-2654.

Garofalo, D. (2013). In: Advances in Astronomy.

Ghisellini, G. (2012). In: Radiative process in high energy astrophysics arXiv:1202.5949.

Ghisellini, G., F. Haardt, and G. Matt (1994). In: Monthly Notices of the Royal Astronomical Society, 267, 743.

Ghisellini, G. and F. Tavecchio (2015). In: Monthly Notices of the Royal Astronomical Society, 448.2, 1060-1077.

Ghisellini, G. et al. (2009). In: Monthly Notices of the Royal Astronomical Society, 399, L24.

Ghisellini, G. et al. (2010). In: Monthly Notices of the Royal Astronomical Society, 402, 497.

Ghisellini, G. et al. (2014). In: Nature, 515(7527), 376-378.

Ghisellini, G. et al. (2015). In: Monthly Notices of the Royal Astronomical Society, 450, L34-L38.

Ghisellini, G. et al. (2017). In: Monthly Notices of the Royal Astronomical Society, 469(1), 255-266.

Graham, A. W. et al. (2011). In: Monthly Notices of the Royal Astronomical Society, 412, 221.

Granato, G. L. and L. Danese (1994). In: Monthly Notices of the Royal Astronomical Society, 268, 235.

Greene, J. E. et al. (2010). In: The Astrophysical Journal, 721, 26.

Grier, C. J. et al. (2012). In: The Astrophysical Journal, 755(1), 60.

— (2013). In: The Astrophysical Journal, 773, 90.

— (2017). In: The Astrophysical Journal, 849(2), 146.

Gu, M. (2013). In: The Astrophysical Journal, 773, 176.

Gu, M. F. and S. L. Li (2013). In: Astronomy & Astrophysics, 554, A51.

Guerras, E. (2013). In: The Astrophysical Journal, 764(2), 160.

Gültekin, K., D. O. Richstone, and K. Gebhardt (2009). In: The Astrophysical Journal, 698, 198.

Gunn, J. E. and B. A. Peterson (1965). In: The Astrophysical Journal, 142, 1633.

Haardt, F. and P. Madau (2012). In: The Astrophysical Journal, 746, 125.

Haas, M. et al. (2011). In: Astronomy & Astrophysics, 535, A73.

Haiman, Z. (2004). In: The Astrophysical Journal, 613, 36.

Haiman, Z. and A. Loeb (2001). In: The Astrophysical Journal, 552, 459-463.

Hanawa, T. (1989). In: The Astrophysical Journal, 341, 948.

Hao, H. et al. (2013). In: Monthly Notices of the Royal Astronomical Society, 434, 3104.

Häring, N. and H.-W. Rix (2004). In: The Astrophysical Journal Letters, 604, L89.

Hatziminaoglou, E. et al. (2008). In: Monthly Notices of the Royal Astronomical Society, 386, 1252.

Hernán-Caballero, A. et al. (2004). In: Monthly Notices of the Royal Astronomical Society, 463, 2064-2078.

Hicks, E. K. S. and M. A. Malkan (2008). In: The Astrophysical Journal Supplements, 174, 31.

Ho, L. C. (1999). In: Observational Evidence for Black Holes in the Universe, ed. S. K. Chakrabarti (Dordrecht: Kluwer), 157.

Ho, L. C., A. V. Filippeko, and W. L. Sargent (1999). In: The Astrophysical Journal Supplement Series, 98, 477-593.

Hönig, S. F. (2019). In: The Astrophysical Journal, 884(2), 171.

Hönig, S. F. and M. Kishimoto (2010). In: Astronomy & Astrophysics, 523, 27.

Hoyle, F. and R. A. Lyttleton (1939). In: Proc. Camb. Phil. Soc., 35, 592.

Hubeny, I. and T. Lanz (1995). In: The Astrophysical Journal, 439, 875.

Hubeny, I. et al. (2000). In: The Astrophysical Journal, 533, 710.

Hubeny, I. et al. (2011). In: The Astrophysical Journal, 559(2), 680.

Ichimaru, S. (1977). In: The Astrophysical Journal, 214, 840-855.

Irwin, M. J. et al. (1989). In: The Astrophysical Journal, 98, 1989.

Ishibashi, W. (2020). In: Monthly Notices of the Royal Astronomical Society, 495(2), 2515-2523.

Ishibashi, W., A. C. Fabian, and C. S. Reynolds (2019). In: Monthly Notices of the Royal Astronomical Society, 486(2), 2210-2214.

Jaffe, W. et al. (2004). In: Nature, 429, 47.

Jaroszynski, M., M. A. Abramowicz, and B. Paczynski (1980). In: Acta Astron., 30, 1-34.

Jaroszynski, M., J. Wambsganss, and B. Paczynski (1992). In: The Astrophysical Journal, 396, L65.

Jiang, L. et al. (2007). In: The Astrophysical Journal, 656, 680.

Jones, D. H. et al. (2009). In: Monthly Notices of the Royal Astronomical Society, 399(2), 683-698.

Kammoun, E. S., E. Nardini, and G. Risaliti (2018). In: Astronomy and Astrophysics, 614, A44.

Kaspi, S. et al. (2000). In: The Astrophysical Journal, 533, 631.

— (2007). In: The Astrophysical Journal, 659, 997.

Katz, J. I. (1977). In: The Astrophysical Journal, 215, 265.

Kawakatu, N. and K. Ohsuga (2011). In: Monthly Notices of the Royal Astronomical Society, 417(4), 2562-2570.

Kellermann, K. I. et al. (1989). In: The Astrophysical Journal, 98, 1195.

Kennicutt, R. C. (1992). In: The Astrophysical Journal, 388, 310.

Kennicutt, R. C. et al. (2003). In: The Publications of the Astronomical Society of the Pacific, 115(810), 928.

King, A. R. and K. A. Pounds (2003). In: Monthly Notices of the Royal Astronomical Society, 345, 657.

King, A. R., J. E. Pringle, and M. Livio (2007). In: Monthly Notices of the Royal Astronomical Society, 376, 1740-1746.

Kinney, A. L. (1991). In: The Astrophysical Journal Supplement Series, 75, 645-717.

Kishimoto, M. et al. (2008). In: Nature, 454, 492.

Kollatschny, W. (2003). In: Astronomy & Astrophysics, 412, L61.

Kollatschny, W. and M. Zetzl (2013). In: Astronomy & Astrophysics, 558, A26.

Konigl, A. and J. F. Kartje (1994). In: The Astrophysical Journal, 434, 446.

Koratkar, A. and O. Blaes (1999). In: The Publications of the Astronomical Society of the Pacific, 111, 1.

Koushiappas, S. M., J. S. Bullock, and A. Dekel (2004). In: Monthly Notices of the Royal Astronomical Society, 354, 292.

Krogager, J. K., S. Geiser, J. P. U. Fynbo, et al. (2015). In: The Astrophysical Journal Supplement Series, 217(1), 5.

Krolik, J. K. (1999). In: The Astrophysical Journal, 515, L73.

Krolik, J. K. and M. C. Begelman (1988). In: The Astrophysical Journal, 329, 702.

Krolik, J. K. and J. M. Vrtilek (1984). In: The Astrophysical Journal, 279, 521.

Kubota, A. and C. Done (2018). In: Monthly Notices of the Royal Astronomical Society, 480(1), 1247-1262.

Kuhr, H. et al. (1981). In: The Astrophysical Journal, 86, 854.

Kuhr, H. et al. (1983). In: The Astrophysical Journal, 275, L33.

Kuo, C. Y. et al. (2011). In: The Astrophysical Journal, 727, 2.

Lamastra, A., G. C. Perola, and G. Matt (2006). In: Astronomy & Astrophysics, 449, 551-558.

Landt, H. et al. (2011). In: Monthly Notices of the Royal Astronomical Society, 414(1), 218-240.

— (2013). In: Monthly Notices of the Royal Astronomical Society, 432(1), 113-126.

Laor, A. (1990). In: Monthly Notices of the Royal Astronomical Society, 246, 369.

Laor, A. and S. Davis (2011). In: Monthly Notices of the Royal Astronomical Society, 417.1, 681-688.

Laor, A. and H. Netzer (1989). In: Monthly Notices of the Royal Astronomical Society, 238, 897.

Lapi, A. et al. (2014). In: The Astrophysical Journal, 782(2), 69.

Lawrence, A. (1991). In: Monthly Notices of the Royal Astronomical Society, 252, 586-592.

Lawrence, A. and M. Elvis (1982). In: The Astrophysical Journal, 256, 410-426.

Lawrence, C. R. et al. (1996). In: The Astrophysical Journal SUpplement Series, 107(2), 541.

Leftley, J. H. et al. (2018). In: The Astrophysical Journal, 862, 17.

Leipski, C., K. Meisenheimer, F. Walter, et al. (2014). In: The Astrophysical Journal, 785(2), 154.

Lewis, G. F. et al. (1998). In: Monthly Notices of the Royal Astronomical Society, 295, 573.

Li, G. X., Y. F. Yuan, and X. Cao (2010). In: The Astrophysical Journal, 715(1), 623.

Li, L.-X. (2004). In: The Publications of the Astronomical Society of Japan, 56, 685.

— (2012). In: Monthly Notices of the Royal Astronomical Society, 424(2), 1461-1470.

Li, L.-X. et al. (2005). In: The Astrophysical Journal Supplement Series, 157(2), 335.

Li, Y. et al. (2007). In: The Astrophysical Journal, 665, 187-208.

Li, Y. R. et al. (2018). In: The Astrophysical Journal, 869(2), 137.

Lohfink, A. M., C. S. Reynolds, R. Vasudevan, et al. (2014). In: The Astrophysical Journal, 788(1), 10.

Lu, Y. J. et al. (1996). In: The Astrophysical Journal, 347, 148.

Lubinski, P. et al. (2016). In: Monthly Notices of the Royal Astronomical Society, 458, 2454.

Lusso, E., A. Comastri, B. D. Simmons, et al. (2012). In: Monthly Notices of the Royal Astronomical Society, 425, 623.

Lusso, E. and G. Risaliti (2017). In: Astronomy & Astrophysics, 602, A79.

Lyu, J. and G. H. Rieke (2018). In: The Astrophysical Journal, 866(2), 92.

Lyu, J., G. H. Rieke, and Y. Shi (2017). In: The Astrophysical Journal, 835, 527.

Lyu, J., G. H. Rieke, and P. S. Smith (2019). In: The Astrophysical Journal, 866(1), 33.

López-Gonzaga, N. et al. (2016). In: Astronomy & Astrophysics, 591, A47.

Ma, X.-C. and T.-G. Wang (2013). In: Monthly Notices of the Royal Astronomical Society, 430, 3445.

Madau, P. (1995). In: The Astrophysical Journal, 441, 18-27.

Madau, P. and M. J. Rees (2001). In: The Astrophysical Journal Letters, 551, L27.

Magdis, G. E. et al. (2012). In: The Astrophysical Journal, 760(1), 6.

Magorrian, J. et al. (1998). In: The Astrophysical Journal, 115, 228.

Majia-Restrepo, J. E. et al. (2016). In: Monthly Notices of the Royal Astronomical Society, 460, 187.

Majia-Restrepo, J. E. et al. (2018). In: Nature, 2(1), 63-68.

Malkan, M. A. (1983). In: The Astrophysical Journal, 268, 582.

Manucci, F. et al. (2001). In: Monthly Notices of the Royal Astronomical Society, 326, 745.

Marconi, A. et al. (2008). In: The Astrophysical Journal, 678, 693.

Marculewicz, M. and M. Nikolajuk (2020). In: The Astrophysical Journal, 897(2), 117.

Masini, A. et al. (2019). In: The Astrophysical Journal, 882(2), 83.

Matsuoka, Y. et al. (2019). In: The Astrophysical Journal Letters, 872, L2.

McClintock, J. E., R. Narayan, and J. F. Steiner (2013). In: The Physics of Accretion onto Black Holes, pp. 295-322, Springer, New York, NY.

McClintock, J. E. et al. (2006). In: The Astrophysical Journal, 652, 518.

McLure, R. J. and J. S. Dunlop (2004). In: Monthly Notices of the Royal Astronomical Society, 352, 1390.

McLure, R. J. and M. J. Jarvis (2002). In: Monthly Notices of the Royal Astronomical Society, 337, 109.

Mediavilla, E. et al. (2018). In: The Astrophysical Journal, 862, 104.

— (2019). In: The Astrophysical Journal, 880(2), 95.

Menci, N. et al. (2008). In: The Astrophysical Journal, 686, 219-229.

Merloni, A. et al. (2014). In: Monthly Notices of the Royal Astronomical Society, 437, 3550.

Miniutti, G. and A. C. Fabian (2004). In: Monthly Notices of the Royal Astronomical Society, 349, 1435.

Miyoshi, M. et al. (1995). In: Nature, 373, 127.

Momjian, E. et al. (2014). In: The Astrophysical Journal, 147, 6.

Mor, R. and H. Netzer (2012). In: Monthly Notices of the Royal Astronomical Society, 420, 526.

Mor, R., H. Netzer, and M. Elitzur (2009). In: The Astrophysical Journal, 705, 298.

Mortlock, D. J. et al. (2011). In: Nature, 474, 616.

Mosquera, A. M. and C. S. Kochanek (2011). In: The Astrophysical Journal, 738, 96.

Moustaka, L. et al. (2019). In: Bulletin of the American Astronomical Society, 51(3), 487.

Narayan, R. and I. Yi (1995). In: The Astrophysical Journal, 444, 231-243.

Nenkova, M. et al. (2008a). In: The Astrophysical Journal, 685, 147.

Nenkova, M. et al. (2008b). In: The Astrophysical Journal, 685, 160.

Netzer, H. (1990). In: AGN emission lines. In Active Galactic Nuclei, pp. 57-158, Springer, Berlin, Heidelberg.

— (2015). In: Annual Review of Astronomy and Astrophysics, 53, 365-408.

Netzer, H. and B. M. Peterson (1997). In: Astrophysics and Space Science Library, 218, 85.

Neugebauer, G. et al. (1979). In: The Astrophysical Journal, 230, 79.

Novikov, I. D. and K. S. Thorne (1973). In: Astrophysics of Black holes, ed. C. De Witt and B. De Witt (New York: Gordon and Breach), 343.

Nuñez, F. Pozo et al. (2019). In: Monthly Notices of the Royal Astronomical Society, 490(3), 3936-3951.

Onken, C. A. et al. (2004). In: The Astrophysical Journal, 615, 645.

— (2007). In: The Astrophysical Journal, 670, 105.

Osterbrock, D. E. and W. G. Mathews (1986). In: Annual review of astronomy and astrophysics, 24(1), 171-203.

O'Leary, R. M. et al. (2006). In: The Astrophysical Journal, 637, 937.

Paczynski, B. and P. J. Wiita (1980). In: Astronomy & Astrophysics, 88, 23-31.

Padovani, P. (1997). In: 32nd Rencontres de Moriond: High-Energy Phenomena in Astrophysics, arXiv preprint astro-ph/9704002.

Padovani, P. et al. (2017). In: Astron. Astrophys. Rev. 25, 2.

Page, D. N. and K. S. Thorne (1974). In: The Astropysical Journal, 191, 507.

Pan, Z. and H. Yang (2020). In: The Astropysical Journal, 901(2), 163.

Park, D. et al. (2012). In: The Astropysical Journal, 747, 30.

Pearson, E. A., S. Eales, L. Dunne, et al. (2013). In: Monthly Notices of the Royal Astronomical Society, 435(4), 2753-2763.

Pelupessy, F. I., T. D. Matteo, and B. Ciardi (2007). In: The Astropysical Journal, 665, 107.

Peterson, B. M. (1993). In: The Publications of the Astronomical Society of the Pacific, 105, 247.

Peterson, B. M. (2006). In: The broad-line region in active galactic nuclei, In Physics of Active Galactic Nuclei at all Scales, pp. 77-100, Springer, Berlin, Heidelberg.

— (2010). In: IAU Symposium, 267, 151.

— (2011). In: in *Narrow-Line Seyfert 1 Galaxies and their Place in the Universe*, Proceedings of Science, vol. NLS1, 32.

Peterson, B. M. et al. (2004). In: The Astrophysical Journal, 613, 682.

Petrucci, P. O. et al. (2017). In: arXiv:1710.04940.

Pettini, M. and A. Boksenberg (1984). In: The Astrophysical Journal, 294, L73-L78.

Pier, E. A. and J. H. Krolik (1993). In: The Astrophysical Journal, 418, 673.

Pounds, K. A. et al. (2003). In: Monthly Notices of the Royal Astronomical Society, 346, 1025.

Proga, D. and T. R. Kallman (2004). In: The Astrophysical Journal, 616, 688.

Proga, D., J. M. Stone, and T. R. Kallman (2000). In: The Astrophysical Journal, 543, 686.

Rauch, K. P. and R. D. Blandford (1994). In: The Astrophysical Journal, 421, 46.

Reb, L. et al. (2018). In: Monthly Notices of the Royal Astronomical Society, 478(1), L122-L126.

Rees, M. J. et al. (1969). In: Nature, 223, 788.

Rees, M. J. et al. (1982). In: Nature, 295, 17-21.

Reeves, J. N., P. T. O'Brien, and M. J. Ward (2003). In: The Astrophysical Journal, 593, L65.

Reines, A. E. and M. Volonteri (2015). In: The Astrophysical Journal, 813, 82.

Reis, R. C. and J. M. Miller (2013). In: The Astrophysical Journal Letter, 769, L7.

Reynolds, C. S. (2020). In: Annual Review of Astronomy & Astrophysics, 59.

Ricci, C. et al. (2017). In: Nature, 549(7673), 488-491.

Ricci, C. et al. (2020). In: The Astrophysical Journal Letter, 898, 1.

Richards, G. T. et al. (2004). In: The Astrophysical Journal, 610, 679.

— (2006). In: The Astrophysical Journal Supplements, 166, 470.

Riffel, R. et al. (2006). In: Astronomy & Astrophysics, 457(1), 61-70.

Riffert, H. and H. Herold (1995). In: The Astrophysical Journal, 450, 508.

Risaliti, G. and M. Elvis (2010). In: Astronomy & Astrophysics, 516, A89.

Risaliti, G., M. Elvis, and F. Nicastro (2002). In: The Astrophysical Journal, 571(1), 234.

Risaliti, G. and E. Lusso (2019). In: Nature Astronomy, 3(3), 272-277.

Rokaki, E., C. Boisson, and S. Collin-Souffrin (1992). In: Astronomy & Astrophysics, 253, 57.

Rosa, G. De et al. (2014). In: The Astrophysical Journal, 790(2), 145.

— (2018). In: The Astrophysical Journal, 866(2), 133.

Ross, R. R. and A. C. Fabian (2005). In: Monthly Notices of the Royal Astronomical Society, 358, 211.

Rudge, C. M. and D. J. Raine (2000). In: Monthly Notices of the Royal Astronomical Society, 311(3), 621-628.

Ruszkowski, M. and M. C. Begelman (2003). In: The Astrophysical Journal, 586, 3.

Sadowski, A. (2009). In: The Astrophysics Journal Supplements, 183, 171.

Sadowski, A. et al. (2009). In: Astronomy & Astrophysics, 502, 7.

— (2011). In: Astronomy & Astrophysics, 527, A17.

Salpeter, E. E. (1964). In: The Astrophysical Journal, 140, 796.

Sanders, D. B. et al. (1989). In: The Astrophysical Journal, 347, 29.

Savic, D. et al. (2018). In: Astronomy & Astrophysics, 614, A120.

Sazonov, S. et al. (2012). In: The Astrophysical Journal, 757.2, 181.

Sbarrato, T. et al. (2013). In: Monthly Notices of the Royal Astronomical Society, 433, 2182.

Sbarrato, T. et al. (2016). In: Monthly Notices of the Royal Astronomical Society, 462, 1542-1550.

Schartmann, M. et al. (2005). In: Astronomy & Astrophysics, 437, 861.

Scheuer, P. A. G. (1965). In: Nature, 207, 963.

Schlegel, D. J., D. P. Finkbeiner, and M. Davis (1998). In: The Astrophysical Journal, 500, 525.

Schneider, D. P. et al. (2010). In: The Astrophysical Journal, 139, 2360.

Schnittman, J. D. and E. Bertschinger (2003). In: Astrophysics - Physics, 606, 1098.

Seoane, P. A. et al. (2013). In: "The gravitational universe" arXiv preprint arXiv:1305.5720.

Shakura, N. I. and R. A. Sunyaev (1973). In: Astronomy and Astrophysics, 24, 337.

— (1976). In: Monthly Notices of the Royal Astronomical Society, 175. 613.

Shang, Z. H. et al. (2005). In: The Astrophysical Journal, 619, 41.

— (2011). In: The Astrophysical Journal Supplements, 196, 2.

Shaw, M. S., R. W. Romani, and G. Cotter (2012). In: The Astrophysical Journal, 748, 49.

Shen, J. et al. (2008). In: The Astropysics Journal, 135, 928.

Shen, Y. et al. (2011). In: The Astropysics Journal Supplements, 194, 45.

— (2019). In: The Astropysics Journal Letters, 883, L14.

Shields, G. A. (1977). In: Astropysics Letters, 18, 119.

Shima, I. et al. (1985). In: Monthly Notices of the Royal Astronomical Society, 217, 367.

Shimura, T. and F. Takahara (1995). In: The Astrophysical Journal, 445, 780-788.

Shklovski, I. S. (1965). In: Soviet Astron.-AJ, 8, 638.

Sikora, M., L. Stawarz, and J.-P. Lesota (2007). In: The Astrophysical Journal, 658, 815.

Sim, S. A. et al. (2008). In: Monthly Notices of the Royal Astronomical Society, 388, 611.

Simpson, C. (2005). In: Monthly Notices of the Royal Astronomical Society, 360, 565-572.

Slone, O. and H. Netzer (2012). In: Monthly Notices of the Royal Astronomical Society, 426, 656-664.

Sluse, D. et al. (2011). In: Astronomy & Astrophysica, 528, 100.

Smith, M. G. et al. (1981). In: Monthly Notices of the Royal Astronomical Society, 195, 437.

Stalevski, M. et al. (2016). In: Monthly Notices of the Royal Astronomical Society, 458(3), 2288-2302.

Straub, O., C. Done, and M. Middleton (2013). In: Astronomy & Astrophysics, 533, A61.

Straub, O. et al. (2011). In: Astronomy & Astrophysics, 533, A67.

Sturm, E. et al. (2018). In: Collaboration, GRAVITY, Nature, 563, 10.1038/s41586-018-0731-9.

Subovas, K. and A. R. King (2019). In: arXiv:1908.02630.

Sun, W.-H. and M. A. Malkan (1989). In: The Astrophysical Journal, 346, 68.

Szuszkiewicz, E., M. A. Malkan, and M. A. Abramowicz (1996). In: The Astrophysical Journal, 458, 474.

Tacconi, L. J. et al. (1994). In: The Astrophysical Journal, 426, L77.

Tanaka, T. and Z. Haiman (2009). In: The Astrophysical Journal, 696, 1798.

Tarchi, A. (2012). In: IAU Symp., 287, 323 (arXiv: 1205.3623).

Tchekhovskoy, A. and J. C. McKinney (2012). In: Monthly Notices of the Royal Astronomical Society, 423(1), L55-L59.

Tchekhovskoy, A., R. Narayan, and J. C. McKinney (2011). In: Monthly Notices of the Royal Astronomical Society, 418, L79-L83.

Thorne, K. S. (1974). In: The Astrophysical Journal, 191, 3, pp. 507–519.

Toba, T. et al. (2021). In: The Astrophysical Journal (accepted), arXiv:2102.04620.

Tombesi, F. et al. (2010). In: Astronomy & Astrophysics, 521, A57.

— (2011). In: The Astrophysical Journal, 742, 44.

Trakhtenbrot, B. (2014). In: The Astrophysical Journal Letters, 789(1), L9.

Trakhtenbrot, B. and H. Netzer (2012). In: Monthly Notices of the Royal Astronomical Society, 427, 3081.

Trakhtenbrot, B., M. Volonteri, and P. Natarajan (2017). In: The Astrophysical Journal Letters, 836, L1.

Treister, E., J. H. Krolik, and C. Dullemond (2008). In: The Astrophysical Journal Letters, 679, 140-148.

Trevese, D. et al. (2014). In: The Astrophysical Journal, 795, 164.

Tripp, T. M., J. Bechtold, and R. F. Green (1994). In: The Astrophysical Journal, 433, 533.

Tristram, K. R. W. et al. (2007). In: Astronomy & Astrophysics. 474, 837.

Tsuzuki, Y. et al. (2006). In: The Astrophysical Journal, 650, 57.

Ueda, Y. et al. (2003). In: The Astrophysical Journal, 598, 886-908.

Urry, C. M. and P. Padovani (1995). In: The Publications of the Astronomical Society of the Pacific, 107, 803.

Uzdensky, D. A. (2004). In: The Astrophysical Journal, 603, 652.

Vasudevan, R. V. and A. C. Fabian (2009). In: Monthly Notices of the Royal Astronomical Society, 392, 1124-1140.

Venemans, B. P. et al. (20017). In: The Astrophysical Journal, 837, 146.

Vestergaard, M. (2004). In: The Astrophysical Journal, 571, 733.

Vestergaard, M. and P. S. Osmer (2009). In: The Astrophysical Journal, 699, 800.

Vestergaard, M. and B. M. Peterson (2006). In: The Astrophysical Journal, 641, 689.

Volonteri, M. (2007). In: The Astrophysical Journal, 641, 689.

— (2010). In: Astronomy & Astrophysics Review, 18, 279.

Volonteri, M., F. Haardt, and P. Madau (2003). In: The Astrophysical Journal, 582, 559.

Volonteri, M. and P. Natarajan (2009). In: Monthly Notices of the Royal Astronomical Society, 400, 1911.

Volonteri, M. and M. J. Rees (2005). In: The Astrophysical Journal, 633, 624.

Wada, D. (2015). In: The Astrophysical Journal, 812, 82.

Walter, R. and H. H. Fink (1993). In: Astronomy & Astrophysica, 274, 105.

Walton, D. J. et al. (2013). In: Monthly Notices of the Royal Astronomical Society, 428(4), 2901-2920.

Wandel, A., B. M. Peterson, and M. A. Malkam (1999). In: The Astrophysical Journal, 526, 579.

Wandel, A. and V. Petrosian (1988). In: The Astrophysical Journal, 329, L11.

Wang, D.-X. (1998). In: "General Relativity and Gravitation", 30, 7, 1025-1035.

Wang, D.-X. et al. (2003). In: The Astrophysical Journal, 595, 109.

Wang, F. et al. (2018). In: arXiv:1810.11925.

— (2020). In: The Astrophysical Journal, 896(1), 23.

— (2021). In: Accepted for publication in the Astrophysical Journal Letters, arXiv:2101.03179.

Wang, J. G. et al. (2009). In: The Astrophysical Journal, 707, 1334.

Wang, J. M. et al. (2014). In: The Astrophysical Journal, 793(2), 108.

Wielgus, M. et al. (2016). In: Astronomy & Astrophysics, 587, A38.

Wilkes, M. Vestergaard B. J. (2001). In: The Astrophysical Journal Supplements, 134, 1.

Willott, C. J., R. J. McLure, and M. J. Jarvis (2003). In: The Astrophysical Journal, 587, L15.

Wills, B. J. and I. W. A. Browne (1986). In: The Astrophysical Journal, 302, 56.

Wills, B. J., H. Netzer, and D. Wills (1985). In: The Astrophysical Journal, 288, 94.

Wright, E. L. et al. (2010). In: The Astrophysical Journal, 140, 1868.

Yang, J. et al. (2020). In: The Astrophysical Journal Letters, 897, L14.

Yi, W. M. et al. (2014). In: The Astrophysical Journal, 795, L29.

Yoo, J. and J. M. Escude (2004). In: The Astrophysical Journal, 614, L25-L28.

York, D. G. et al. (2000). In: The Astrophysical Journal, 120, 1579.

Younes, G., A. Ptak, L. C. Ho, et al. (2019). In: The Astrophysical Journal, 870(2), 73.

Zeldovich, Y. B. and I. B. Novikov (1964). In: Dokl. Acad. Nauk SSSR, 158, 811.

Zhang, S. N., W. Cui, and W. Chen (1997). In: The Astrophysical Journal, 482, L155.

Zhang, S. X. et al. (2019). In: The Astrophysical Journal, 876(1), 49.

Zhao, X. et al. (2020). In: arXiv:2011.03851.

Zhuang, M. Y., L. C. Ho, and J. Shangguan (2018). In: The Astrophysical Journal, 862(2), 118.